

An investigation of depositional mechanisms of
pyroclastic density currents using anisotropy of magnetic
susceptibility (AMS) and a detailed stratigraphic study of the
La Caleta Formation, Tenerife.

Clare Maher

For the degree of Doctor of Philosophy

Department of Geology, University of Leicester

September 2006

CONTAINS

PULLOUTS

Dedicated to

Bill and Pearl who have watched my dream become a reality,

and

*my grandmother Joyce, who instilled in me the importance of a good
education.*

I did it!

Acknowledgments

Since I was four years old I have had a fascination with volcanoes and my ambition in life was to do a PhD and become a volcanologist. Many years and tears later I have finally realised my dream, but not without the help of many people.

Firstly I would like to thank the Department of Geology at the University of Leicester for providing me with so many opportunities over the last eight years and for funding my PhD. Thank you also to the BSRG and the IAS, who provided additional funding, and to the Department of Earth Sciences at the University of Birmingham for allowing me to use their facilities. I would also like to thank my examiners Jan Zalasiewicz and Peter Kokelaar.

Secondly my supervisors; thanks to Mike Branney for pushing me that bit further and for his volcanological wisdom; Bill Owens for his endless patience when explaining the detailed ins and outs of AMS for the hundredth time and also Sarah Davies for reading my work and her on going support. The technical staff, Colin, Lyn, Nick, Rob and Dave that reside in the deepest, darkest depths of the department, also deserve my thanks for their time and expertise and also Rod Branson and Rob Wilson for their assistance with the SEM and microprobe. Thanks also to Paul Ayto for his assistance in all things financial!

I cannot go on without thanking all my fellow postgrads in the department. Many of whom have become good friends, particularly Rowan Whittle, David Jones and Dave Cornwall. Special thanks have to be reserved for Graham Andrews, who has offered support and encouragement when I needed it the most and who has helped me maintain my sanity over the last four years.

Thank you to all my field assistants, including Matt Switzer, Robert Duller, Claire Pannell, Ben Ellis, Pablo Davila-Harris, my husband Matt and last but not least, my Mum Gladys! Without you my fieldwork would have been impossible and I would have truly lost my mind.

A big thank-you to all my family, particularly my mum who has proved herself to be a very versatile lady. If anyone deserves an honorary degree this lady does! Thanks also to my Dad Terry, for all his support and my brothers, Matt and Jason, for constantly reminding me that I needed to get a 'proper' job. I must also thank my Grandad Henman for his support and making it possible for me to pursue my dreams.

Finally, but by no means least I have to thank my husband, Matt. Without him I could not have achieved what I have done. His love and support has been endless. Thank-you so much!

An investigation of depositional mechanisms of pyroclastic density currents using anisotropy of magnetic susceptibility (AMS) and a detailed stratigraphic study of the La Caleta Formation, Tenerife.

Clare Maher

This thesis describes La Caleta Formation and its eruptive history interpreted using sedimentary logs, isopach and isopleth data, granulometry and geochemical studies. The formation has been subdivided into six members, which were emplaced during five eruptive phases. The eruption commenced with fallout from a Plinian eruption column that collapsed, generating a rapid succession of short-lived pyroclastic density currents that deposited extensive ignimbrites and co-ignimbrite ash layers, culminating in a more sustained pyroclastic current that deposited a thick, predominantly massive ignimbrite, capped with a lithic breccia interpreted to represent caldera collapse.

Fine ash layers can be deposited by ashfall or pyroclastic density currents and their fine grain size coupled with poor exposure, can hinder interpretations of their depositional origin, which is vital if using ash layers for hazard assessment. A new method of discriminating between these two types of deposit is presented in this thesis. Samples of unequivocal depositional origin were collected from formations within the Bandas del Sur Group and their fabrics, analysed using Anisotropy of Magnetic Susceptibility (AMS). This revealed differences in the distribution of susceptibility axes, the imbrication of the magnetic foliation and the strength and shape of the anisotropy between the two types of deposit. However the discrimination using the traditional AMS plots was found to be equivocal in some instance, so a new discriminant plot has been devised, which can successfully discriminate between the two types of ash layer.

AMS has been used to categorise cross-stratified, stratified, diffusely bedded and massive lithofacies, and to interpret flow-boundary conditions and depositional mechanisms. Samples were collected from ignimbrites and ash layers from the Bandas del Sur Group and their AMS fabrics compared. The distribution of the magnetic susceptibility axes on the stereonet has been used to infer flow-boundary conditions; girdle distributions represent more tractional processes, whereas well-grouped distributions represent more granular processes and random distributions represent fluid escape dominated flow-boundary zones. The most significant outcome was the recognition of different types of massive deposit, based on variations in the distribution of the susceptibility axes, which are interpreted to have been deposited at a fluid-escape dominated flow-boundary influenced by other processes (traction and/or granular shear). This indicates that not all massive deposits are emplaced in the same way.

Contents

1.0 Introduction	1
1.1 Thesis objectives	1
1.2 Methods of data collection	3
1.3 Terminology	4
1.4 Previous work on depositional mechanisms of catastrophic density currents	6
1.4.1 Transportation mechanisms of density currents	7
1.4.2 Depositional mechanisms of density currents	11
1.4.3 Fully dilute currents	16
1.4.4 Granular-fluid based currents	17
1.5 Previous work on grain fabrics	21
1.6 An introduction to Anisotropy of Magnetic Susceptibility (AMS)	23
1.7 Previous applications of Anisotropy of Magnetic Susceptibility (AMS)	28
1.8 Methodology	30
1.8.1 Geological background	30
1.8.2 Collection and preparation of AMS samples	35
1.8.3 Measurements of AMS samples	37
1.8.4 Susceptibility v temperature	40
1.9 Thesis outline	41
2.0 Event-stratigraphy of the La Caleta Formation.	42
2.1 Introduction	42
2.2 Lithostratigraphy of the La Caleta Formation	44
2.3 Description and interpretation of the members	47
2.3.1 Member 1	47
2.3.2 Member 2	53
2.3.3 Member 3	64
2.3.4 Member 4	67
2.3.5 Member 5	70
2.3.6 Member 6	75
2.4 Co-ignimbrite ash layers	82
2.5 Eruptive volumes	85
2.6 Geochemistry	87
2.7 Discussion: an eruptive history	96
2.7.1 Phase 1: Plinian ash fallout	96
2.7.2 Phase 2: Plinian lapilli fallout	97
2.7.3 Phase 3: Emplacement of PCD's with corresponding co-ignimbrite ash layers	97
2.7.4 Phases 4 and 5: Sustained pyroclastic currents and climactic phase	97
2.8 Conclusions	99
3.0 Using anisotropy of magnetic susceptibility (AMS) to distinguish between ash layers deposited by fallout from those deposited from density currents: a case study from Tenerife.	100
3.1 Introduction	100
3.2 Methodology	105
3.3 Results	114
3.3.1 AMS characteristics of ashfall deposits	117
3.3.2 AMS results of fine ash pyroclastic density current deposits	119
3.4 Discussion	125
3.5 Summary and conclusions	129
4.0 Fabric-characterisation of ignimbrite lithofacies: constraints on depositional mechanisms.	132
4.1 Introduction	132
4.2 Previous work	134
4.3 Methodology	137
4.4 Cross-stratified tuff lithofacies	139
4.4.1 Cross-stratified lithofacies and their depositional mechanisms	139
4.4.2 AMS characterisation of cross-stratified lithofacies: new data	139
4.5 Stratified tuff lithofacies	148
4.5.1 Parallel stratified lithofacies and their depositional mechanisms	148
4.5.2 AMS characterisation of stratified lithofacies: new data	148
4.6 Diffuse bedded lapilli-tuff lithofacies	154
4.6.1 Diffuse bedded lithofacies and their depositional mechanisms	154

4.6.2 AMS characterisation of diffusely bedded lithofacies: new data	155
4.7 Massive lapilli-tuff lithofacies	163
4.7.1 Massive lapilli-tuff lithofacies and their depositional mechanisms	163
4.7.2 AMS characterisation of massive lapilli-tuffs lithofacies: new data	164
4.8 Massive tuff lithofacies	175
4.9 The impact of topography on AMS fabrics in massive and diffuse bedded lapilli-tuff	179
4.10 Summary and conclusions	187
5.0 Conclusions and further work	192
5.1 The event history of the La Caleta eruption	192
5.2 Discrimination of fine ash fallout and fine ash current deposits, using AMS	192
5.3 Characterisation of different ignimbrite lithofacies and their depositional mechanisms	193
5.4 Suggestions for further work	195
5.4.1 The event history of the La Caleta eruption	195
5.4.2 Discrimination of fine ash fallout and fine ash current deposits	196
5.4.3 Characterisation of different types of massive deposits and its application to the oil industry	196
References	197
 Appendix 1: Granulometry equations	 212
Appendix 2: XRF sample preparation	213
Appendix 3: Microprobe phenocryst analyses	214
Appendix 4: Microprobe glass analyses	221
Appendix 5: Computer programme instructions	226

Chapter 1: Introduction, background theory and methodology

1.1 Thesis Objectives

Pyroclastic and turbidity currents are catastrophic density currents that transport large volumes of sediment down slope, but their opaque, unpredictable and hazardous nature, make it impossible to observe their transportation and depositional processes. With pyroclastic currents, it is primarily the deposits (ignimbrites) that provide valuable information about how an eruption evolves and what the flow-boundary conditions and depositional mechanisms were. Understanding current behaviour and the direction in which density currents travel has important implications for hazard assessment in active volcanic regions, and also for hydrocarbon exploration where large quantities of oil and gas are found in thick sandstones deposited by turbidity currents.

There were three principal objectives for this research: (1) To describe and correlate the La Caleta Formation (Tenerife), with the intention of interpreting its eruptive history; (2) To develop a means of distinguishing fine ash fallout deposits from fine ash pyroclastic current deposits using Anisotropy of Magnetic Susceptibility (AMS); (3) To explore what AMS can reveal about the depositional mechanisms of cross-stratified, stratified and diffuse bedded lithofacies and whether different types of massive lithofacies could be identified, with the ultimate aim of better understanding the depositional mechanisms.

These objectives have been realised by detailed fabric analysis of Quaternary pyroclastic deposits from the Upper Bandas del Sur Group in southern Tenerife, Canary Islands (Brown et al., 2003). This area was chosen because the exceptional exposure reveals longitudinal and lateral variations in the deposits and the relationships between deposits and palaeotopography can be traced and recorded in detail. The pyroclastic deposits are well constrained from previous studies (Brown, 2001; Brown et al., 2003; Brown and Branney, 2004a; Brown and Branney, 2004b; Bryan et al., 2000; Bryan et al., 1998; Bryan et al., 2002; Edgar et al., 2002; Edgar et al., 2006), providing a solid foundation on which to build. The deposits are lithified, enabling collection of orientated samples, and have no imposed tectonic fabric. Finally, pyroclastic rocks were selected for this investigation because their rapid diagenesis means they suffer considerably less burial compaction-deformation than siliclastic sedimentary

sandstones and mudrocks, which may overprint the depositional fabric. In addition the underlying subaerial substrate topography is better constrained than in turbidite basins.

New work on the stratigraphy of the La Caleta Formation is presented in this thesis (Chapter 2). The La Caleta Formation was correlated across the southeast flanks of Tenerife and is described in detail, which has allowed eruptive volumes and eruption column heights to be calculated and the evolution of the La Caleta eruption to be interpreted. This work highlights the importance of recognising the depositional origin of ash layers (pyroclastic density current versus fallout), and emphasises the importance of distinguishing between Plinian /subplinian fine ash fallout and co-ignimbrite fine ash fallout, since the latter signifies the occurrence of a preceding pyroclastic density current, even if there is no pyroclastic density current deposit. This information is vital when constructing hazard assessments of populated volcanically active regions. The study of the La Caleta Formation has also formed the foundations for the discriminating between fine ash fallout deposits and fine ash current deposits (Chapter 3), allowing fine ash layers of both depositional origins to be identified with confidence.

The discrimination between fallout deposits and pyroclastic density current deposits is important in the reconstruction of volcanic histories and is therefore a fundamental part of hazard assessment. This distinction is typically made on the basis of granulometry (sorting), sedimentary structures, and by the nature of topographic relationships: fallout deposits drape topography with no change in thickness, whereas current deposits tend to infill topography and typically thicken into topographic lows. Consolidated deposits render sieving, to determine the sorting characteristics, impractical, and it is not always possible to determine the origin of fine ash layers that lack cross-bedding where poor exposure prevents field relationships (e.g. draping of topography) from being evaluated. This thesis presents a new, relatively quick and cost effective methodology that can be applied to lithified deposits, which can distinguish fine ash fallout deposits from fine ash current deposits, due to differences in their AMS fabrics, and a new discriminant plot has been devised to facilitate this (Chapter 3).

Sedimentary structures, such as ripples and cross-bedding, provide important information about the properties of the current (e.g. velocity and turbulence) and its depositional mechanisms. Less is known about deposits that lack sedimentary structures, and their interpretation is problematic. Massive deposits, however, may contain information in the form of grain fabrics. In general, massive deposits were assumed to be deposited rapidly due to

current unsteadiness (e.g. Sparks, 1973). This has commonly been referred to as “en masse” or instantaneous deposition (Sparks, 1976; Wright & Walker, 1981; Carey, 1991). Not all fabrics are discernable to the human eye and massive lithofacies can contain a wealth of cryptic information with the potential to assist in the interpretation of depositional mechanisms. Seemingly massive sandstone slabs have been photographed using radiography, which revealed previously indiscernible sedimentary structures, including cross-stratification (Hamblin, 1962, 1965). The presence of these hidden sedimentary structures proves how misleading massive deposits can be, and it is therefore appropriate to reconsider the depositional mechanisms responsible for their emplacement. It is possible that there may be a variety of different types of massive deposit, resulting from different depositional mechanisms. This thesis presents the AMS characteristics of a variety of lithofacies, which have been used to interpret flow-boundary zone conditions and depositional mechanisms. A variety of massive types have been identified, and using the information gained from the analysis of AMS signatures of other lithofacies, the flow-boundary conditions and the depositional mechanisms have been interpreted (Chapter 4).

In this chapter the methods of data collection are outlined, key terminology defined, and an account of previous work on transport and depositional mechanisms of density currents, grain fabrics and Anisotropy of Magnetic Susceptibility (AMS) are given. The geological background of Tenerife and its deposits is presented followed by the methodology used in the collection, preparation and measurement of the AMS samples. Although the focus of this thesis is the depositional mechanisms of pyroclastic density currents, direct parallels can be drawn with turbidity currents. Much of the early research carried out on turbidity currents and their deposits (turbidites) can be of use when discussing pyroclastic density currents and is referred to.

1.2 Methods of data collection

The primary dataset for this thesis was collected during 13 weeks of fieldwork in southern Tenerife, which consisted of classification and categorisation of lithofacies within the ignimbrites, which were logged in detail and palaeotopographic relationships recorded. The thesis is composed of three principal studies: (1) A description, correlation and interpretation of the Quaternary La Caleta Formation as a case-study; (2) the development of a methodology

to discriminate fine ash fallout and fine ash current deposits, using Anisotropy of Magnetic Susceptibility (AMS); (3) an AMS investigation of different lithofacies, with particular attention to massive deposits, to develop a better understanding of flow-boundary conditions and depositional mechanisms of pyroclastic density currents.

1.3 Terminology

Terminology is key to the understanding of certain concepts and processes, however individual researchers may use the same terms, to encompass slightly different meanings or to infer different processes. The terminologies used in this thesis follows that of Branney and Kokelaar (2002) and a few key terms that are used in this thesis are outlined below.

Throughout this thesis the general term *pyroclastic density current* will be employed for currents of pyroclasts and hot gases that move across the landscape as a result of having a greater density than the surrounding atmosphere. The term is used irrespective of particle concentration (Branney & Kokelaar, 2002).

Ignimbrites are pumice-rich deposits derived from pyroclastic density currents, and are typically composed of poorly-sorted lapilli-tuff, but can be fine ash tuffs, and can be subdivided into lithofacies. A lithofacies is a purely descriptive, non-generic and non-stratigraphic term. Specified combinations of clast size, shape, distribution, sorting, composition, sedimentary structures and grain fabrics define lithofacies and there are potentially an infinite number. Clast size definitions used here follows the Wentworth sedimentary grain-size scale (Wentworth, 1922)

The term *imbrication*, generally used for grain fabrics, is herein also applied to AMS fabrics and is used to infer flow-boundary conditions. Two types of imbrication will be referred to: A-type imbrication has the long axis parallel to the flow direction and the A-B plane is inclined upstream. This type of imbrication is produced in currents of higher concentrations, where particles are orientated within a shearing granular-fluid. B-type imbrication has the long axis normal to the flow direction with the B-C plane inclined upstream. This type of imbrication is associated with more turbulent, lower concentration currents (e.g. Ort et al., 1993).

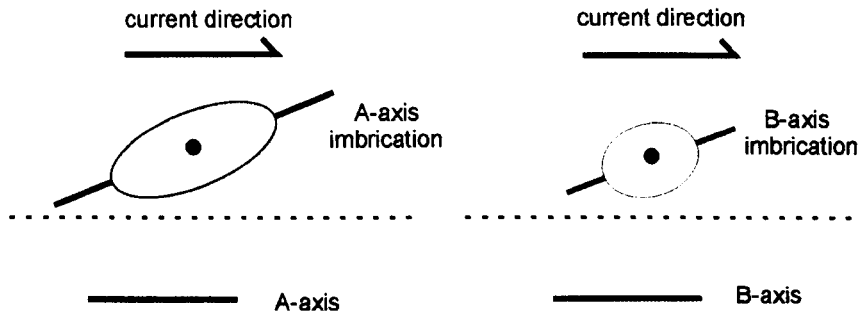


Figure 1.1: The different types of imbrication. A-type imbrication has its long axis (A-axis) orientated parallel to the current direction and dips back towards the source and the B-axis is perpendicular to the current direction (coming out of the page). B-type imbrication has the A-axis perpendicular to the current direction (coming out of the page) and the B-axis parallel to the current direction, dipping back towards the source.

The term *co-ignimbrite ash layer* refers to an ash layer deposited immediately after the passage of a pyroclastic density current deposited from fallout or dilute pyroclastic density currents. Previously co-ignimbrite clouds were thought to have been generated by fluid-escape from the underlying plug-flow (Wilson & Walker, 1982; Sparks et al., 1973; Gómez-Tuena & Carrasco- NÚñez, 1999) and were interpreted to be responsible for the emplacement of Layer 3 of the standard ignimbrite (Sparks et al., 1973: see section 1.4.2). The lack of sheared fluid escape structures in ignimbrites refutes this idea. In this study co-ignimbrite ash layers are interpreted to be derived from ash clouds (Phoenix cloud) that were a result of thermal expansion and lofting (Dobran et al., 1993; Sparks et al., 1997).

The term *flow-boundary zone* refers to a zone that incorporates the base of the current and the top of the deposit. The flow-boundary zone is where the characteristics of the lithofacies are thought to be formed (Branney & Kokelaar, 2002), according to the depositional mechanisms, which are controlled by the rates of deposition, rates of shear and the concentration of the flow-boundary zone.

Accretionary lapilli, coated pellets and *pellets* are common in some ash deposits. Pellets are the simplest of these structures and consist of an initially structureless, ellipsoidal, amorphous amalgamation of volcanic ash (Brown et al., 2004). Coated pellets consist of a pellet surrounded by a single rim of fine ash. In this thesis the term accretionary lapilli refers to spheroidal lapilli with a nucleus composed of a pellet, lithic or pumice clast, surrounded by two or more concentric layers of fine ash. Their formation has been attributed to hydrostatic and electrostatic agglomeration (Schumacher & Schmincke, 1991; Gilbert & Lane, 1994) and more recently Brown et al. (2004) proposed that accretionary lapilli are further developed by

being dropped into the turbulent part of a pyroclastic density current in which they accreted concentric laminations. In this study, the presence of accretionary lapilli does not infer any particular depositional process.

1.4 Previous work on transport and depositional mechanisms of catastrophic density currents.

Density currents are highly mobile and may travel at great velocities driven by the density contrast between the suspended sediment and the surrounding fluid. They are density-stratified, with a higher density at the base that decreases upwards through the current (Simpson, 1999). Density currents can be cold and subaqueous (turbidity currents) that travel across lake or sea floors, depositing sandy and muddy turbidites, or they can be hot, subaerial pyroclastic currents that deposit ignimbrites. It is thought that flow-boundary processes and depositional mechanisms in turbidity currents and pyroclastic currents are qualitatively similar, despite the differences in fluid phase and clast type, and aqueous experiments are commonly used to model gaseous pyroclastic currents (e.g. Bursik & Woods, 1996; Stix, 1999)

Since Florel (1885) first noted an undercurrent where the Rhone River entered Lake Geneva, there has been a great deal of research about the fluid mechanics and flow structure of turbidity currents (Kuenen, 1951; Bouma, 1962; Middleton, 1966a, 1966b; Kneller, 1995; Kneller and Buckee, 2000; Felix, 2001; Felix, 2002) and their deposits. Pyroclastic currents have been studied less intensively, but experimentally, theoretically, and in the field studies have been carried out (e.g. Wilson, 1980; Wright & Walker, 1981; Wilson, 1984; Huppert et al., 1986; Valentine & Whohletz, 1989; Colella & Hiscott, 1997; Stix, 1999; Calder et al., 2000). In the last two decades, the transport and depositional mechanisms of pyroclastic currents has been a topic of much debate (Wilson, 1980; Wilson & Walker, 1982; Fisher, 1983; Walker, 1983; Walker & McBroome, 1985; Branney & Kokelaar, 1992; Bursik et al., 1998; Cas & Wright, 1998; Druitt, 1998; Hughes & Druitt, 1998). An important development has been the recognition that the transport and depositional mechanisms are distinct and different (Walker, 1967; Lowe, 1982; Stow, 1985; Branney & Kokelaar, 1992), even though it is not possible to completely separate them from one another as they affect each other. For the sake of clarity, however, they will be reviewed separately below.

1.4.1 Transportation mechanisms of density currents

Flow may be laminar and/or turbulent and is best described in terms of streamlines. Laminar flow has straight or smoothly curved streamlines that remain separated from each other and mixing occurs on a molecular scale only (Allen, 1994). A variety of laminar flow is plug-flow, in which most of the shear occurs within the basal part of the current. The plug-flow model was favoured for many years as the transportation mechanism of granular pyroclastic density currents (e.g. Sparks, 1976; Wilson & Head, 1981; Wilson, 1985). A high concentration plug-like body of material moves along a basal shear zone with little velocity variation with height. The concept was adapted from models of non-Newtonian, cohesive debris flows (Johnson, 1970). Shear within the plug zone is prevented because the yield strength is greater than the exerted shear stress (Iverson et al., 1997; Johnson, 1970). A decrease in velocity, triggered by a decrease in gradient, was thought to lead to a decrease in the thickness of the shear zone at the base of the flow, causing the lower margin of the plug zone to come into direct contact with the substrate, making the entire flow come to an instantaneous halt across its length. Plug-flow requires very high concentrations, and how they develop from low-concentration dispersions erupted from source was problematic. Plug-flow is now thought to be restricted to specific situations (e.g. slow moving pumice dams and levees; Branney & Kokelaar, 2002; Pitarri et al., 2004).

In turbulent flow, streamlines are entangled and undergo rapid change, so that mixing occurs on a macro- and microscopic scale (Allen, 1994). The degree of turbulence can be expressed by the Reynolds (Re) number, and is controlled by the current density (ρ), the characteristic velocity (U), the current thickness (d) and the effective viscosity of the current (μ_s).

$$\text{Re} = \rho U d / \mu_s \quad (1)$$

The Reynolds number describes the balance between the internal flow forces and the viscous flow forces, and is an indication of stability (Allen, 1960). In a Newtonian fluid, turbulence occurs when the Reynolds number is greater than 500-1000. The Reynolds equation shows, in most instances, that an increase in velocity causes increase turbulence, whereas an increase in viscosity can act to suppress turbulence.

Many density currents that contain particles are density-stratified with a decrease in concentration and density with height above the base so there is no unique particle concentration or Reynolds number. The internal structure of the current affects the transport and depositional mechanisms, and there are various types of density stratification including laminar stratified currents (Schaflinger et al., 1990), turbulent currents with a laminar basal part (Fischer, 1966; Hein, 1982; Todd, 1989; Vrolijk & Southard, 1998), turbulent currents with a granular fluid base (Hans & Bowen, 1985) and currents with sharp or gradational variations in concentration and density (Sigurdsson et al., 1987; Valentine, 1987; Cole and Scarpato, 1993). Relatively little is known about these possible types of current and how the current evolves spatially and temporally, and it is feasible that a continuum exists between them.

Aqueous flume experiments have been carried out to investigate how variations in density and concentration (Gladstone et al., 2004) and viscosity stratification (Amy et al., 2004) affect the behaviour of stratified density currents. Gladstone et al., (2004) found that strongly stratified currents with a concentrated basal part have high initial velocities, but rapid deceleration since the upper dilute part of the current cannot keep up with the lower concentrated part of the current. In this instance mixing was found to be minimal. In contrast, they found that in weakly stratified currents, the upper layer was able to catch up and intrude into the lower more concentrated zone, promoting mixing. They concluded that the ability for a current to decouple or mix is dependent on the density ratio between the two layers. Amy et al., (2004) used glycerol solutions of varying viscosities/densities and found that if the lower basal region had a concentration of >75% glycerol, it had lower velocities, interpreted to be a result of increased drag, which is characteristic of high viscosity flows. This allows the upper more dilute part of the current to overrun the denser lower part. Basal regions with concentrations <75% glycerol resulted in a faster moving base that outran the more dilute overriding part of the current. Currents with weak viscosity stratification had concentrated basal regions that surged forward driven by inertia, whereas the concentrated basal layer of currents with relatively strong viscosity stratification was controlled by viscous forces and lagged behind regardless of the relative buoyancy (Amy et al., 2004). This decoupling of density-stratified currents could determine the vertical succession of the deposits. For example, currents with a fast-moving high concentration phase are anticipated to produce high concentration 'flow' deposits (i.e. a coarse grained poorly sorted deposit) overlain by a low concentration 'flow' deposit (i.e. finer grained, better sorted deposits, with possible laminations; Amy et al., 2004),

whereas currents with a slow moving high concentration phase would have a high concentration 'flow' deposit sandwiched between low concentration 'flow' deposits (Amy et al., 2004). Examples of such successions have been observed in the field and may reveal something about how the current behaved and its structure.

These experiments revealed that concentrated parts of the currents might decouple from and outrun the less dense layers within the stratified current. Decoupling of stratified pyroclastic density currents has been witnessed during volcanic eruptions (e.g. the 1991 Mt Unzen eruption; Yamamoto et al., 1993) where the lower, denser part of the current was controlled by topography, whilst the upper, dilute part of the current flow over obstacles (Fischer, 1995; Gladstone & Sparks, 2002; Gladstone et al., 2004). Decoupling has been ascribed to gravity segregation, erosion of the underlying substrate, interaction of the flow with the surrounding atmosphere and fluidisation (Fisher, 1995). All of these processes can change the concentration gradient within a current, by increasing the sediment content and/or segregating it.

In turbulent flow, particles may be transported via rolling and/or saltating along the substrate (Bagnold, 1956; 1973; Murphy & Hooshari, 1982) and in suspension. Parameters that control the particle motion include velocity, turbulence, particle mass and the ratio of surface area to mass of the particle (e.g. Hjelmfelt & Mockros, 1966; Squires & Eaton, 1990; Elghobashi, 1994; Kaitori et al., 1995; Nichol, 1999). An increase in current velocity promotes increased saltation and suspension by enhancing turbulence, allowing particles of higher mass to be entrained into and supported by the current.

Fluidisation is an important means of particle support within density currents. Pyroclastic density currents are only semi-fluidised, as complete fluidisation would result in the loss of fines and is not compatible with the broad spectrum of particle sizes observed in many pyroclastic current deposits (Sparks, 1976; Wilson, 1980). Four models have been proposed: (1) flow fluidisation; (2) bulk self-fluidisation; (3) grain self-fluidisation; (4) sedimentation fluidisation. Flow fluidisation involves the migration of gas from the substrate, possibly derived from surface water, snow or ice, and into the current. Although produced experimentally (Botterill & Halm, 1978; Ishida & Hatano, 1983), there are no known natural examples and the natural flux from the substrate is unlikely to be sufficient to maintain current's mobility. Bulk self-fluidisation is caused by the upward of escape of air that is

entrained at the head of the current (Walker et al, 1980; Wilson & Walker, 1983). Although perhaps effective in high concentration currents that would be better able to entrain air due to their greater density, this model would be ineffective for low concentration and sustained currents (Branney & Kokelaar, 2002). Grain fluidisation is a result of the upward migration of gas exsolved from juvenile material (Sparks, 1978), burning vegetation or steam resulting from entrained ice and snow. This model fails in hot and arid environments where there is little to no surface water, and secondary pyroclastic currents, generated from the collapse of unlithified pyroclastic current deposits months to years after their initial deposition (e.g. Torres et al., 1996), by which time all the gas will have exsolved from the juvenile material. Sedimentation fluidisation is a result of fluid escaping during hindered settling and is a consequence of a decrease in the net rate at which particles settle within dispersion (Branney & Kokelaar, 2002). This is influenced by clast interactions (collisions), interactions of clasts with their fluid wakes and the upward flow of displaced fluids due to settling clasts (Selim et al., 1983). Particles with a high surface area to mass ratio promote suspension due to their lower settling velocities. Suspended sediment results in density difference, which leads to downslope movement. This generates friction and turbulence in dilute currents, maintaining suspension and therefore the density differences, which is the driving force of the current (Middleton and Hampton, 1973; Stow, 1994).

Granular flow is also an important transport mechanism in pyroclastic density currents. High particle concentrations suppress turbulence and result in frequent particle collisions in which kinetic energy is dissipated due to the inelastic properties of the particles (Iverson & Vallance, 2001; Poliakov, 2002). The clast vibrations are referred to as granular temperature (Ogawa, 1978; Campbell & Brennen, 1983; Haff, 1983; Savage, 1983, 1984), which generates a dispersive pressure (Bagnold, 1954) that forces the particles apart, allowing them to move as a shearing mass (grain flow) in the direction of the average motion vector (Bagnold, 1954; Savage, 1979; Campbell & Brennen, 1983) without the support of interstitial fluids (e.g. Iverson & Vallance, 2001; Poliakov, 2002). Pyroclastic density currents do not have true grain flows at their base; rather they are modified by interstitial fluids (Lowe, 1982), which alters the grain flow properties and its behaviour (e.g. Hanes & Bowen, 1985; Jiang, 1995; Iverson & Vallance, 2001).

Experimental work on the fluidisation of granular flows has revealed that flow mobility of initially fluidised beds of particles depends on the fluidisation behaviour and deaeration rate of the particles (Roche et al., 2002). They found that flows containing fine particles in a fluidised state had a far greater mobility than those with fluidised coarser components and non-fluidised flow. This was attributed to lower gas velocities required to fluidise fine material and that fine grained fluidised granular flows deaerated more less rapidly (Roche et al., 2002). Experimental work on granular flows has also been used to infer various flow regimes and the morphology of the resulting deposits has been compared with natural pyroclastic density current deposits (Felix & Thomas, 2004).

1.4.2 Depositional mechanisms of density currents

En masse deposition from a plug-flow was the preferred interpretation for the deposition of material from pyroclastic density currents, particularly those displaying massive lithofacies. A widespread view was that high-density suspensions collapsed as a result of variations in velocity induced by changes in topographic gradient. It was proposed that once deposition began, it caused the particle concentration to decrease, promoting further “collapse” (Dzulynski & Sanders, 1962; Lowe, 1982; Lowe, 1988; Middleton, 1970). Alternatively the opposite view was that a current decelerated and “deflated” (increased in concentration) until it stopped en masse (Sheridan & Ragan, 1976), once the shear stress at the base of the ‘flow’ dropped below the yield strength (Wright, 1981; Wright & Walker, 1981). Proximal massive ignimbrites with a high proportion of fines and matrix-supported lapilli (Druitt & Sparks, 1982; Walker, 1985) and lithic breccias (Walker, 1985) were interpreted to represent deposition from a deflated plug flow. Such a rapid proximal change from the erupted low-concentration current, to a very high-concentration current is difficult to explain. For example, during ‘deflation’ fines should be lost due to elutriation. Druitt and Sparks (1982) suggested that gas compression at the base of a tall collapsing eruption column might account for the development of a sufficiently concentrated flow to prevent the loss of fines via elutriation. However, this has not been modelled and it seems unlikely that it would then be able to flow from source in its compressed state.

Sparks et al., (1973) noted that many ignimbrites display similar characteristics and proposed a ‘standard’ ignimbrite with three layers (Fig. 1.2). Layer one is a fine-grained stratified or cross-stratified tuff. Layer two is divided into 2a, a thin inversely graded layer, overlain by 2b, which is a much thicker, poorly-sorted lapilli tuff layer with well-developed coarse-tail

grading patterns (normal grading of lithic lapilli and inverse grading of pumice lapilli). Layer 3 consists of a fine ash that mantles topography. Sparks et al., (1973) interpreted this 'standard' ignimbrite in terms of the plug-flow model and *en masse* deposition, with the thickness of the deposit (layer 2) representing the thickness of the pyroclastic flow. Pyroclastic flows were considered to be poorly expanded, high concentration, non-turbulent granular fluids. Layer 1 had a variety of origins, including deposition from turbulence generated from the interaction of the flow with irregular substrate topography, or as a product of an accompanying or preceding ground surge (Sparks et al., 1973). The inverse graded Layer 2a was thought to record the base of the main body of the flow, which was thought to form a semi-fluidised high yield strength plug that moved along a basal shear zone (Sparks et al., 1973).

The high-yield strength of the flow was interpreted to support clasts within a mobile matrix, denser lithic clasts 'sinking' towards the base and the less dense pumice clasts 'floating' towards the flow top to produce the grading patterns observed in layer 2b. This explanation is contradictory, as a flow with high yield strength would prevent pumices from rising to its top. Above the flow, an upper turbulent, dilute component was thought to be made up of the ash elutriated from the underlying semi-fluidised flow (Wilson & Walker, 1982; Sparks et al., 1978; Gómez-Tuena & Carrasco-Núñez, 1999), which deposited a co-ignimbrite ash-cloud surge or fallout deposit (Layer 3)

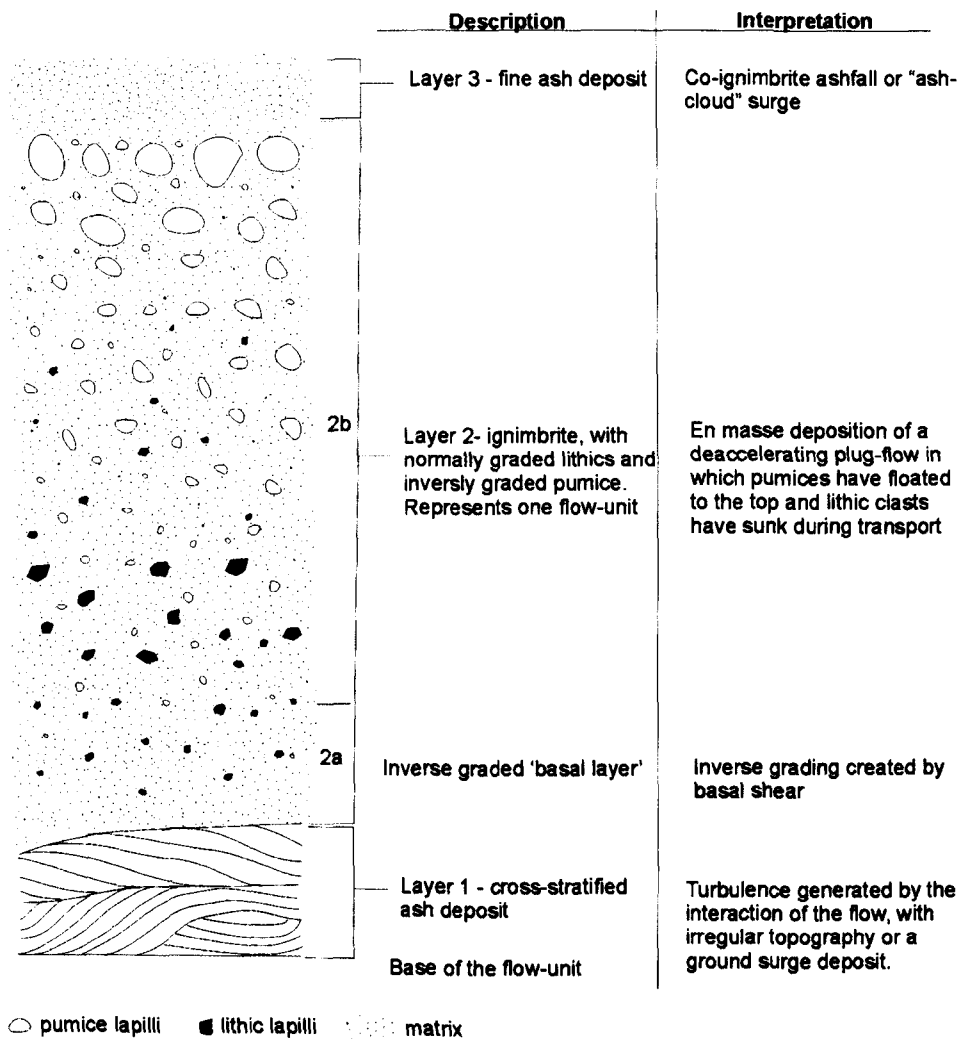


Figure 1.2: A schematic section of the ‘standard ignimbrite’ proposed by Sparks et al., (1973). Most ignimbrites on Tenerife do not show this pattern and some of the interpretations are no longer thought to be correct.

There are a number of key observations that question the plug-flow model and en masse deposition (Branney & Kokelaar, 1992). For example, ignimbrites commonly display vertical chemical zonation, which may be recognising multiple flow units, but chemical zonation within individual flow units is difficult to reconcile with ‘plug flow’ because this model would require all the juvenile material of different compositions to be erupted and then deposited at the same time and therefore there could be no systematic chemical zonation (cf. Cas and Wright, 1987; Sheridan, 1979; Wright and Walker, 1981). Such chemical zoning is best explained by the progressive emptying of a zoned magma chamber, which is not compatible with en masse deposition. Vertical variations in palaeocurrent direction, as determined by Anisotropy of Magnetic Susceptibility (AMS) (e.g. Hillhouse & Wells, 1991), and the lateral gradations from cross-stratified/stratified lithofacies into massive lithofacies (Rowley et al., 1985; Sigurdsson et al., 1987; Fierstein & Hildreth, 1992; Cole & Scarpati,

1993; Scott et al., 1996; splay-and-fade of Branney & Kokelaar, 2002; Brown et al., 2004), are also incompatible with en masse deposition. This is because a plug-flow should produce a uniform palaeocurrent direction throughout the thickness of the deposit and its high concentrations would prevent the turbulence required for the formation of cross-stratified and stratified lithofacies. Displacement of interparticle fluid within the current and the underlying deposit makes en masse deposition unlikely, because partial fluidisation would hinder deposition, and topographic variations would prevent an extensive plug-flow from stopping instantaneously (Branney and Kokelaar, 1992, 2002).

The plug flow/en masse deposition concept still has some advocates (e.g. Gomez-Tuena & Carrasco-Núñez, 1999; Fierstein and Wilson, 2005) and as an end-member process may still have a role in slow moving terminal pumice dams and levees (Branney & Kokelaar, 2002; Pitarri et al., 2004) and in stepwise aggradation (Branney & Kokelaar, 1992). However, deposition of pyroclastic density currents is more commonly interpreted using the concept of progressive aggradation, an idea initially proposed by Fisher (1966), but then abandoned in favour of the plug-flow theory. Progressive aggradation refers to the progressive deposition from the base of a density current and Branney and Kokelaar (1992) proposed that this model could better account for the wide variety of lithofacies that may result from variations in rates of sedimentation and rates of shear around the flow-boundary. This is now commonly, but not unanimously, accepted to be the predominant means of deposit emplacement from density currents (e.g. Pitarri et al., 2004; Edgar et al., 2006). However, we still have much to learn about the processes and conditions involved. In this model the deposit aggrades with time from the base of the overriding current at the flow-boundary zone, and the rate of aggradation relates to the current steadiness. Progressive aggradation best accounts for gradational chemical zoning (Branney & Kokelaar, 1997; Carrasco-Núñez and Branney, 2005) and avoids the spatial problems inherent in plug flow. For example across the length of the flow, the substrate will be of varying steepness and it is difficult to envisage how a pyroclastic current can stop simultaneously across its entire length, which according to the depositional record of some ignimbrites is 10's of kilometres.

Progressive aggradation can account for rapid spatial variation of a current as it interacts with the evolving topography, and temporal variation as current conditions and eruption dynamics evolve. This is expressed by complex architectures of lithofacies that can be found in close vertical and lateral proximity to one another, frequently undergoing gradational change from

one lithofacies to another or can be non-uniform and laterally discontinuous. This occurs because a current can deposit at one location, whilst eroding or bypassing at another (Brown & Branney, 2004).

The character of the lithofacies reflects depositional mechanisms and the conditions within a flow-boundary zone at a specific moment in time, and has little bearing on the conditions of the overriding parts of the current. For example, a current may be relatively dilute and turbulent overall, but conditions in the flow-boundary zone may be of much higher concentration, so that grain interactions dominate and turbulence is suppressed, resulting in laminar flow at the site of deposition.

Pyroclastic density currents have two end members. One extreme is dilute and turbulent (a surge) and the other more concentrated and laminar (flow) (e.g. Burgisser & Bergantz, 2002). These two end members used to be treated in isolation, but they are now recognised to operate on a continuum (Branney & Kokelaar, 2002; Burgisser & Bergantz, 2002). In fully dilute currents clast interactions are few and unimportant in terms of particle support and the current is dilute all the way through to the substrate (Branney & Kokelaar, 2002). Currents with a high concentration or a granular-fluid base have a modified grainflow at the base of the current, where clast interaction is a fundamental part of particle support and because of the high concentration at the base of the current, turbulence is typically inhibited (Branney & Kokelaar, 2002).

In association with these two end-member density currents, Branney and Kokelaar (2002) introduced the concept of flow-boundaries, of which there are four hypothetical flow-boundaries: (1) direct fall out dominated flow-boundary; (2) traction dominated flow-boundary; (3) a granular flow dominated flow-boundary; (4) a fluid escape dominated flow-boundary (Branney and Kokelaar, 2002; Fig.1.2A). Which flow-boundary dominates depends on the concentration of the current, shear rate and the rate of deposition (Fig. 1.2A). It is important to regard these as end-members and there are intermediate types depending upon the three controls. The rate of supply is also an important consideration because this will influence the development of a granular fluid base, which will influence the depositional mechanism at the flow boundary.

1.4.3 Fully-dilute currents

Direct fallout dominated flow-boundary zone.

In this type of flow-boundary zone, pyroclasts fall directly out of a fully dilute current that is travelling at low velocity and there is negligible particle interaction and fluid escape due to the low concentration (Branney & Kokelaar, 2002). The rate of deposition is low but exceeds the rate of supply preventing the development of a granular-fluid base. In this case there is a sharp rheological contrast at the top of the substrate, with only a minor increase in velocity profile, so that traction is negligible (Fig.1.3). The low velocity of such a current would result in low levels of shear at the flow-boundary and the particles fall directly from the current, without additional movement via saltation. One would expect deposits from this type of flow-boundary zone to have similar characteristics to fine ash fallout deposits. For example, they may be expected to have predominantly oblate fabrics, with a negligible amount of imbrication and a rather weak linear component, because the current velocity was insufficient to orientate particles. Occasional turbulent eddies may impinge upon the flow-boundary, generating fabrics with a greater linear component, depending on the current strength.

Fallout can result from lofting (Branney & Kokelaar, 2002; Stow, 1994): as a current becomes depleted in sediment, it becomes increasingly buoyant, eventually forming an ascending co-ignimbrite plume or 'Phoenix cloud'. Ashfall may occur from this plume, especially when atmospheric moisture promotes the agglomeration of ash particles, increasing their effective size and settling velocity (Brown & Branney, 2004). Such ash layers are referred to as co-ignimbrite ash layers (e.g. Walker et al., 1981).

Traction dominated flow-boundary zone.

A traction dominated flow-boundary zones occur in fully dilute currents with higher velocities and rates of supply than in direct fallout dominated flow-boundary zones (Fig.1.3). However, the rates of supply are still not significant enough to establish a granular-fluid base. There would be a prominent decrease in concentration and a marked step in velocity at the base of the current (Branney & Kokelaar, 2002: Fig.1.3). The low concentration and high velocity promote turbulence and the interaction of turbulent eddies with the flow-boundary zone causes clasts to slide, roll and saltate providing an effective sorting mechanism and the development of a variety of bedforms, including sandwaves that give rise to cross-stratification. As a result the deposits are moderately well-sorted, and one might expect well-

developed directional fabrics that are imbricated with respect to bedding. The dilute nature of the current and low granular shear rates mean that Type-B imbrication (long axis perpendicular to current direction) is more likely as clasts are rolled along the substrate. The linear fabric component would be weaker compared to deposits emplaced at a granular dominated flow-boundary zone, but greater than that found from a direct fallout dominated flow-boundary zone.

1.4.4 Granular-fluid based currents

Granular flow dominated flow-boundary zone.

Granular flow (review by Campbell, 1990) occurs within flow-boundary zones of relatively high concentrations where discrete particles shear under the direct influence of gravity (e.g. Iverson & Vallance, 2001; Poliakov, 2002) or are driven by an overriding density current. The rate of supply is high allowing the development of a granular-fluid base of high concentrations and the rate of deposition is not so high as to prevent the development of lateral shear within the flow-boundary. In the case of pyroclastic currents, granular flow is a rapid process in which clasts bounce against each other forming a dilated granular dispersion (Savage, 1979, 1983, 1984).

Granular flow cannot sustain itself indefinitely and is partly reliant on the shear generated by the overriding parts of the current (Poliakov, 2002). In short-lived and unsustained currents, deposition from thin modified grain flows could occur en masse (e.g. Roche et al., 2002; Pitarri et al., 2004), once all the kinetic energy has dissipated and the fluid-pore pressure equilibrates. The flow then deflates and frictional interlocking of clasts would bring the flow to a halt. In this instance the inverse grading that is commonly observed in the deposits of grain flows can be explained by mechanical sieving caused by the continual agitation of particles, resulting in the inverse coarse-tail grading of light clasts and/or normal coarse tail grading of dense clasts (e.g. Cagnoli & Manga, 2005). Grading can also be a result of finer material percolating down between larger clasts (Scott & Bridgewater, 1975; Bridgewater et al., 1985; Savage & Lun, 1988).

During the passage of more sustained currents with a thicker granular-fluid base caused by higher rates of supply, deposition may be via progressive aggradation from the base of the modified grain flow. During steady deposition this might result in the deposition of a massive

lithofacies with no grading patterns (Branney & Kokelaar, 2002). Alternatively, in an unsteady current, thin-bedded or diffuse bedded lithofacies might be generated as a result of periodic turbulent eddies impinging on the flow-boundary or shear being exerted to the top of the granular-fluid base (grain flow) by turbulent eddies in the overriding current (Branney & Kokelaar, 2002). The exact formation of the bedded/diffuse bedded lithofacies will depend on the thickness of the granular-fluid base and/or the strength of the turbulent eddies. Reverse grading in these instances is a result of a waxing current that progressively carries coarser material further from source with time (Branney & Kokelaar, 2002)

The increased granular shear at granular dominated flow-boundary zones would enhance clast orientation. Deposits emplaced under these conditions are therefore expected to have a strong linear component in the fabric as defined by well-developed grain fabrics i.e. A-type imbrication. The hypothetical rheological boundary between the deposit and the current is sharp but there is not such a dramatic decrease in concentration profile when compared to the direct fallout flow-boundary end member and the velocity increases gradationally up through the current (Fig.1.3).

Fluid- escape dominated flow-boundary zone.

Fluid escape is the escaping of interstitial fluid in a compacting granular mass. It becomes the dominant mechanism of clast support in flow-boundary zones composed of a well developed granular-fluid of high, caused by high rates of supply and rapid deposition at low shear rates (Fig.1.3). The clast concentration just below the flow-boundary is similar to those immediately above and decreases gradually with little rheological contrast between the lowermost part of the current and the upper, loose part of the deposit. This is a result of rapid deposition causing the upward migration (return flow) of interstitial fluids (water in the case of turbidity currents and dusty gas in the case of pyroclastic currents), which cause a decrease in settling velocity and hinders deposition (e.g. Druitt 1995; Blanchette & Bush, 2005). The degree of hindered settling is dependent on the size, shape and sorting of the particles and the effect of hindered settling increases with clast irregularity (e.g. Tomkins et al., 2005) as with poor sorting, which lowers the porosity of the dispersion. The concentration profile below the flow-boundary increases downwards due to compaction and decreasing fluid escape with depth (Branney & Kokelaar, 2002). The migration of fluids can lead to localised depletion of fines as the development of elutriation pipes and soft state deformation, involving possible disruption of pre-existing fabrics resulting in massive lithofacies. The absence of a sharp

rheological boundary between the substrate and the overriding current (Fig.1.3), and the high concentrations and rapid deposition at the flow-boundary inhibit traction and the formation of modified grain flows, preventing the formation of bedforms. As a result the deposits lack stratification and poorly developed fabrics should be expected (Branney & Kokelaar, 2002). Depending on the concentration of the flow-boundary zone, the shear rates and the rates of deposition there will be many intermediate flow-boundaries. The deposits only provide an insight into the conditions of the flow-boundary zone and do not provide any information about the overriding current. Progressive aggradation is the preferred model for deposition from pyroclastic density currents because it can account for vertical chemical zoning and the rapid changes in flow-boundary conditions reflecting changes in topography, current conditions and eruption dynamics and can easily explain the gradational changes and discontinuous nature of lithofacies within density current deposits.

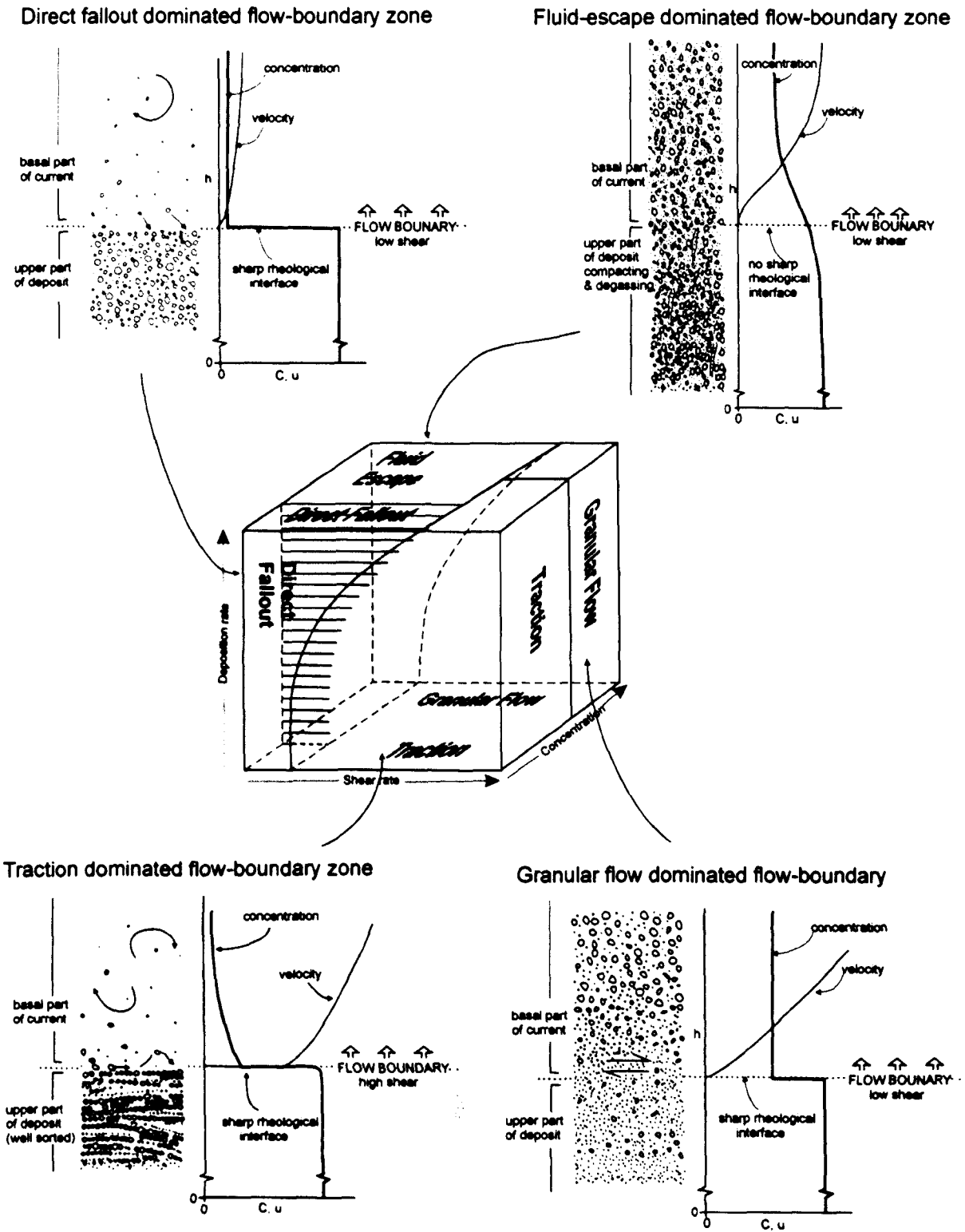


Figure 1.3: A sketch of a theoretical construct of the qualitative relationship of the different types flow-boundary with increasing shear rate, deposition rates and increasing concentration based upon deduction and the hypothetical conditions and processes at a direct fallout-dominated flow-boundary, granular flow-dominated flow-boundary,traction dominated flow-boundary, and a fluid escape-dominated flow-boundary (modified from Branney & Kokelaar, 2002).

1.5 Previous work on grain fabrics

Grain fabric studies of clastic rocks have been carried out since the 1940s (e.g. Dapples & Rominger, 1945) and have been applied in a variety of different fields, including sedimentology, glaciology and volcanology to identify palaeocurrent directions, source location and information regarding depositional mechanisms. The study of grain fabrics reveals the size, shape and sorting of a deposit's components and can provide clues about the depositional regime and mechanisms. Early grain fabric studies concentrated on identifying the palaeocurrent direction (e.g. Crowell, 1955; Rusnak, 1957) and were based on field observations. For example, Schminke & Swanson (1967) used the imbrication of pumice clasts and primary features (e.g. cross-bedding, stretched pumices) in pyroclastic current deposits to define the palaeocurrent direction. Elston & Smith (1970) used "fluidal textures" in welded ignimbrites to determine palaeocurrent directions. Key criteria for interpreting palaeoflow include the orientation of non-equidimensional and equidimensional fork-shaped glass shards, fragment imbrication, the penetration of pumices or deformation of glass shards by crystals or xenoliths, the orientation of spindle-shaped objects and the blocking effect (accumulation of smaller clasts up current of a bigger clast). These criteria have been applied to ignimbrites elsewhere to locate source calderas (Rhodes Smith, 1972; Sides, 1981).

Subsequent fabric studies were used to investigate depositional mechanisms, mostly of turbidity currents (e.g. Parkash & Middleton, 1970; Taira & Scholle, 1979; Hiscott & Middleton, 1980). Experimentally produced deposits have been produced under controlled laboratory conditions and the resulting fabrics were analysed and interpreted in terms of the known flow conditions i.e. concentration, grain size, slope gradient, velocity and so on (e.g.; Middleton, 1967; Hamilton et al., 1968; Rees, 1968; Rees, 1983; Sakai et al., 2002). Experiments carried out by Rees (1968, 1979, 1983) addressed grain orientation. Transverse fabrics (long axis/ k axis normal to flow) have been suggested to be a result of clasts rolling along the substrate (Hand, 1961) or of clast collision (Rees, 1968; Taira & Scholle, 1979) and require relatively higher concentrations. This is at odds with interpretations of transverse AMS fabrics, which are interpreted to represent more dilute flow-boundary conditions and the rolling of elongate particles (e.g. Ort, 1993). The experiments carried out by Rees (1983), suggesting that higher concentrations are required to produce transverse fabrics, were produced from non-turbulent dispersions within liquid plaster of paris, so may not be truly representative of the transport and depositional mechanism of density currents.

Variations in the angles of imbrication have been investigated experimentally and compared to fabrics found in real deposits (e.g. Sakai et al., 2002). They found that the imbrication angles decreased up through the deposit, which was interpreted as a change in rates of deposition; higher angles of imbrication indicated higher rates of deposition (Arnott & Hand, 1989). The lower and middle parts of the deposit produced in the experiments by Sakai et al., (2002) were compared to Bouma A division turbidites, which have been demonstrated to show similar characteristics (wider variation in imbrication angles and down-current imbrication; e.g. Bouma, 1962; Colburn, 1968; Onions & Middleton, 1968; Taira & Scholle, 1979; Hiscott & Middleton, 1980). The upper section of the experimentally produced deposit was compared to the Bouma B-division, because of its near-horizontal imbrication angles.

To define a grain fabric, three mutually perpendicular sections are required. Such sections have been cut from an orientated block sample, or from rock surfaces in the field (Hughes & Druitt, 1998), and measurements were made manually, which was a time consuming process. However, modern technology now allows digital images of surfaces to be analysed automatically using computer software (e.g. Cappaccioni & Sarocchi, 1996; Capaccioni et al., 2001; Karátson et al., 2002). This enables macro- and microscopic fabrics to be analysed and makes it possible to define fabrics that may otherwise go undetected. Vertical variations in the orientation of particles and the strength of the fabric within the Orevieto-Bagnoregio Formation, Italy, have been interpreted to represent progressive aggradation (Capaccioni & Sarocchi, 1996; Capaccioni et al., 2001) and comparisons have been made with welded ignimbrites, which have a much more homogeneous mean orientation and lower degrees of anisotropy (Capaccioni et al., 2001). Karátson et al., (2002) used a photo-statistical method to analyse preferred clast orientations in volcanoclastic mass flow deposits, and found that the clast size did not influence the degree of alignment and that the fabric became stronger with distance from source ($\leq 1\text{km}$), after which there was no systematic improvement in alignment.

X-ray imagery is another technique that might be used to identify fabrics that would otherwise go undetected. Hamblin (1962) first used this technique on apparently massive sands and x-ray images revealed numerous and varied sedimentary structures. If the fabrics are defined by clasts of differing composition that are similar in appearance, the fabrics will not be easily discernable. X-ray imagery is capable of detecting density differences and therefore showing otherwise invisible structures. The presence of such structures in massive deposits has profound implications with regards to their emplacement and the flow-boundary conditions.

1.6 An introduction to Anisotropy of Magnetic Susceptibility (AMS)

Anisotropy of Magnetic Susceptibility (AMS) is a property of rocks that can define the shape, orientation and strength of three-dimensional fabrics on a fine scale, even when the rock appears visually isotropic. Detailed documentation of the theory behind AMS and its applications has been documented elsewhere (e.g. Butler, 1992), but a brief review of the subject is appropriate.

Magnetic susceptibility (K) is a dimensionless quantity and is the ratio that relates the magnetization (M) to the inducing magnetic field (H) (equation 1).

$$M = KH \quad (1)$$

In most instances it can be considered a symmetric second rank tensor in its principal axis frame:

$$K = \begin{bmatrix} k_{11} & k_{12} & k_{13} \\ k_{21} & k_{22} & k_{23} \\ k_{31} & k_{32} & k_{33} \end{bmatrix}$$

Anisotropy of magnetic susceptibility examines the different values of magnetic susceptibility along three mutually perpendicular axes creating an ellipsoid (Fig 1.4) whose axes represent the maximum (K_1), intermediate (K_2) and minimum (K_3) magnetic susceptibilities (e.g. Butler, 1992), each of which has an orientation in three-dimensional space (k_1 , k_2 , & k_3 respectively). If the induced magnetisation is parallel to the applied field, the susceptibility is isotropic. Anisotropy arises when the induced magnetisation is not parallel to the applied field and there are different susceptibility values when measured in three directions.

There are three types of anisotropy; (1) magnetocrystalline anisotropy, which relates to the crystal structure; (2) magnetostrictive anisotropy, which is a result of changes in the crystal structure caused by magnetisation; (3) magnetostatic anisotropy, which is a result of shape, with the principle axes of susceptibility relating to the long, medium and short axes of a clast. Usually the k_1 axis lies along the elongation axis of the grain and is typically interpreted to

represent the direction of flow (e.g. Knight et al., 1986; Wolff et al., 1989; MacDonald and Palmer 1990; Seamann et al., 1991). When a magnetic field is applied a demagnetisation field is generated that opposes the applied magnetic field. Because the attracting poles of the grain are further apart and cover a smaller surface area, along the elongation axis of a grain, it has a weaker demagnetisation force and therefore a higher susceptibility (Fig. 1.5A). If a magnetic field is applied along the short axis, the attracting poles are closer together and cover a larger surface area resulting in a larger demagnetising field and a lower magnetic susceptibility (Fig. 1.5B)

Because magnetite has a weak susceptibility at low magnetic fields, magnetostatic anisotropy dominates the AMS signature and any crystalline effects are overwhelmed. Magnetostatic anisotropy is related to the preferred orientation of anisotropic grains. However, isotropic magnetic minerals can also show AMS due to their distribution. For example, a linear fabric can be formed by elongated grains arranged in a line. The AMS signature can be described as a linear fabric, mirroring the grain fabric generated by the deformation (e.g. and Howard, 1981).

All materials are magnetically susceptible and will exhibit an AMS signature, to what degree is determined by their chemistry and whether they are diamagnetic, paramagnetic or ferromagnetic (1.7). Diamagnetic material produces a magnetisation antiparallel to the applied field (Fig. 1.1A) while paramagnetic material produce a magnetisation parallel to the

Figure 1.4: An AMS ellipsoid showing three principle axes of susceptibility; $k1$ is the maximum axis of susceptibility; $k2$ is the intermediate axis of susceptibility; $k3$ is the minimum axis of susceptibility.

magnetisation when the applied field is removed. Ferromagnetism (1.8) arises when there is long range ordering and interaction of ions in a crystal lattice. There are three categories; (1) ferromagnetism (1.8), which consists of ions on adjacent lattice sites with parallel atomic moments, e.g. iron (Fig. 1.6C); (2) antiferromagnetism, which consists of ions in adjacent sites having opposing atomic moments of equal strength, thus their effects cancel (Fig. 1.6D); (3) ferrimagnetism, which consists of two lattice sites occupied by ions of different atomic moments, e.g. Fe^{2+} , Fe^{3+} in magnetite, resulting in a net magnetisation and a similar to ferromagnetism (1.8) signature.

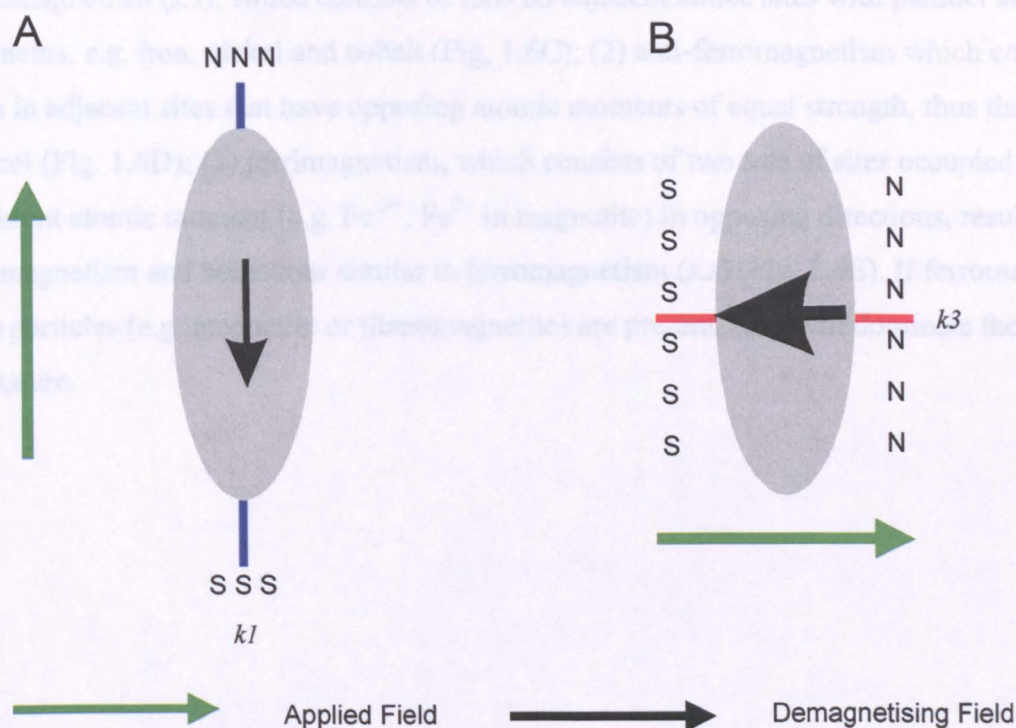


Figure 1.5 (A) An anisotropic magnetic particle being magnetised along its elongation axis ($k1$), resulting in a reduced area covered by, and an increased separation, of the magnetic poles. This results in a weaker demagnetising field, making it easier to magnetise the particle in that direction (higher susceptibility); (B) An anisotropic magnetic particle being magnetised along its short axis ($k3$), resulting in an increased area covered by, and a decreased separation, of the magnetic poles. This results in a stronger demagnetising field, making it harder to magnetise the particle in that direction (lower susceptibility).

Because magnetite has a weak susceptibility at low magnetic fields, magnetostatic anisotropy dominates the AMS signature and any crystalline effects are overwhelmed. Magnetostatic anisotropy is related to the preferred orientation of anisotropic grains. However, isotropic magnetic minerals can also create anisotropy depending on their distribution. For example, a linear fabric can be created from isotropic spherical clasts when arranged in a line. The AMS signature can be held by magnetic minerals that have subsequently crystallised, mirroring the grain fabric generated by the depositional processes (Ellwood and Howard, 1981).

All materials are magnetically susceptible and will exhibit an AMS signature; to what degree is determined by their chemistry and whether they are diamagnetic, paramagnetic or ferromagnetic (*s.l*). Diamagnetic material, produces a magnetisation antiparallel to the applied field, (Fig. 1.6A) whilst paramagnetic material produce a magnetisation parallel to the applied field (Fig. 1.6B). Neither diamagnetic nor paramagnetic material retains the magnetisation when the applied field is removed. Ferromagnetism (*s.l*) arises when there is long range ordering and interaction of ions in a crystal lattice. There are three categories; (1) ferromagnetism (*s.s*), which consists of ions on adjacent lattice sites with parallel atomic moments, e.g. iron, nickel and cobalt (Fig. 1.6C); (2) anti-ferromagnetism which consists of ions in adjacent sites that have opposing atomic moments of equal strength, thus their effects cancel (Fig. 1.6D); (3) ferrimagnetism, which consists of two sets of sites occupied by ions of different atomic moment (e.g. Fe^{3+} , Fe^{2+} in magnetite) in opposing directions, resulting in a net magnetism and behaviour similar to ferromagnetism (*s.s*) (Fig. 1.6E). If ferromagnetic (*s.l*) particles (e.g. magnetite or titanomagnetite) are present, they will dominate the AMS signature.

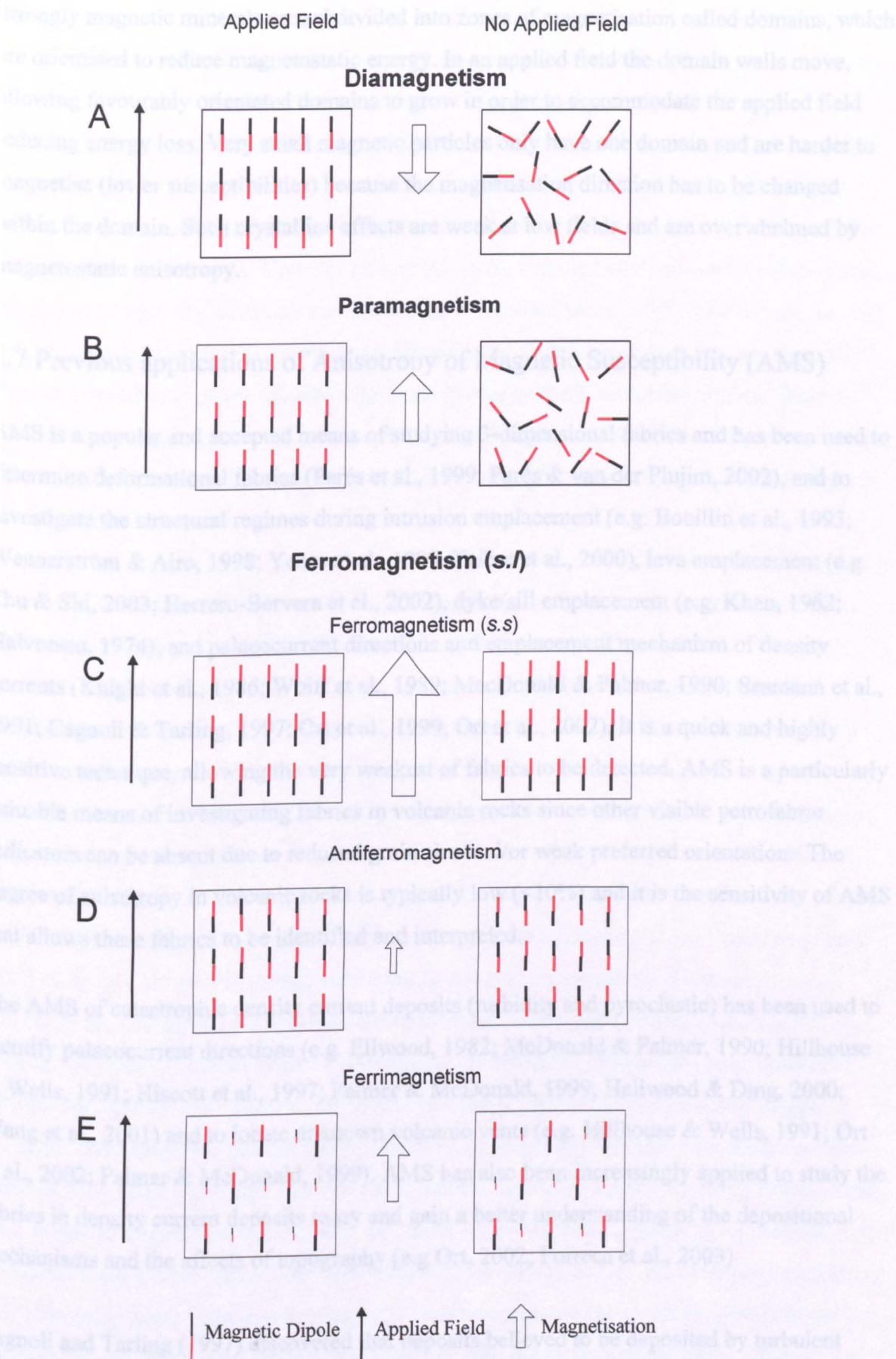


Figure 1.6: The magnetic response of (A) diamagnetic, (B) paramagnetic and (C-E) ferromagnetic (s.l) substances in an applied field.

Strongly magnetic minerals are subdivided into zones of magnetisation called domains, which are orientated to reduce magnetostatic energy. In an applied field the domain walls move, allowing favourably orientated domains to grow in order to accommodate the applied field reducing energy loss. Very small magnetic particles only have one domain and are harder to magnetise (lower susceptibilities) because the magnetisation direction has to be changed within the domain. Such crystalline effects are weak at low fields and are overwhelmed by magnetostatic anisotropy.

1.7 Previous applications of Anisotropy of Magnetic Susceptibility (AMS)

AMS is a popular and accepted means of studying 3-dimensional fabrics and has been used to determine deformational fabrics (Parés et al., 1999; Parés & van der Pluijm, 2002), and to investigate the structural regimes during intrusion emplacement (e.g. Bouillin et al., 1993; Wennerström & Airo, 1998; Yenes et al., 1999; Talbot et al., 2000), lava emplacement (e.g. Zhu & Shi, 2003; Herrero-Bervera et al., 2002), dyke/sill emplacement (e.g. Khan, 1962; Halvorsen, 1974), and palaeocurrent directions and emplacement mechanism of density currents (Knight et al., 1986; Wolff et al., 1989; MacDonald & Palmer, 1990; Seaman et al., 1991; Cagnoli & Tarling, 1997; Ort et al., 1999; Ort et al., 2002). It is a quick and highly sensitive technique, allowing the very weakest of fabrics to be detected. AMS is a particularly valuable means of investigating fabrics in volcanic rocks since other visible petrofabric indicators can be absent due to reduced grain size and/or weak preferred orientation. The degree of anisotropy in volcanic rocks is typically low (<10%) and it is the sensitivity of AMS that allows these fabrics to be identified and interpreted.

The AMS of catastrophic density current deposits (turbidity and pyroclastic) has been used to identify palaeocurrent directions (e.g. Ellwood, 1982; McDonald & Palmer, 1990; Hillhouse & Wells, 1991; Hiscott et al., 1997; Palmer & McDonald, 1999; Hailwood & Ding, 2000; Wang et al., 2001) and to locate unknown volcanic vents (e.g. Hillhouse & Wells, 1991; Ort et al., 2002; Palmer & McDonald, 1999). AMS has also been increasingly applied to study the fabrics in density current deposits to try and gain a better understanding of the depositional mechanisms and the affects of topography (e.g. Ort, 2002; Porreca et al., 2003)

Cagnoli and Tarling (1997) discovered that deposits believed to be deposited by turbulent processes showed well-grouped k_3 axes and a sub-horizontal girdle distribution of k_1 and k_2 ,

whilst deposits assumed to be emplaced by laminar currents produced well aligned AMS axes. Ort et al. (1999, 2002) used this as a foundation and discussed both variations in AMS fabrics with distance from source and the effects of topography on deposition of the Campanian Ignimbrite, Italy. Ort et al., (1999) found the proximal deposits of the Campanian ignimbrite produced more oblate, poorly lineated AMS fabrics, whereas the more distal deposits produced AMS fabrics that were moderately oblate to moderately prolate and had a stronger linear component. They interpreted this to be a result of the proximity to the source vent, suggesting that close to source the current was more chaotic, with more turbulence, and that any laminar shear was unstable preventing a good alignment of particles. As the current travelled from source, they inferred a decrease in energy and more stable laminar shear conditions, promoting laminar flow and an increased alignment of particles. They concluded that the difference in AMS results of proximal and distal deposits might represent changes in flow-boundary processes.

Ort et al., (2003) investigated the effects of topography on the depositional processes using AMS fabrics (Campanian Ignimbrite, Italy). The AMS revealed a general radial transport direction from the source, although steep palaeotopography caused irregular deviations, perhaps due to back flow of the current due as it interacted with the steep topography. This highlights the importance of palaeotopography and its role in the transportation and deposition of current deposits. The well-grouped nature of the AMS axes in the Campanian Ignimbrite is not compatible with en masse deposition, which would produce more random orientated AMS fabrics that would weaken upward from the base due to weaker shear (Ort et al., 2002). Rather than a decrease in shear, the shear sense changed and was interpreted as a result of several currents merging, producing an average palaeocurrent direction.

Porreca et al., (2003) compared AMS fabrics of palaeovalley and overbank facies of the Peperino Albano Ignimbrite (Italy) to investigate the effects of topography on depositional mechanism. Palaeovalley fill deposits produced triaxial fabrics and well-defined magnetic foliations and lineations. The magnetic foliation dipped slightly upslope with the magnetic lineation orientated down dip. The overbank deposits exhibited a good magnetic foliation that predominately dipped upslope. As with the palaeovalley-fill facies, the magnetic lineation was orientated approximately down dip with respect to the foliation, but was more dispersed along the foliation. In some instances the magnetic lineation appeared as two orthogonal clusters, orientated along the dip and strike of the foliation. The magnetic susceptibility values of the two different facies were statistically different, being higher in the palaeovalley fill facies, and

this was interpreted by Porreca et al., (2003) to be a result of variations in concentrations at each of the topographic settings.

AMS studies of welded tuffs can reflect original depositional mechanisms or the affects of welding and rheomorphism (e.g. Ellwood, 1982; Knight et al., 1986; Wolff et al., 1989). Ellwood (1982) carried out an AMS study on densely welded ignimbrites from the central San Juan Mountains, Colorado. The AMS fabrics of these deposits produced a sub-horizontal magnetic foliation, defined by the maximum and intermediate susceptibility axes. Such findings would indeed be expected of deposits that have undergone compaction and welding. The maximum and intermediate axes were well grouped rather than spread across the sub-horizontal plane, suggesting a linear component, which can be traced back to a known source. This suggests that the fabric was of a depositional origin. Where rheomorphism had occurred (Ellwood 1982) the AMS fabrics was a result of grain alignment in response to secondary flow (Ellwood, 1978, 1979; Knight & Walker, 1988). Since the slope over which it is passing determines rheomorphic flow, the AMS fabrics may still provide primary flow direction information (Wolff et al., 1989).

1.8 Methodology

1.8.1 Geological background

Tenerife is the largest island of the Canarian archipelago, situated in the eastern Atlantic Ocean, northwest of the African margin. Subaerial volcanism began in the late Miocene commencing with the emplacement of the 'Old Basaltic Series' (12 Ma to 3.3 Ma). Volcanic activity became increasingly evolved and explosive resulting in the construction of Las Cañadas shield volcano. This is composed of phonolitic ignimbrites and other pyroclastic rocks, interstratified with phonolitic to basaltic lavas and cinder cones, with a central nested caldera (Ancochea et al., 1999; Marti & Gundmundsson, 2000). There have been at least three sector collapse events (Ablay & Hürlimann, 2000; Hürlimann & Garcia-Piera, 2000; Masson & Watts, 2002), which may or may not be linked to caldera collapse. The Upper Bandas del Sur Group (Brown et al., 2003) is situated on the pyroclastic apron of Las Cañadas volcano on its south-eastern flanks (Fig. 1.7A). It is composed of several formations that have been correlated along ~45 km of the south-eastern flanks (Brown et al., 2003).

The pyroclastic formations are predominantly phonolitic, although some display compositional zoning (Wolff, 1985; Bryan et al., 1998; Brown, 2001; Bryan et al., 2002). All are non-welded, with the exception of the Arico ignimbrite, which is locally partially welded. The Eras Formation marks the base of the Upper Bandas del Sur Group but is of an undetermined age. The overlying Arico Formation has been dated at 668 ka \pm 4 ka (Brown et al., 2003) and the remainder of the Bañdas del Sur Group was erupted over a period of 499kyrs (Fig. 1.7B).

The Bandas del Sur Group is well documented (e.g. Bryan et al., 1998; Bryan et al., 2000; Brown 2001; Bryan et al., 2002; Edgar et al., 2002; Brown et al., 2003; Brown and Branney 2004; Pitarri et al., 2004, 2005a, 2005b, 2006; Edgar et al., 2006) and well exposed, with exceptional, clear palaeotopographic relationships. This allows units to be easily correlated, which is of great importance in the development of a methodology to discriminate between fine ash fallout and fine ash current deposits and to constrain the interpretation of the La Caleta eruption. No tectonic fabric has been imposed upon them, making them ideal deposits from which to study depositional fabrics and their well-consolidated nature makes sampling relatively easy.

The formations that have been focused on for this thesis include the Arico Formation (e.g. Fritsch and Reiss, 1868; Schmincke and Swanson, 1967; Alonso et al., 1988; Bryan et al., 1998; Brown, 2001; Brown et al., 2003), the Fasnía Formation (e.g. Brown et al., 2003), the Poris Formation (e.g. Edgar et al., 2002; Brown et al., 2003), the La Caleta Formation (Bryan et al., 1998; Edgar et al., 2006) and the Abrigo Formation (Nichols et al., 2002; Brown et al., 2003; Pitarri et al., 2004; Pitarri et al., 2005 a & b). These formations were selected because of their diverse variety of lithofacies, their high level of exposure, their excellent palaeotopographic relationships and the presence of fine ash layers. Samples were also taken from the Caldera del Rey tuff ring, situated near Los Cristianos, which displays very well-developed, planar and cross stratification. A brief overview of each of these formations follows, with more detailed descriptions in the relevant chapters.

Caldera del Rey tuff ring

The Caldera del Rey Formation has a provisional date of 953 ± 13 ka (Pringle and Branney unpublished data) and is a stratified and cross-stratified tuff to lapilli-tuff, with intercalated fine ash and pellet layers. It is not part of the Upper Bandas del Sur Group and its lithostratigraphic position is yet to be firmly established.

Arico Formation

The Arico Formation has a recorded date of 668 ± 4 ka and overlies Plinian fallout deposits and the Las Eras Formation (Brown et al., 2003; Fig. 2.4B), which consists of a highly characteristic, although commonly eroded or absent basal fallout deposit. The basal layer was first described by Brown et al. (2003), and consists of three layers; a very fine ash layer, a clast-supported 'millet-seed' layer, and a pumice lapilli layer. The overlying ignimbrite is chemically zoned and exhibits partial welding and a eutaxitic texture and columnar jointing at some locations. The colour varies from white at the base to dark grey with increasing welding intensity. It can also be orange in appearance, as a result of thermal alteration (Brown et al., 2003). The physical appearance of the Arico Formation is highly variable, which has resulted in misidentification (Bryan et al., 1998; Brown et al., 2003).

Abades Formation

The Abades Formation (Brown et al., 2003) has a recorded age of 596 ± 14 ka (Bryan et al., 1998) and has been described by Bryan et al. (1998) and Brown et al. (2003). It sits on top of the Arico Formation (Brown et al., 2003; Fig. 2.4B) and is a phonolitic ignimbrite containing cream pumice lapilli and characteristic black tephriphonolite pumice lapilli and blocks. No pumice lapilli fallout deposit has been reported, although the base is commonly erosional (Brown et al., 2003). It contains fine ash layers that contain accretionary lapilli, interpreted by Brown et al. (2003) to be of probable co-ignimbrite origin.

Granadilla Formation

The Granadilla Formation has a recorded age of 600 ± 9 ka (Brown et al., 2003) and has been described in detail (Booth, 1973; Bryan et al., 1998, 2000, 2002 & 2006). It sits on top of the Abades Formation (Brown et al., 2003; Fig. 2.4B) and is stratigraphically overlain by the Aldea Blanca pumice fallout deposits (see Brown et al., 2003 for additional logs). It consists of a thick, diffusely bedded Plinian fallout deposit (≤ 9 m thick), overlain by a variably

massive to diffusely bedded/stratified, phonolitic ignimbrite that exhibits compositional zoning (≤ 30 m thick).

Fasnia Formation

The Fasnia Formation has a recorded age of 289 ± 6 ka (Brown et al., 2003) and was previously referred to as the 'Lower Grey Member' (Bryan et al., 1998). It consists of phonolitic fallout deposits, lithic-rich ignimbrites and accretionary lapilli-bearing fine ash layers, and sits on top of the Aldea Blanca fallout deposits (Brown et al., 2003; Fig. 2.4B). The Fasnia fallout deposits have a distinctive internal stratigraphy and contain subordinate banded pumice, producing a very characteristic appearance. The lithic-rich ignimbrites display a variety of lithofacies including massive, diffusely bedded and stratified, and pass laterally into low-angle, cross-stratified tuffs. These are intercalated within the fallout deposits and are overlain by fine ash layers bearing abundant accretionary lapilli. Accretionary lapilli-bearing ash layers are also locally found at the base of the formation. The Fasnia Formation also contains a previously undiscovered clast-supported unit with low-angle cross-stratification, which has been interpreted as reworked material, emplaced during a brief hiatus in the emplacement of primary volcanic material. These deposits have been found in the Tajao area and near Montaña Magua.

Poris Formation

The Poris Formation has a recorded date of 273 ± 5 ka (Brown et al., 2003), overlies the Fasnia Formation and is overlain by the Sabinita Formation (Brown et al., 2003; Fig. 2.4B). It is subdivided into 11 members composed of a series of ignimbrites and corresponding fallout deposits (Brown et al., 2001, 2003, 2004b). Member one consists of eight fall deposit layers. Members 2-4 are thin ignimbrites with associated pellet layers, believed to be fallout deposits. Member 5 is a Plinian pumice fall deposit, whilst Members 6 and 7 are massive to cross-stratified ignimbrites. Member 8 is a lithic breccia that was previously named the 'Upper Grey Member' (Bryan et al., 1998) and Member 9 is a diffusely bedded to massive ignimbrite that is commonly framework-supported. Member 10 is a mafic fallout deposit that is followed by volcanoclastic sandstones that make up Member 11.

La Caleta Formation

The La Caleta Formation has a recorded date of 221 ± 5 ka, sits on top of the Sabinita Formation and is overlain by variable fallout deposits and the Abrigo Formation (Brown et

al., 2003; Fig. 2.4B). It has previously been described by Bryan et al. (1998), Brown et al. (2003) and Edgar et al. (2006), and will be described in detail in Chapter 3, in terms of its constituent members, interpreting these in terms of their depositional mechanism and the evolution of the La Caleta eruption. Briefly, it consists of Plinian fallout deposits, followed by a sequence of ignimbrites and co-ignimbrite ash layers, culminating in a large ignimbrite capped by a lithic breccia, which is interpreted to represent caldera collapse.

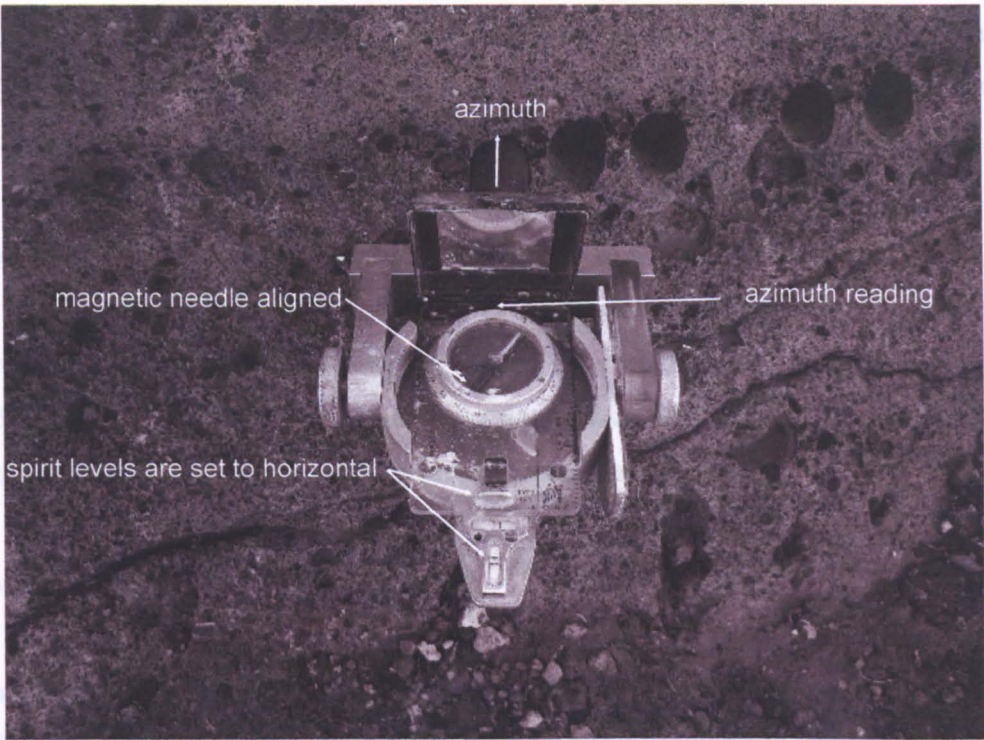
Abrigo Formation

The Abrigo Formation has a recorded date of 169 ± 1 ka and is the youngest formation in the Upper Bandas del Sur Group (Brown et al., 2003; Fig. 2.4B). The Abrigo Formation has been previously described by Nichols et al. (2002) Brown et al. (2003), Pitarri et al. (2004), Pitarri et al., (2005 a & b, 2006). No Plinian fallout deposit is associated with the Abrigo Formation although the base of the ignimbrite is erosive (Brown et al., 2003). The ignimbrite is phonolitic and is a variably lithic-rich lapilli-tuff, with prominent pumice lapilli-rich lobes (Pitarri et al., 2005). It also contains intercalated fine ash layers, containing rare accretionary lapilli (Brown et al., 2003).

1.8.2 Collection and preparation of AMS samples

Orientated core samples were drilled in the field wherever possible, using a petrol-operated drill and 25 mm diameter diamond drill bit. In total over 570 cores were collected and approximately 1700 plugs prepared during this research. The number of cores taken from each ash layer at each locality varied from 5 – 23 depending on the size and condition of the cores. A minimum of 20 orientated plugs were collected from each sample site wherever possible. This minimum number of plugs was selected because it was found that the average data remained the same beyond this number of plugs. A horizontal orientation line was marked on to the rock surface and the orientation of that line and the dip of the rock surface were noted. Care is required to avoid drilling into other lithofacies, so cores were drilled as close to horizontal as possible. To ensure a fabric that is truly representative of depositional processes, areas of soft-state deformation or where there had been interaction with vegetation were avoided. The layers sampled were horizontal to sub-horizontal to rule out down slope movement. After drilling, the azimuth and the plunge of each core were recorded (Fig. 1.8).

A



B

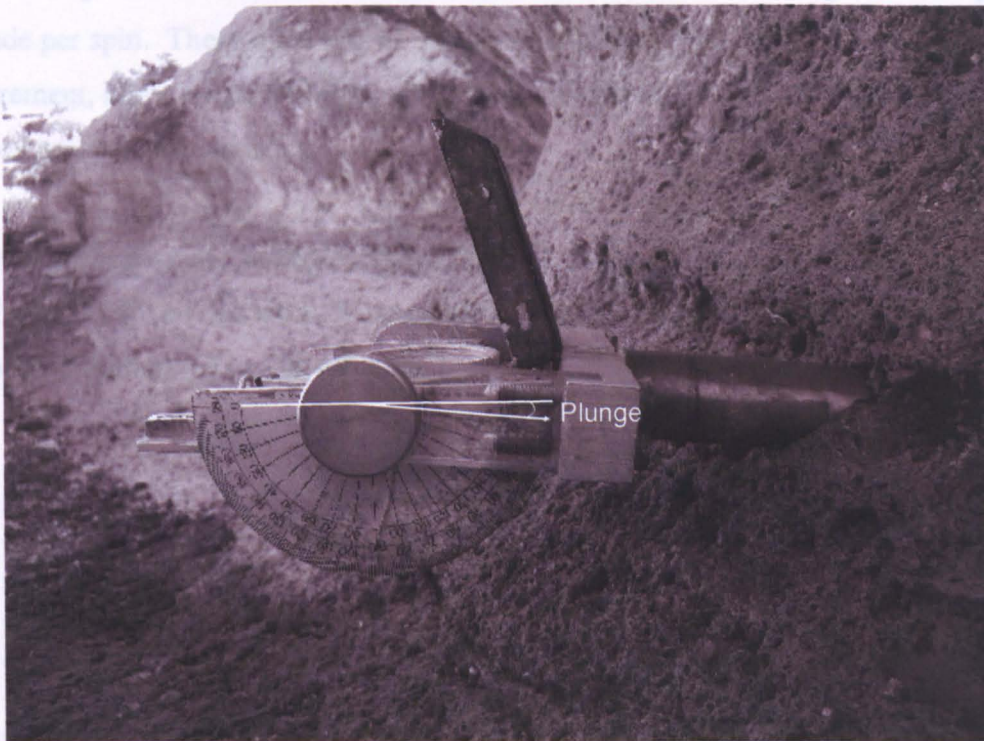


Figure 1.8: (A) Photo demonstrating how the azimuth of the core is measured. The instrument is inserted into the hole and, using the spirit level, the base of the compass is moved so it is horizontal. The compass is rotated so the compass needle is aligned to the north and the measurement is recorded: (B) Photo demonstrating how the plunge of the core is measured. Once the base of the compass is horizontal the plunge reading can be recorded off the protractor on the side of the instrument.

If drilling in the field was not possible, orientated block samples were taken and drilled in the laboratory. The block was securely clamped to ensure there was no movement during drilling and a drill line (horizontal and level line) was drawn on the surface, using a spirit level, from which the drill pitch and drill dip were recorded (Fig. 1.9).

Orientation and way-up markers were transferred down the side of each core (Fig. 1.10B & C), which was then cut into plugs 22mm in length (Fig. 1.10D), and the way-up markers were transferred on to each individual plug (Fig. 1.10E). Errors in the orientation process can arise when drawing the orientation line on an irregular surface, and if the core is not perfectly straight. In general, errors in orientation are estimated as $<5^\circ$.

1.8.3 Measurements of AMS samples

The magnetic susceptibility of the individual plugs was measured in a KLY3-S Kappabridge at the University of Birmingham. The KLY-3S Kappabridge is a precision, fully automated inductivity bridge. Samples are placed into the machine, in three orthogonal positions and spun at 0.5 r.p.s in a field of 300 Am^{-1} where 64 measurements of changes in susceptibility are made per spin. These three sets of measurements, combined with one bulk susceptibility measurement, allow a susceptibility tensor to be calculated using SUSAR software, which is based on multivariate statistics.

This produces magnetic susceptibility values (K_1 , K_2 and K_3) and their orientation in space (k_1 , k_2 and k_3). From this the bulk susceptibility (K_m), the percentage lineation (L) and percentage foliation (F) can be calculated.

$$K_m = \frac{K_1 + K_2 + K_3}{3} \quad (2)$$

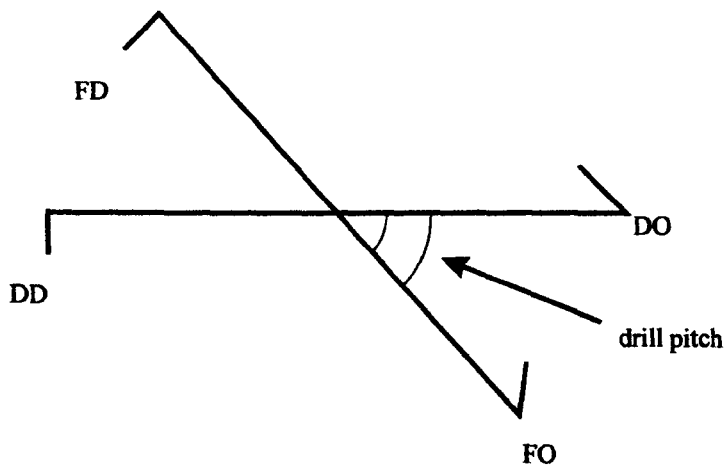
$$L = \frac{K_1 - K_2}{K_m} \quad (3)$$

$$F = \frac{K_2 - K_3}{K_m} \quad (4)$$

The raw data are processed using a series of MS DOS programs (Owens, unpublished). The initial program restores the data to its correct geographical orientation and corrects for the effects of bedding. The corrected data is passed through a second program to produce stereonet, displaying the eigenvectors for each individual plug, providing information about the orientation and distribution of the fabric. A third series of programs allows the calculation of mean eigenvectors and plots them on stereonet with 95% confidence ellipses. Finally, a fourth program allows a foliation /lineation (F/L) plot to be constructed, providing a graphical representation of the shape of anisotropy (μ) and the strength of anisotropy (H) (Fig. 1.11).

$$\mu = \tan^{-1} \frac{K1 - K2}{K2 - K3} \quad (5)$$

$$H = \frac{K1 - K3}{Km} \quad (6)$$



FD = field dip

Figure 1.9 The measurements required when drilling a block sample. These include the drill pitch, which is the angle between the orientation line marked in the field (FL), and the drill line (DL), and the drill dip (DD), which is the dip of the rock surface at 90° to the drill line, when clamped in place.

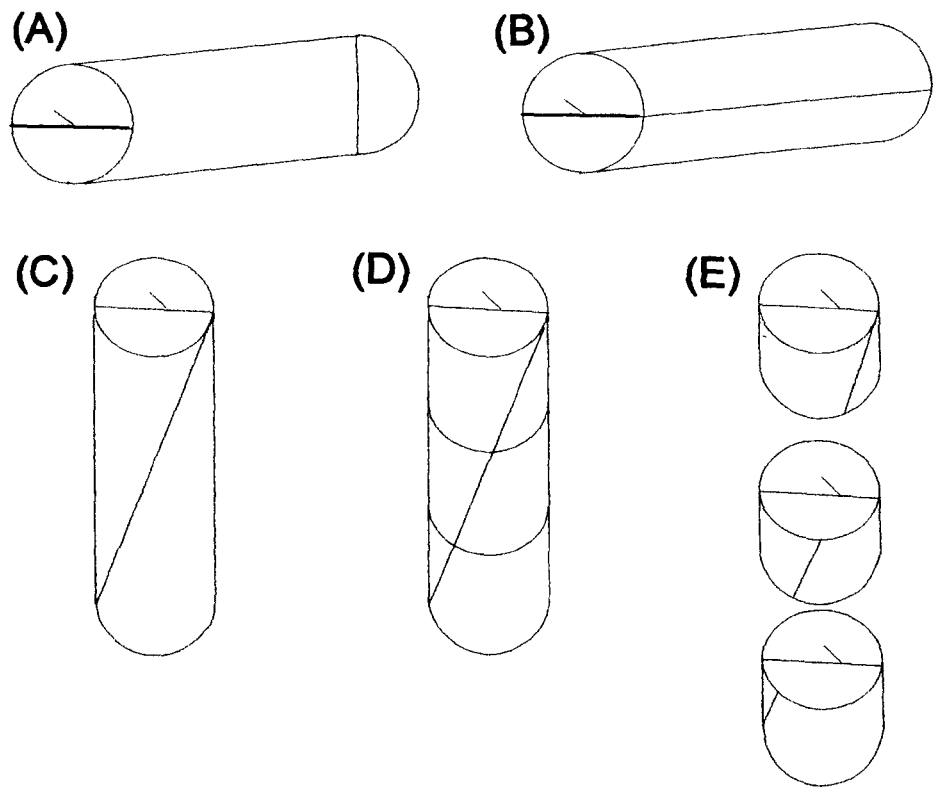


Figure 1.10 : The preparation of the cores and the transfer of orientation marks: (A) Core with the field line on the top surface, which is used to draw straight lines down the length of the core (B). A diagonal line is drawn across the length of the core (C), so as the way up and the order of the individual plugs can be identified after they have been cut (D) Finally the field orientation is marked on to each of the plugs, using the lines drawn down the side of the cores (E).

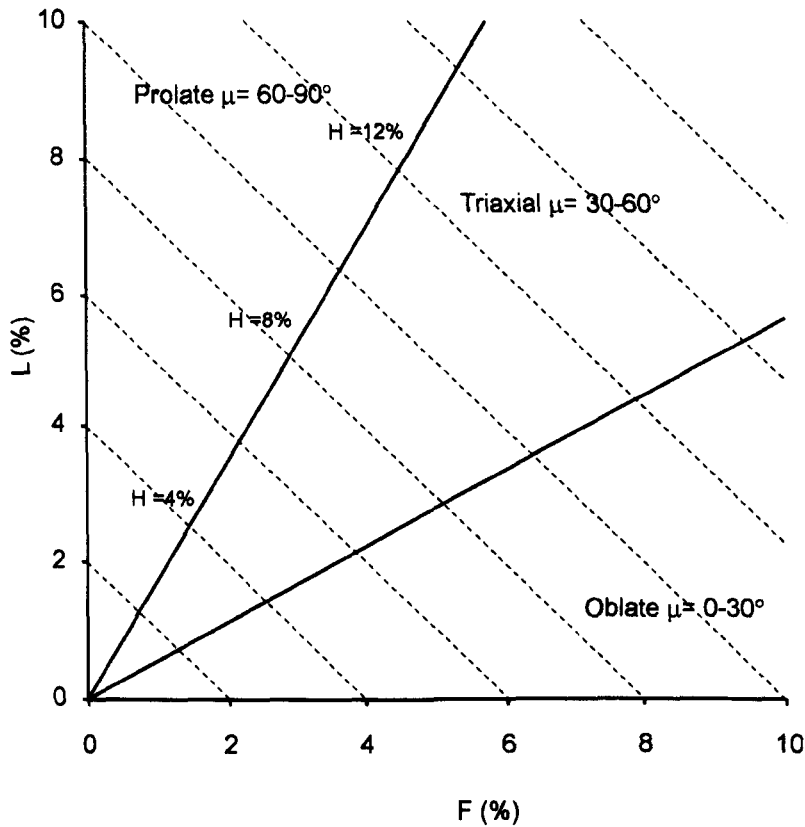


Figure 1.11: Foliation- Lineation plot displaying the different fields according to the shape of anisotropy (oblate, triaxial, prolate) according to their μ value and how changes in the foliation and/or the lineation can affect the strength of anisotropy (H).

1.8.4 Susceptibility v temperature measurements

Susceptibility vs temperature measurements were made using an Agico CS-3 temperature control unit, with a sensitivity of 1×10^{-7} SI. An AMS plug, of representative bulk susceptibility, is crushed and ground to a fine powder and placed into a narrow glass tube into which a thermocouple is inserted. This is then placed into a sealed cooling unit and repeatedly lowered into the KLY-3S Kappabridge, heating from 40 °C to 800°C, measuring the variations in susceptibility throughout the heating process. This process is then repeated in reverse during cooling. Suste software allows heating and cooling curves to be produced, from which Curie temperatures can be identified and interpreted in terms of the magnetic mineralogy of the sample.

1.9 Thesis outline

This thesis consists of a further four chapters. Chapter two presents a new stratigraphy for the La Caleta Formation and its eruptive history. Chapter three describes a method of distinguishing fine ash fallout deposits from fine ash current deposits using Anisotropy of Magnetic Susceptibility (AMS). Chapter four explores the information that AMS can reveal about the depositional mechanisms of a variety of different lithofacies, including thinly bedded, stratified and cross-stratified deposits. This information is then used in the identification and interpretation of different types of massive deposit. How topography can influence flow-boundary conditions and therefore the depositional fabrics will be discussed and a new fabric-based lithofacies scheme is presented. Finally, Chapter five will present the overall conclusions of the thesis and suggestions for further work.

Chapter 2: Event stratigraphy of the La Caleta Formation

Abstract: The 221 ka La Caleta Formation of the Bandas del Sur Group, Tenerife, records a phonolitic explosive caldera-forming eruption that devastated an area of $>533 \text{ km}^2$ in SE Tenerife. It produced a $<38\text{m}$ succession consisting of a Plinian fall deposit overlain by ignimbrites and co-ignimbrite ash layers. Six members have been defined on the basis of 45 logs, granulometry and geochemistry, and were emplaced during five eruptive phases. Phase 1 comprised of a fluctuating Plinian eruption, with dispersal axes towards the SE that deposited an extensive, laminated ash to thin-bedded pumice fallout layer (Member 1). In Phase 2, the main Plinian phase, the eruption column reached c. 36 km high and dispersed to the SE as the eruption waxed, producing a $< 3 \text{ m}$ thick Plinian pumice fall layer, with an upper lithic-rich layer recording increased vent erosion. Phase 3 was the onset of column collapse, with generation of a rapid succession of short-lived pyroclastic density currents that deposited a series of extensive ignimbrites and fine ash layers (Members 3-5). The first density current widely bypassed the island, and its passage is recorded by c. 1 m erosion of the underlying Plinian deposit, which is draped by its associated co-ignimbrite ashfall layer. The eruption climaxed during Phases 4 and 5, with a sustained pyroclastic density current that deposited $> 25 \text{ m}$ thick ignimbrite (Member 6) containing lithic breccias that probably mark the onset of caldera collapse (Phase 5). The eruption unit is compositionally zoned, and has a more complex internal lithostratigraphy than previously documented, sharing numerous similarities with the older Poris Formation.

2.1 Introduction

The 221 ka La Caleta Formation records one of over seven major Quaternary ignimbrite eruptions that devastated the southern flanks of Tenerife (Brown et al. 2003). It covers a minimum area of 533 km^2 from El Medano to Güimar and from the coast to north of Sabinita and El Bueno (Fig. 2.1). The explosive eruption deposited a cream phonolitic, compound ignimbrite sheet, up to 38 m thick and comprises of Plinian fallout layers overlain by pyroclastic density current deposits, intercalculated with co-ignimbrite ash layers. The eruption was compositionally zoned, and culminated with the emplacement of lithic breccias. This chapter describes the internal lithostratigraphy of the formation, interprets the depositional processes and reconstructs the eruption history.

This chapter describes the La Caleta Formation stratigraphy in detail, with reference to over one hundred measured sections across the Bandas del Sur. The most complete sections are around Tajao and Maretas (Fig. 2.1) and are the type locations for The La Caleta Formation in this study. Six members are interpreted in terms of emplacement mechanisms and eruptive

history. Isopach and isopleths of fallout deposits have been mapped and the granulometry, lithic populations of individual layers and geochemistry have been analysed, to reconstruct the eruptive history.

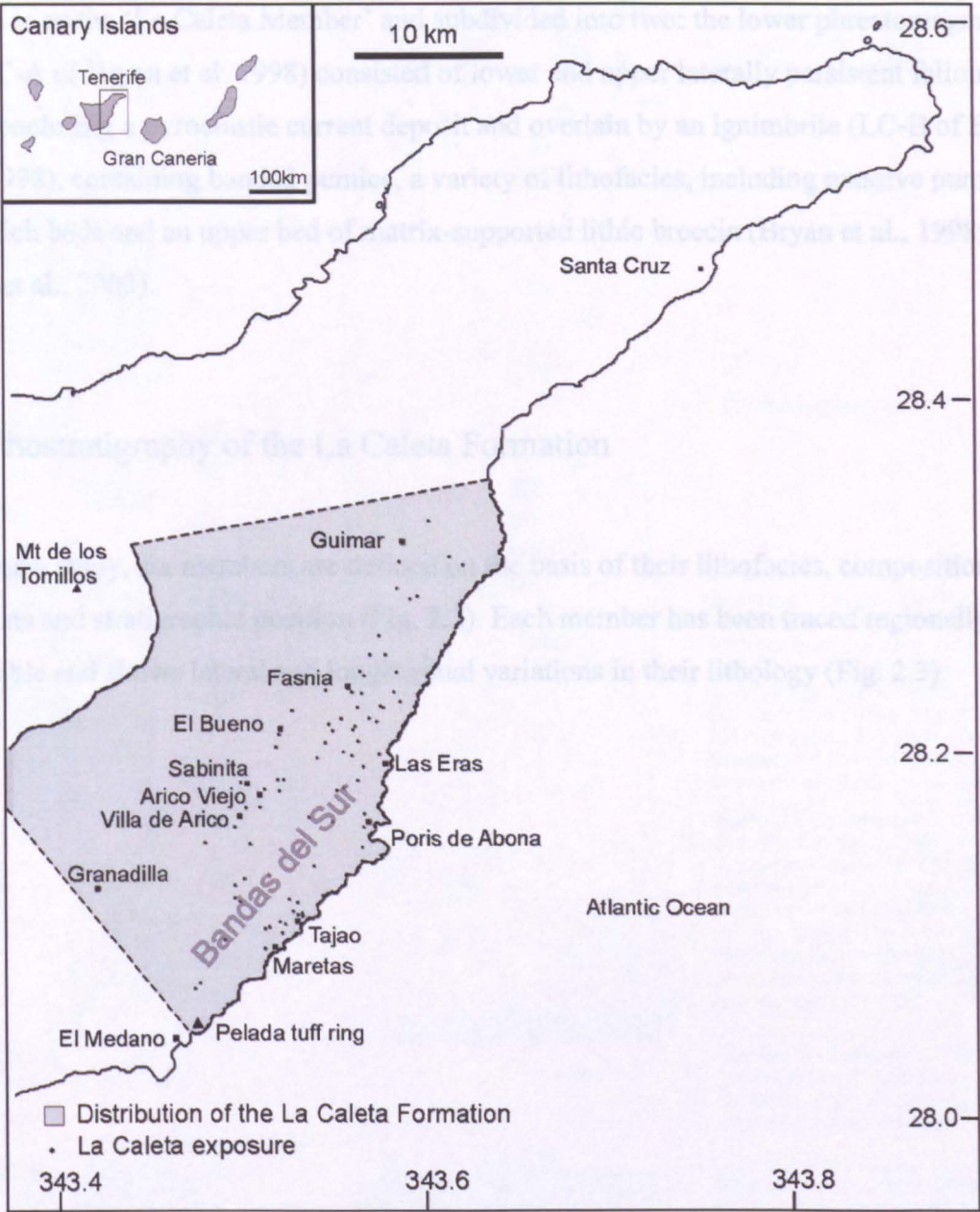


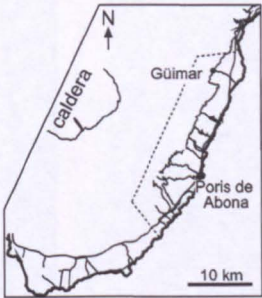
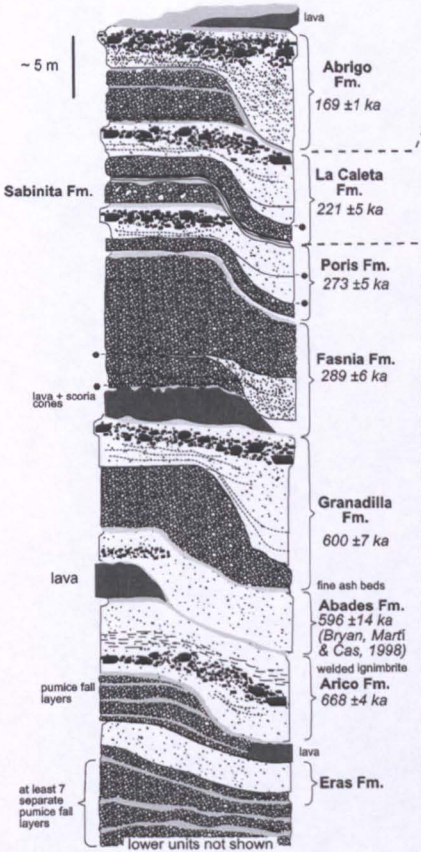
Figure 2.1: Location map of Tenerife with the distribution of the La Caleta Formation and the principal La Caleta exposures. Coordinates are in latitude and longitude.

The Caleta Formation was named by Brown et al. (2003), and general characteristics were previously reported by Alonso (1989), Bryan et al. (1998) and Edgar et al. (2006), but there has been no detailed study. A lower laminated ash and a pumice lapilli fallout deposit (Wavy Deposit Member of Bryan et al. 1998) and the overlying pyroclastic current deposits were referred to as the 'La Caleta Member' and subdivided into two: the lower phreatomagmatic unit (LC-A of Bryan et al. 1998) consisted of lower and upper laterally persistent fallout layers, enclosing a pyroclastic current deposit and overlain by an ignimbrite (LC-B of Bryan et al., 1998), containing banded pumice, a variety of lithofacies, including massive pumice lapilli-rich beds and an upper bed of matrix-supported lithic breccia (Bryan et al., 1998; Brown et al., 2003).

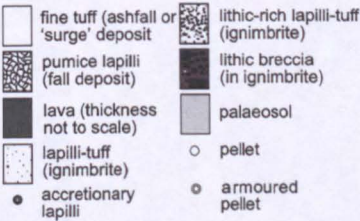
2.2 Lithostratigraphy of the La Caleta Formation

In this new study, six members are defined on the basis of their lithofacies, compositional variations and stratigraphic position (Fig. 2.2). Each member has been traced regionally as far as possible and shows lateral and longitudinal variations in their lithology (Fig. 2.3).

A: Upper Bandas del Sur Group

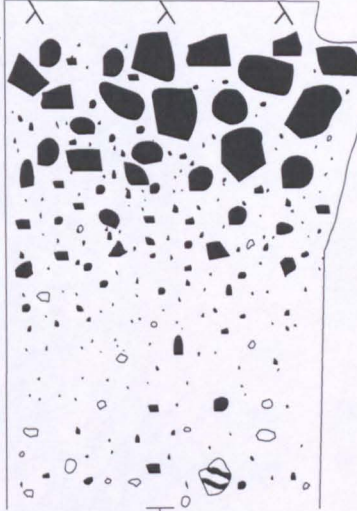


Key



B: La Caleta Formation

Unnamed fallout deposits/ Abrigo Formation

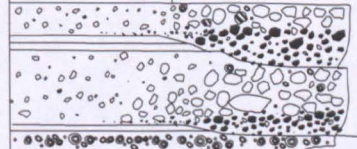


Member 6 - massive pumice and lithic lapilli-tuff with local diffuse-bedding and stratification, particularly near palaeovalley margins. Lithic breccia at the top. Lithic segregation structures and sedimentary dykes. Contains banded pumice lapilli.

(26 m not shown)



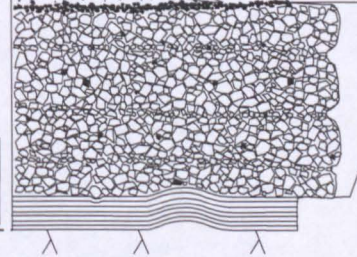
Member 5 - Six couplets: Couplet 1a, 5a & 6a have an inversely graded, matrix-supported lithic-rich lapilli-tuff base overlain by a matrix-supported pumice-rich lapilli-tuff, ± accretionary lapilli and armoured pellets. Couplets 1a & 5a are draped by co-ignimbrite ash with pellets and armoured pellets (1b & 5b). Couplets 2, 3 & 4 are incomplete and form a sequence of framework-supported pellets.



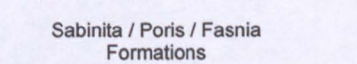
Member 4 - Massive white fine ash tuff (4a). Contains occasional pumice and lithic lapilli. Cross-stratification towards the base. Contains internal erosion surfaces. Characteristic lithic trains. Accretionary lapilli are abundant towards the top. Overlain by a co-ignimbrite ash. Predominately matrix-supported pellets and armoured pellets. Framework-supported examples can be found.



Member 3 - Rare lower pumice lapilli-tuff ignimbrite (3a) draped by a pink co-ignimbrite ashfall layer (3b) consisting of framework-supported pellets towards the top of the layer.

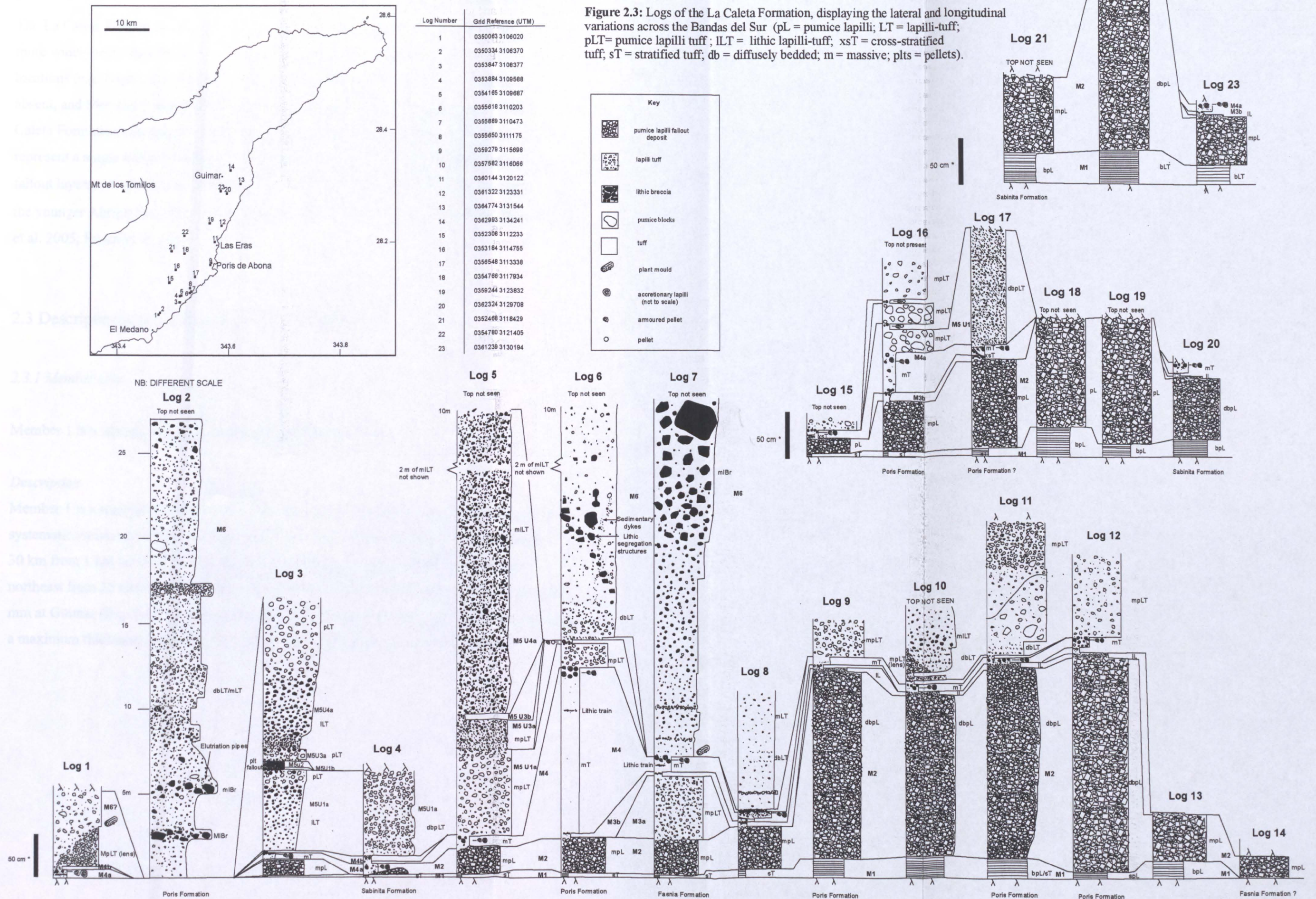


Member 2 - Massive to diffusely-bedded, framework supported, pumice lapilli fallout deposit. Capped by a lithic lapilli layer.



Member 1 - Fine to coarse laminated to thin-bedded fallout deposit. Contains pellet layers and plant moulds. Impact structures in the fine ash caused by pumice lapilli from overlying Member 2. Mound-like structures.

Figure 2.2: (A) A general vertical section of the Bandas del Sur Group (Brown et al., 2002) with a map showing the area from which information was taken; (B) A general vertical section through the La Caleta Formation. The entire thickness of Member 6 is not present due to scale and size restrictions. Ornamentation and ash layers are to approximate scale only.



* unless otherwise stated

The La Caleta Formation locally overlies a palaeosol developed in the Sabinita Formation, but more widely rests directly upon the older Poris and Fasnía formations (Fig. 2.2A). At some locations (e.g. Logs 1 & 2; Fig 2.3) members 1 and 2 are absent. At others, members 1-5 are absent, and Member 6 rests directly on the Poris Formation (e.g Log 2 Fig. 2.3). The La Caleta Formation contains no internal palaeosols and reworked horizons, and is inferred to represent a single eruption without prolonged hiatuses. It is overlain by unnamed pumice fallout layers, (Ar/Ar date of $204.8 \text{ ka} \pm 8.5 \text{ ka}$; Panell, unpublished PhD thesis, 2005), and the younger Abrigo Formation ($169 \text{ ka} \pm 1 \text{ ka}$ Brown et al. 2003; Pitarri & Cas, 2004; Pitarri et al. 2005; Pitarri et al. 2006).

2.3 Description and interpretation of the members

2.3.1 Member One:

Member 1 is a laminated to thin-bedded Plinian fallout deposit.

Description

Member 1 is a regionally extensive ash layer that drapes topography and displays regional systematic variations in thickness and grain size (WD-A of Bryan et al. 1998). It extends 30 km from 1 km northeast of Granadilla industrial estate to Guimar. It thickens to the northeast from 35 mm to 240 mm at Las Eras (GR: 0360144 3120122) and then thins to 200 mm at Güimar (Fig. 2.4). It has been traced 7-8 km inland to El Bueno and Sabinita, reaching a maximum thickness of 460 mm near Arico Viejo, but potentially extends further.

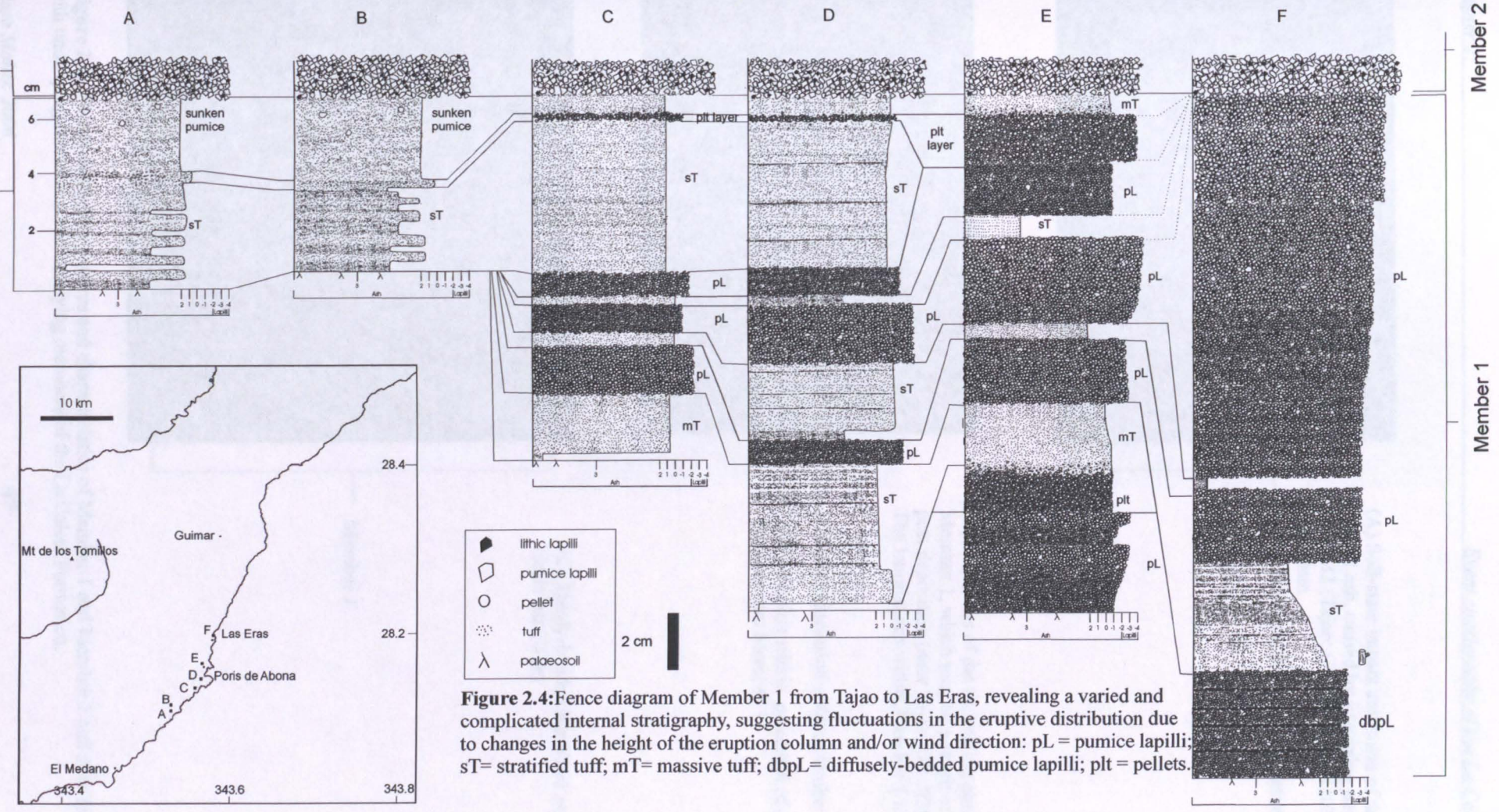
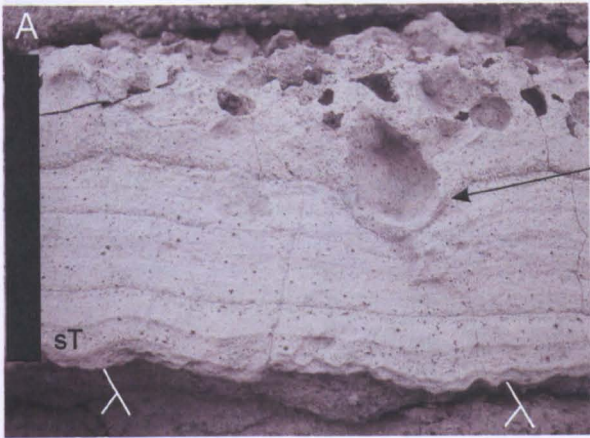


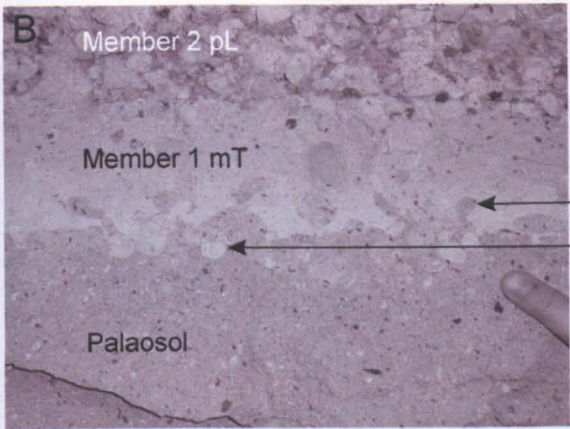
Figure 2.4: Fence diagram of Member 1 from Tajao to Las Eras, revealing a varied and complicated internal stratigraphy, suggesting fluctuations in the eruptive distribution due to changes in the height of the eruption column and/or wind direction: pL = pumice lapilli; sT= stratified tuff; mT= massive tuff; dbpL= diffusely-bedded pumice lapilli; plt = pellets.



(A) Soft-state impact structures of the Member 1 fallout ash, caused by impacting pumice lapilli from M2 (Tajao; GR:0355664 3110387). Scale bar 50mm

Impact structure, deforming the underlying laminations

Member 1



(B) Inclusions of the underlying palaeosol within Member 1, which may be a result of bioturbation post deposition (near Tajao; GR: 0355203 3111356). The laminations within Member 1 have been destroyed.

Palaeosol inclusion within Member 1

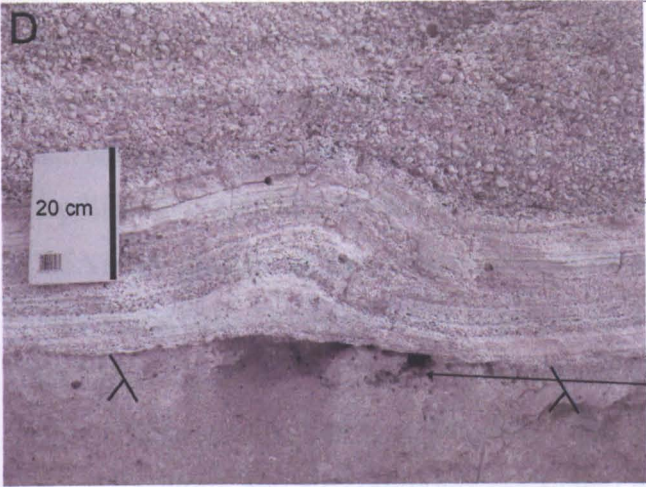
Ash inclusion within palaeosol of material derived from Member 1



(C) Thinly-bedded Member1 near Las Eras. Scale bar 20 cm

Member 1

Figure 2.5: Photos displaying features and characteristics of Member 1 and Member 2 and their relationship with underlying formations and overlying members of the La Caleta Formation.

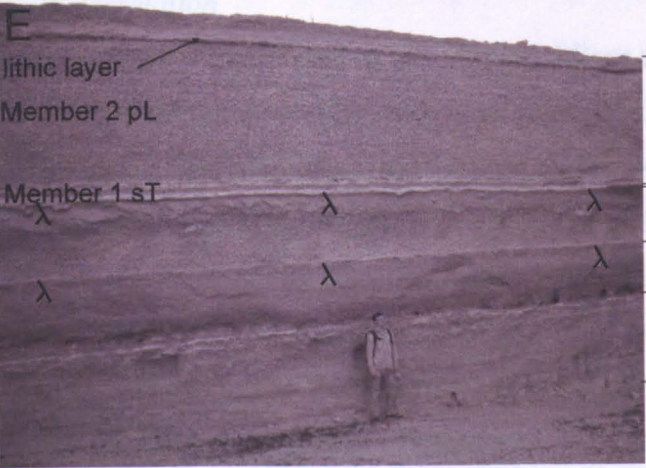


(D) Mound-like structures within Member 1, interpreted as the interaction of ash fallout on vegetation (Poris de Abona -Arico road GR: 0356626 3115917).

Member 2

Member 1

Root moulds



(E) Member 1 overlying the Sabinita and Fasnja Formations, followed by a pumice lapilli fallout deposit exhibiting diffuse bedding (Member 2), overlain by a lithic lapilli fallout layer (GR: 0356826 3119910).

La Caleta Formation

Sabinita Formation fallout deposit

Fasnja Formation(?) fallout deposit

Figure 2.5 continued:

Member 1 is composed of white laminated ash (e.g. Tajao Fig. 2.5A), and thickens and coarsens to a layer of thinly-bedded, framework-supported angular pumice lapilli, with clast-supported pellet layers (e.g. Las Eras Fig. 2.5C). The bedding alternates between fine/coarse ash and pumice lapilli producing an overall upward-coarsening sequence. Impacting pumice lapilli from overlying Member 2 have caused impact structures in the laminated ash (Fig. 2.5A) and, upslope of Tajao, Member 1 contains small irregular shaped inclusions of the underlying palaeosol (Fig. 2.5B). A variety of lithic clast types are present (250-2000 μm), including black, grey and hydrothermally altered. The hydrothermally altered lithics are absent from specific horizons. Mound-like structures, composed of draping layers, occur at some locations, and are commonly associated with plant moulds (e.g. near Poris de Abona; Fig. 2.5D).

Interpretation

Member 1 is interpreted to be a Plinian fallout deposit on the basis of its draping relationship of underlying topography, and of the regional and systematic variations in thickness and grain size. The Member 1 isopachs are highly asymmetrical, with two dispersal axes (Fig. 2.6): Axis 1 centres over Poris de Abona in a SE direction and intersects the Las Cañadas Caldera, at Mt de los Tomillos, which is the inferred source area for the Poris eruption (Edgar et al. 2002). The shape of the 20 m and 10 m isopach contours generates an asymmetry and Axis 2 lies over Las Eras and intersects the Las Cañadas Caldera, NE of Mt de los Tomillos. It seems that the dispersal of Member 1 was not straightforward and the upward coarsening pattern within Member 1 and regional variations in the internal stratigraphy suggest an increase in eruption column height (Fig. 2.4). For example, at Tajao the fine laminated ash layer that represents Member 1 has been traced across coastal regions of Tenerife and only represents the final stages of this phase of the eruption (Fig. 2.4). At other localities there is a preceding fallout deposit that is absent at Tajao. This can be accounted for by an increase in dispersal caused by an increase in eruption column height, thus encountering different wind directions, resulting in an anticlockwise shift in the dispersal axis. An increase in eruption column height would require an increase in mass flux, which can be triggered by a change in volatile content due to variations in the geochemistry of the magma or vent widening, causing magma decompression (Legros et al. 2000; Legros & Kelfoun, 2000; Varekamp, 1993). This would result in the rapid expansion of volatiles and an increase in the rate of vesiculation within the magma causing it to ascend rapidly (Scandone, 1996). The periodic appearance of hydrothermally altered lithics suggests that there were times when material was drawn up

from greater depths, suggesting an unsteady and pulsating phase of the eruption. There is no evidence of magma mingling in Member 1, so an increase in mass flux due to a change in volatile content linked to variations in magma geochemistry seems less likely, although this may have played a role later in the eruption (members 5 and 6; Section 2.6). The unusual isopach contours of Member 1 were also noticed by Edgar et al. (2006).

The origins of the mound-like structures in Member 1 have been interpreted as being of fallout origin (Alonso, 1989), the shearing effect of a “wet” surge (Marti et al. 1995) and dewatering structures (Bryan et al. 1998). Brown et al. (2003) suggested they are the result of draping shrubs similar to those on present day Tenerife. This is supported by the presence of plant moulds within and beneath some of these mound-like structures and the presence of rootlets in the underlying palaeosol of the now decomposed shrubs. Ash draping the shrubs would account for the chaotic nature of the cores of some of the mound-like structures and could explain variations in thickness of internal units. The irregular palaeosol inclusions within Member 1 may have been caused by bioturbation post deposition by organisms trying to escape from the volcanic ash.

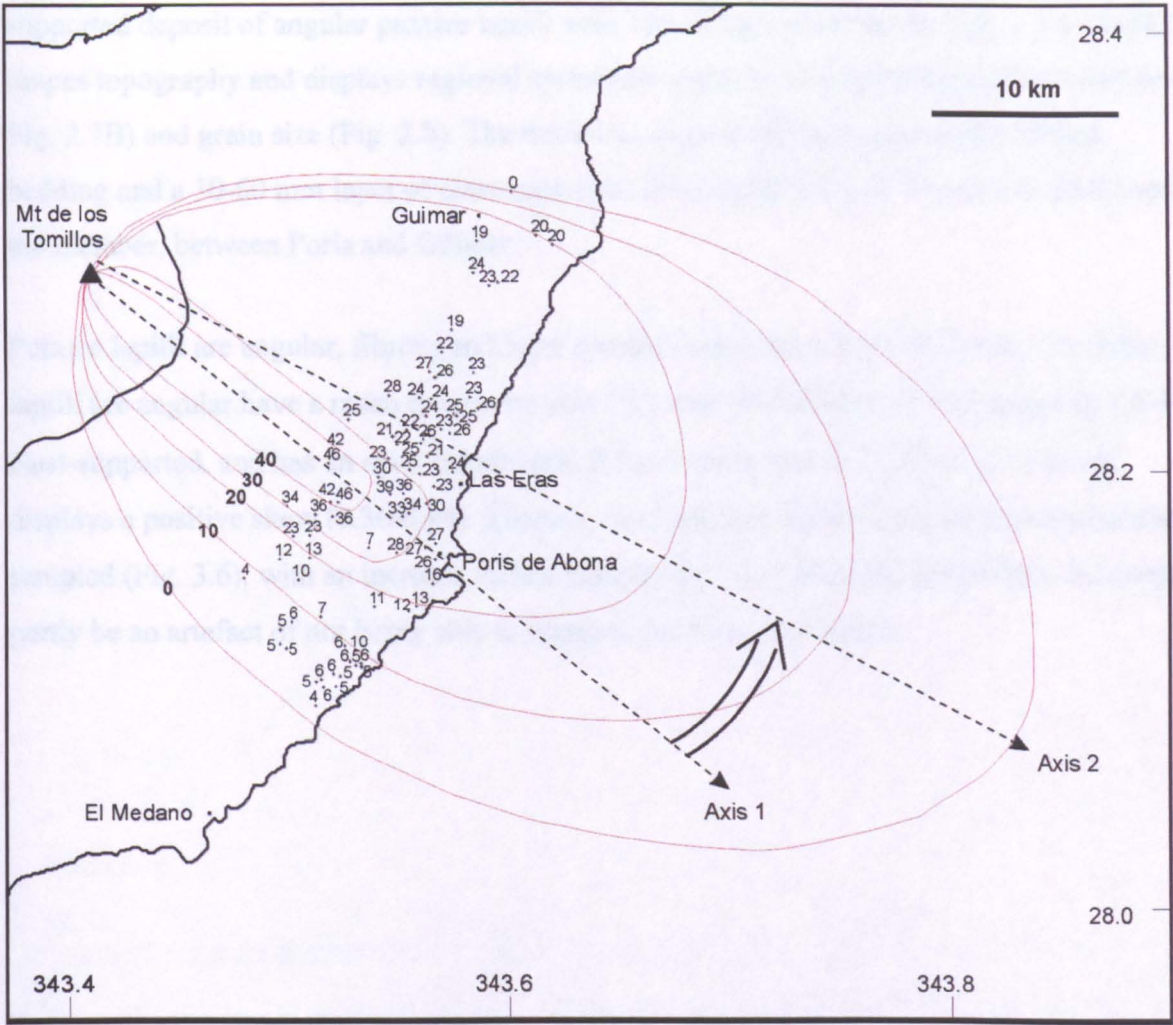


Figure 2.6: Isopach map of Member 1 displaying its distribution. The isopach contours are asymmetric and two plume axes have been interpreted. The first has a more southeast direction, centring over Poris de Abona, with a source near the present day Mt de le Tolmillos. The second plume axis has rotated anticlockwise, centering over Las Eras and has a source northeast of Mt de los Tolmillos.

2.3.2 Member 2

Member 2 is a Plinian pumice lapilli fallout deposit with a lithic lapilli fallout layer at the top of the member

Description

Member 2 (WD-B of Bryan et al. 1998), extends 36 km from 1 km east of the Granadilla industrial estate to just northeast of Guimar. It thickens to the northeast from 20 cm to 230 cm at Las Eras (Logs 3 & 11; Fig 2.3) and then thins to 45 cm further eastwards towards Güimar (Log 13; Fig. 2.3). It has been traced 7-8 km inland to El Bueno and Sabinita (but potentially extends further; Fig. 2.1), reaching a maximum thickness of 280 cm. It is a well-sorted, clast-

supported deposit of angular pumice lapilli with subordinate lithic lapilli (Fig. 2.5 E), which drapes topography and displays regional systematic variations in thickness (20 cm –280 cm; Fig. 2.7B) and grain size (Fig. 2.8). The thickest, coarsest sections show subtle diffuse bedding and a 30-60 mm layer of clast-supported lithic lapilli (Fig. 2.7B) occurs at the top of the member, between Poris and Güimar.

Pumice lapilli are angular, fibrous and have a mean maximum size of 41.2 mm. The lithic lapilli are angular have a mean maximum size 19.9 mm. The deposit is well sorted (ϕ 1.4-1.9), clast-supported, and has an open framework. It has a mean size of -2.53 to -3.16ϕ and displays a positive skew (0.36-0.49). There is a bimodal grainsize distribution at the locations sampled (Fig. 3.6), with an increase in fine material ($\phi >4$). The peaks in the fines tail could partly be an artefact of not being able to separate the fines any further.

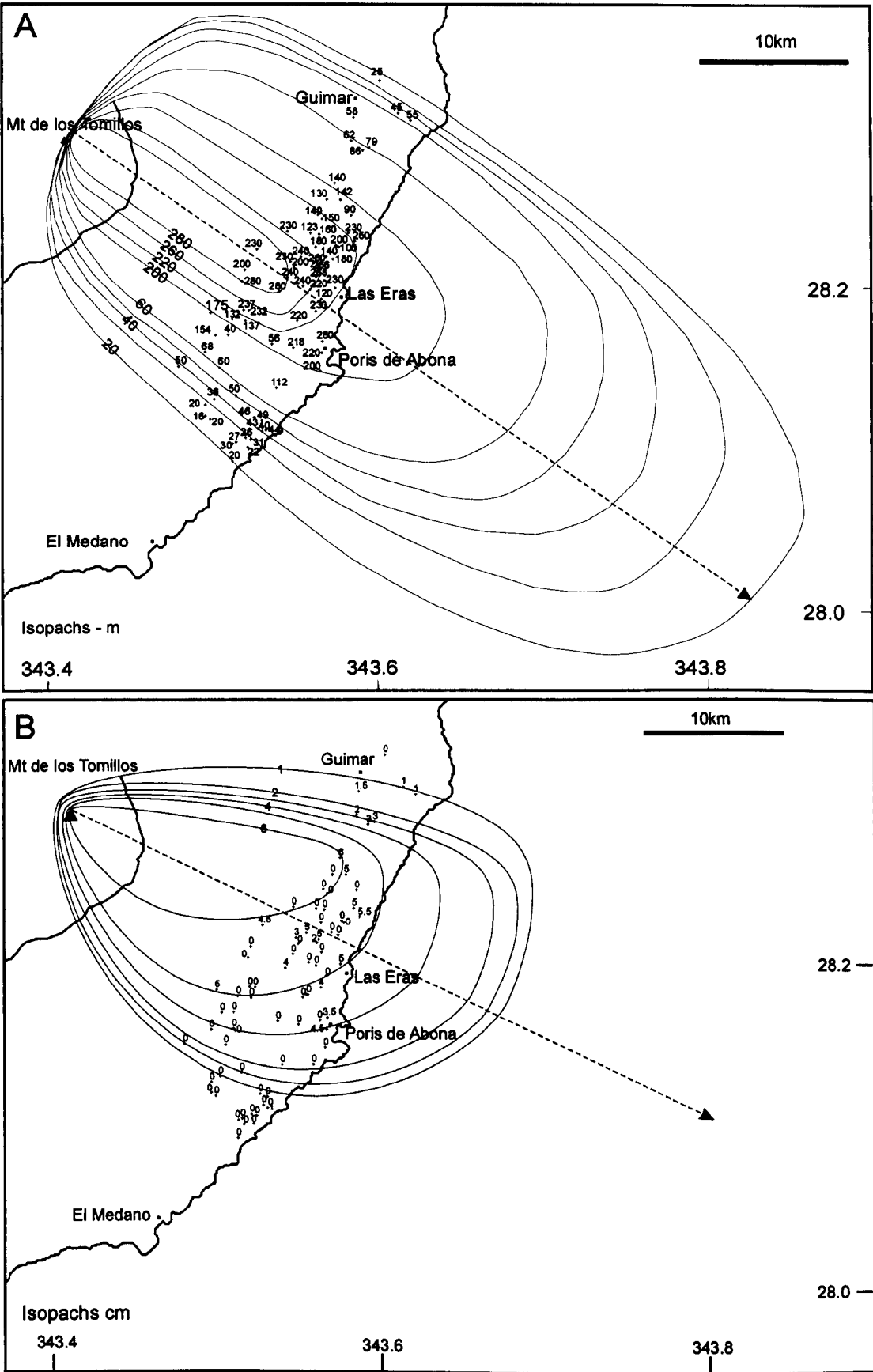


Figure 2.7: (A) Isopach map of Member 2, displaying the distribution of the member and the plume axis, indicating a SE wind direction: (B) Isopach map of the lithic lapilli layer at the top of Member 2, displaying its distribution and a plume axis indicating ESE wind direction. Note the anticlockwise rotation of the plume axis.

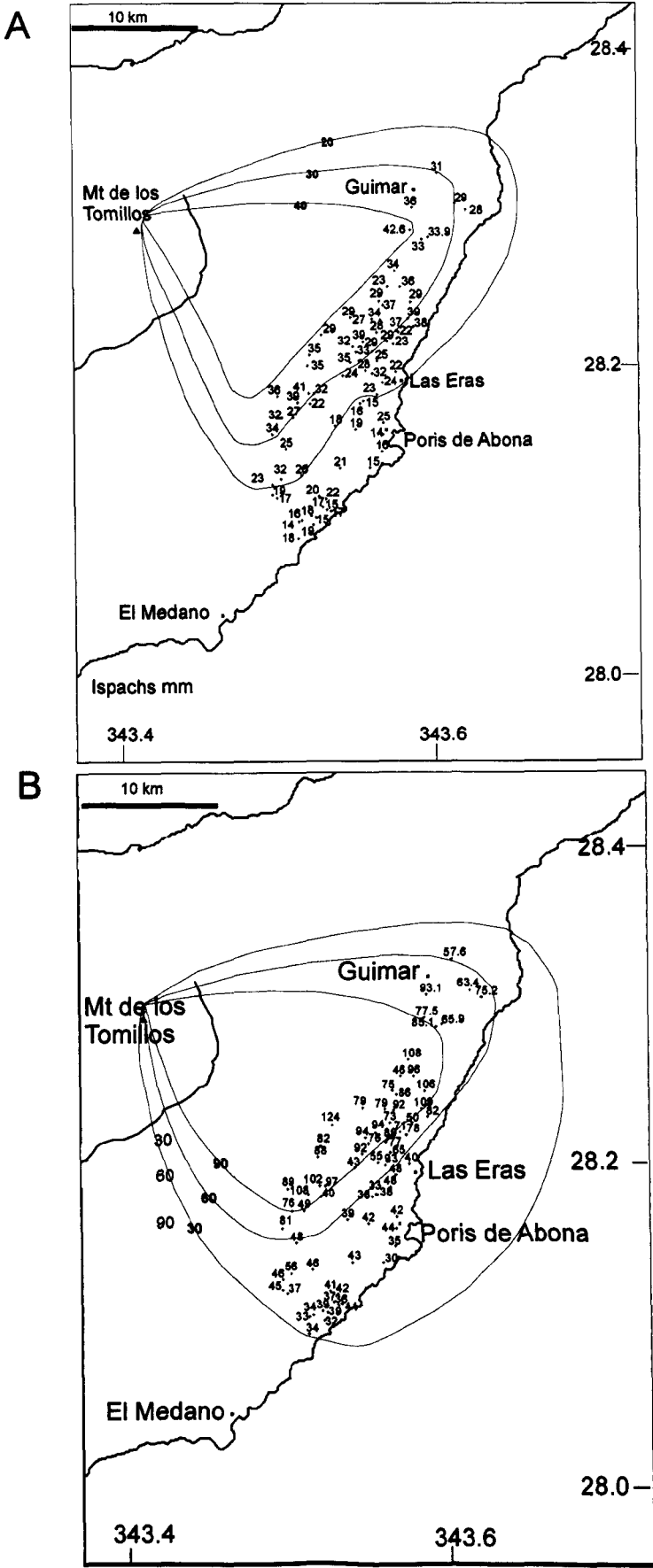


Figure 2.8: (A) Isopleth map of the maximum lithics taken from Member 2, which has been used to help calculate the eruption column height: (B) Isopleth map of the maximum sized pumices from Member 2 .

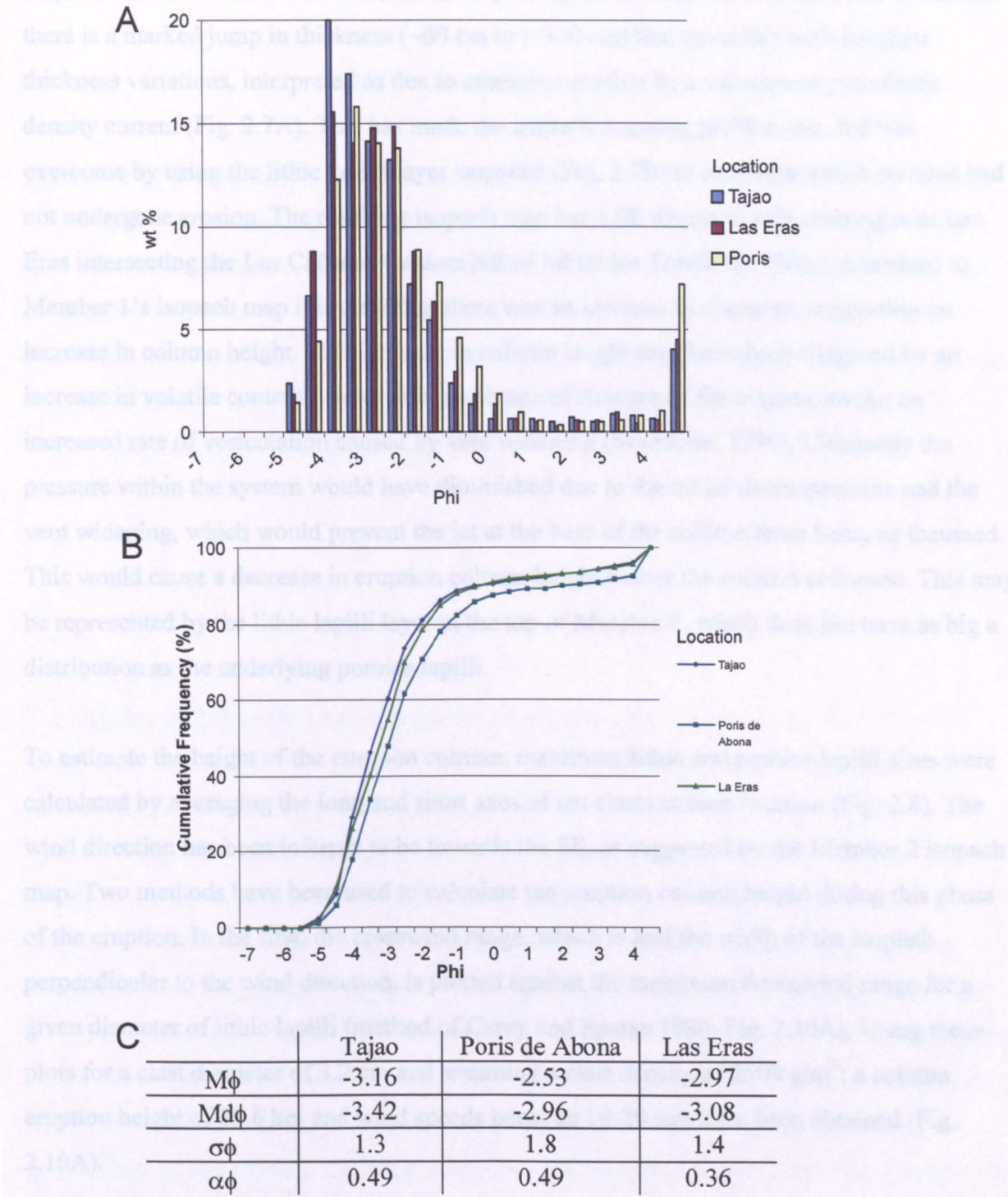


Figure 2.9:(A) Histogram of the granulometry of Member 2 , from three locations (a) Tajao, (b) Poris de Abona (c) Las Eras, showing a positive skewness and demonstrating that Member 2 at all three locations is well-sorted: (B) Cumulate frequency curves of the granulometry of Member 2 from the fore-mentioned locations re-enforce the well-sorted nature of Member 2 by the steep slope, with a small step in the curve towards 100%, reflecting the increase in fines. These curves have been used in the calculations of the parameters outlined in C.: (C) Table displaying the mean phi ($M\phi$), the median phi ($Md\phi$), the sorting ($\sigma\phi$) and the skewness ($\alpha\phi$) values for Member 2 (see appendix 1 for calculations).

Interpretation

Isopach data from Maretas to Villa de Arico plots systematically but beyond Poris de Abona, there is a marked jump in thickness (~60 cm to ~200 cm) that coincides with irregular thickness variations, interpreted as due to extensive erosion by a subsequent pyroclastic density current (Fig. 2.7A). This has made the isopach mapping problematic, but was overcome by using the lithic lapilli layer isopachs (Fig. 2.7B) to constrain which sections had not undergone erosion. The resulting isopach map has a SE dispersal axis centring near Las Eras intersecting the Las Cañadas Caldera NE of Mt de los Tomillios. When compared to Member 1's isopach map it is clear that there was an increase in dispersal, suggesting an increase in column height. This increase in column height may have been triggered by an increase in volatile content linked with geochemical changes of the magma, and/or an increased rate of vesiculation caused by vent widening (Scandone, 1996). Ultimately the pressure within the system would have diminished due to the initial decompression and the vent widening, which would prevent the jet at the base of the column from being as focussed. This would cause a decrease in eruption column height before the column collapsed. This may be represented by the lithic lapilli layer at the top of Member 2, which does not have as big a distribution as the underlying pumice lapilli.

To estimate the height of the eruption column, maximum lithic and pumice lapilli sizes were calculated by averaging the long and short axes of ten clasts at each location (Fig. 2.8). The wind direction has been inferred to be towards the SE, as suggested by the Member 2 isopach map. Two methods have been used to calculate the eruption column height during this phase of the eruption. In the first, the crosswind range, which is half the width of the isopleth perpendicular to the wind direction, is plotted against the maximum downwind range for a given diameter of lithic lapilli (method of Carey and Sparks 1986; Fig. 2.10A). Using these plots for a clast diameter of 3.2 cm and assuming a clast density of 2500 g/m³; a column eruption height of 35.6 km and wind speeds between 10-20 m/s have been obtained (Fig. 2.10A).

A second method involves plotting the natural log (ln) of the clast size against the $\sqrt{\text{isopleth area}}$ (method of Pyle, 1989). From this, the maximum clast size can be obtained from the intersection of the line with the y-axis (Fig. 2.10B). If the slope of the line (k) is known, equation 2.1 when rearranged can be used to calculate the height of neutral buoyancy (H_B) (equation 2.2).

$$-k = 0.95H_B^{-1}(H_B^{1/2} - 7.3) \quad (2.1)$$

$$H_B^{1/2} = -0.95 \pm \sqrt{0.95^2 + 27.74k/2k} \quad (2.2)$$

The height of neutral buoyancy can be related to the total column height (H_T) using equation 2.3 (Sparks, 1986), which when rearranged can provide a total column height (equation 2.4). This method produced a total column height of 36.64 km, which is comparable with the value obtained using the Carey & Sparks (1986) method. The eruption column of the Granadilla Formation was estimated to have reached altitudes of up to 30 km (Bryan et al. 2000) and the eruption of Mt Pinatubo in 1991 produced an eruption column height ranging from 25 to 40km high (Paladio-Melosantos et al. 1996).

$$H_B / H_T = 0.7 \quad (2.3)$$

$$H_B / 0.7 = H_T \quad (2.4)$$

The addition of further data may change the dimensions of the isopleths contours. If the source was found to sit 1 km further to the NW from its current interpreted position, this would increase its maximum downwind range. However, on the plot devised by Carey and Sparks (1986), this would only have the effect of inferring higher wind velocities and not a change in eruption column height (Fig. 2.10A). If there was an increase in the crosswind range as a result of new data being found this would have the affect of inferring a greater eruption column height and lower wind velocities (Fig. 2.10A). In the method used by Pyle (1989) the height of an eruption column height, is controlled by the slope of the line (k) on the \ln clast size – (isopleths area)^{1/2} plot (Fig. 2.10B). This is controlled by the square root of the area of the isopleths contours. Providing the change in the area of the isopleth contours is proportional to one another, the slope of the line will remain unchanged and therefore so will the calculated height of the eruption column.

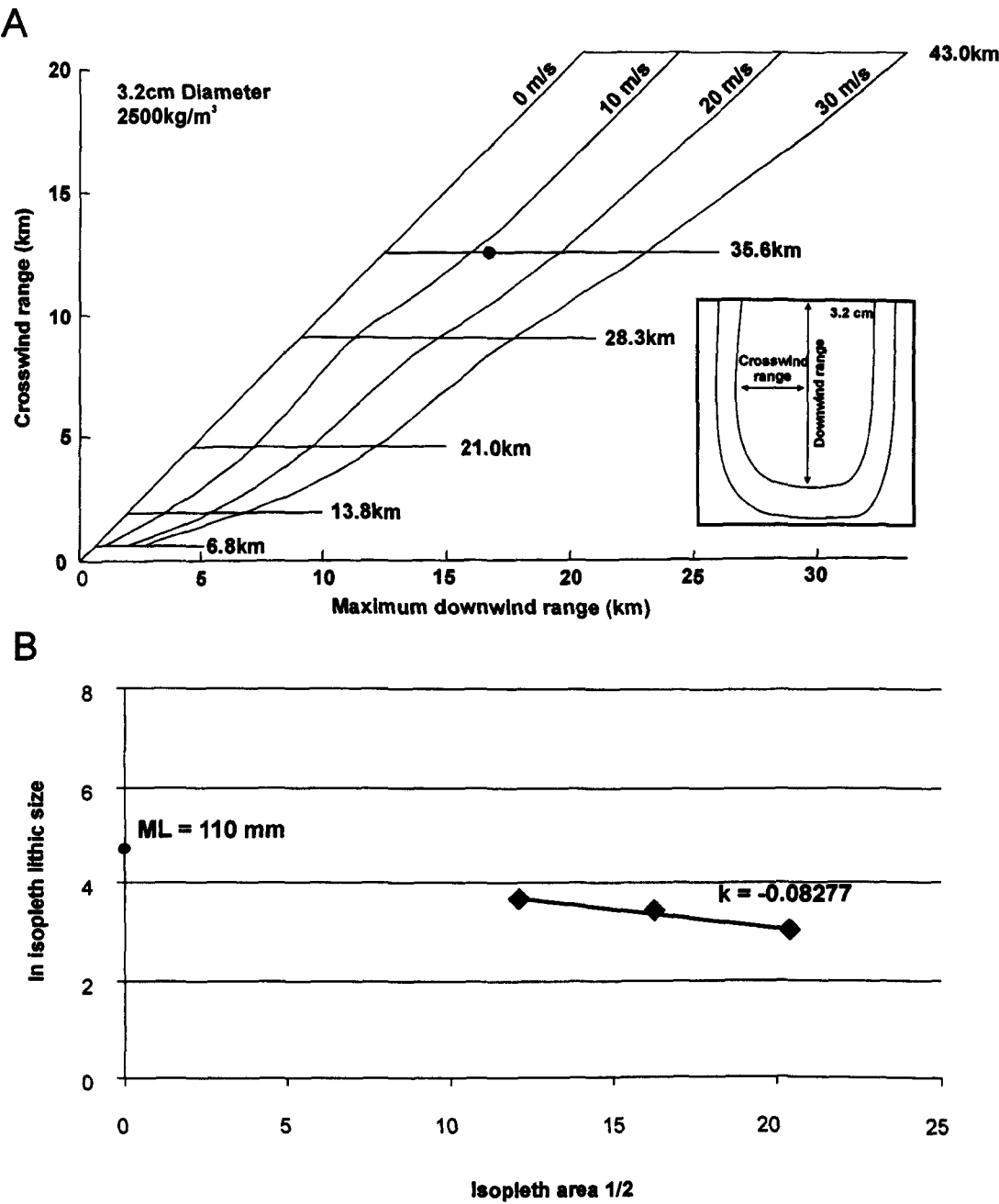


Figure 2.10: (A) A plot of the maximum downwind range against the crosswind range of the 3.2 cm lithic clast isopleth (Carey and Sparks, 1986), Suggesting a column height of 35.6 km and wind velocities just over 10 m/s to determine the eruption column height and wind velocities during the deposition of Member 2. The insert shows how the downwind and crosswind ranges are measured (B) Natural log of the lithic clast isopleths against the isopleth area 1/2, from which k can be calculated and the maximum predicted lithic size (T_o) determined. This information, in conjunction with equations 4.2 & 4.4 provides an estimation of an eruption column height of 36.4 km.

Variations in lapilli grainsize and lithic types with height in Member 2

At locations where Member 2 had a thickness of ~2 m, there is a subtle but distinct internal stratigraphy that suggests eruption dynamics fluctuated during the Plinian phase. To explore variations in column height, isopleth data were collected at 50 cm intervals through one of the thickest sections (Log 11, Fig. 2.3) at Las Eras to see how column height, and lithic types and proportions, varied with time.

The mean maximum pumice size in the lower 50 cm of Member 2 is 28.8 mm, increasing systematically to 56.25 mm at 100-150 cm above the base of Member 2. The mean maximum pumice lapilli size then decreases through intervals 150-200 cm and 200-225 cm, returning to a size similar to that at the start of the deposition of Member 2 (Fig. 2.11A). This suggests an increase in eruption column height from the onset of this phase, increasing the dispersal and allowing coarser clasts to progressively deposit further from source. The decrease in grain size would suggest a decrease in the eruption column height.

The mean maximum lithic lapilli size initially increases from 13.3 to 21.3 mm beyond which the grainsize remains almost constant. The last 5 cm is the lithic lapilli layer and there is an increase in the mean maximum lithic size (29.93 mm) (Fig. 2.11A). There is an initial increase in the total weight of 40 lithic clasts collected at each horizon, which is consistent with increase in grainsize (Fig. 2.11B). However, rather than the weight remaining at a near constant level like the grainsize, it decreases (Fig. 2.11B). This can only be attributed to a decrease in density of the lithic lapilli. Less dense lithic lapilli could have been supported for a longer time in the umbrella region, and deposited in the later stage of Phase 1, and/or there was a change in the lithic lapilli type as the geometry of the conduit and vent evolved with time. For example, figure 2.11C illustrates an increase in weight percentage of less dense intrusive and hydrothermally altered lithic lapilli, indicating a waxing eruption that was drawing material from greater depths with time (e.g. Bryan, 2000).

The presence of a clast-supported lithic lapilli layer at the top of the pumice lapilli deposit indicates a pause in the eruption of juvenile material and a period of conduit and vent erosion. The lithic lapilli are significantly smaller overall suggesting a decrease in column height as the mass flux began to diminish. The lithic lapilli types include a variety of fine-grained mafic lithic lapilli, a limited amount of hydrothermally altered lithic lapilli, syenite and scoria.

It has been suggested that members 1 and 2 were a separate eruption, with the presence of highly altered pumice lapilli and an increase in induration towards the top of this member interpreted to represent a time gap (Bryan et al. 1998). However, there is no soil and Brown et al (2003) interpreted the Plinian fallout deposits and the overlying ignimbrites as part of the same eruption. The altered pumice and increased induration can be accounted for by the presence of a widespread ash layer (Member 3b), which would promote alteration of the pumice lapilli due to the increased surface area of the ash particles. Where the lithic lapilli fallout layer is intact and the ash layer is not in direct contact with the pumice lapilli, the alteration is less apparent. Induration of this porous and highly reactive rock is expected, with hot fluids permeating through shortly after the eruption, and if overlying deposits then restrict the migration of these fluids, the affects of diagenesis will be more apparent.

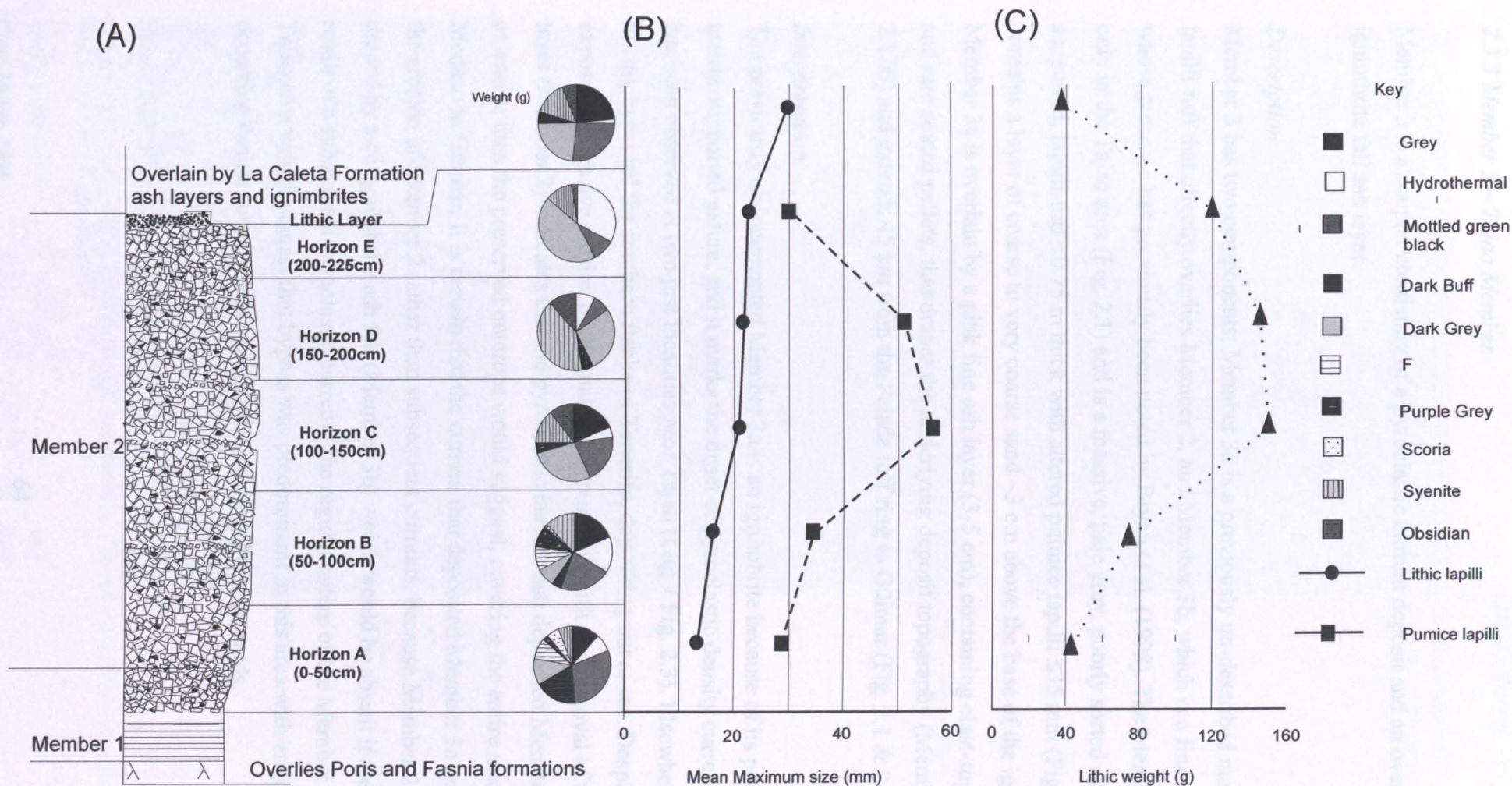


Figure 2.11: (A) A graph showing the vertical variation in mean maximum size of pumice and lithics in Member 2: (B) A graph showing the variation in the weight of 40 lithics with height in Member 2: (C) Pie charts displaying the lithic population at 0.5 m intervals, within Member 2.

2.3.3 Member 3 – Tajao Member

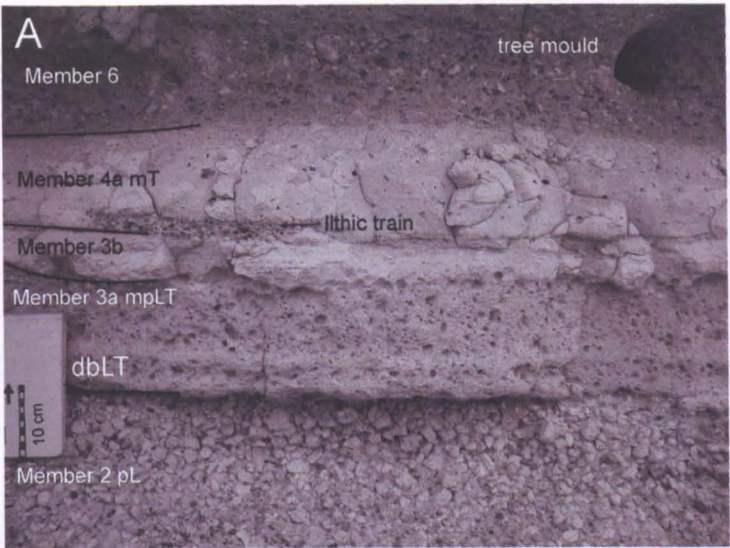
Member 3 is a couplet consisting of a pyroclastic current deposit and an overlying co-ignimbrite fall ash layer.

Description

Member 3 has two components; Member 3a is a previously un-described massive pumice lapilli-tuff that directly overlies Member 2, and Member 3b, which is a fine ash pellet layer, whose presence has previously been noted by Bryan et al. (1998). The Member 3a is found only in the Tajao area (Fig. 2.1) and is a massive, pale grey, poorly sorted and matrix-supported, lapilli-tuff <0.75 m thick with altered pumice lapilli ≤ 35 mm (Fig. 2.12A). It contains a layer of coarse to very coarse sand ~3 cm above the base of the ignimbrite. Member 3a is overlain by a pink fine ash layer (3-5 cm), containing clast-supported pellets and rare coated pellets, that drapes the underlying deposit topography (Member 3b; Fig. 2.12B) and extends 45 km from the Pelada tuff ring to Güimar (Fig. 2.1 & 2.3).

Interpretation

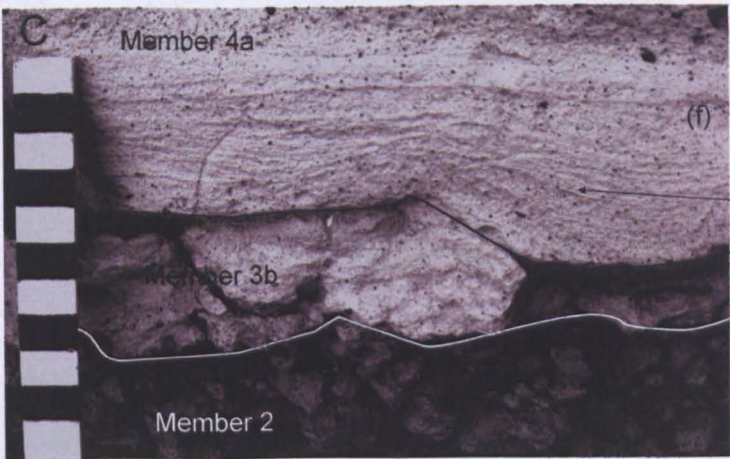
The previously undocumented Member 3a is an ignimbrite because of its poorly sorted, matrix-supported nature, and it marks the onset of pyroclastic density currents. Member 3a has been observed at two just localities near Tajao (Log 7 Fig. 2.3). Elsewhere it is absent, having bypassed the southern flanks of Tenerife, depositing out at sea. Despite limited exposure, extensive erosion of the underlying pumice lapilli and removal of the lithic lapilli layer (Member 2) indicates that the pyroclastic current that deposited Member 3a was more extensive than the preserved outcrops would suggest, covering the entire area from El Medano to Güimar. It is certain that the current that deposited Member 3a was responsible for the erosion of Member 2 rather than subsequent currents, because Member 2 is commonly draped by a co-ignimbrite ash fall (Member 3b) which would be absent if the erosion was a result of a subsequent pyroclastic current. The regular nature of the Member 2 isopachs in the Tajao area would suggest that bypass was predominant in this area with erosion and bypass occurring further round to the north- northeast from Poris onwards.



(A) Illustration of the relationship of Member 3a with the under- and overlying units. Location 9c, near Tajao (GR: 0355889 3110473).

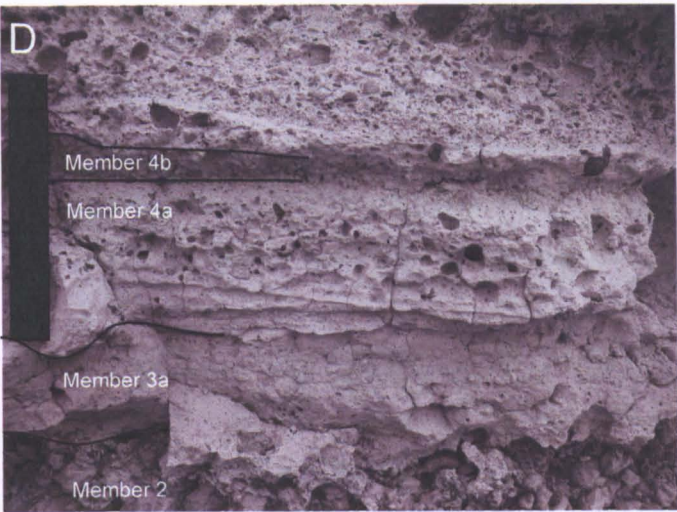


(B) A clast-supported pellet layer (Member 3b)

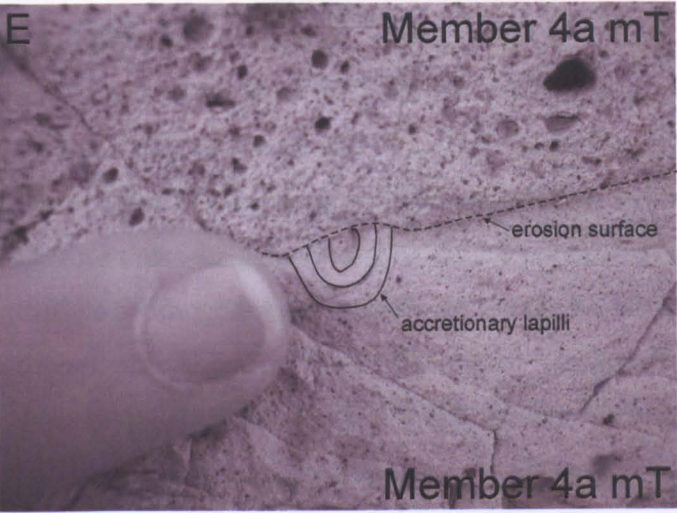


(C) Member 2 draped by Member 3b. The irregular base of Member 4a and truncation of Member 3b indicate an erosion surface. The fine ash layer of Member 4a is cross-stratified. (Tajao GR: 0355618 3110203).

Figure 2.12: Photos displaying features and characteristics of Member 3 and Member 4 and their relationships with under- and overlying members.



(E) Member 2 overlain by Member 3a, followed by a fine cross-stratified ash (Member 4a), overlain by a clast-supported pellet layer (Member 4b.) Scale bar 10 cm (Tajao GR: 0355650 3111175).



(F) Internal erosion surface within Member 4a, truncating an accretionary lapillus. This truncation suggests rapid diagenesis of Member 4a (GR: 0354122 3112855)

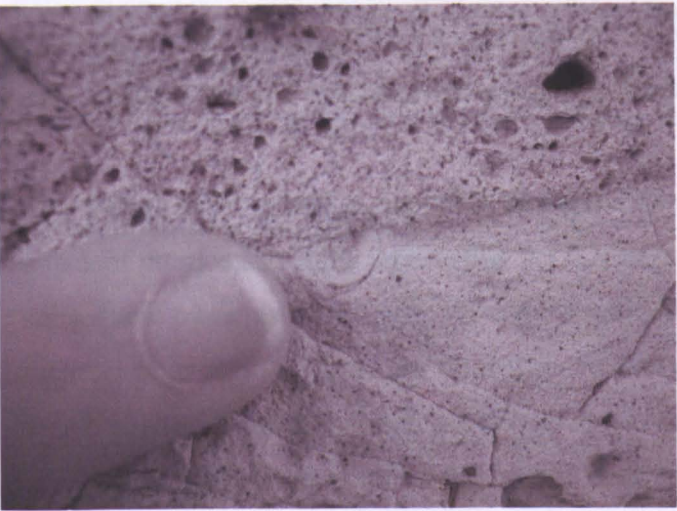


Figure 2.12 continued

Member 3b is interpreted as a co-ignimbrite ashfall deposit, because of its lateral persistence, its uniform thickness, draping irregular topography (except where it is eroded: logs 4 & 17 Fig. 2.3), and the lack of pumice and lithic lapilli. The clast-supported ash pellets also support this interpretation. The widespread presence of Member 3b is also additional evidence that the pyroclastic density current that deposited Member 3a was far more widespread than the exposure indicates, because co-ignimbrite ash layers are derived from ash rising up from pyroclastic currents. Member 3b will be discussed in more detail in section 2.4.

2.3.4 Member 4

Member 4 is a couplet consisting of a pyroclastic current deposit (Member 4a; and of Bryan et al. (1998) and a corresponding fine ash layer (Member 4b).

Description

Member 4a extends 45 km from just outside El Medano (Log 1; Fig 2.3) to Güimar and 6 km inland. It is a predominately massive, white, fine ash tuff that contains scarce lithic and pumice lapilli, thickens into palaeovalleys and thins over topographic highs (Fig. 2.13). Diffuse cross-stratification (Fig. 2.12 C) is present towards the base of the member and diffuse bedding, defined by pumice lapilli. Rare colour banding can be observed on topographic highs and near palaeovalley margins. It locally contains carbonate concretions and erosional scours. Higher in the member, occasional pumice lapilli appear, and the matrix becomes coarser and darker. Lithic lapilli trains one clast thick (5 mm) (Fig. 2.12A) are characteristic of Member 4a and are present near palaeovalley margins and on palaeotopographic highs. There are prolific accretionary lapilli (2-3 laminations) with associated pellets and coated pellets present towards the top of the member

Member 4b overlies this and consists of a thin fine ash layer (≤ 40 mm) containing pellets with a lack of pumice and lithic lapilli (Fig. 2.12D). It is typically absent, having been eroded by subsequent pyroclastic currents. At some localities towards the southwesterly limits of the member (e.g. Maretas) Member 4b is well-developed and consists of clast-supported pellets, which changes to matrix-supported pellets and coated pellets further round the coastline to the northeast. Locally it drapes topography but there are some unexpected regional variations (i.e. being thicker in coastal areas than areas closer to source).

Kokelaar, 2002). The paucity of other lithic lapilli suggests the competence of the current was commonly too low to entrain or support lithic lapilli >1 mm.

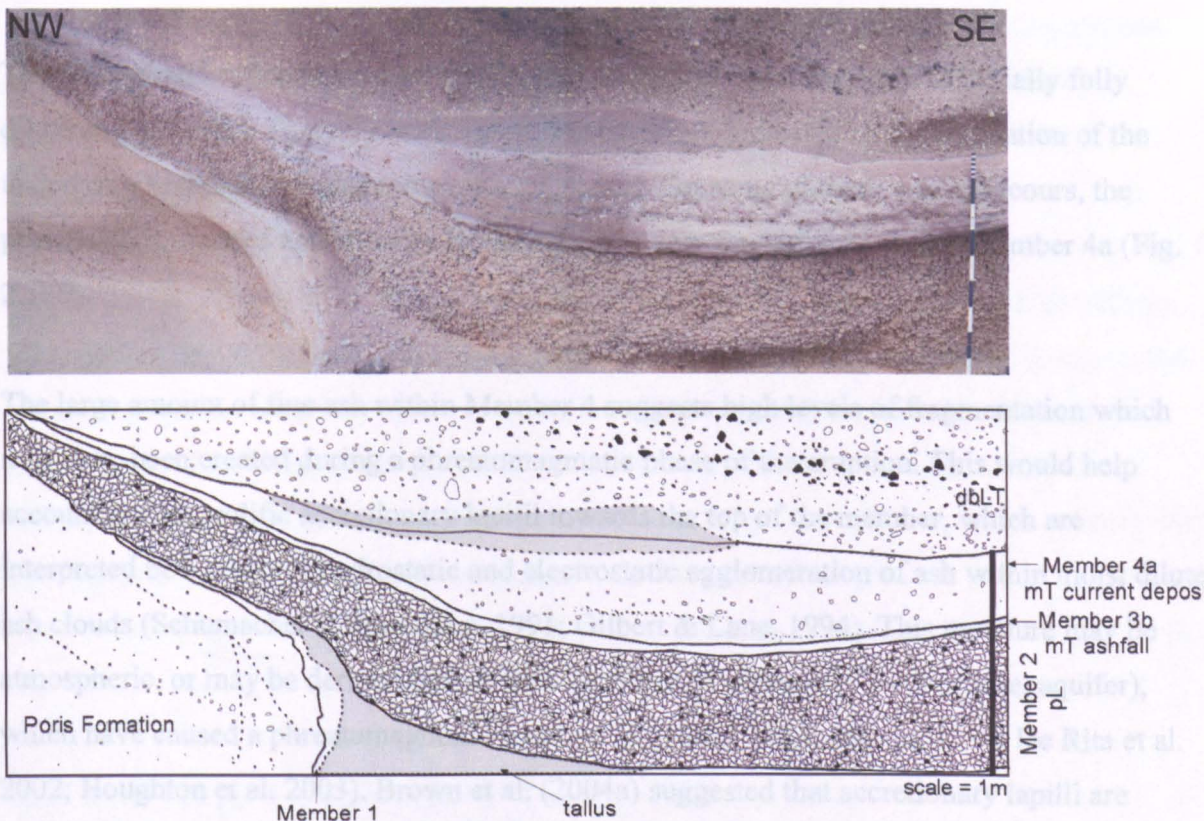


Figure 2.13: A small palaeovalley infilled by the La Caleta Formation. Member 3b drapes topography, whereas Member 4a thickens into the palaeovalley and thins towards the topographic high. Member 4a is diffusely bedded in the valley fill facies and contains lithic trains (Tajao, GR: 0355908 3110300).

Interpretation

Member 4a’s distinctive fine-grained nature, regardless of its relationship with palaeotopography, and paucity of pumice lapilli, suggest a phreatomagmatic origin that resulted in extensive fragmentation. The massive nature suggests rapid deposition from a granular fluid based current, with diffuse bedding and lithic lapilli trains indicating periodic impingement of turbulence, where the thickness of the granular-fluid component of the current may have been thinner.

The lithic lapilli trains indicate crude, laterally discontinuous layering in an otherwise predominantly massive deposit and support a progressive aggradational mode of deposition. Lithic lapilli trains have been attributed to periods of reduced deposition allowing turbulence to impinge upon the flow-boundary (Bryan et al., 1998b). However it is the concentration of the current that controls the level of turbulence, not the rate of deposition (Branney &

Kokelaar, 2002). The paucity of other lithic lapilli suggests the competence of the current was commonly too low to entrain or support lithic lapilli >1 mm.

The cross-stratification at the base of Member 4a indicates the current was initially fully dilute and turbulent. There were also periods of erosion, indicated by the truncation of the underlying Member 3b and internal erosion scours. On some of these erosion scours, the presence of truncated accretionary lapilli indicates very rapid diagenesis of Member 4a (Fig. 2.12E).

The large amount of fine ash within Member 4 suggests high levels of fragmentation which may have been created during a phreatomagmatic phase of the eruption. This would help account for the prolific accretionary lapilli towards the top of the member, which are interpreted to be a result of hydrostatic and electrostatic agglomeration of ash within moist dilute ash clouds (Schumacher & Schminke, 1991; Gilbert & Lane, 1994). This moisture may be atmospheric, or may be derived from standing bodies of water (e.g. caldera lake, aquifer), which have caused a phreatomagmatic eruption (e.g. Self, 1983; Mastin, 1997; De Rita et al. 2002; Houghton et al. 2003). Brown et al. (2004a) suggested that accretionary lapilli are further developed by tractional processes when they fall into under-riding pyroclastic density currents.

Member 4b is interpreted as a co-ignimbrite ash layer due to the lack of pumice and lithic lapilli. Its frequent absence due to its widespread erosional removal makes it difficult to assess its original thickness variations, in order to establish its depositional origin. Where it is composed of clast-supported pellets, it is clearly of fallout origin. The unusual regional thickness variations are the opposite to what is expected of fallout deposits. This, along with the presence of coated pellets and their matrix-supported nature, suggests that at certain geographical locations deposition was influenced by the wake of a pyroclastic density current and deposition may have been occurring from a direct fallout-dominated flow-boundary where there was an element of lateral shear. Similar interpretations have been made for ash layers found in the Abrigo Formation (Pitarri et al. 2006). This may help account for the unusual thickness variations and the presence of coated pellets and will be discussed further in Section 2.4.

2.3.5 Member 5 - Las Maretas Member

Member 5 is a complex sequence of at least six couplets, consisting of ignimbrites and co-ignimbrite ash layers, but not all of the couplets are complete. The couplets are grouped together somewhat arbitrarily because individual couplets are not always sufficiently distinctive to be traced laterally. This is because alteration has locally obscured the composition/colour of pumice, which is the basis for their discrimination. Couplets 1, 5, and 6 each have a lithic lapilli-rich base overlain by pumice lapilli concentrations with or without accretionary lapilli. Couplets 1 and 5 are draped by fine ash layers containing pellets, coated pellets and rare accretionary lapilli. At some locations these ash layers are well-developed, clast-supported pellet layers. Couplets 2, 3 and 4 are only found near Maretas and are incomplete, composed of clast-supported pellet layers. (Fig. 2.14). The complete couplets will be described first, followed by a description of the incomplete couplets.

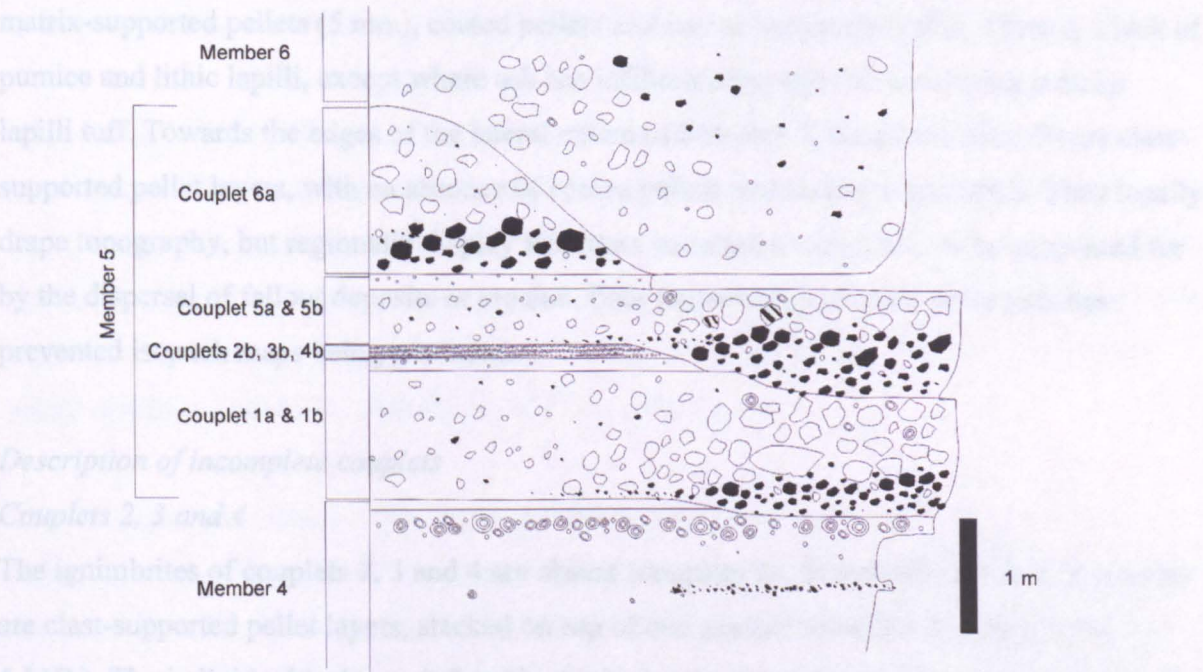


Figure 2.14: General vertical section of Member 5. Couplets 1 and 5 are complete and consist of an inversely graded lithic lapilli tuff overlain by a pumice lapilli tuff, capped by a co-ignimbrite ash layer, which can be fallout (clast-supported pellets) or wake deposits (matrix-supported pellets and coated pellets). Couplet 6 is missing its co-ignimbrite ash layer. Couplets 2, 3 and 4 are missing the ignimbrites and only the co-ignimbrite pellet layers are present. Their presence is important because it indicates that there were intervening pyroclastic density currents, that did not deposit.

Description of the complete couplets: Couplet 1 and 5

Couplets 1 and 5 are the only complete examples in Member 5 and are very similar. They can reach thicknesses of up to 5 m thick but are predominately <1 m. They consist of a lapilli-tuff

(Couplet 1a and 5a), which has a localised lithic-rich base with inverse grading and its principal components are clasts of lava from upslope. (Fig. 2.3 Log 3; Fig. 2.15A, B & C). This is overlain by a massive pumice lapilli-rich lithofacies, composed of high concentrations ($\leq 70\%$) of sub-rounded pumice lapilli (4 cm), with little matrix (20%), and contains accretionary lapilli and coated pellets towards the top of the ignimbrite (Log 3; Fig. 2.3). Thinner sections are diffusely bedded, with lower concentrations of pumice and more matrix. The bases of the couplets are locally erosive. Couplet 1a is defined by green sub-angular to sub-rounded pumice lapilli (≤ 25 mm), which contain rare small pumiceous mafic inclusions (<15 mm), whilst Couplet 5a contains grey pumice lapilli that contain rare pumiceous mafic inclusions and banded pumice makes its first appearance. Pumice lapilli-rich layers on top of Member 4a have previously been documented within the La Caleta. (Bryan et al. 1998).

Fine ash layers, which are up to 5 cm thick, overlie both couplets and predominately contain matrix-supported pellets (5 mm), coated pellets and rare accretionary lapilli. There is a lack of pumice and lithic lapilli, except where ash has infiltrated through the underlying pumice lapilli tuff. Towards the edges of the lateral extent of Member 5, Couplet 1b and 5b are clast-supported pellet layers, with an absence of coated pellets and accretionary lapilli. They locally drape topography, but regionally display thickness variations, which cannot be accounted for by the dispersal of fallout deposits or erosion. Poor preservation of these ash layers has prevented isopach maps being produced.

Description of incomplete couplets

Couplets 2, 3 and 4

The ignimbrites of couplets 2, 3 and 4 are absent (couplets 2a, 3a and 4a) and all that remains are clast-supported pellet layers, stacked on top of one another (couplets 2b, 3b, 4b; Fig. 4.14B.). The individual beds are defined by limited amounts of fine ash and each layer is ~25 mm thick. The pellets are up to 5 mm and there is no lithic component. Occasional pumice lapilli occur at the base of some of these layers. This small sequence has only been observed west of Mareas (Log 3; Fig. 2.3).

Couplet 6

Couplet 6 is essentially the same as couplets 1 and 5, with an inversely graded lithic breccia with blocks up to 10 cm, overlain by a massive pumice lapilli-rich tuff (Log 3, Fig. 2.3). The

pumice lapilli are grey and no banded pumice lapilli have been observed. A co-ignimbrite ash layer has not been observed to date.

Interpretation

Member 5 is an amalgamation of several couplets consisting of ignimbrites and co-ignimbrite ash layers. Couplets 1, 5 and 6 are composed of very similar sequences of lithofacies. The lithology of the principal components of the lithic-rich layer suggests that the pyroclastic density currents were initially erosive, eroding and accumulating material (lava) from upslope with the current undergoing temporal waxing, creating inverse grading. A contributing factor in the generation of these inversely graded lithic layers may be due to higher velocities, increasing shear and dispersal forces, causing granular segregation. These lithic lithofacies have only been observed in the Las Maretas and Tajao areas, suggesting that erosional effects were localised (Fig. 2.3). The overall coarsening of each successive lithic layer suggests an overall waxing of the eruption.

This was followed by deposition of juvenile pumice lapilli. The areas of higher concentration may represent the distal limit of a waning current where snouts and dams form. The thickness variations give an indication of the rates of advance i.e. thicker lithofacies indicate pauses in advance whilst thinner parts indicate rapid advance. As the current waxes the position of these high pumice concentrations will advance. The pumice lapilli-rich lithofacies have a much wider distribution than the underlying lithic-rich lithofacies.

The ash layers (couplets 1b, 2b, 3b, 4b and 5b) are interpreted as co-ignimbrite ashfall deposits, because they drape topography and lack pumice and lithic lapilli. As with Member 4b, there are areas where pure fallout occurred, indicated by the presence of clast-supported pellets, but elsewhere the ash layer contains matrix-supported pellets and coated pellets that are interpreted as wake deposits that were emplaced from a direct fallout-dominated flow-boundary, resulting from the dilute wake of the preceding pyroclastic current. This indicates that depositional mechanisms varied diachronously. This is supported by unusual thickness variations that are not associated with fallout deposits or can be explained by erosion (Section 2.4).

The absence of the ignimbrites associated with couplets 2b, 3b and 4b means that either the pyroclastic currents did not extend that far and there was a prolonged hiatus, or the pyroclastic

density currents bypassed the area, leaving no record of their occurrence. Occasional pumice lapilli between the pellet layers suggest the latter. Due to the limited exposure of these couplets, this cannot be confirmed. This sequence of three pellet layers is very localised and has either been removed elsewhere via erosion or was only able to deposit on the lateral extent of the La Caleta Formation where the pyroclastic currents were not as sustained.

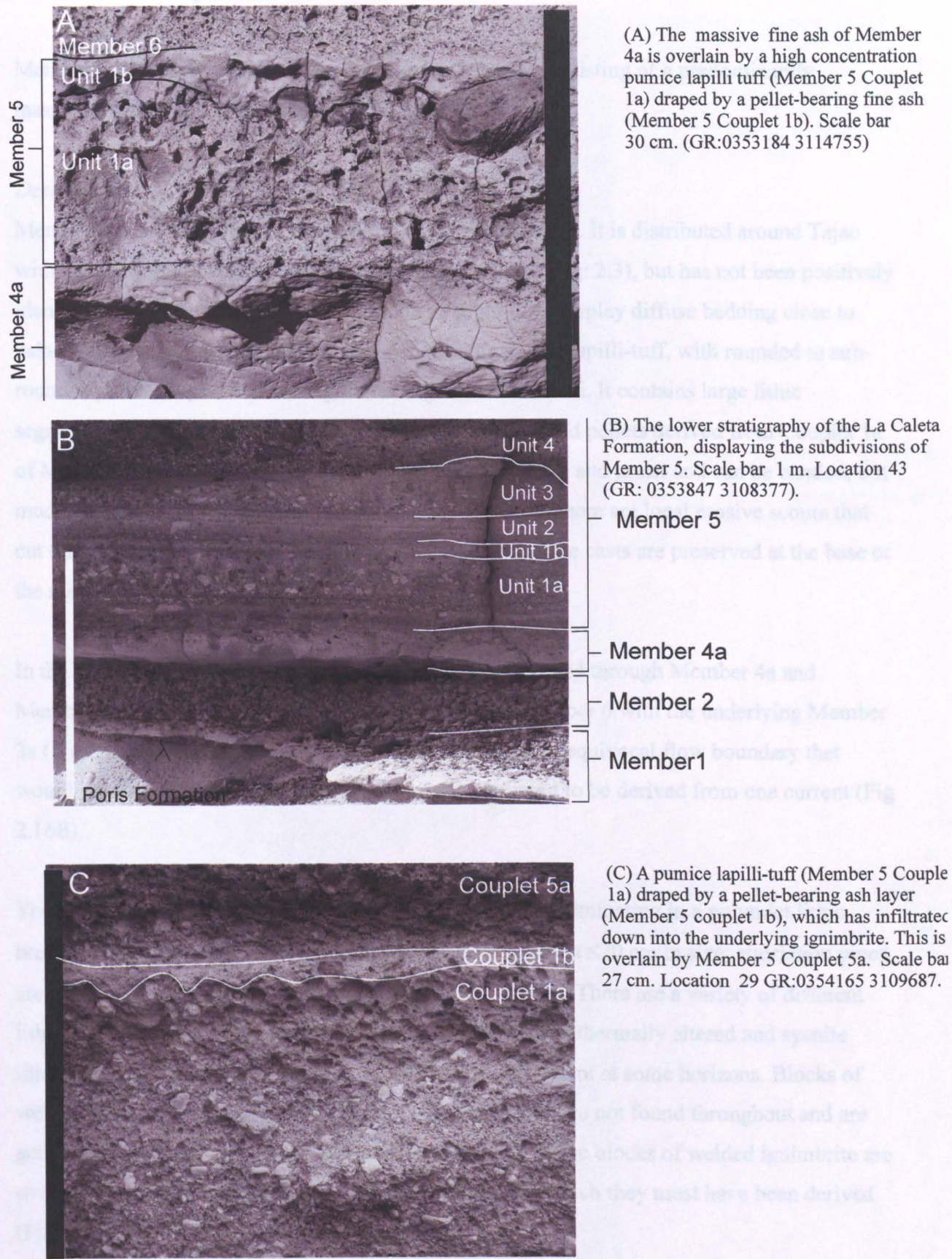


Figure 2.15: Features of Member 5 and its relationship with under- and overlying members.

2.3.6 Member 6: Tajao Member

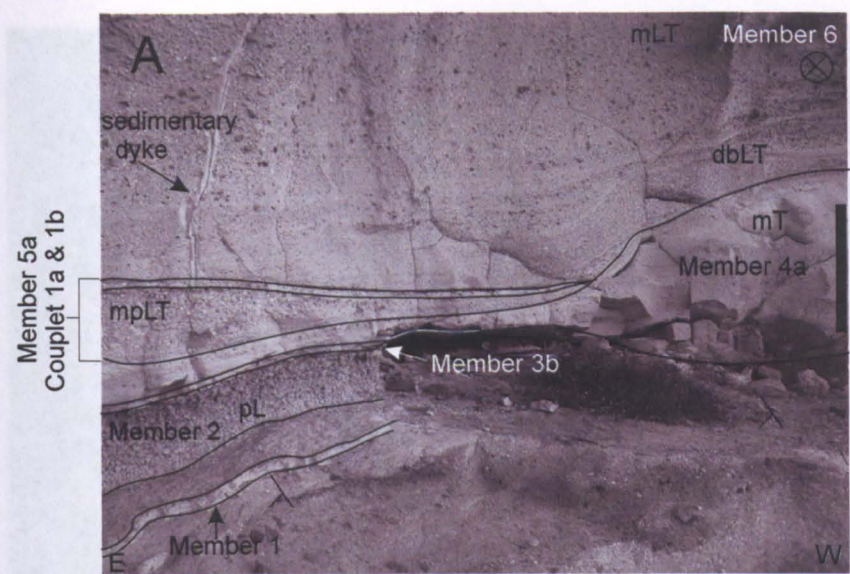
Member 6 is a large pyroclastic density current deposit, consisting of a predominantly massive ignimbrite and lithic breccia

Description

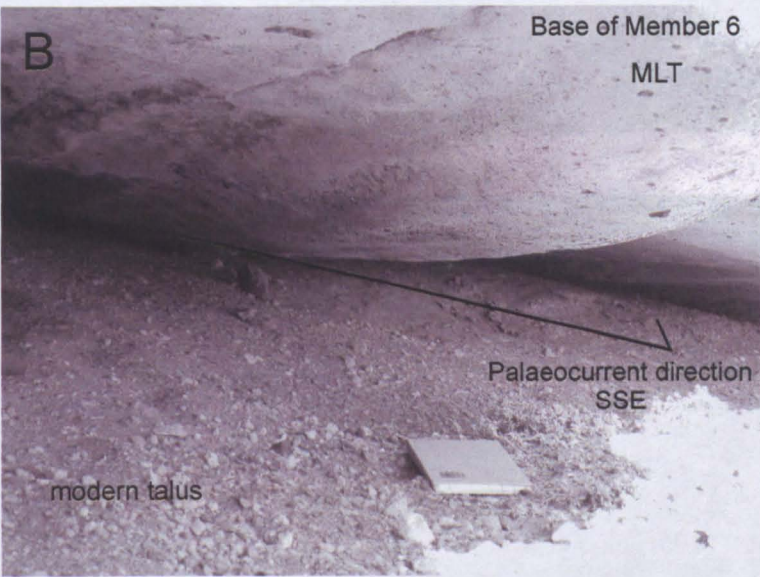
Member 6 is the main ignimbrite of the La Caleta Formation. It is distributed around Tajao with the greatest thickness (27m) near El Medano (Log 2 Fig: 2.3), but has not been positively identified east of Tajao. It is commonly massive, but does display diffuse bedding close to palaeovalley margins (Fig. 2.16A). It is a matrix-supported lapilli-tuff, with rounded to sub-rounded pumice lapilli and subangular to angular lithic lapilli. It contains large lithic segregation structures and sedimentary dykes of fine ash and pellets derived from Couplet 1a of Member 5 (Fig. 2.16H & I). The pumice lapilli are glassy and green and can be banded, but much is altered to yellow, or more rarely, to orange clay. There are local erosive scours that cut through underlying members (Fig. 2.16C) and large flute casts are preserved at the base of the member (Fig. 2.16B).

In the Tajao area the current that deposited Member 6 eroded through Member 4a and Member 3b. The result was to almost seamlessly join Member 6 with the underlying Member 3a (Fig 2.16D), and allows an opportunity to observe an unequivocal flow boundary that would otherwise go unnoticed and the ignimbrite assumed to be derived from one current (Fig 2.16E).

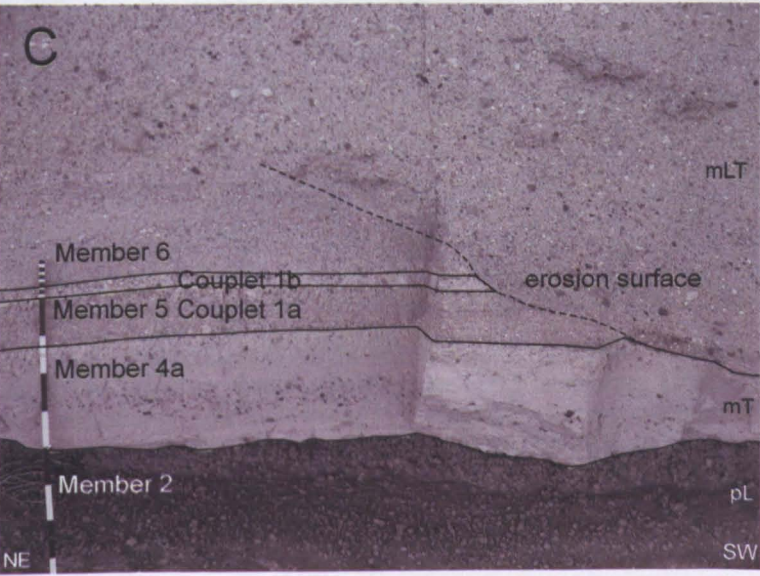
The size and abundance of lithic lapilli increase upwards culminating in a polymict lithic breccia composed of sub-rounded to sub-angular lithic clasts ≤ 20 cm in size; elutriation pipes are associated with some of these large blocks (Fig. 2.16E). There are a variety of different lithic types with an overall increase in the presence of hydrothermally altered and syenite lithics (Fig. 2.17A & B), although they are periodically absent at some horizons. Blocks of welded ignimbrite with a eutaxitic texture are present, but are not found throughout and are generally found high up in the succession (Fig. 2.17A). Some blocks of welded ignimbrite are over 2 m in size and found 20 km from the caldera from which they must have been derived (Fig. 2.15D).



(A) Member 6 displaying diffuse stratification overlying Member 5 (Couplet 1a and 1b), Member 4, Member 3b, Member 2 and Member 1. Scale bar 1 m. Near Tajao GR: 0355618 3110203. Palaeocurrent direction to the south

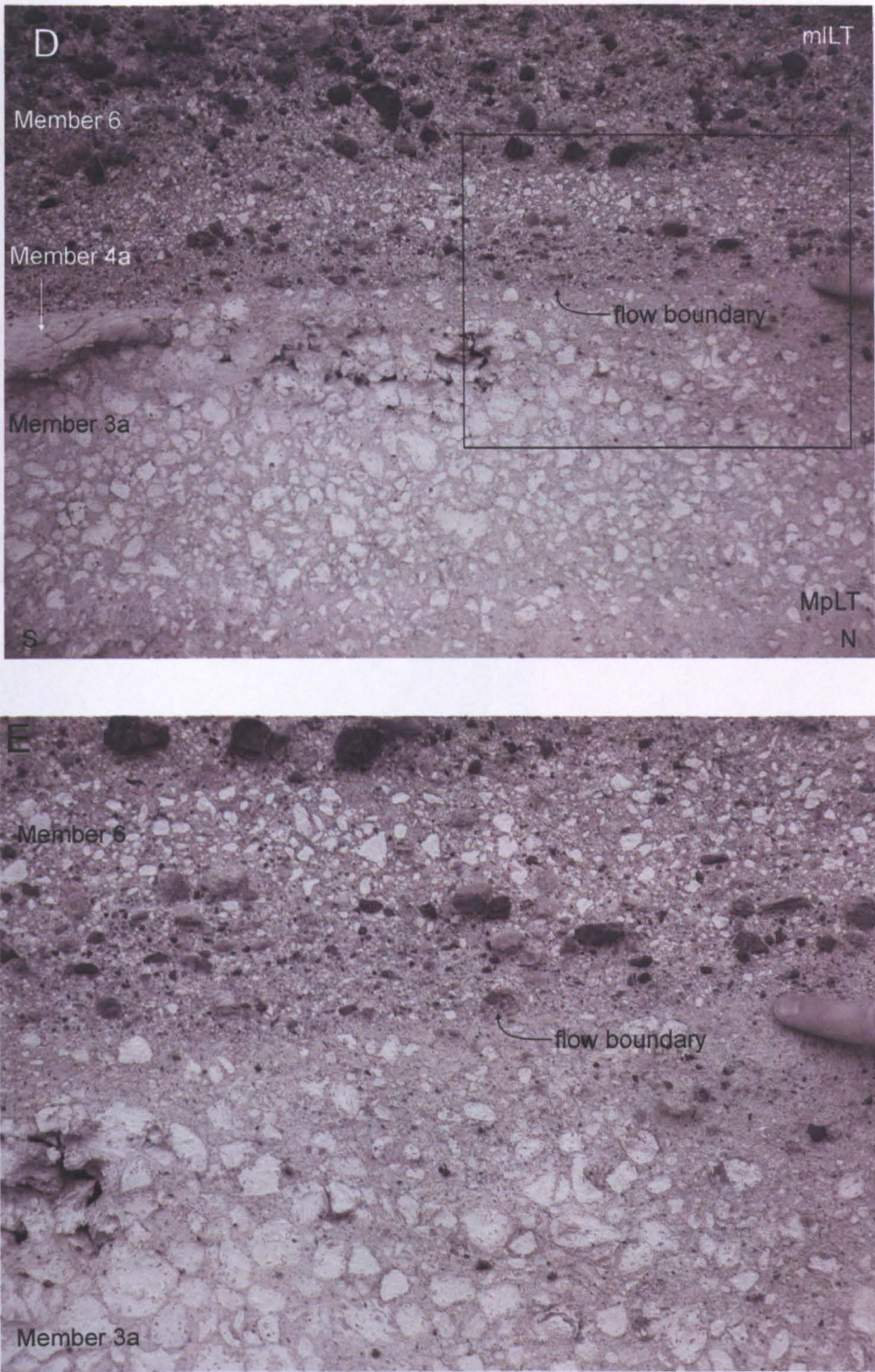


(B) Flute casts at the base of ignimbrite Member 6 near location 10 (Tajao), indicating a palaeocurrent direction to the SSE. Book is 20 cm long. GR: 0356332 3110450.



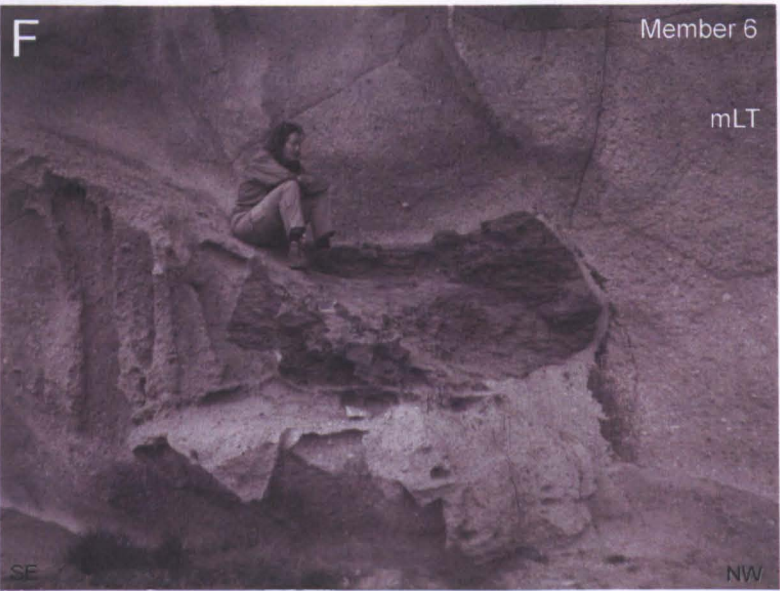
(C) An internal erosion surface within Member 6 cutting down into underlying members. Palaeocurrent direction to the south. Near Tajao, GR:0355618 311020.

Figure 2.16: Features of Member 6 and its relationship with underlying members.

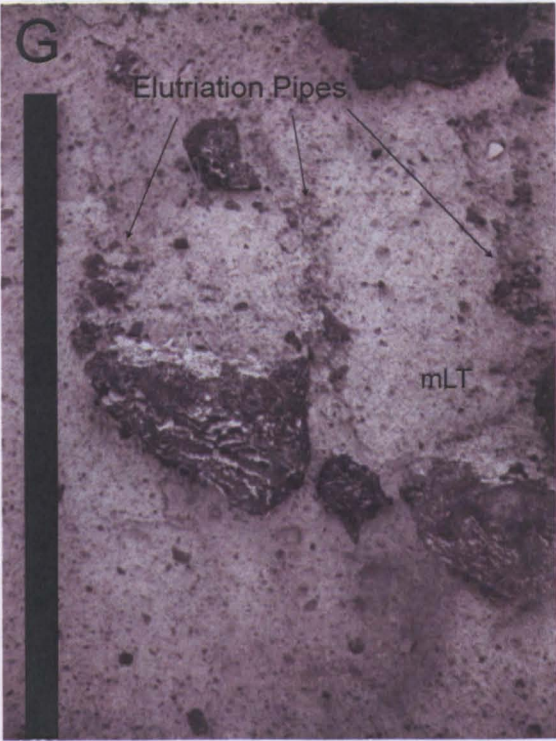


(D) Flow-boundary between Member 3a and Member 6. This photo provides a rare opportunity to observe an unequivocal flow boundary. Without the presence of the intervening Member 4a and Member 3b (out of frame) (E: boxed area), members 3a and 6 could be misinterpreted as a continuous sequence deposited from a single pyroclastic density current. Near Tajao, GR: 0355889 3110473 (Location 9c)

Figure 2.16: continued

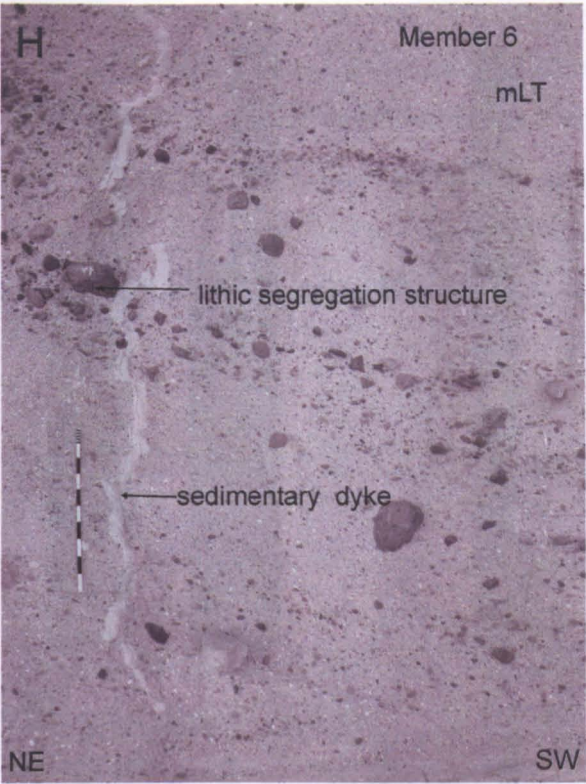


(F) Matrix-supported block of welded ignimbrite in Member 6 approximately 20 km from source. Near Tajao, GR: 0355725 3113750



(G) Elutriation pipes in Member 6 caused by the loading of lithic blocks. Scale bar 36 cm. Near El Medano, GR:0350334 3106370

Figure 2.16: continued



(H) Sedimentary dykes in Member 6, composed of a fine ash derived from Member 5 Couplet 1b. Near Tajao, GR:0355618 3110203.



(I) Lithic segregation structures in Member 6, Tajao. Scale bar 1 m. Near Tajao, GR:0355618 3110203.

Figure 2.16: continued

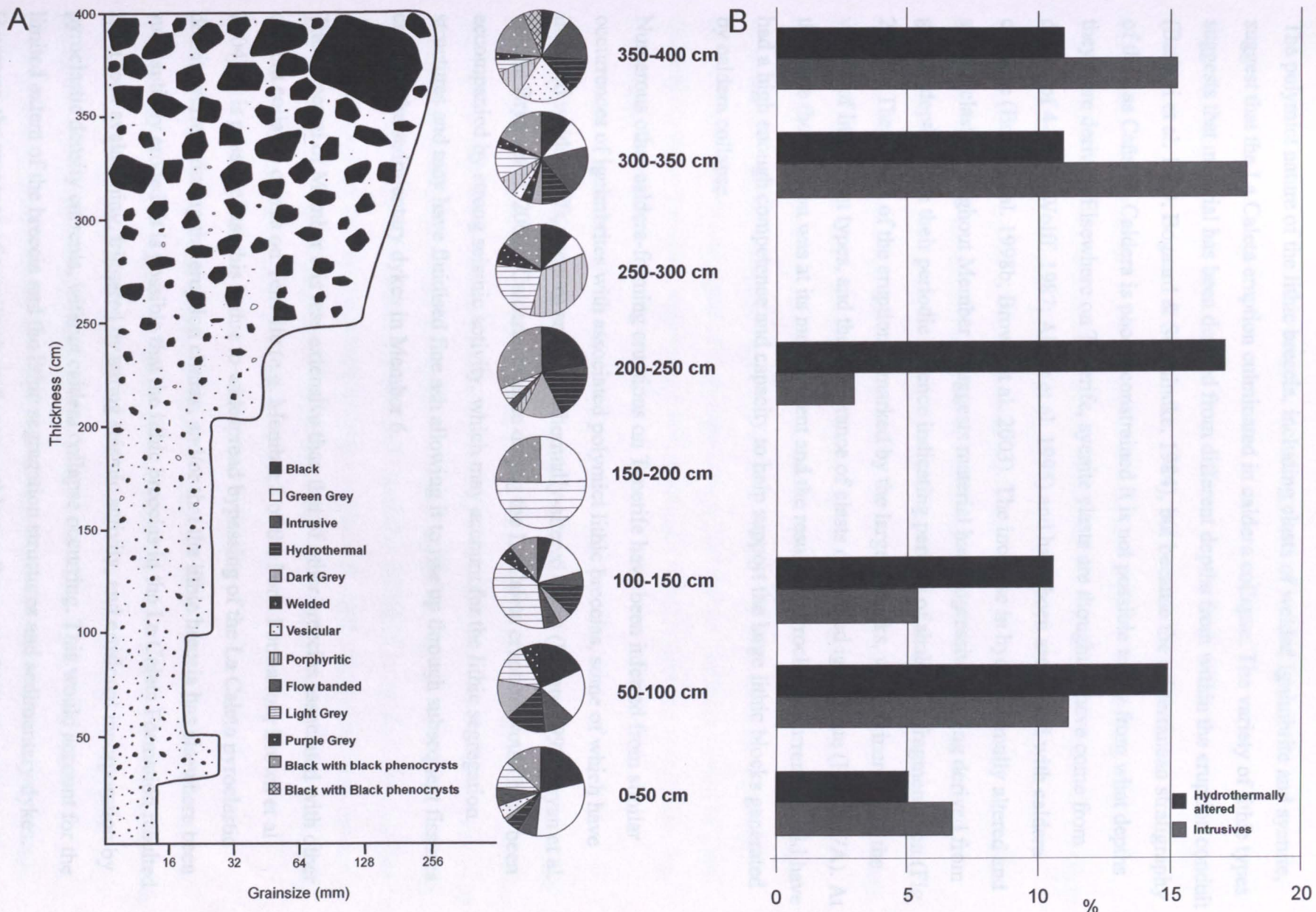


Figure 2.17: (A) A sedimentary log through Member 6 near Tajao with the variation in lithic population, at 50 cm intervals: (B) The percentage variation of hydrothermally altered and intrusive lithic lapilli/ blocks with height in Member 6.

Interpretation

The polymict nature of the lithic breccia, including clasts of welded ignimbrite and syenite, suggest that the La Caleta eruption culminated in caldera collapse. The variety of lithic types suggests that material has been derived from different depths from within the eruption conduit (Barberi et al. 1989; Bogaard & Schmincke, 1984), but because the subterranean stratigraphy of the Las Cañadas Caldera is poorly constrained it is not possible to say from what depths they were derived. Elsewhere on Tenerife, syenite clasts are thought to have come from depths of 4-7 km (Wolff, 1987; Ablay et al. 1995) and have been associated with caldera collapse (Bryan et al. 1998b; Brown et al. 2003). The increase in hydrothermally altered and syenite clasts throughout Member 6 suggests material has progressively being derived from greater depths, with their periodic absence indicating periods of shallower fragmentation (Fig 2.17B). The climax of the eruption is marked by the largest blocks, with an increase in the variety of lithic clast types, and the appearance of clasts of welded ignimbrite (Fig. 2.17A). At this time the eruption was at its most violent and the resulting pyroclastic currents would have had a high enough competence and capacity to help support the large lithic blocks generated by caldera collapse.

Numerous other caldera-forming eruptions on Tenerife have been inferred from similar occurrences of ignimbrites with associated polymict lithic breccias, some of which have included welded tuffs, syenites and hydrothermally-altered clasts (Bryan, 1998; Bryan et al. 1998b; Bryan et al. 2000). Caldera collapse during the La Caleta eruption would have been accompanied by strong seismic activity, which may account for the lithic segregation structures and may have fluidised fine ash allowing it to rise up through subsequent fissures creating the sedimentary dykes in Member 6.

The dispersal of Member 6 is less extensive than that of other breccias associated with other caldera collapse events on Tenerife (e.g. Member 8 of the Poris Formation; Brown et al. 2004). It is possible that this is due to widespread bypassing of the La Caleta pyroclastic density current during the eruption climax, and/or that the lithic breccia has elsewhere been substantially eroded. It is possible that the lithic breccias in the La Caleta Formation resulted from rock avalanching, triggered by strong seismic activity, and erosional incorporation by pyroclastic density currents, without caldera collapse occurring. This would account for the limited extent of the breccia and the lithic segregation structures and sedimentary dykes. However, the presence of syenite clasts favours caldera collapse, as this is the only means of

excavating rocks from such great depths. The large eruptive volume of the La Caleta Formation (see section 2.5) also supports this interpretation.

2.4 Co-ignimbrite ash layers

Members 3, 4 and couplets 1 and 5 of Member 5 are all capped by fine ash layers. The absence of pumice and lithic lapilli and their widespread nature with little change in character (i.e. grainsize), suggests a co-ignimbrite origin. They consist of a fine ash and contain abundant ash pellets, with or without coated pellets and rare accretionary lapilli. Their fine grainsize, draping of topography and lack of lapilli and tractional sedimentary structures suggest a fallout origin. Member 3b presents the most information about its depositional origin and is well preserved due to minimal erosion by succeeding pyroclastic density currents. It is found across the entire study area, both near the coast and higher up on the volcano flanks. This has allowed topographical relationships to be traced over large distances and it consistently drapes topography, supporting a fallout origin. Unlike most of the other ash layers, Member 3b is composed of clast-supported pellets that are particularly well defined towards the top of the layer, supporting a fallout origin. Coated pellets and accretionary lapilli are absent.

The other fine ash layers are less well exposed and are matrix-supported, containing fine ash pellets, coated pellets, and rare accretionary lapilli. These layers locally drape topography, but the unusual thickness variations of these layers suggest that they may have been influenced by the wake of pyroclastic density currents (wake deposits), generating fluctuations in thickness that are incompatible with fallout deposits and cannot be attributed to erosion. For example, some ash layers are thicker at coastal localities compared to localities immediately upslope towards source. Impersistent preservation of these ash layers has prevented isopach mapping that would help to constrain their depositional origin.

Some of these ash layers are composed of clast-supported pellets towards the outer limits of the deposit and become matrix-supported in more central zones of deposition (e.g. Couplet 1b Member 5). This suggests that while fallout was possible at some geographical locations, the deposition of the same ash layer was elsewhere simultaneously being influenced by the wake of the preceding pyroclastic density current, with deposition occurring from a direct fallout-

dominated flow-boundary. This could account for the presence of coated pellets in some ash layers (e.g. Member 4b) and not in others, and will be discussed later in this section.

Member 5 has a small sequence of clast-supported pellet layers. This suggests that there was a prolonged hiatus at this locality or that current deposits were never emplaced. There are occasional pumice lapilli between the pellet layers that may represent the passage of pyroclastic density currents for which there is no depositional record. The presence of co-ignimbrite ashfall layers indicates a hiatus between successive pyroclastic density currents, and more importantly it is an indication that a pyroclastic density current did pass over the area, even if they did not deposit. This is particularly relevant for Member 5, which contains three incomplete couplets where the ignimbrite is absent. The recognition of co-ignimbrite fallout deposits, in the absence of its associated ignimbrite, is therefore vital for hazard assessment of populated volcanically active regions.

The significance of pellet, coated pellets and accretionary lapilli

Accretionary lapilli have historically been taken to indicate a fallout origin in the presence of atmospheric moisture, where layers of ash accreted round a nucleus whilst dropping through an ash plume, until they reached a sufficient mass allowing them to fall out. However, accretionary lapilli have also been found in some ignimbrites (Poris Formation) and Brown et al. (2004) proposed that they may originate in co-ignimbrite ash plumes as ash pellets or other nuclei that then drop to lower levels within the current and accrete additional layers of ash whilst transported in the density current, before being deposited. The accretionary lapilli in the La Caleta Formation are not as well-developed as those found in Member 6 of the Poris Formation (Brown et al. 2004) and have only two or three concentric laminations. This might suggest that they were not transported for long in turbulent conditions, indicating that the currents were of short duration and provides an insight into the competency of the current and/or eruption dynamics. For example a current with a greater competency could support accretionary lapilli for longer, allowing them to accrete more layers. Equally, a more powerful eruption will keep material suspended in a volcanic plume for longer allowing the formation of well-developed accretionary lapilli.

Clast-supported pellets in the Poris Formation were interpreted to be fallout layers derived from co-ignimbrite ash plumes (Brown et al. 2004). Similar clast-supported pellet layers occur in the La Caleta Formation (Member 3b, Member 4b and Member 5 Couplet 1b). Some

of these layers change laterally into layers of matrix-supported pellets and coated pellets that have been interpreted to represent current-influenced fallout or wake deposits. The presence of fine ash coatings on pellets is interpreted as an indication of limited exposure to lateral shear; the pellets fall from the co-ignimbrite ash plume, briefly interacting with the wake of the pyroclastic density current, and were subjected to lateral shear and turbulence, allowing the accretion of a single rim of fine ash. The presence of coated pellets may have the potential to identify wake deposits, although rapid deposition from density currents could also yield coated pellets, since insufficient time would prevent the accretion of multiple concentric laminations. Until more research is done, it is premature to use the presence of accretionary lapilli, coated pellets and pellets as criteria to distinguish current deposits, wake deposits and ash fall deposits, as accretionary lapilli do form clast-supported fallout deposits (e.g. Fasnia Formation, Tenerife) as well as appearing in ignimbrites (e.g. Self, 1983).

2.5 Eruption volumes

Calculating the volume of pyroclastic eruptions is notoriously difficult and at best provides only a minimum value. The thickness and grain size of fallout deposits decay exponentially away from source (e.g. Booth et al. 1978) and this is used to calculate the volume based on isopach maps, from which the area enclosed by each isopach can be calculated. Traditionally the natural log (\ln) of the thickness was plotted against the \ln (area) of each isopach and the resulting line extrapolated to 0.001 m thickness (e.g. Walker, 1981). The volume is then calculated by integrating the area beneath the curve. The two problems with this method are, firstly, the curvature of the line is a direct consequence of the exponential dependence (Pyle, 1989), and secondly, the data are normally collected from intermediate thicknesses, so that the curvature of the line, which only occurs at extremes of thickness, is not observed, resulting in an apparent linear relationship, which has the effect of exaggerating the area enclosed by the isopach, causing inaccurate volume and dispersal calculations (Pyle, 1989).

Pyle (1989) proposed data should be plotted on \ln (thickness)- \ln ($\sqrt{\text{isopach area}}$) plots. These produce one or two straight lines, confirming an exponential dependence of parameters (i.e. thickness) and allow the calculation of volumes without unnecessary extrapolation of field data. The result is a graph from which the intersection of the line with the y-axis provides a maximum thickness (T_0), while the slope of the line allows the calculation of the thickness

half distance (b_t) (equation 2.5; Fig. 2.18). These two parameters can then be used to calculate the volume of the deposit (equation 2.6).

$$b_t = \ln(2)/(k\sqrt{\pi})$$

k = the slope of the line

(2.5)

$$V=13.08T_0b_t^2 = 2 T_0/k^2$$

(2.6)

Volumes for members 1 and 2 of the La Caleta Formation have been estimated following the method of Pyle (1989) and are solid rock equivalents. The area enclosed by the isopachs was calculated and the square root of the isopach area is plotted against the *ln* (thickness) (Fig. 2.18). Assuming no over-thickening near to source, the estimated maximum thickness (T_0) and slope of the straight line (k) for members 1 and 2, can be seen in Table 1, from which volumes of 0.25 km³ for Member 1 and 10.3 km³ for Member 2 have been calculated. These volumes only represent an approximation, particularly for Member 2 where extensive erosion has made the construction of isopach contours difficult. The isopach contours were constructed using the location of the lithic lapilli layer at the top of Member 2 as a guide to identify complete sections. Further isopach data are required higher on the flanks of southern Tenerife to better constrain these volumes, but there is little exposure there. Estimates of the volume of the Granadilla Pumice (3.53 km³ Booth, 1973; 5.12 km³ Bryan et al. 2000), and the Poris fallout deposit (5.7 km³, Edgar et al. 2002) have been made, but do not include the overlying ignimbrites belonging to the same formations.

Member	T ₀ (cm)	k	Volume (km ³)
1	60.9	-0.07018	0.25
2	336.6	-0.02555	10.3

Table 1: The volumes of Member 1 and Member 2 calculated using the predicted maximum thickness (T_0) and the slope of the line (k) from figures 4.18A &B.

An estimation of the volume of the overlying ignimbrites and co-ignimbrite ash layers of the La Caleta Formation is more problematic because the dispersal of the ignimbrite will be less systematic, and mostly offshore. The data available suggest a volume of 3.8 km³, which has been calculated on the basis of the La Caleta ignimbrites having a total mean thickness of 7.16 m, potentially covering an area of 533 km². This is likely to be a small fraction of the total volume as it is thought that the majority of the currents largely bypassed the flanks and

flowed into the ocean. This is thought to have been the case for other Bandas del Sur formations (e.g. Poris Formation; Brown, 2001) and accounts for presence of a 700 m thick succession of volcanoclastic material off the southern coast of Tenerife as detected by seismic profiling (reported in Bryan et al. 1998). The overall volume estimated for the La Caleta Formation in this study has been estimated to be 14.55 km^3 , which is comparable to the 15 km^3 estimated by Edgar et al. (2006).

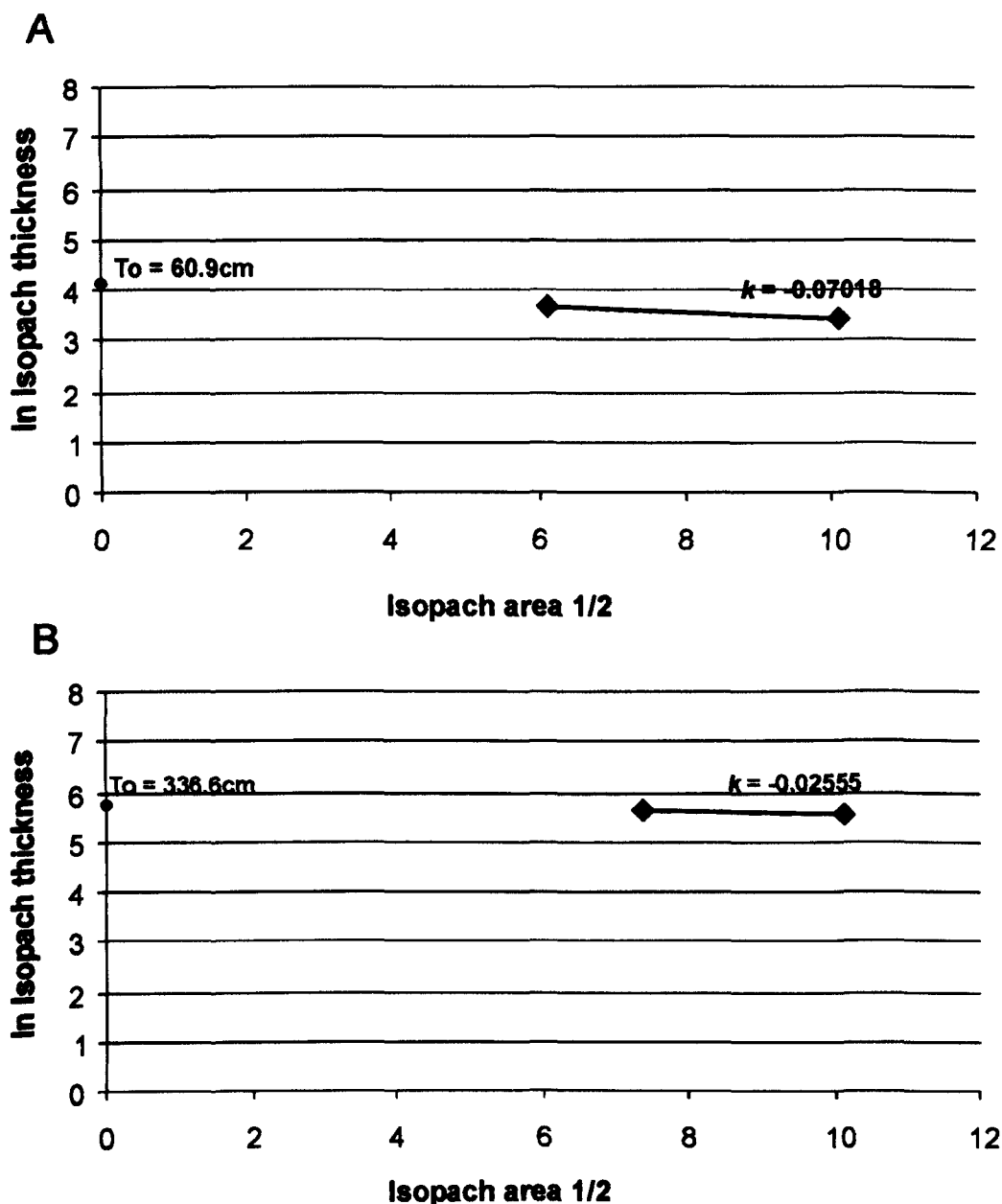


Figure 2.18: In isopach thickness - isopach area $\frac{1}{2}$ graph for (A) Member 1; and (B) Member 2, which can be used in conjunction with equation 4.6 to calculate the volume of Member 2.

2.6 Geochemistry

Pumice clasts were sampled throughout the La Caleta Formation for XRF and microprobe analysis, to assess chemical variations during the La Caleta eruption. Samples were taken from Member 2, Member 5 (couplet 1a and 5a) and Member 6 (Fig. 2.19A). Choice of samples was often restricted due to the extensive alteration of the juvenile material, which has frequently destroyed the entire clast. Smaller clasts and those that are embedded in a fine matrix are particularly affected.

The pumice clasts low in the formation are white and microvesicular, with a fibrous texture (members 1-4), but take on a more green appearance in Member 5 (Couplet 1a of Member 5; Fig. log) and small black pumiceous inclusions and banded pumices are seen for the first time (Couplet 5a of Member 5; Fig. 2.3). Member 6 has very glassy dark green pumice clasts that can contain abundant feldspar phenocrysts and banded pumice, which are more abundant than in Member 5.

The pumices contain alkali feldspar, biotite, nosean/hauyne, titanomagnetite, ilmenite and sphene. Kaersutite, augite and plagioclase phenocrysts are also present but are not as common (Fig. 2.20). Plagioclase is present in the pumice clasts towards the base of the La Caleta Formation, but diminishes with height and is replaced by increasing amounts of anorthoclase (Fig. 2.20). The feldspar phenocrysts (plagioclase in particular) have embayed margins and dissolved central regions in thin section (Fig. 2.21).

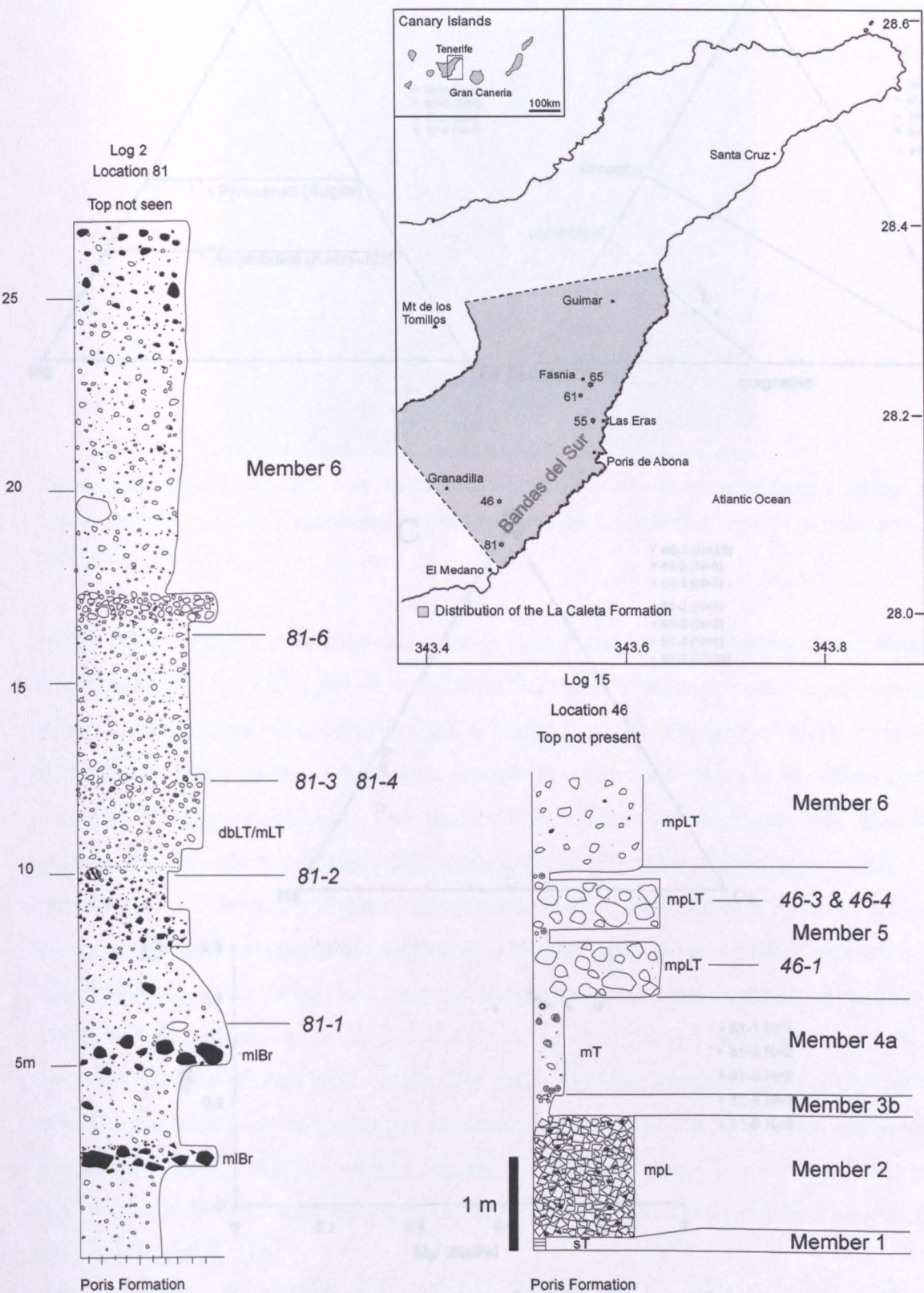


Figure 2.19: Location map of where geochemical samples were obtained and sedimentary logs to identify the stratigraphic horizon from which they were taken. Samples M255, M261 and M265 were from locations 55, 61 and 65 respectively and were sampled ~1.5 m from the base of the La Caleta Formation.

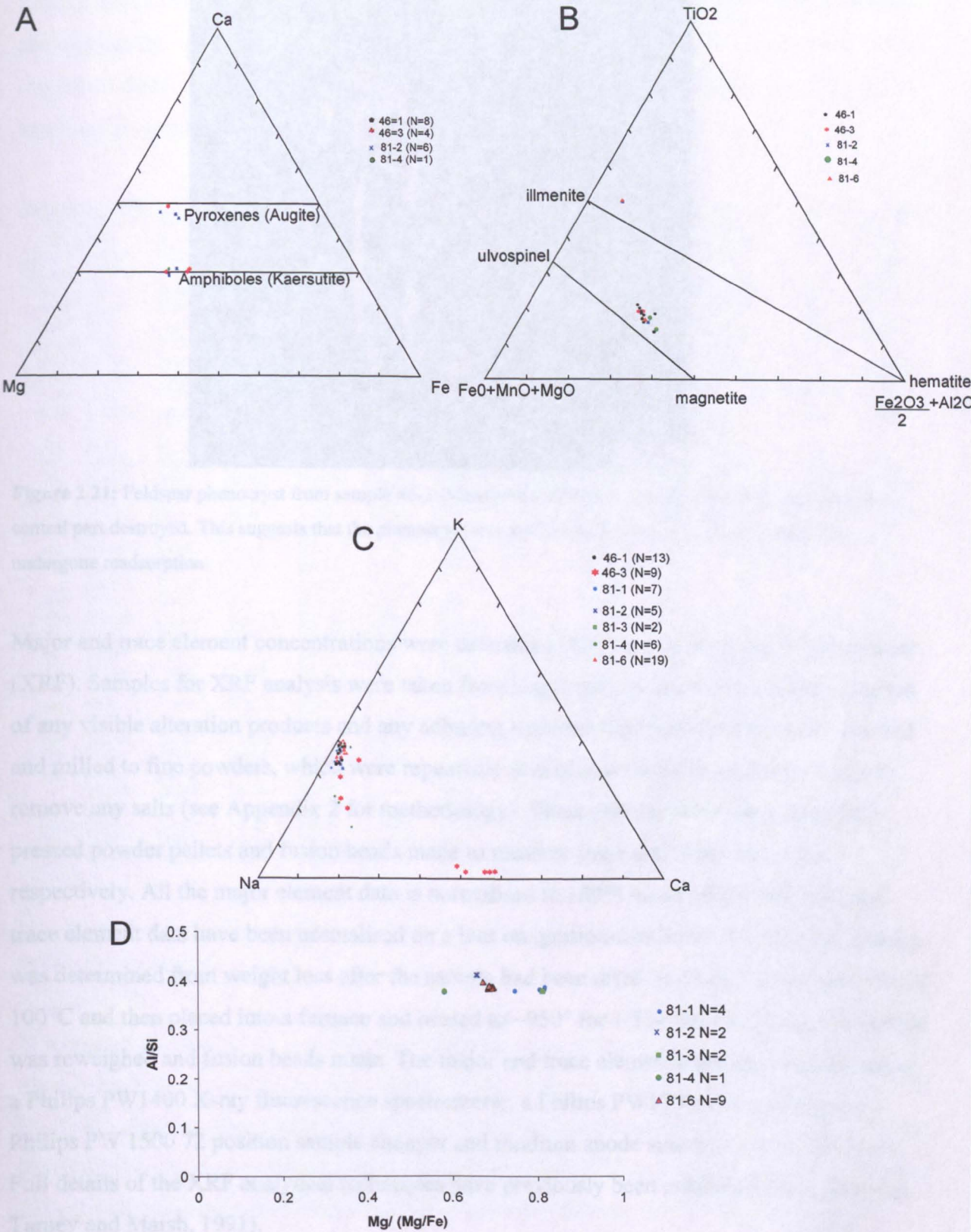


Figure 2.20: Phase diagrams with the geochemistry of the phenocrysts. (A) Pyroxenes and Amphiboles; (B) Iron oxides; (C) Feldspars and (D) Biotites in pumices sampled from members 1, 5 and 6.

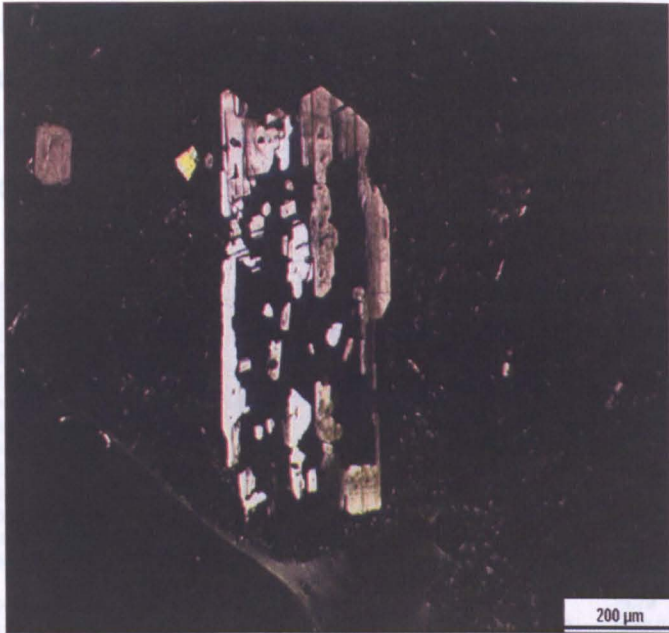


Figure 2.21: Feldspar phenocryst from sample 46-3 (Member 5) which has embayed margins and has had its central part destroyed. This suggests that the phenocryst was not in equilibrium with the melt and it has undergone readorption.

Major and trace element concentrations were determined by x-ray fluorescence spectrometry (XRF). Samples for XRF analysis were taken from single pumice clasts, which were cleaned of any visible alteration products and any adhering material. The pumice clasts were crushed and milled to fine powders, which were repeatedly soaked and rinsed in deionised water to remove any salts (see Appendix 2 for methodology). These powders were then dried and pressed powder pellets and fusion beads made to measure trace and major elements respectively. All the major element data is normalised to 100% on an anhydrous basis and trace element data have been normalised on a loss on ignition-free basis. The loss on ignition was determined from weight loss after the sample had been dried overnight at temperatures of 100°C and then placed into a furnace and heated to ~950° for 1.5 hours. Once cool the sample was reweighed and fusion beads made. The major and trace element data was obtained using a Philips PW1400 X-ray fluorescence spectrometer, a Philips PW1730 series generator, a Philips PW 1500 72 position sample changer and rhodium anode side window X-ray tubes. Full details of the XRF analytical techniques have previously been published elsewhere (e.g. Tarney and Marsh, 1991).

The major element analysis (Table 2) suggests an overall phonolitic composition (Fig. 2.22A), but displays vertical chemical zoning, with the juvenile material becoming increasingly evolved with time as demonstrated by increasing amounts of Zr and Nb (Fig.

2.22B). This corresponds well with the decrease in plagioclase and increase in anorthoclase phenocrysts throughout the La Caleta Formation. The embayed margins and dissolved central regions of these phenocrysts suggest that they were not always in equilibrium with the melt, resulting in readorption.

Sample	M255	M261	M269	81-1	81-2	81-3	81-5	81-6	46-1	46-3	46-4	AZ
SiO ₂	54.31	56.02	53.86	55.26	55.21	56.29	55.08	56.90	55.58	56.82	56.45	63.78
TiO ₂	0.52	0.52	0.53	0.62	0.88	0.66	0.64	0.67	0.51	0.49	0.54	0.68
Al ₂ O ₃	18.18	18.96	18.38	18.45	17.86	18.61	18.22	18.67	19.81	19.71	20.66	16.58
Fe ₂ O ₃	2.61	2.71	2.60	3.35	3.51	3.50	3.33	3.37	2.67	2.63	2.80	3.30
MnO	0.140	0.148	0.139	0.228	0.180	0.231	0.220	0.221	0.156	0.154	0.147	0.080
MgO	1.32	0.95	2.15	0.33	0.66	0.41	0.34	0.34	0.32	0.36	0.40	1.46
CaO	2.47	1.28	2.64	1.59	2.92	0.70	1.98	0.84	1.11	1.02	1.28	2.09
Na ₂ O	7.18	7.55	7.19	9.77	8.70	9.73	9.66	9.82	8.28	8.66	7.56	2.83
K ₂ O	6.523	6.885	6.361	6.164	5.717	6.220	6.213	6.322	6.868	6.780	6.076	4.868
P ₂ O ₅	0.085	0.064	0.073	0.066	0.159	0.063	0.081	0.057	0.057	0.056	0.054	0.196
LOI	5.65	4.54	6.19	3.64	3.57	3.13	4.01	2.54	3.42	2.79	3.94	3.97
Total	98.99	99.64	100.10	99.46	99.36	99.54	99.77	99.75	98.80	99.47	99.92	99.85
As	3.06	4.57	1.81	5.13	3.49	5.11	3.81	4.49	5.79	4.65	7.13	5.01
Ba	268.49	263.87	261.57	27.44	717.11	33.61	21.39	27.08	292.08	261.71	294.88	1396.44
Ce	88.1	90.72	75.96	245.76	200.26	252.88	250.34	266.7	102.77	100.31	105.95	188.82
Co	3.73	2.88	3.74	5.99	6.14	6.79	4.31	6.09	4	3.32	4.15	5.89
Cr	5.62	6.61	2.17	4.04	0.54	1.09	0.91	2.82	5.2	1.86	-1.24	-1.97
Cs	1.34	3.18	2.27	6.04	7.63	2.98	3.57	4.35	1.99	6.26	3.27	8.45
Cu	-0.75	-1.46	-1.84	1.3	1.72	2.92	1.61	5.59	0.31	0.06	0.7	4.85
Ga	23.11	22.7	21.82	30.59	25.1	30.73	30.86	31.55	27.23	26.92	27.88	20.1
La	64.01	74.06	61.17	140.13	110.63	144.41	142.04	144.45	74.08	72.66	72.71	97.76
Mo	4.16	3.34	3.8	5.64	6.24	6.12	5.97	7.36	5.06	5.56	3.2	2.57
Nb	126.42	125.34	117.38	301.83	206.26	316.55	305.04	311.69	155.21	148.8	150.03	29.51
Nd	21.3	25.42	21.31	71.33	67.37	72.32	70.03	79.63	21.83	22.64	23.01	73.36
Ni	-0.66	-2.07	-1.12	-3.11	-3.62	-1.96	-2.56	-1.21	-2.39	-3.3	-2.04	0.78
Pb	11.23	9.32	12.73	13.53	8.23	13.25	14.99	13.13	13.09	12.26	12.64	26.25
Rb	140.13	145.51	126.7	171.99	118.23	178.04	171.22	173.76	167.12	170.44	149.56	159.66
Sc	5.52	-0.55	1.68	1.38	1.42	-2.23	-0.96	-0.66	2.28	0.56	4.7	6.73
Sn	0.83	3.71	-1.88	6.67	-0.53	6	7.39	3.47	5.64	1.76	-2.32	-2.59
Sr	101.94	80.17	113.21	20.2	161.95	14.32	20.68	8.75	78.15	74	82.75	502.47
Th	22.98	24.44	21.58	32.88	24.04	33.79	35.63	35.8	29.46	32.69	30.13	33.77
U	5.72	5.67	3.59	5.47	5.55	7.34	7.14	7.64	7.05	7.97	7.82	3.84
V	22.58	22.79	21.45	28.47	37.9	28.49	31.45	32.87	20.26	23.3	22.92	27.75
W	-0.46	-0.1	-0.06	3.7	5.57	4.51	5.04	7.92	1.67	0.52	-0.1	0.33
Y	20.03	16.52	14.88	52.06	44.39	55.27	53.99	55.22	16.35	17.99	16.39	28.98
Zn	83.5	73.61	66.82	130.06	100.73	138.6	131.6	132.49	86.19	83.51	81.83	51.25
Zr	812.06	807.02	742.6	1281.58	813.6	1334.84	1312.31	1293.26	980.42	939.96	949.34	465.47

Table 2 : XRF analyses of major and trace elements of pumice samples taken from members 2, 5 and 6 at different height intervals.

The banded pumice (81-2) is less evolved than the other samples and has smaller amounts of Zr, causing it to sit off the line of evolution on the Nb/Zr plot (Fig. 2.22B). The different bands of volcanic glass in sample 81-2 were subjected to microprobe analysis, which revealed bands of phonolitic and tephriphonolitic glass (Fig. 2.22C). There is less Na in the analyses of the volcanic glass than observed in the whole pumice analyses, which might suggest that some Na was lost during microprobe analysis, due to vaporisation. This would artificially increase the SiO₂ weight percentage in the glass analysis.

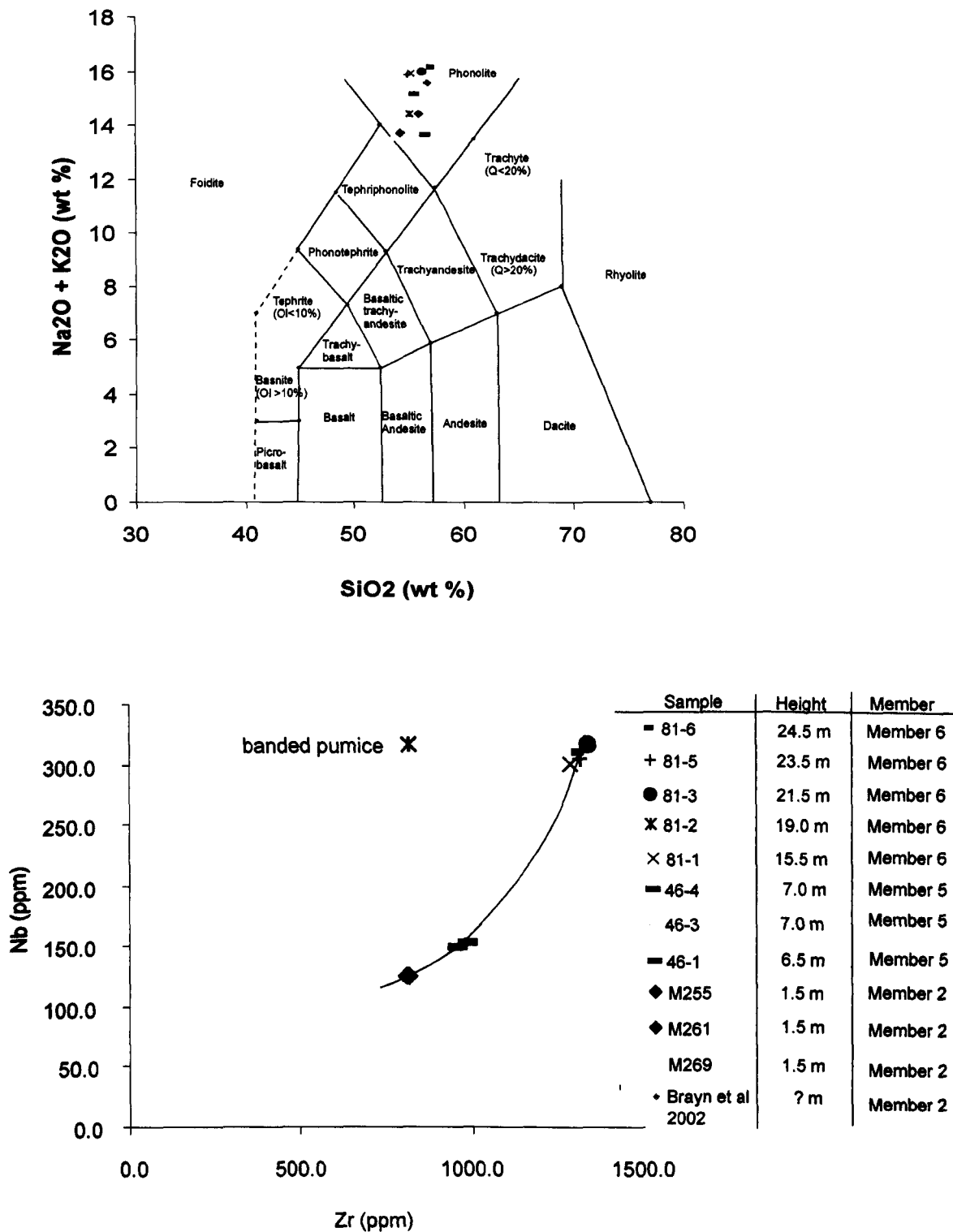


Figure 2.22: (A) TAS diagram with the bulk composition of pumice samples collected from Member 2, Member 5 and Member 6 of the La Caleta Formation.. All the samples are phonolitic: (B) Nb/Zr plot showing a curvilinear distribution with the composition of the pumice samples becoming increasingly evolved with height. Sample 81-2 is less evolved and sits off the line of evolution. This is a banded pumice, containing a less evolved glass, which is interpreted to be from a secondary source.

The apparent curvilinear distribution on the Nb/Zr plot would suggest that the magma evolved via the physical fractionation of the magma rather than being the result of magma mixing, although more data required confirming whether the curvilinear distribution is real or an artefact of limited sampling. The less evolved tephriphonolite in the banded pumice (81-2) would explain why it does not sit on the line of evolution and supports the idea that the tephriphonolite was derived from a secondary source.

The first appearance of the tephriphonolite is as small discrete inclusions (Member 5 couplet 1a), which is followed by banded pumice that increases in abundance. This would suggest that mixing was initially restricted, but increased with time resulting in an increased abundance of banded pumice during the eruption of Member 6. The overall relative rarity of the banded pumice suggests that the magmas did not mix readily, which is supported by the curvilinear distribution of the Nb/Zr plot (Fig. 2.22A). The degree of mixing would have been controlled by flow rate within the magma chamber and the relative densities and viscosities of the magma types (Turner & Campbell, 1986; Wilson, 1997). The slower the flow rate and the greater the viscosity difference, the less mixing would have occurred. This influx of tephriphonolite magma may have been responsible for triggering the more sustained pyroclastic fountaining, represented by Member 5 and Member 6, which may have culminated in caldera collapse.

The presence of kaersutite and plagioclase as subordinate phenocryst phases has been documented in the Granadilla Formation (Bryan, 2006) and their presence suggests a hydrous magma at higher pressures, which would have lowered the melting temperature, indicating lower eruption temperatures and perhaps a more evolved source than in previous eruptions (e.g. Arico Formation). Unlike magma supplies for older formations in the Upper Bandas del Sur Group (e.g. the Arico, Granadilla and Poris formations), which became less evolved with time, the magma supply for the La Caleta eruption became more evolved, with no evidence of double zoning. This relatively more evolved magma would have had a greater viscosity and a higher volatile content. This would have increased the explosivity of the eruption with time and resulted in more sustained pyroclastic currents and ultimately caldera collapse. This type of geochemical zoning is incompatible with the emptying of a stratified magma chamber, with the denser less evolved magma at the base of the chamber, overlain by progressively more evolved magma, which would produce a deposit with pumice becoming less evolved with time (Fig. 2.24). The chemical zoning seen in the La Caleta Formation could have resulted

from eruptive withdrawal from the base of a compositionally stratified magma chamber that progressively drained the more evolved magma above (Fig. 2.24), or there may have been a second vent.

Previous eruptions on Tenerife produce straight lines on the Zr v Nb plot, which may indicate that mixing played a more important role (Fig. 2.22B). The slope of the La Caleta data is steeper, particularly compared to data from the Poris and Fasnía formations (Fig. 2.24). The quantity of Nb changes at a faster rate than Zr, suggesting that Nb became incompatible at a faster rate during the La Caleta eruption than during the Poris and Fasnía eruptions. This may reflect the presence of amphibole and ilmenite in the La Caleta Formation, since the Nb partition coefficient for amphiboles is higher than in other minerals (e.g. Rawlinson, 1993). The slopes of the Granadilla and Arico data are steeper.

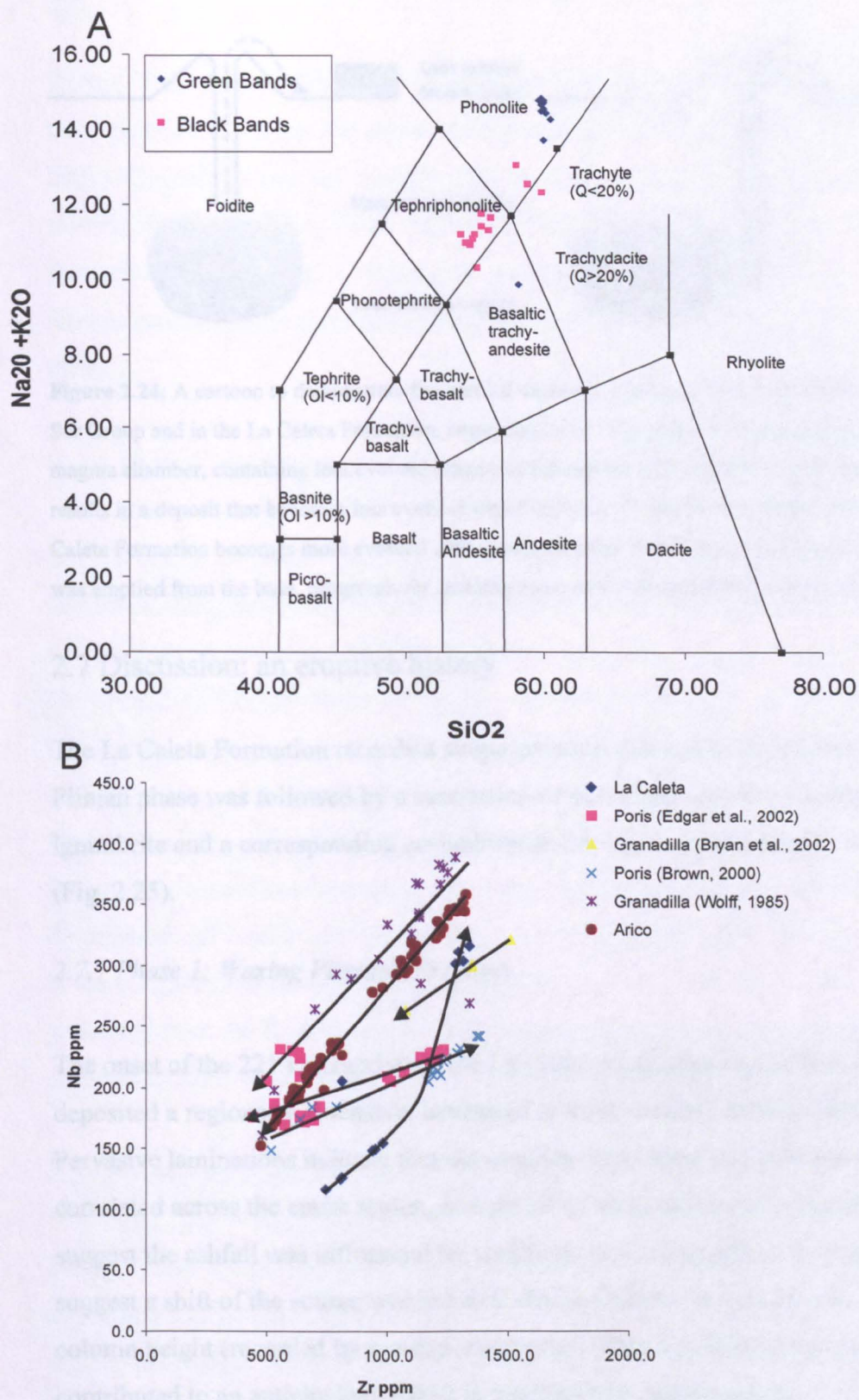


Figure 2.23: (A) TAS diagram with the composition of the different glass types in the banded pumice (sample 81-2), revealing the presence of a phonolitic and tephriphonolitic glass. The tephriphonolite magma is interpreted to be of secondary source and is perhaps responsible for sample 81-2 sitting off the line of evolution on the Nb/Zr plot (Fig. 2.22): (B) Nb/Zr plot comparing data from older formations with the La Caleta Formation. The La Caleta is different because it becomes more evolved, whereas the older formations become less evolved with time. The line of evolution is also much steeper for the La Caleta Formation, which may be due to the presence of amphibole and illmenite which will take up Nb more readily.

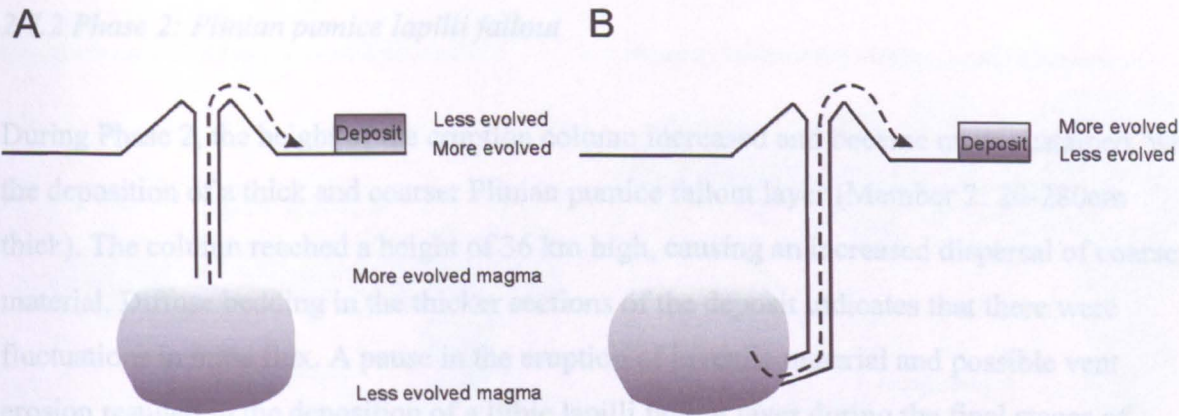


Figure 2.24: A cartoon to demonstrate the vertical chemical zoning in older formations of the Upper Bandas del Sur Group and in the La Caleta Formation, respectively. (A) Progressive emptying from the top of a stratified magma chamber, containing less evolved magma at the base and the more evolved magma at the top, which results in a deposit that becomes less evolved with height e.g. Granadilla Formation (Bryan et al. 2000). The La Caleta Formation becomes more evolved with time; a possible explanation would be that the magma chamber was emptied from the base, progressively draining more evolved magma from above (B).

2.7 Discussion: an eruptive history

The La Caleta Formation records a single eruption that can be divided into five phases. A Plinian phase was followed by a succession of pyroclastic density currents, each depositing an ignimbrite and a corresponding co-ignimbrite ash layer, culminating in a caldera collapse (Fig. 2.25).

2.7.1 Phase 1: Waxing Plinian ash plume.

The onset of the 221 ka eruption of the La Caleta Formation began with Phase 1, which deposited a regionally extensive, laminated to thinly bedded ashfall deposit (Member 1). Pervasive laminations indicate that the eruption was unstable. Each lamination has not been correlated across the entire region, and not all of them are present at all locations, which suggest the ashfall was influenced by variations in wind dispersal. Isopach and isopleths suggest a shift of the source within Las Cañadas Caldera, and an increase in the eruption column height (recorded by upward coarsening). This would have increased dispersal and contributed to an anticlockwise shift in the dispersal, resulting from a waxing eruption. This increase in column height may be linked to changes in vent geometry or volatile content of the magma, causing an increase in mass flux.

2.7.2 Phase 2: *Plinian pumice lapilli fallout*

During Phase 2, the height of the eruption column increased and became more sustained, with the deposition of a thick and coarser Plinian pumice fallout layer (Member 2: 20-280cm thick). The column reached a height of 36 km high, causing an increased dispersal of coarser material. Diffuse bedding in the thicker sections of the deposit indicates that there were fluctuations in mass flux. A pause in the eruption of juvenile material and possible vent erosion resulted in the deposition of a lithic lapilli fallout layer during the final stages of Phase 2.

2.7.3 Phase 3: *Emplacement of pyroclastic density currents and co-ignimbrite ash plumes*

Phase 3 marks the onset of much unsteadiness in the eruption column, causing intermittent low fountaining generating at least 5 pyroclastic density currents that breached the caldera wall, and associated co-ignimbrite ash plumes across the Bandas del Sur region, (recorded by Members 3-6). Co-ignimbrite ash layers containing pellets and coated pellets were deposited between the short-lived density currents. Some were deposited by pure fallout from Phoenix clouds, but some may have been locally influenced by the turbulent conditions of the wake of the passing current (e.g. Member 4b, Member 5 Couplet 1b & 5b) and deposited from a direct fallout-dominated flow-boundary. The Plinian eruption column and its umbrella cloud had diminished sufficiently so that no Plinian fallout occurred, hence the absence of pumice lapilli in the co-ignimbrite ash layers. During the passage of pyroclastic density currents, any fallout generated from the Phoenix cloud fell into the current and was either destroyed or, if sufficiently lithified, survived forming coated pellets and/or the nucleus of accretionary lapilli.

2.7.4 Phase 4 and Phase 5: *Sustained pyroclastic currents and climactic phase*

During Phase 4 sustained quasi-steady pyroclastic density currents passed over the area, depositing a thick ignimbrite (Member 6) that is more homogeneous than any lower in the succession. As the eruption waxed the abundance and size of the lithic clasts increased, marking the onset of the climactic phase of caldera collapse (Phase 5). The absence of evidence for a waning phase in the formation suggests that a complete eruptive history has not been preserved, possibly as a result of erosion.

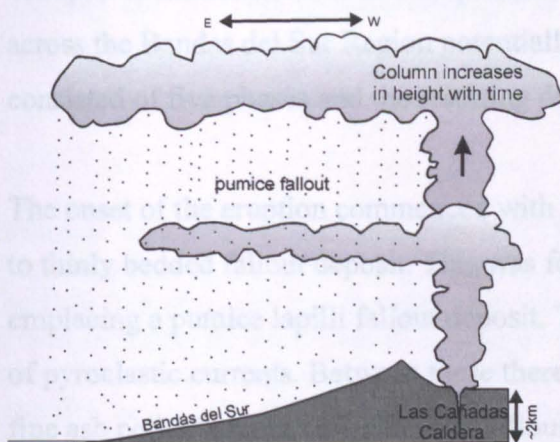
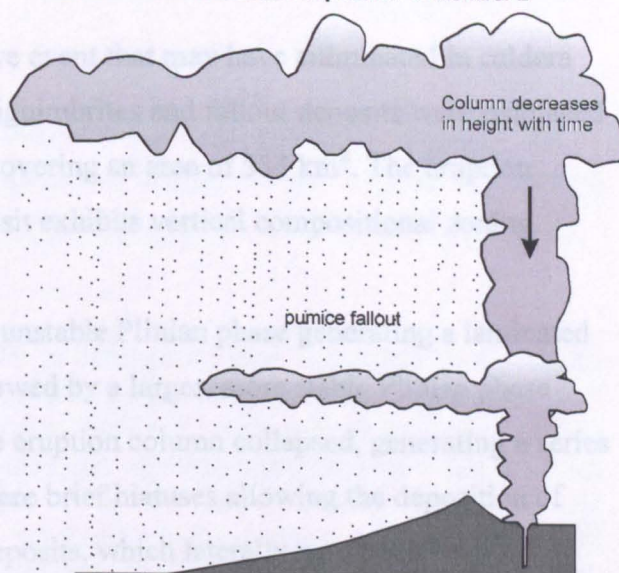
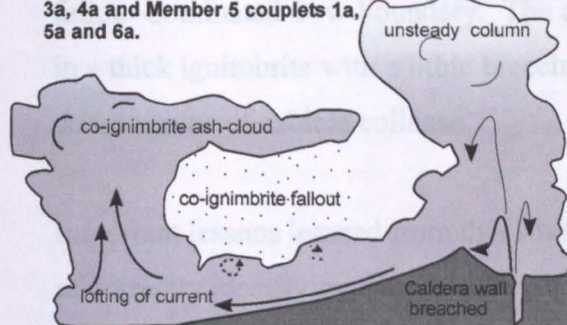
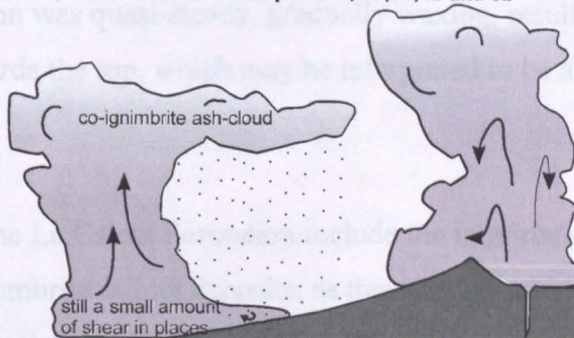
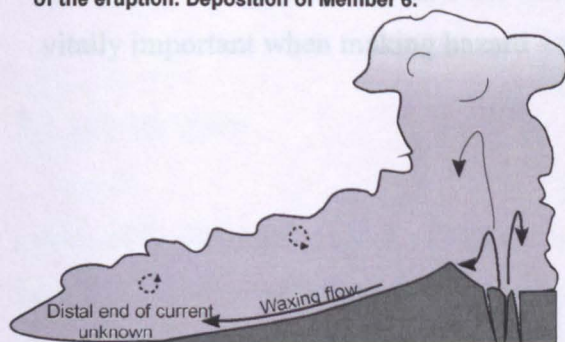
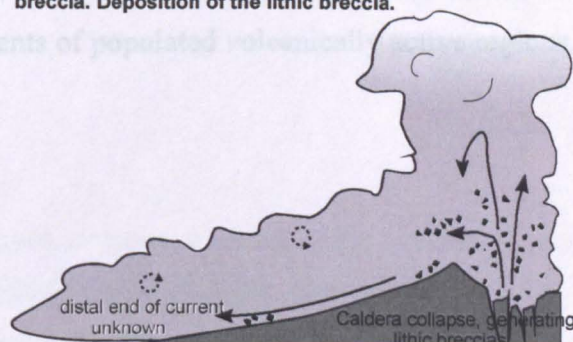
Phase 1: Plinian fallout and deposition of Member 1**Phase 2 : Plinian fallout and deposition of Member 2****Phase 3: Intermittent fountaining creating successive pyroclastic density currents. Deposition of members 3a, 4a and Member 5 couplets 1a, 5a and 6a.****Deposition of co-ignimbrite fallout. Deposition of members 3b, 4b and Member 5 couplets 1b, 2b,3b,4b and 5b****Phase 4: Sustained pyroclastic fountaining and waxing of the eruption. Deposition of Member 6.****Phase 5: Caldera collapse and emplacement of lithic breccia. Deposition of the lithic breccia.**

Figure 2.25: Illustrations of the major eruptive phases showing how the La Caleta eruption evolved with time. Phase 1: Fluctuating eruption column, increasing in height and encountering changes in the prevailing wind direction, causing an anticlockwise shift of the dispersal axis (Fig. 2.6). Phase 2: Increase in column height with a more stable and sustained Plinian phase, ending in a decrease in column height and vent erosion. Phase 3: Onset of pyroclastic density current, between which there was deposition of co-ignimbrite ash layers. These ash layers represent fallout and a hiatus in pyroclastic currents, but locally represent wake deposits, where the fallout has been influenced by the wake of the preceding current. Phase 4: Waxing phase of the eruption, resulting in a more sustained pyroclastic density current, which predominantly bypassed the southeast flanks of Tenerife and deposited out to sea. Phase 5: Climax of the eruption. Culminating in possible caldera collapse, represented by the inversely graded lithic breccia, containing increased quantities of intrusive and hydrothermally altered clasts and welded ignimbrite.

2.8 Conclusions

The 221 ka La Caleta eruption was an explosive event that may have culminated in caldera collapse. A minimum of 15 km³ of phonolitic ignimbrites and fallout deposits were emplaced across the Bandas del Sur Region potentially covering an area of 533 km². The eruption consisted of five phases and the resulting deposit exhibits vertical compositional zoning.

The onset of the eruption commenced with an unstable Plinian phase generating a laminated to thinly bedded fallout deposit. This was followed by a larger, more stable Plinian phase emplacing a pumice lapilli fallout deposit. The eruption column collapsed, generating a series of pyroclastic currents. Between these there were brief hiatuses allowing the deposition of fine ash pellet-bearing co-ignimbrite fallout deposits, which laterally may have been influenced by the wake of the preceding pyroclastic currents and deposited from a direct fallout-dominated flow-boundary. The eruption was quasi-steady, gradually waxing, resulting in a thick ignimbrite with a lithic breccia towards the top, which may be interpreted to be a consequence of caldera collapse.

Important lessons learned from this study of the La Caleta Formation include the importance of correctly identifying the presence of co-ignimbrite fallout deposits, as they signify a hiatus in the passage of pyroclastic density currents and, more importantly, they signify the passage of a pyroclastic density current even when there is no depositional record of one. This is vitally important when making hazard assessments of populated volcanically active regions.

Chapter 3: Using anisotropy of magnetic susceptibility (AMS) to distinguish ash layers deposited by fallout from those deposited from density currents: a case study from Tenerife.

Abstract: Volcanic ashfall layers can be difficult to distinguish from ash layers deposited by pyroclastic density currents where the deposit layers are fine-grained and lack cross-stratification. The very fine grain size coupled with poor exposure of such ash layers can hinder interpretations of their depositional origin, which is vital when using ash layers in hazard assessments. Fine ash layers of known depositional origin were sampled from the Upper Bandas del Sur Group, Tenerife, and their AMS fabrics have been investigated to develop a new method of distinguishing between deposits of ashfall and current deposits. Fine ashfall deposits display oblate, near horizontal circular distributions on the stereonet, which have mean magnetic foliations (as defined by the mean maximum and intermediate susceptibility axes) that dip by $<10^\circ$ relative to bedding and have a numerical mean lineation of $<0.5\%$. The data are well-grouped on the foliation-lineation plots. Fine ash layers deposited by pyroclastic density currents display a lot more variability in their AMS fabrics, which are oblate to triaxial, and the stereonet show girdle distributions defined by the maximum and intermediate susceptibility axes, which show variable degrees of grouping (clustering). This pattern is interpreted in terms of depositional processes. The mean magnetic foliation (as defined by the mean maximum and intermediate susceptibility axes) nearly always dips by $>10^\circ$ relative to bedding and has a mean numerical lineation of $>0.5\%$. Traditional AMS plots are not always sufficient to discriminate between ashfall and pyroclastic density current deposits, so a new discrimination plot has been devised that incorporates the dip of the mean magnetic foliation and the mean numerical lineation. This successfully discriminates between the two types of deposit.

3.1 Introduction

Layers of fine-grained volcanic ash or tuff are common in volcanic successions and are deposited from fallout and pyroclastic density currents. Pyroclastic density currents do not always deposit massive lapilli tuffs or cross-stratified deposits; locally they are capable of depositing thin veneers of fine ash. It is important that the correct origin of such ash layers can be determined in order to undertake hazard assessments of active volcanoes and to reconstruct the pattern of eruptive activity of explosive volcanoes. Inaccurate hazard assessments caused by the misidentification of the origin of these ash layers could jeopardise the safety of human populations in active volcanic regions.

Volcanic fallout and pyroclastic density current deposits are traditionally distinguished from each other on the basis of their field relationships and granulometry. Fallout deposits are typically well- to very well-sorted, framework-supported deposits of angular pumice lapilli, with subordinate, smaller lithic lapilli. They drape topography with systematic and regional grain size and thickness variations that are independent of the local topography. Pyroclastic current deposits are typically very poorly sorted, matrix-supported deposits, with a wide variety of clast sizes and shapes that may exhibit imbrication and/or cross-stratification, and unlike fallout deposits, they thicken in valleys and thin over topographic highs (e.g. Wright et al., 1980) (Fig. 3.1). However it has become increasingly recognised that even large and highly destructive pyroclastic density currents sometimes leave only thin veneers of fine-grained ash (e.g. Schumacher & Schmincke, 1990)

The fine grain size of some ash layers makes it impossible to observe variations in grain size, shape and sorting. Discrimination based on granulometry is only applicable to unlithified deposits and remains equivocal, since granulometry fields overlap (Fig. 3.2 ; Walker 1971)) and fine ash commonly deposits as aggregates (Carey & Sigurdsson, 1982; Schumacher & Schmincke, 1991, 1994; Rose et al. 2001). Poor exposure prevents lateral palaeotopographic relationships from being traced making the origin and significance of some ash layers more difficult to interpret.

The aim of this study was to develop a method of distinguishing ashfall layers from fine ash deposits of pyroclastic density current deposits using Anisotropy of Magnetic Susceptibility (AMS) that can be applied to lithified or partly lithified deposits, where other diagnostic criteria are not readily available. AMS has been used to identify and study palaeoflow directions within ignimbrites (e.g. Ellwood, 1980, 1981; McDonald & Palmer, 1990; Hillhouse & Wells, 1991; Hiscott et al. 1997; Palmer & McDonald, 1999; Haliwood & Ding, 2000; Wang et al. 2001), and has been used to locate hidden volcanic vents (Ellwood 1982; Hillhouse et al. 1991; Lemarche and Froggatt 1993; Palmer & MacDonald, 1999). More rarely, it has been used to infer depositional mechanisms of ignimbrites (Le Pennec et al. 1998; Ort 2003). Surprisingly, there has been no AMS work undertaken to interpret the origin of the fine ash layers.

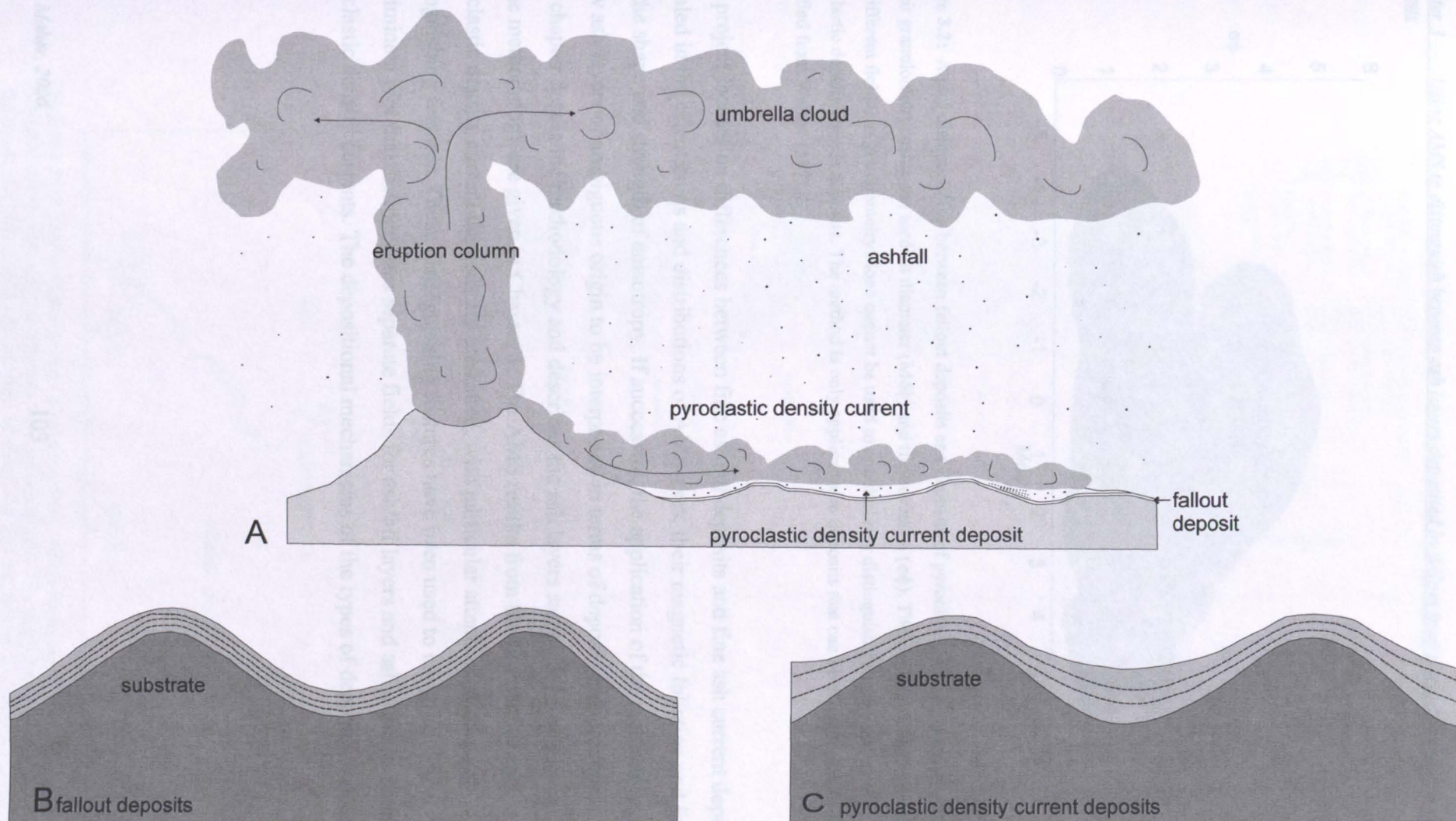


Figure 3.1: (A) Ashfall and pyroclastic density currents and their relationships with topography. Ashfall layers drape topography, whereas pyroclastic density current deposits infill topography thinning over topographic highs and thickening in topographic lows. (B) The relationship of a fallout deposit with the underlying topography; note the way individual layers drape topography, remaining a uniform thickness: (C) The relationship of pyroclastic density current deposits with the underlying topography; note the way individual layers thin over topographic highs and thicken into topographic lows.

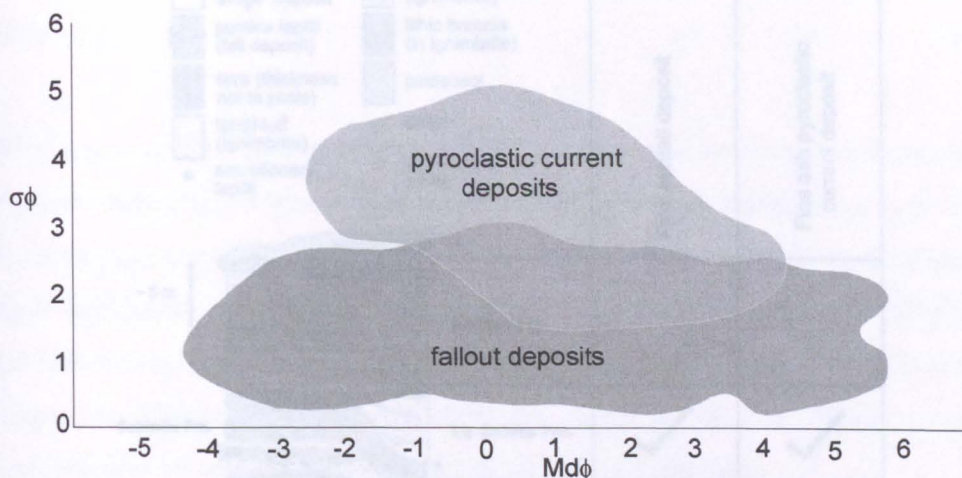


Figure 3.2: A plot distinguishing between fallout deposits and deposits of pyroclastic density currents on the basis of their granulometry, using the median diameter ($Md\phi$) and the deviation ($\sigma\phi$). There is significant overlap of the two different fields, so granulometry alone cannot be used to conclusively distinguish between fallout deposits and pyroclastic density current deposits. The method is only applicable to deposits that can be disaggregated and sieved. Modified from Walker (1971).

This project focuses on differences between fine ashfall deposits and fine ash current deposits revealed in the orientations and distributions of AMS axes, their magnetic foliation and lineation, and the shape and strength of anisotropy. If successful, the application of the methodology would allow ash layers of ambiguous origin to be interpreted in terms of depositional processes. This chapter details the methodology and describes the ash layers sampled. More general details on the methodology are given in Chapter 1. The AMS results from the fine ashfall and pyroclastic density current deposits are presented, with particular attention paid to any distinguishing features. These distinguishing features have been used to construct a new discriminant plot that distinguishes separate fields for ashfall layers and ash deposits from pyroclastic density currents. The depositional mechanisms of the types of deposit are discussed.

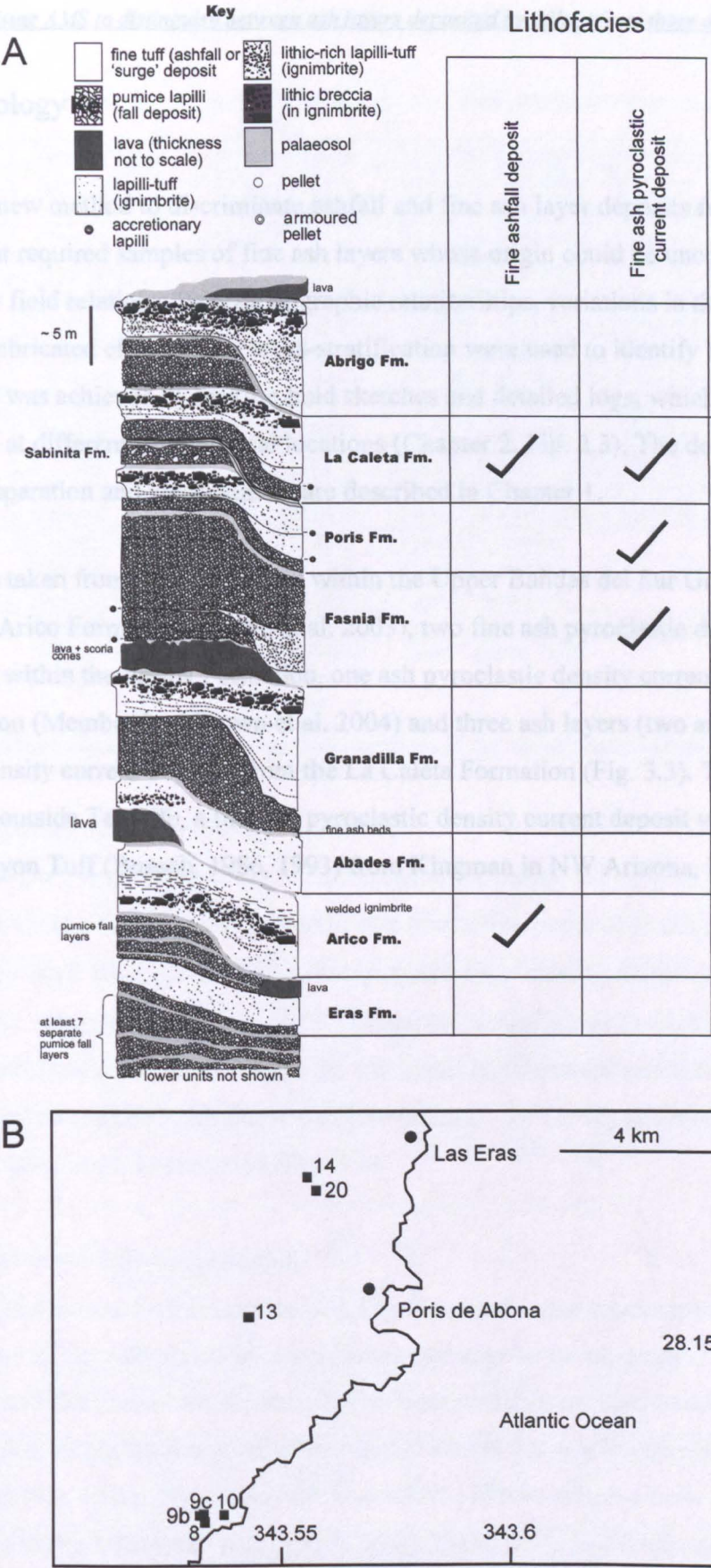


Figure 3.3: (A) A stratigraphic chart displaying from which formations fine ash fallout deposits and fine ash current deposits have been sampled. The log is taken from Brown et al. (2002); (B) Location map of where the fine ash fallout and fine ash pyroclastic density current deposits were sampled.

3.2 Methodology

To develop a new method to discriminate ashfall and fine ash layer deposits from pyroclastic density current required samples of fine ash layers whose origin could be unequivocally established by field relations. Palaeotopographic relationships, variations in thickness, and the presence of imbricated clasts and/or cross-stratification were used to identify fall and current deposits. This was achieved by making field sketches and detailed logs, which enabled ash layers to be sampled at different geographical locations (Chapter 2, Fig. 2.3). The details of sample collection, preparation and measurement are described in Chapter 1.

Samples were taken from five formations within the Upper Bañidas del Sur Group; the basal fine ashfall of the Arico Formation (Brown et al. 2003), two fine ash pyroclastic density current deposits from within the Fasnía Formation, one ash pyroclastic density current deposit from the Poris Formation (Member 2 of Brown et al. 2004) and three ash layers (two ashfall and one pyroclastic density current deposit) from the La Caleta Formation (Fig. 3.3). To test the methodology outside Tenerife, a fine ash pyroclastic density current deposit was sampled from the Cook Canyon Tuff (Buesch, 1986, 1993) from Kingman in NW Arizona, U.S.A. (Table 1).

Sample number	Location	Grid Reference (UTM)	Stratigraphic Location	Ashfall/current
FA10 (Lam)	Tenerife 10	0356332 3110450	La Caleta Formation - Member 1	Fallout
FA9c (Lam)	Tenerife 9c	0355889 3110473	La Caleta Formation - Member 1	Fallout
FA8	Tenerife 8	0355908 3110300	La Caleta Formation - Member 3b	Fallout
FA9b	Tenerife 9b	0355807 3110437	La Caleta Formation - Member 3b	Fallout
FA9c	Tenerife 9c	0355889 3110473	La Caleta Formation - Member 3b	Fallout
FA10	Tenerife10	0356332 3110450	La Caleta Formation - Member 3b	Fallout
FA10(2)	Tenerife 10	0356332 3110450	La Caleta Formation - Member 3b	Fallout
FA14	Tenerife14	0358244 3118660	Arico Formation	Fallout
FL8	Tenerife 8	0355908 3110300	La Caleta Formation - Member 4a	Current
FL9b	Tenerife 9b	0355807 3110437	La Caleta Formation - Member 4a	Current
FL9c	Tenerife 9c	0355889 3110473	La Caleta Formation - Member 4a	Current
FL10	Tenerife 10	0356332 3110450	La Caleta Formation - Member 4a	Current
FL10(2)	Tenerife 10	0356332 3110450	La Caleta Formation - Member 4a	Current
FL10(2i)	Tenerife 10	0356332 3110450	La Caleta Formation - Member 4a	Current
FAS1	Tenerife 20	0358425 3118325	Fasnia Formation	Current
FAS2	Tenerife 20	0358425 3118325	Fasnia Formation	Current
FAS18	Tenerife 18	0356626 3115917	Fasnia Formation	Current
POR	Tenerife 13	0356906 3115344	Poris Formation – Member 2a	Current
AZ	Kingman, Arizona	11767363 3896830	Cook Canyon Tuff	Current

Table 1: A list of the geographical and stratigraphical locations of the fine ash layers sampled in this study (Fig. 3.3)

Fine ash layer in the Arico Formation

A fallout succession at the base of the Arico Formation is composed of three layers (Brown et al. 2003; Fig. 3.4A). The first layer is composed of a fine, white pumiceous ash containing small (375 µm) black lithic clasts. It drapes palaeotopography maintaining a uniform thickness (30–45 mm; Fig. 3.4B), suggesting a fallout origin. Occasional irregularities in thickness (see Fig. 3.4C), attributed to soft state deformation where the ash burial has flattened vegetation, were avoided during sampling so that the AMS fabric was representative of the depositional mechanism. The samples were taken from Location 14 (Fig. 3.3).

Fine ash layers in the Fasnia Formation

Two samples (FAS1 and FAS2; Location 20, Fig. 3.3) were taken from a massive, dirty white ash layer, 25–30 cm thick, with a medium sand matrix and angular to sub-angular lithic lapilli (8 mm), ~2 m above the base of the formation. The local presence of cross-bedding and small-scale grain imbrication within the ash layer at location 20 shows that it was deposited by a pyroclastic density current (Fig 3.5A). The second ash layer (FAS18) was sampled from location 18, 40 cm above the base of the formation. This layer is 30 cm thick, white and composed of a fine-medium

sand matrix with occasional sub-rounded pumice cavities (≤ 35 mm), and angular to sub-rounded lithic lapilli (<10 mm). It is diffusely bedded and contains armoured pellets; some beds exhibit subtle pinch-and-swell structures supporting a pyroclastic current origin (Fig. 3.5B).

Fine ash layer in the Poris Formation

The Poris Formation is composed of a series of fine ash pyroclastic density current deposits with corresponding pellet fallout layers (Fig. 3.6A) (Brown et al. 2004). Member 2a (Fig. 3.6B and C) is pale yellow tuff with rare pumice lapilli (25 mm) and coated pellets (8 mm) and was sampled near to Mt Centinela (Location 13; Fig. 3.3) from a 13 cm thick layer ~ 20 cm from the base of the formation. Lateral variations in thickness documented by Brown et al. (2004) suggest a pyroclastic current origin

Fine ash layers in the La Caleta Formation

Three layers of fine ash were sampled in the Tajao area (Locations 8, 9b, 9c & 10; Fig. 3.3) from the La Caleta Formation (Fig. 4.6A): members 1, 3b, and 4a. Member 1 forms the base of the La Caleta Formation and is a white, 5 cm thick, laminated ash that drapes topography and is interpreted as a fallout deposit (see Chapter 2, Figs 2.4 & 2.5A). Member 3b is locally 50-60 cm above the base of the formation and is a pink, 5-6 cm thick fine ash layer containing clast-supported pellets, which drapes topography with no variation in thickness, and is interpreted to be a co-ignimbrite fallout deposit (Fig. 3.7B and C). Member 4a is locally ~60 cm above the base of the formation, and is a predominately massive white, fine ash which is 5-200 cm thick and contains a mixture of pellets, coated pellets and accretionary lapilli (Fig. 3.7C). It thickens into topographic lows (Fig. 3.7B) and locally contains cross-stratification and internal erosion surfaces (Chapter 2, Fig. 2.12C pg. 62) and is interpreted as the deposit of a pyroclastic density current. Further details concerning these ash layers can be found in Chapter 2, section 2.3.

Fine ash layer in the Cook Canyon Tuff, Arizona.

The Miocene Cook Canyon Tuff (Buesch & Valentine, 1986), in western Arizona (Fig. 4.8A), is a 3-40m thick partially to non-welded ignimbrite that overlies a diffuse bedded pumice lapilli fallout deposit up to 4 m thick (Fig. 4.8B; Buesch & Valentine, 1986; Buesch, 1993). The ignimbrite is predominately grey trachydacite (Fig. 4.8E), with plagioclase, biotite, clinopyroxene and hornblende phenocrysts and subordinate magnetite, sphene and apatite

phenocrysts (Buesch 1993). Two pumice populations provide evidence of magma mixing. The source of the eruption is unknown.

A 25 cm layer of sand grade tuff containing angular lithics of < 1 mm (Fig. 3.8D) that directly overlies the pumice lapilli fallout deposit, was sampled south of Kingman (GR: 11767363 3896830). There is a gradational boundary with the overlying ignimbrite, which becomes increasingly grey, displaying a coarsening upward trend of pumice and lithic lapilli, and becomes matrix-supported (Fig. 3.8 C and D). The base of the ash layer cuts across the diffuse bedding of the underlying pumice lapilli fallout deposit. This suggests that it was deposited by a pyroclastic density current that initially eroded the underlying lapilli fallout deposit.

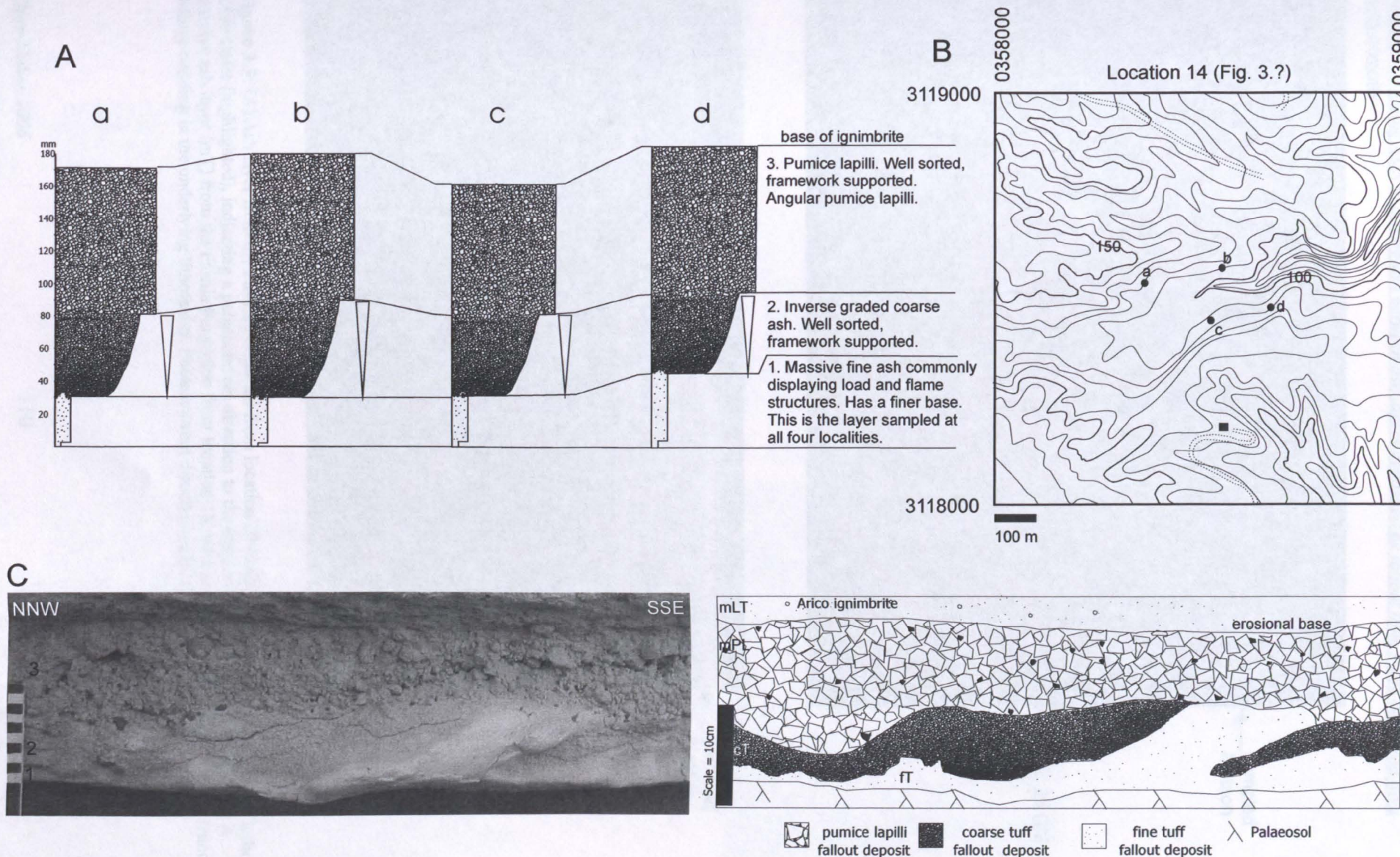


Figure 3.4: (A) Sedimentary logs from the basal fallout layers of the Arico Formation at location 14 (Fig 3.3B) Layer 1 was sampled. Fallout layers 1-3 show little systematic variation in thickness across topography: (B) Locality map illustrating the four sites a-d at location 14 (contours in m): (C) Photo and sketch of the basal layer from the Arico Formation at site c, showing irregular thickness variations interpreted as the interaction of fine ash with palaeovegetation.

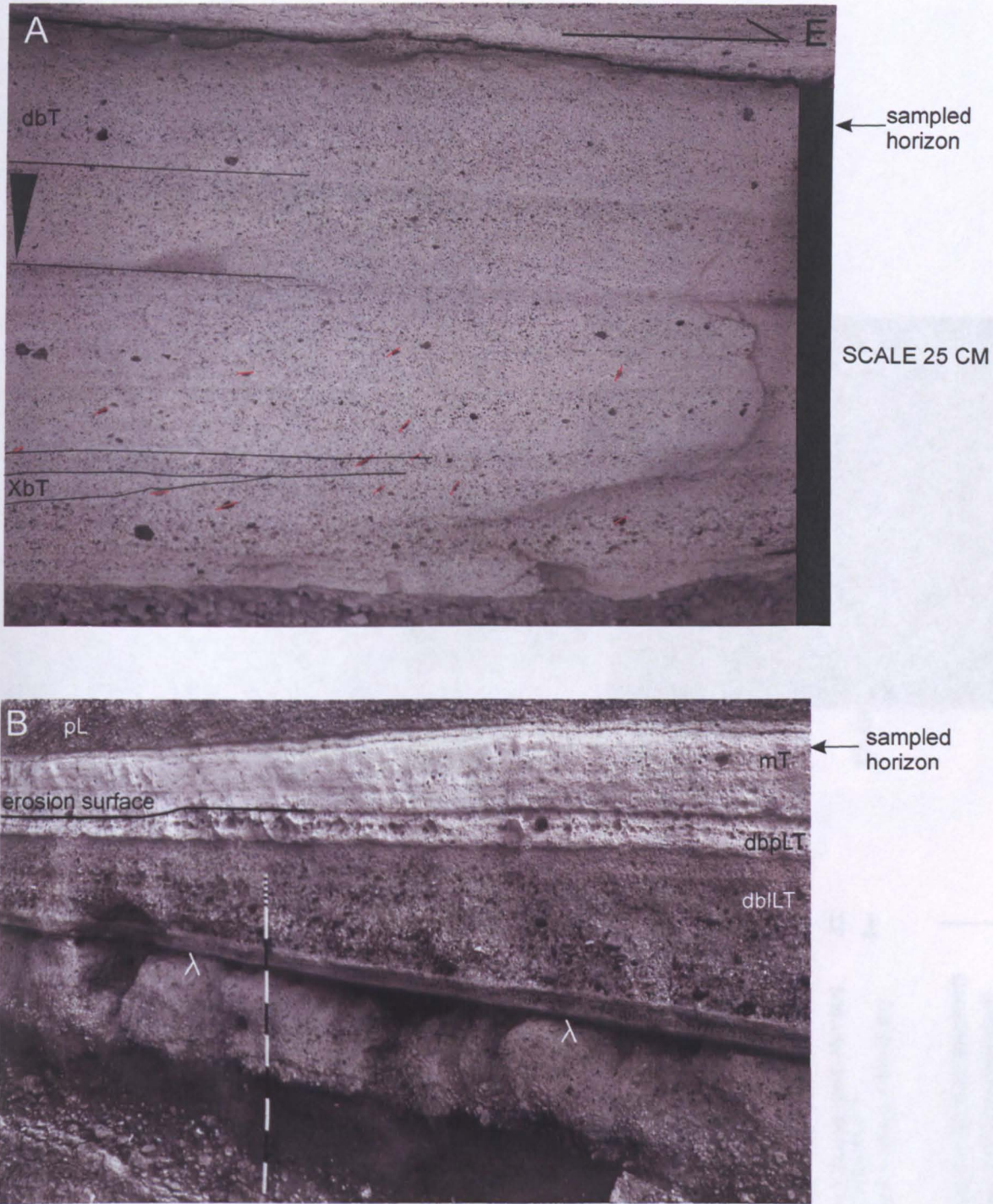


Figure 3.5: (A) Ash layer from the Fasnja Formation from location 20 (FAS1 & FAS2) containing small imbricated lithic clasts (highlighted), indicating a palaeocurrent direction to the east, and contains cross-bedding: (B) A massive ash layer (mT) from the Fasnja Formation from location 18, with an internal erosion surface that truncates diffuse bedding in the underlying lithofacies. Palaeocurrent direction unknown.

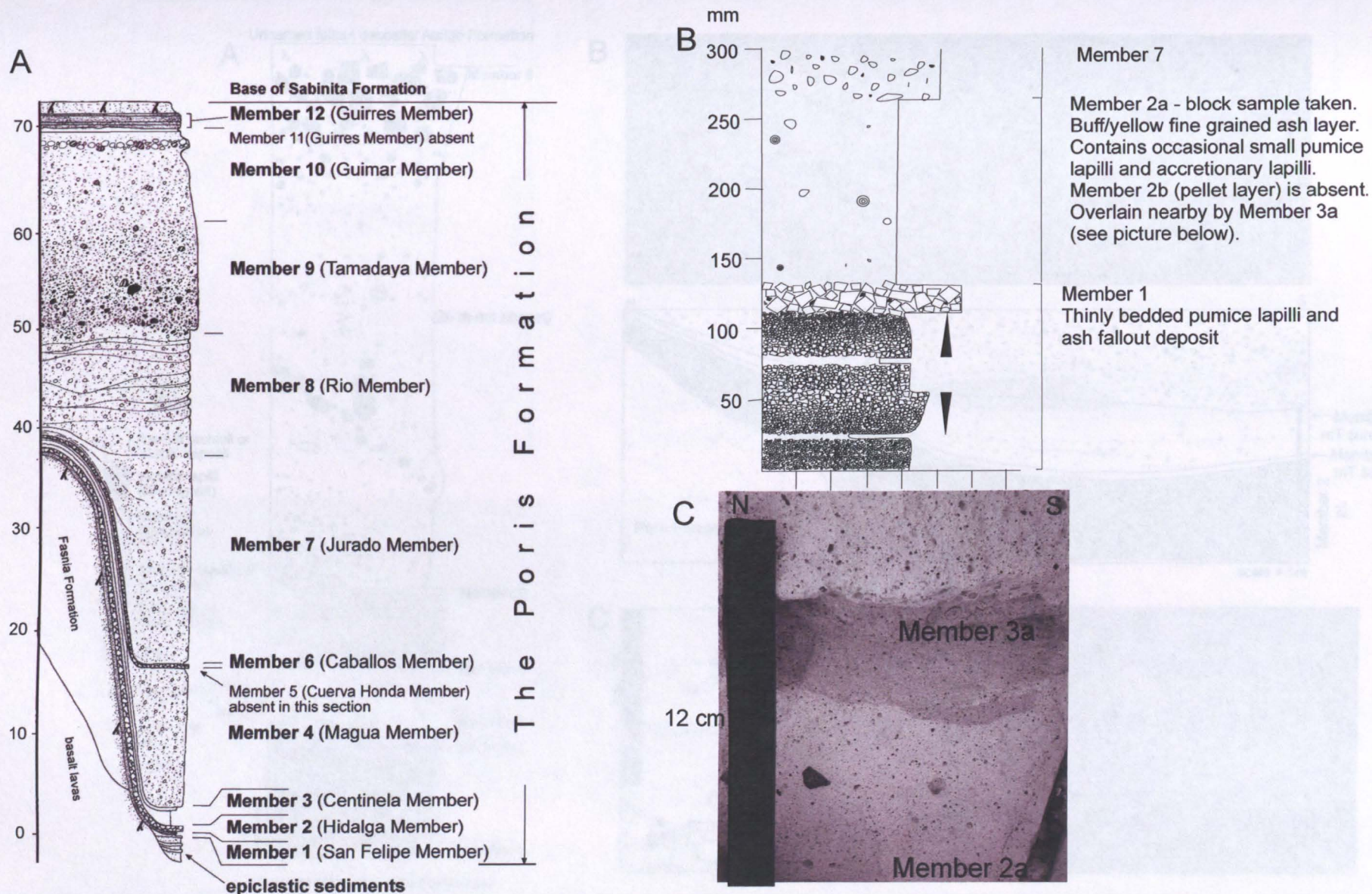


Figure 3.6: (A) A GVS of the Poris Formation (Brown et al., 2004) showing the stratigraphic position Member 2: (B) Sedimentary log of the base of the Poris Formation at location 13, near Mt Centinela GR: 0356906 3115344; Member 1 (fallout deposit) and Member 2a, which was the ash layer sampled. Member 2b, the corresponding pellet layer is absent. Member 3 (between members 2 and 7) can be observed very nearby (C). Palaeocurrent direction assumed to be towards to coast (east).

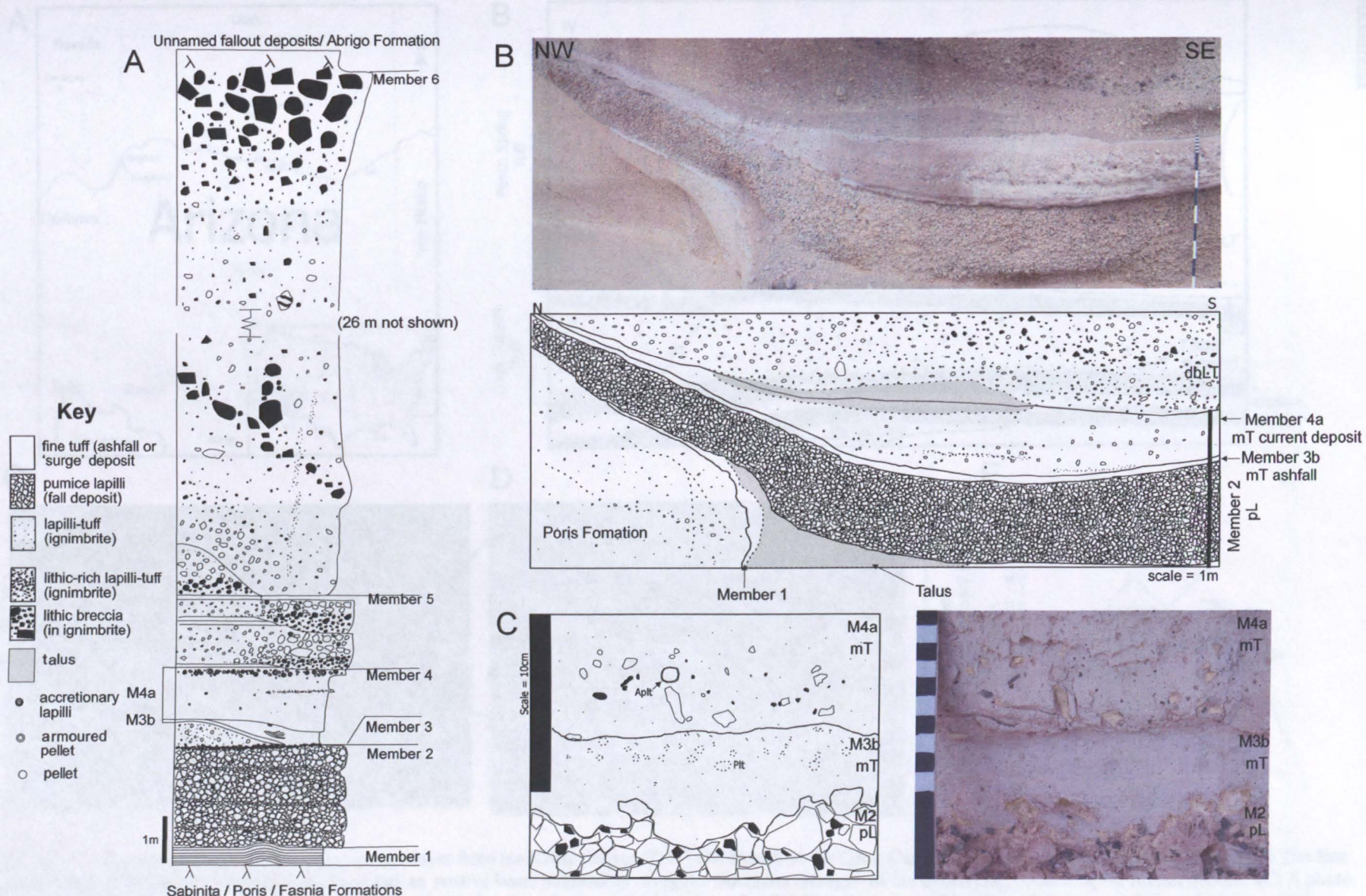


Figure 3.7: (A) A GVS through the La Caleta Formation showing the stratigraphic position of Member 3b (M3b; ashfall) and Member 4a (M4a; current deposit), which were sampled. (B) A photograph and sketch of the palaeotopographic relationships of members 3b and 4a within the palaeovalley. Member 3b drapes topography, and is a constant thickness, whereas Member 4a thickens into the palaeovalley. Near Tajao GR: 0355908 3110300. Palaeocurrent direction ~ towards the reader: (C) Sketch and photo of members 3b and 4a as fine ash layers. Member 3a infills the spaces between the pumice lapilli of Member 2 and contains pellets (Plt). Member 4a contains accretionary lapilli (Acc Lap) and armoured pellets (Aplt).

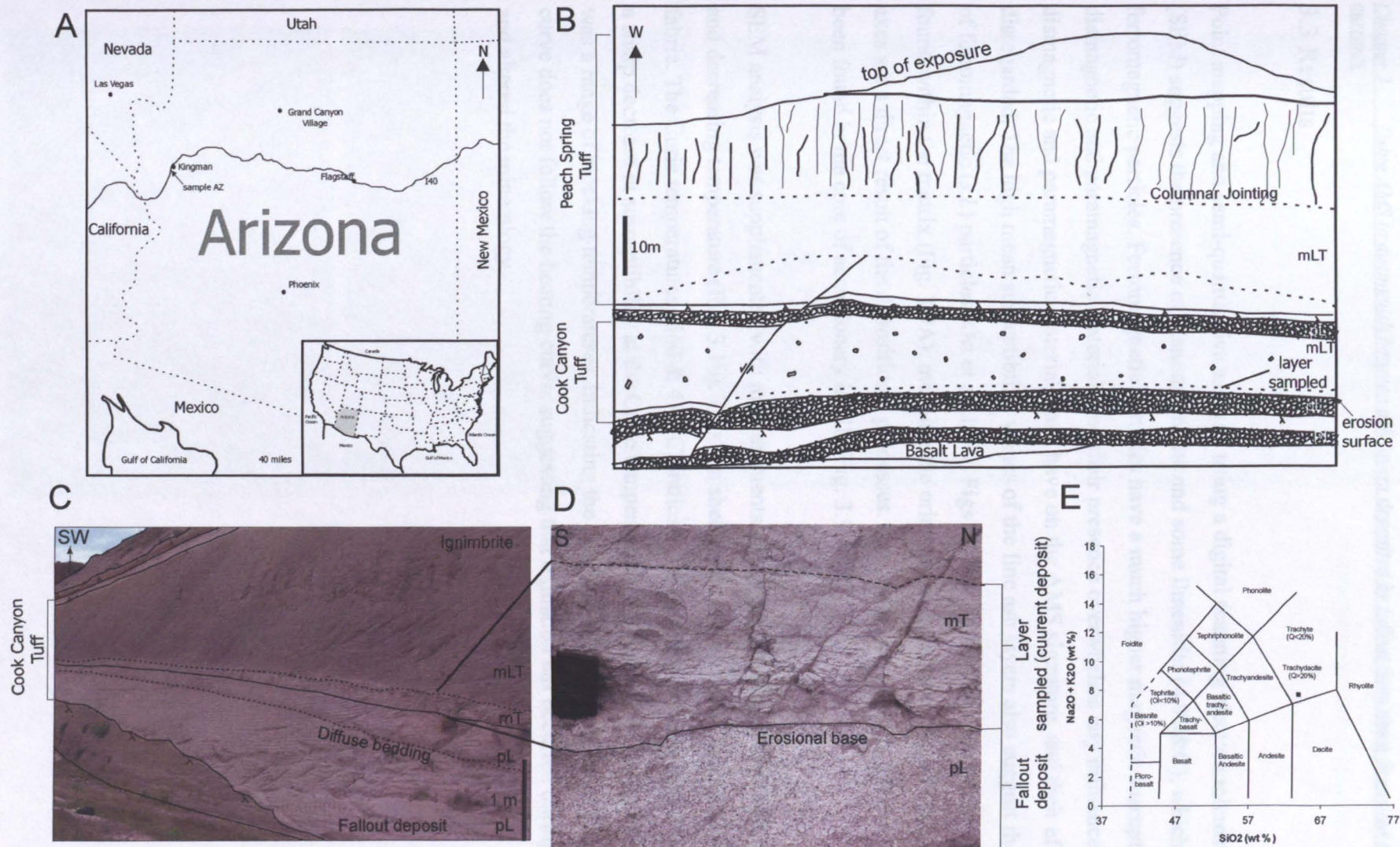
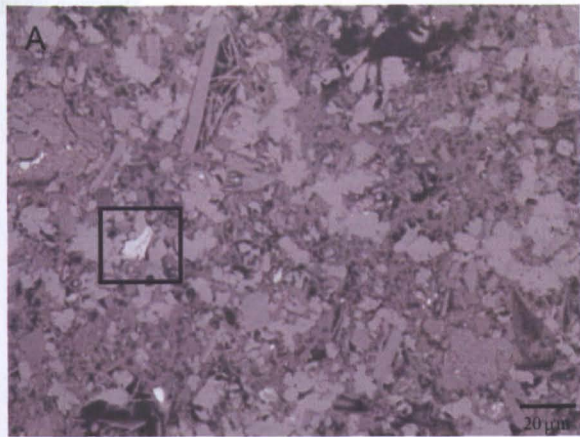


Figure 3.8: (A) Sample location (AZ) for the fine ash layer from the Cook Canyon Tuff : (B) Sketch of the Cook Canyon Tuff and overlying Peach Springs Tuff. The fine ash layer sampled is indicated. The fine ash layer had an erosive base, indicted by irregular thickness changes of the underlying pumice lapilli fallout deposit: (C) A photo of the Cook Canyon Tuff taken from an oblique angle, illustrating how the layer pinch and swells: (D) Close-up photo of the fine ash layer sampled, underlying pumice lapilli fallout deposit. Palaeocurrent direction unknown: (E) TAS diagram with the Cook Canyon Tuff plotting in the trachydacite field.

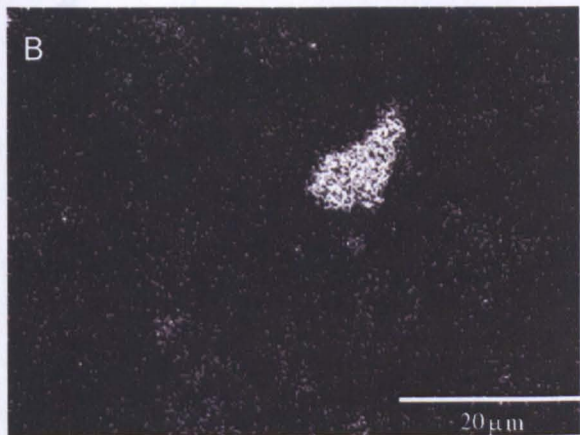
3.3 Results

Point mapping and semi-quantitative analysis using a digital scanning electron microscope (SEM) suggests the presence of titanomagnetite and some ilmenitite (4.9B&C), which are ferromagnetic particles. Ferromagnetic particles have a much higher magnetic susceptibility than diamagnetic and paramagnetic materials and their presence overwhelms any influence that diamagnetic and paramagnetic materials may have on the AMS signature, and their effect can be disregarded. The high mean susceptibility values of the fine ash layers also suggest the presence of ferromagnetic (*s.l.*) particles (Ort et al. 1999; Figs 3.12 & 3.14), which are predominantly found within the matrix (Fig. 3.9A), meaning the orientation and distribution of the susceptibility axes are a direct result of the depositional processes. Ferromagnetic particles have occasionally been found in the core of accretionary lapilli (Fig. 3.9D).

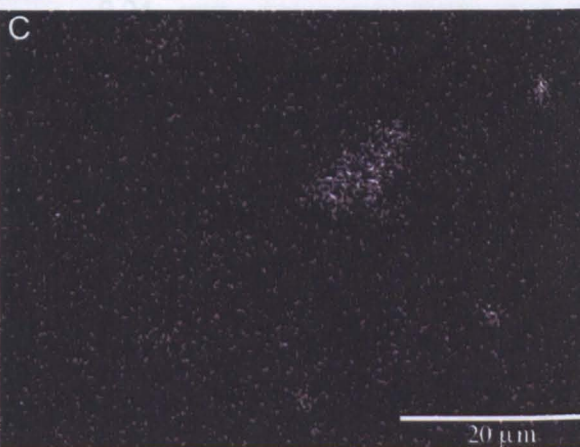
SEM analysis was supplemented with measurements of magnetic susceptibility with increasing and decreasing temperature (Fig. 3.10). This can shed light on the mineral species that carry the fabric. The Curie temperatures (540 & 474°C) indicate the presence of magnetite, but the lack of a sharp decrease in susceptibility at the Curie temperature (e.g. Butler, 1992), suggests that there was a range of blocking temperatures, indicating the presence of titanomagnetite. The cooling curve does not follow the heating curve, suggesting that oxidation has occurred during heating and altered the mineralogy.



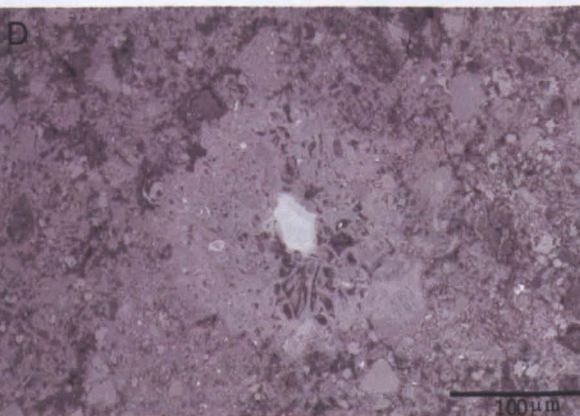
(A) SEM image showing the presence of an oxide within the matrix as highlighted by the box.



(B) Point element map of the highlighted oxide, revealing concentrations of Fe as indicated by the white dots.



(C) Point element map of the highlighted oxide, revealing concentrations of Ti as indicated by the white dots.



(D) A pellet with an iron oxide core.

Figure 3.9: SEM images of the magnetic particles within the fine ash layers sampled (A) Fe and Ti element point maps suggesting the presence of titanomagnetites (B&C) and a pellet with an Fe oxide core.

3.3.1 AMS characteristics of ash fall deposits

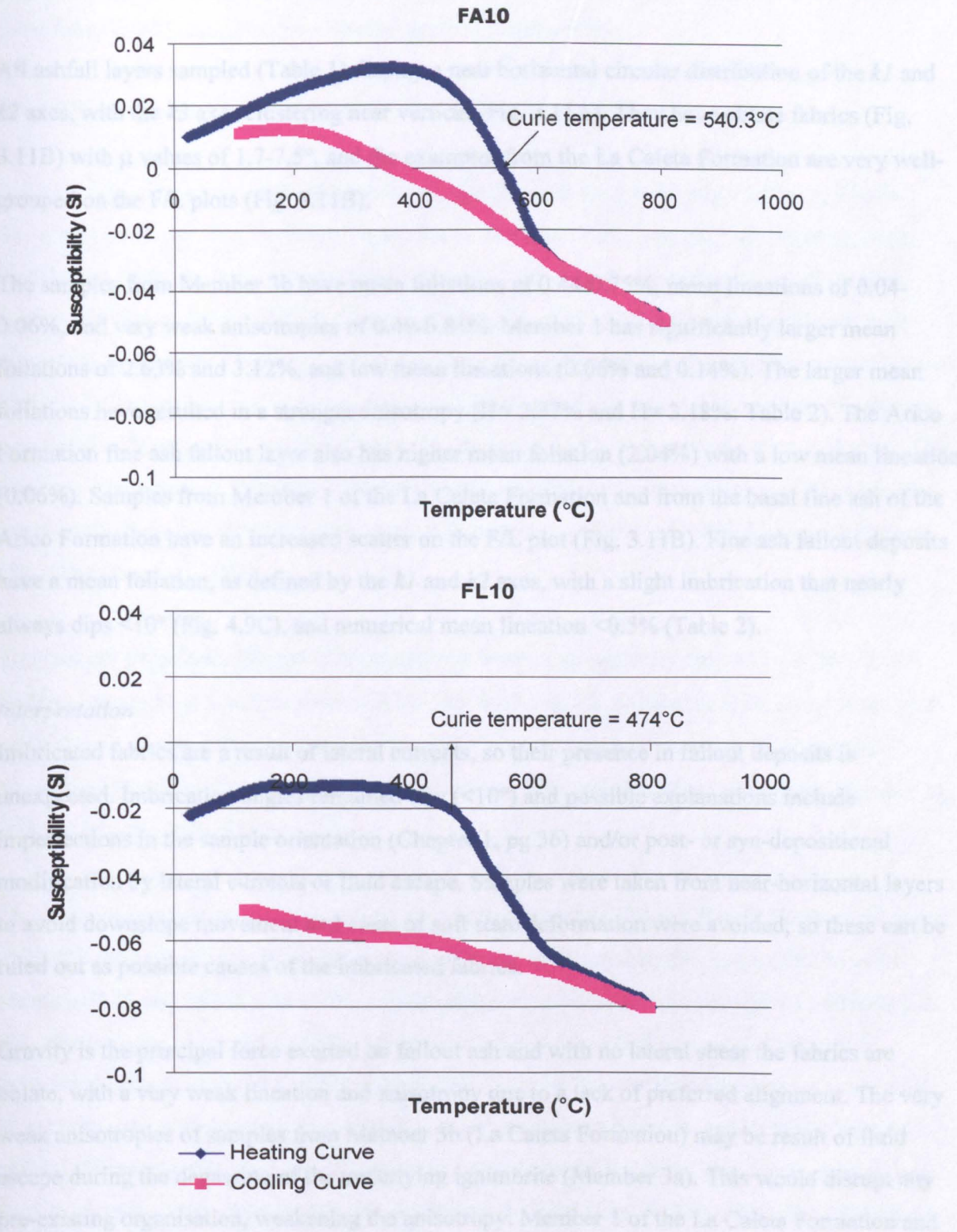


Figure 3.10: Measurements of susceptibility with increasing and decreasing temperature for (A) fine ash fallout deposit and (B) a fine ash current deposit from location 10. The Curie temperature can provide an insight into what the magnetic components are. The Curie temperature of magnetite is 575-585°C.

3.3.1 AMS characteristics of ashfall deposits

All ashfall layers sampled (Table 1) display a near horizontal circular distribution of the $k1$ and $k2$ axes, with the $k3$ axes clustering near vertical (Fig. 3.11A). They have oblate fabrics (Fig. 3.11B) with μ values of 1.7-7.5°, and the examples from the La Caleta Formation are very well-grouped on the F/L plots (Fig. 3.11B).

The samples from Member 3b have mean foliations of 0.44-0.75%, mean lineations of 0.04-0.06%, and very weak anisotropies of 0.49-0.81%. Member 1 has significantly larger mean foliations of 2.63% and 3.12%, and low mean lineations (0.06% and 0.14%). The larger mean foliations have resulted in a stronger anisotropy ($H=2.77\%$ and $H=3.18\%$: Table 2). The Arico Formation fine ash fallout layer also has higher mean foliation (2.04%) with a low mean lineation (0.06%). Samples from Member 1 of the La Caleta Formation and from the basal fine ash of the Arico Formation have an increased scatter on the F/L plot (Fig. 3.11B). Fine ash fallout deposits have a mean foliation, as defined by the $k1$ and $k2$ axes, with a slight imbrication that nearly always dips $<10^\circ$ (Fig. 4.9C), and numerical mean lineation $<0.5\%$ (Table 2).

Interpretation

Imbricated fabrics are a result of lateral currents, so their presence in fallout deposits is unexpected. Imbrication angles remained low ($<10^\circ$) and possible explanations include imperfections in the sample orientation (Chapter 1, pg 36) and/or post- or syn-depositional modification by lateral currents or fluid escape. Samples were taken from near-horizontal layers to avoid downslope movement and areas of soft state deformation were avoided, so these can be ruled out as possible causes of the imbricated fabrics.

Gravity is the principal force exerted on fallout ash and with no lateral shear the fabrics are oblate, with a very weak lineation and anisotropy due to a lack of preferred alignment. The very weak anisotropies of samples from Member 3b (La Caleta Formation) may be result of fluid escape during the degassing of the underlying ignimbrite (Member 3a). This would disrupt any pre-existing organisation, weakening the anisotropy. Member 1 of the La Caleta Formation and the basal ash of the Arico Formation were not deposited on to a hot degassing deposit and this

may account for their stronger anisotropies. The laminated nature of Member 1 (FA9cLam and FA10Lam) would also have the effect of increasing anisotropy.

3.3.2 AMS results of fine ash pyroclastic density current deposits

Samples from fine ash pyroclastic density current deposits have been taken from the Fasnía, Poris, and La Caleta formations on Tenerife and from the Cook Canyon Tuff, Arizona. The distribution of the susceptibility axes predominantly produce girdle distributions of varying quality, defined by the k_1 and k_2 axes (e.g. FAS1; Fig. 3.13A). The k_1 and k_2 axes can form discrete groups on the girdle (e.g. FL10; Fig. 3.13A), well grouped susceptibility axes (AZ, Cook Canyon Tuff), random distributions of susceptibility axes (FL8; Fig. 3.13A) and poorly defined circular distribution of susceptibility axes (FL9b; Fig. 3.13A). The palaeocurrent as indicated by the dip of the magnetic foliation, does not always coincide with the orientation of k_1 , which has traditionally been used to infer palaeocurrent direction (e.g. Ort et al. 1993; Cagnoli & Tarling, 1997; Porreca et al., 2003)

The fine ash pyroclastic density current deposits have predominantly oblate to triaxial fabrics, with one example of a prolate fabric (FL9c; Fig. 3.13A & B), and the μ values range from 10.8-49.6° (Fig. 3.13A and B). Member 4a of the La Caleta Formation has mean foliations and lineations of 0.35-1.27% and 0.2-0.82% respectively. The strength of anisotropy for Member 4a is variable, from 0.55-2.63%.

The samples taken from the Fasnía Formation near Mt Magua (FAS & FAS2), have much larger mean foliations (3.78 & 3.68%), although their mean lineations remain comparable to other samples (0.85 and 0.91%). As a result of the higher mean foliation the strength of anisotropy is also much higher (4.63 and 4.59%). Sample FAS18 also has a higher mean foliation and anisotropy compared to the La Caleta Formation samples, but less than the samples taken from near Mt Magua. The Cook Canyon Tuff has the highest mean foliation and lineation values (5.9 and 1.13% respectively) and the anisotropy is also very high at 7.03%. The degree of scatter on the F/L plots is greater than for the fine ash fallout deposits (Fig. 3.13B) and all the samples have a numerical mean lineation greater than 0.5% (Table 2). They also have variable imbrication

angles of the mean $k1/k2$ foliations, but they are nearly always dipping at $>10^\circ$ (Table 2 & Fig. 3.13C).

Interpretation

Pyroclastic density current deposits are emplaced under highly variable conditions and the orientation and type of AMS fabric will depend on flow-boundary conditions. Because of this natural variability an increase in the scatter on F/L plots is to be expected. The increase in lateral shear at a flow-boundary would account for the increase in the lineation, anisotropy and the imbrication of the $k1/k2$ foliation. The variation in imbrication angle reflects differing flow-boundary conditions (i.e. greater shear would result in lower angles of imbrication). The distribution of the susceptibility axes will also reflect subtle differences in flow-boundary conditions. Girdle distributions have previously been associated with turbulent conditions in dispersions of low concentrations (e.g. Cagnoli & Tarling, 1997; Ort et al. 2002) and would suggest a flow-boundary involving tractional processes. The character of these girdle distributions would perhaps indicate the degree of influence by flow-boundary conditions. Girdle distributions that have an element of grouping of the $k1$ and $k2$ susceptibility axes would indicate an increase in granular shear, suggesting higher concentrations at the flow-boundary, and a thin granular-fluid base. Well-grouped susceptibility axes (e.g. AZ; Fig. 3.13A) would suggest a granular-flow dominated flow-boundary because of the increased granular shear that can be inferred from the lineated fabric. Using the distribution of susceptibility axes to infer flow-boundary conditions will be discussed in more detail in Chapter 4. The position of the $k1$ axis in relation to the dip of the magnetic foliation can be interpreted in terms of flow-boundary condition and will be discussed further in section four of this chapter.

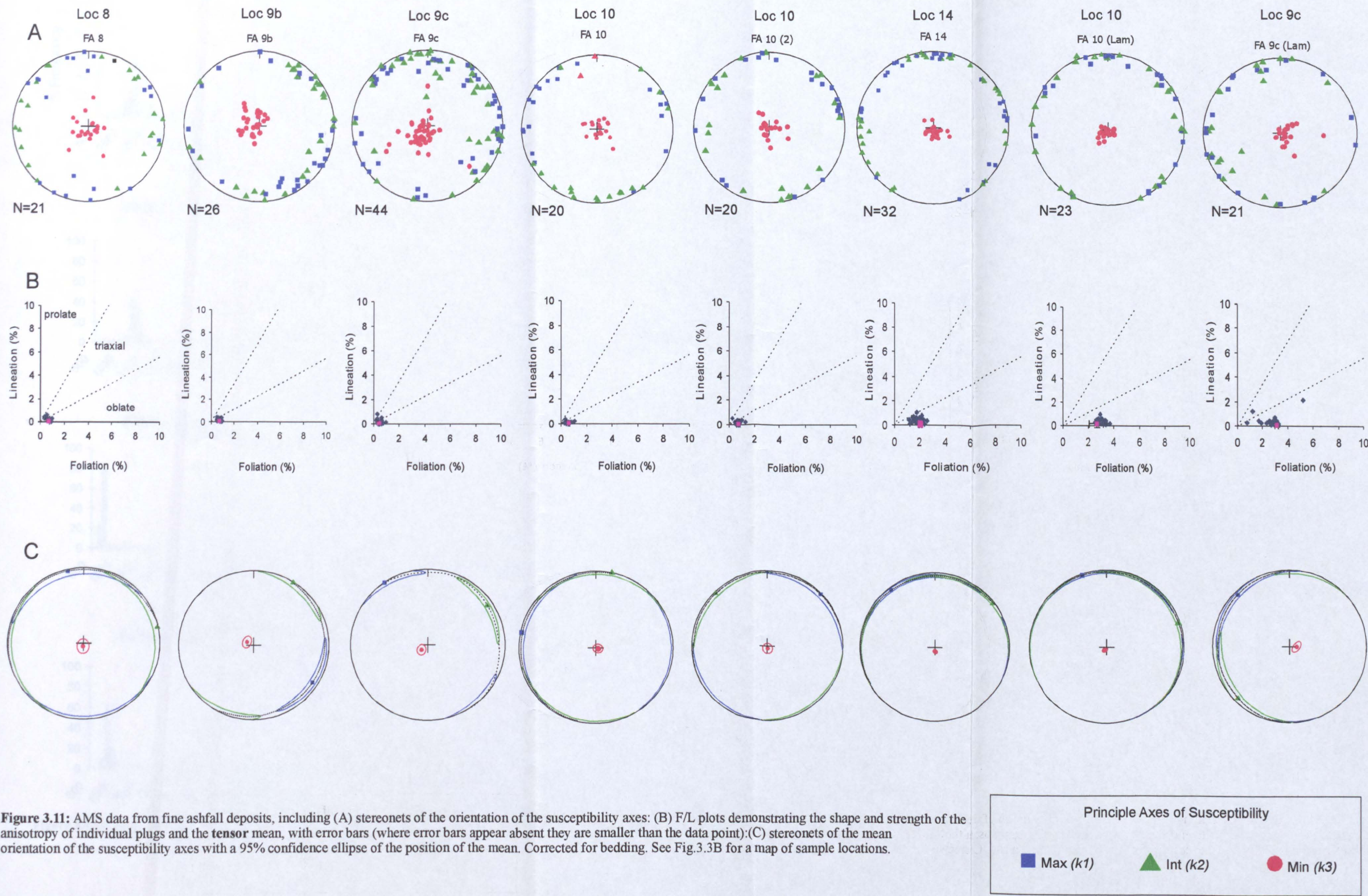


Figure 3.11: AMS data from fine ashfall deposits, including (A) stereonet of the orientation of the susceptibility axes: (B) F/L plots demonstrating the shape and strength of the anisotropy of individual plugs and the **tensor** mean, with error bars (where error bars appear absent they are smaller than the data point): (C) stereonet of the mean orientation of the susceptibility axes with a 95% confidence ellipse of the position of the mean. Corrected for bedding. See Fig.3.3B for a map of sample locations.

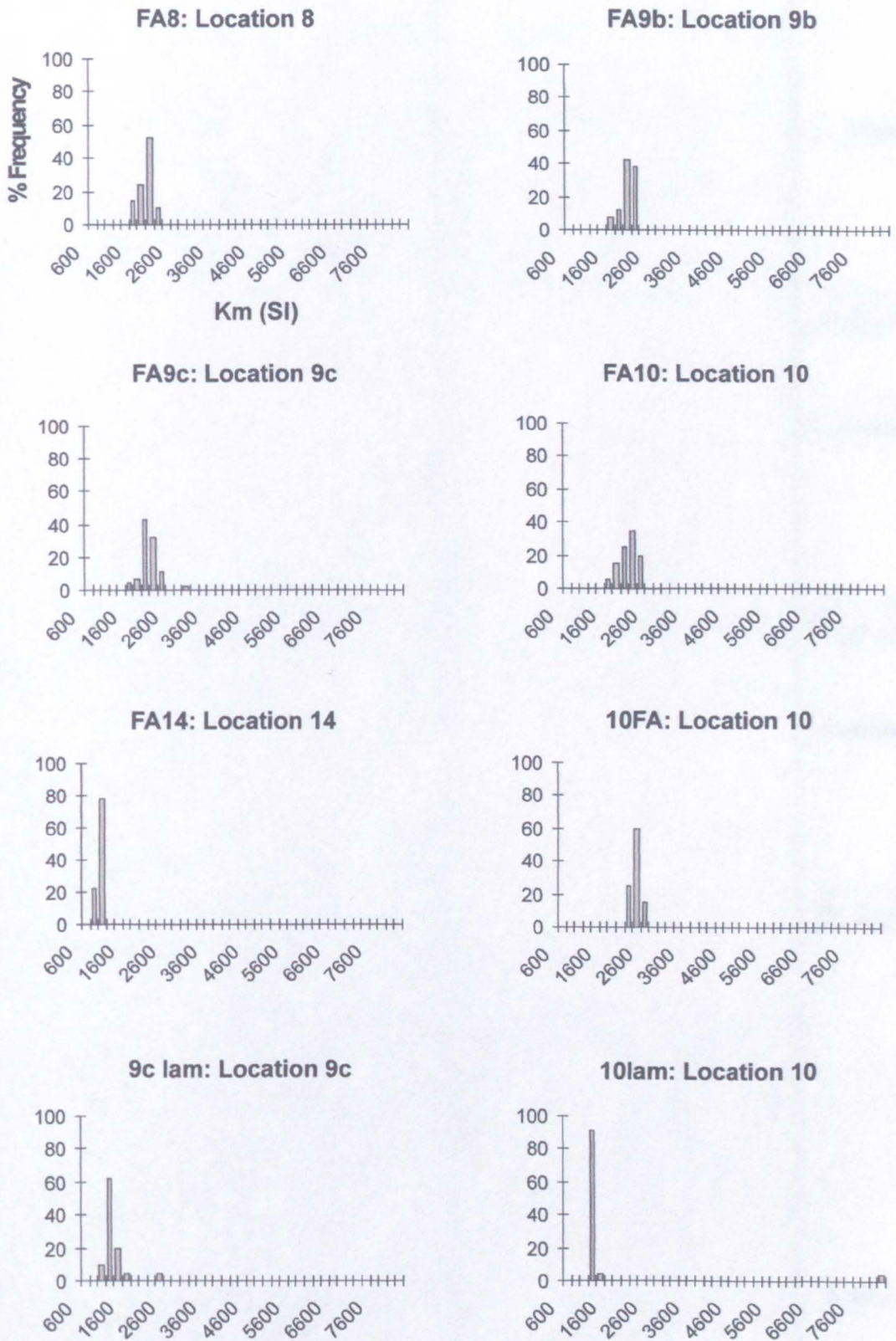


Figure 3.12: Histograms of the mean magnetic susceptibility (Km) of the fine ashfall deposits sampled.

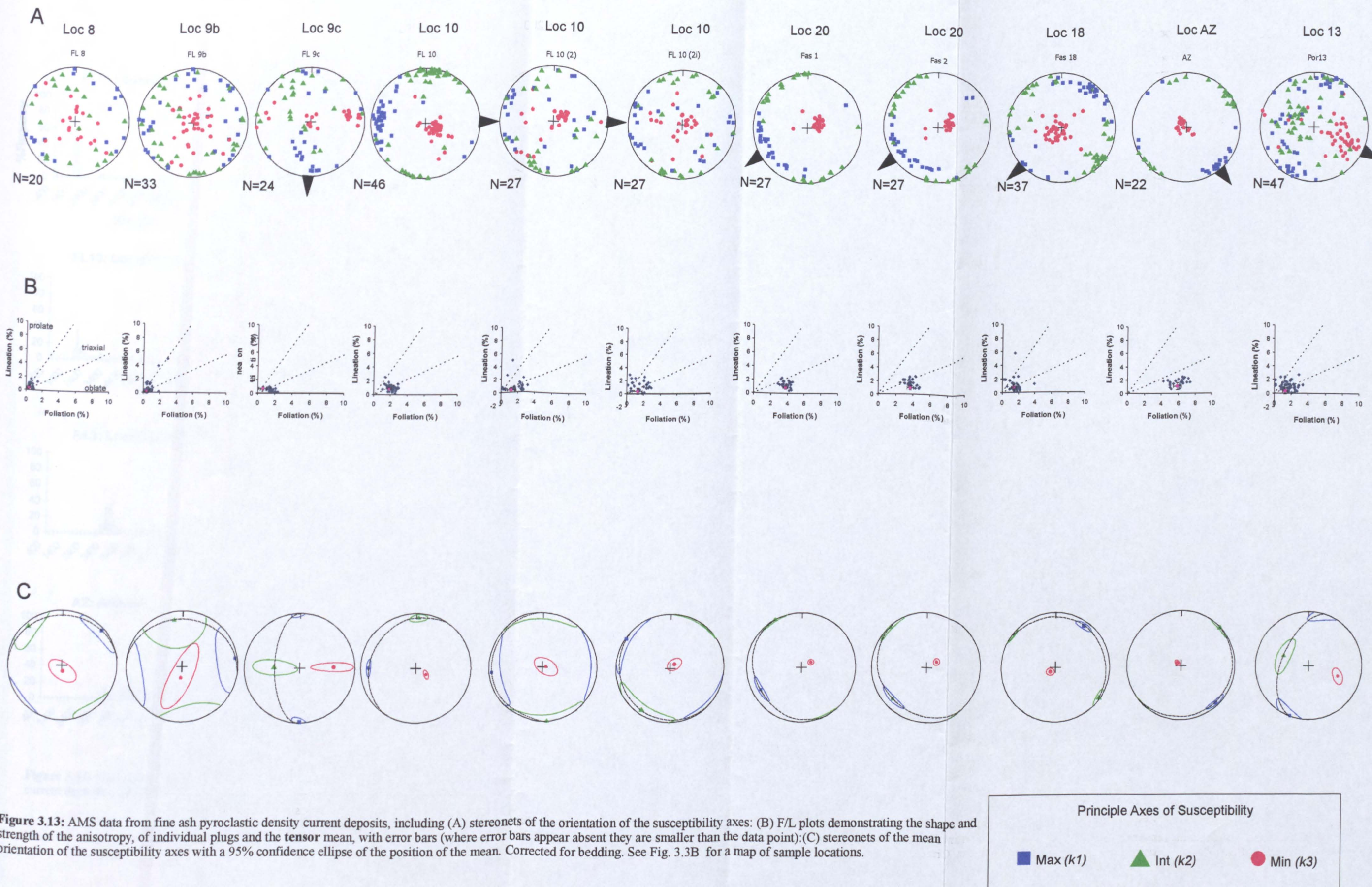


Figure 3.13: AMS data from fine ash pyroclastic density current deposits, including (A) stereonets of the orientation of the susceptibility axes: (B) F/L plots demonstrating the shape and strength of the anisotropy, of individual plugs and the **tensor** mean, with error bars (where error bars appear absent they are smaller than the data point): (C) stereonets of the mean orientation of the susceptibility axes with a 95% confidence ellipse of the position of the mean. Corrected for bedding. See Fig. 3.3B for a map of sample locations.

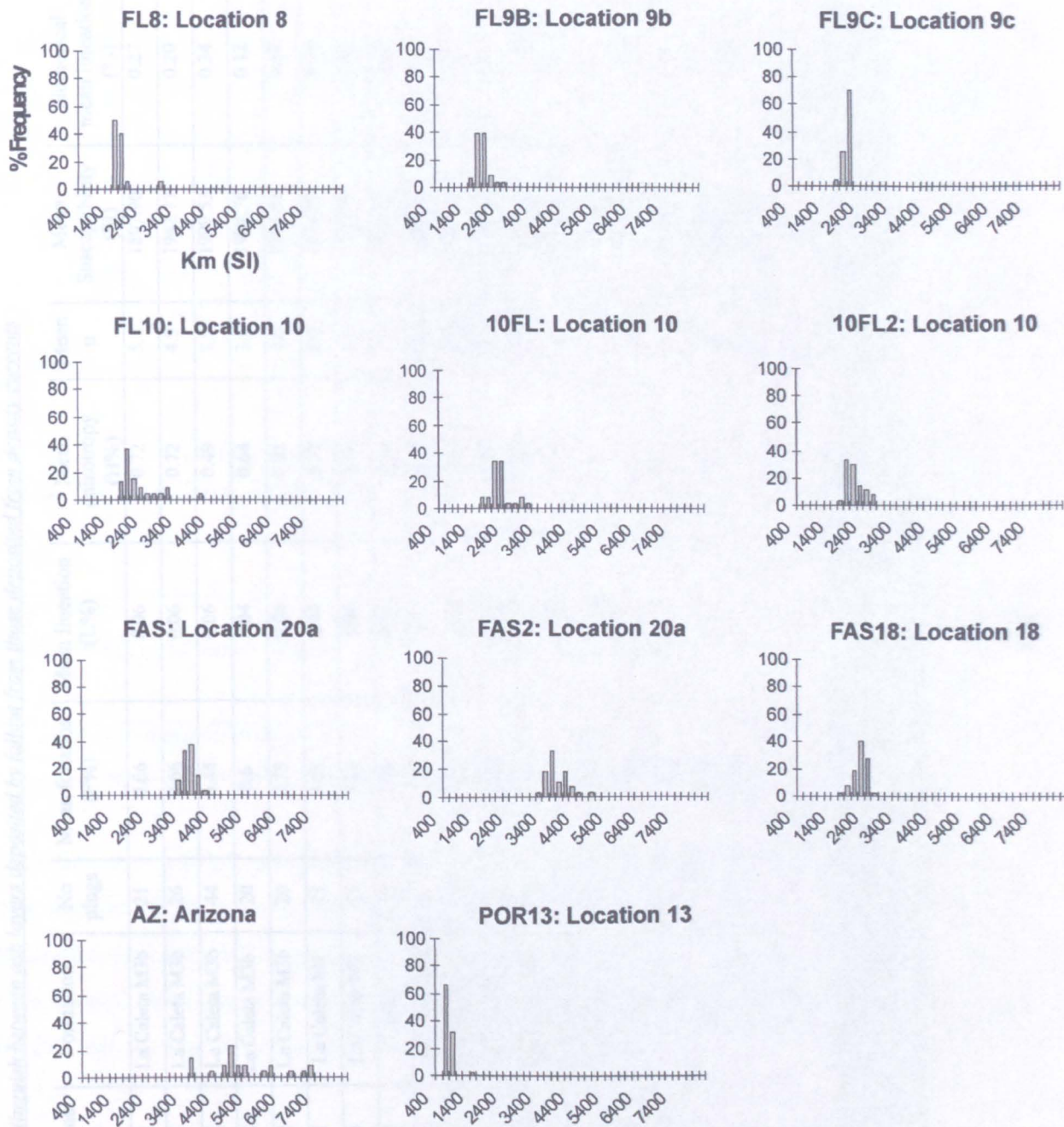


Figure 3.14: Histograms of the mean magnetic susceptibility (Km) of the fine ash pyroclastic density current deposits sampled.

Sample number	Depositional Origin	Formation	No plugs	Mean foliation (F%)	Mean lineation (L%)	Mean anisotropy (H%)	Mean μ	Mean Susceptibility (SI)	Numerical mean lineation (%)	Mean $k1/k2$ inclination
FA8	Ashfall	La Caleta M3b	21	0.66	0.06	0.72	5.1	1807.90	0.27	3.2
FA9b	Ashfall	La Caleta M3b	26	0.66	0.06	0.72	4.9	1942.77	0.20	7.5
FA9c	Ashfall	La Caleta M3b	44	0.44	0.06	0.49	7.5	1999.53	0.34	8.3
FA10	Ashfall	La Caleta M3b	20	0.6	0.04	0.64	3.5	1998.76	0.12	2.3
FA10 (2)	Ashfall	La Caleta M3b	20	0.75	0.06	0.81	4.6	2266.55	0.18	3
FA9c Lam	Ashfall	La Caleta M1	23	2.63	0.14	2.77	3.0	1176.20	0.35	3.4
FA10 Lam	Ashfall	La Caleta M1	21	3.12	0.06	3.18	1.0	1133.73	0.43	7.4
FA14	Ashfall	Arico	32	2.04	0.06	2.10	1.7	836.97	0.35	4.4
FL8	Current	La Caleta M4a	20	0.37	0.32	0.68	40.8	1480.40	0.6	8.9
FL9b	Current	La Caleta M4a	33	0.35	0.20	0.55	30.2	1650.24	0.7	16.6
FL9c	Current	La Caleta M4a	24	0.59	0.69	1.28	49.6	1828.28	0.51	51.8
FL10	Current	La Caleta M4a	46	1.81	0.82	2.63	24.3	2029.35	1.05	18
FL10 (2)	Current	La Caleta M4a	46	1.26	0.3	1.50	14.0	2048.46	0.98	5.1
FL10 (2i)	Current	La Caleta 4a	27	1.27	0.31	1.59	13.8	1936.05	1.25	8.9
FAS	Current	Fasnia	27	3.78	0.85	4.63	12.6	3446.01	1.35	16.3
FAS2	Current	Fasnia	27	3.68	0.91	4.59	14.0	3659.96	1.62	17.4
FAS18D	current	Fasnia	37	1.44	0.78	2.22	28.4	2082.86	1.73	6.6
AZ	Current	Cook Canyon Tuff	22	5.90	1.13	7.03	10.8	5098.65	1.10	9.8
POR13	Current	Poris M2a	47	1.33	0.35	1.67	14.7	594.83	1.07	48.7

Table 2: A table with all the ash layers that were sampled, their geographical and stratigraphical location (M= Member) and the mean AMS data for all the ash layers sampled, including the mean foliation, mean lineation, mean anisotropy, mean μ values and mean susceptibilities of the fine ash layer samples the numerical mean lineation and the mean $k1/k2$ inclination of fine ash fallout deposits and fine ash pyroclastic density current deposits. The numerical mean lineation and the mean $k1/k2$ inclination have been used to construct the new discriminant plot (Fig. 3.15).

3.4 Discussion

The key differences between fine ash fallout deposits and fine ash current deposits are summarised in Table 3. Despite these differences, fine ash current deposits can still have similar AMS characteristics to fine ash fallout deposits, particularly if they were deposited from a direct fallout flow-boundary. For example, at location 10 (2) stereonet from Member 3b (FA 10 (2)) and Member 4a (FL10(2)) of the La Caleta Formation both exhibit circular distributions (Fig. 3.13). Equally, the F/L plots show substantial overlap of data from ashfall and pyroclastic density current deposits (Fig. 3.15), making the distinction between the two depositional origins more difficult.

Fine ash fallout deposits	Fine ash current deposits
Circular distribution of susceptibility axes	Variety of distributions of susceptibility axes. Including girdle distributions, well grouped distributions and random distributions. Circular distributions can occur
Oblate fabrics	Oblate to prolate fabrics
Imbrication of k1/k2 foliation <10°	Imbrication of k1/k2 foliation is predominantly >10°
Numerical mean lineation <0.5%	Numerical mean lineation >0.5%

Table 3: A summary of the key differences between fine ash fallout deposits and fine ash current deposits.

This distinction can be made easier by plotting the numerical mean lineation (<0.5% in ashfall deposits and >0.5% in current deposits; Table 2) against the inclination of the mean *k1/k2* foliation (generally <10° in ashfall and >10° in current deposits; Table 2). These observations have been plotted against one another producing two groups; one for fine ashfall deposits and one for fine ash pyroclastic density current deposits (Fig. 3.16).

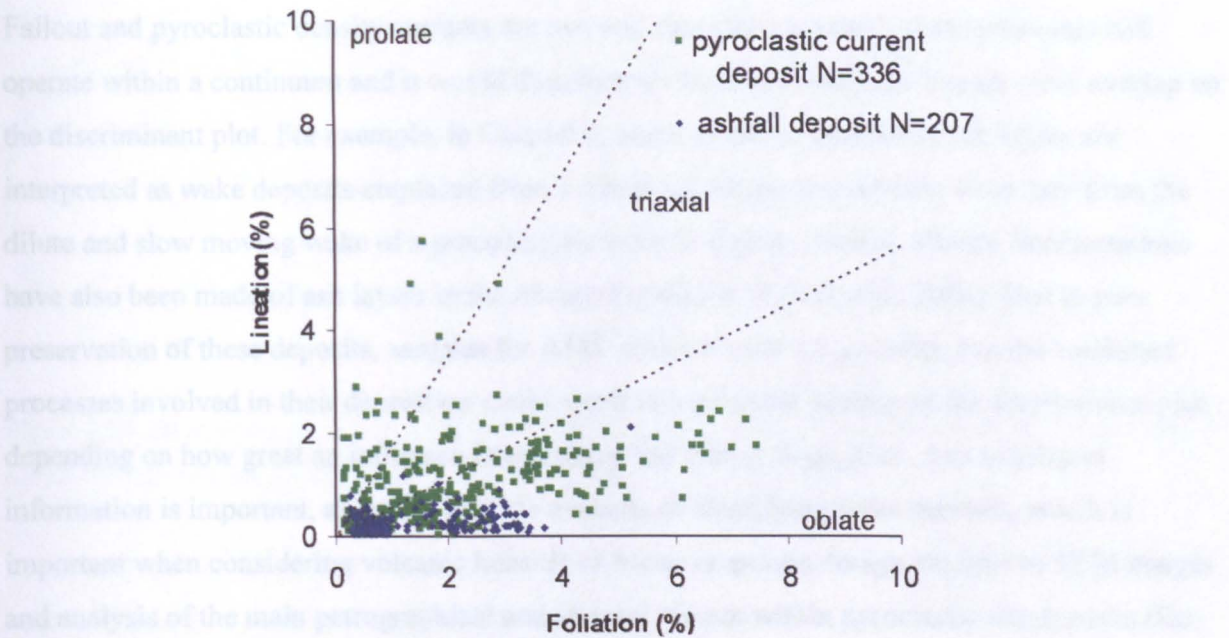


Figure 3.15: A foliation-lineation plot displaying an overlap of data from fine ashfall deposits and fine ash pyroclastic density current deposits from a variety of different localities.

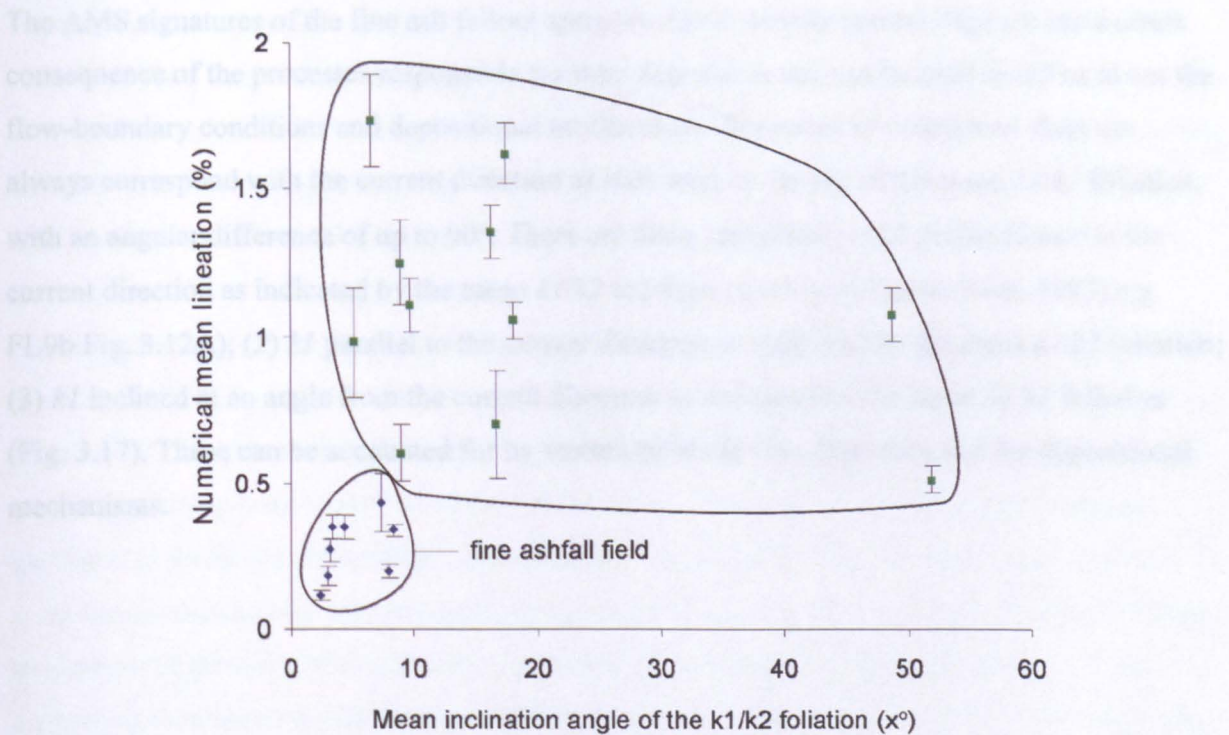


Figure 3.16: New discriminant plot separating fine ash fallout deposits from fine ash pyroclastic density current deposits, using the numerical mean lineation and the mean inclination angle of the k1/k2 foliation of each sample (Table 2). The error bars represent the standard error of the numerical mean lineation. Each data point represents a minimum of 20 plugs (Table 2).

Fallout and pyroclastic density currents are two end members. In reality these processes will operate within a continuum and it would therefore not be unreasonable to expect some overlap on the discriminant plot. For example, in Chapter 2, some of the co-ignimbrite ash layers are interpreted as wake deposits emplaced from a direct fallout-dominated flow-boundary from the dilute and slow moving wake of a preceding pyroclastic density current. Similar interpretations have also been made of ash layers in the Abrigo Formation (Pitarri et al. 2006). Due to poor preservation of these deposits, samples for AMS analysis were not possible, but the combined processes involved in their deposition could result in a potential overlap on the discriminant plot, depending on how great an influence lateral shear had during deposition. Any overlap of information is important, as it may provide a means of identifying wake deposits, which is important when considering volcanic hazards of future eruptions. Image analysis of SEM images and analysis of the main petrographical and textural classes within pyroclastic ash deposits (De Rosa, 1999) may further constrain the depositional origin.

The AMS signatures of the fine ash fallout and pyroclastic density current deposits are a direct consequence of the processes responsible for their deposition and can be used to tell us about the flow-boundary conditions and depositional mechanisms. The mean $k1$ orientation does not always correspond with the current direction as indicated by the dip of the mean $k1/k2$ foliation, with an angular difference of up to 90° . There are three variations (1) $k1$ perpendicular to the current direction as indicated by the mean $k1/k2$ foliation (transverse fabric; Rees, 1983) e.g. FL9b Fig. 3.12A); (2) $k1$ parallel to the current direction as indicated by the mean $k1/k2$ foliation; (3) $k1$ inclined at an angle from the current direction as indicated by the mean $k1/k2$ foliation (Fig. 3.17). These can be accounted for by variations at the flow boundary and the depositional mechanisms.

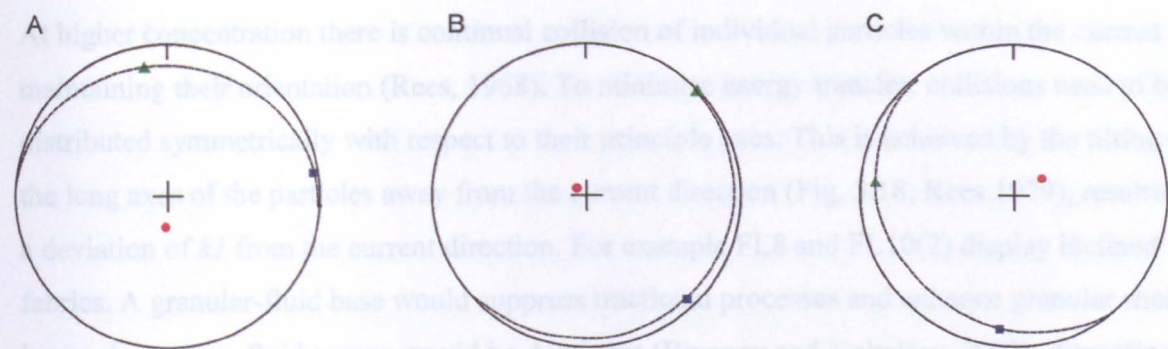


Figure 3.17: Three different types of distribution of the mean susceptibility axes in relation to their position on the $k1/k2$ foliation: (A) Transverse fabric: (B) Flow-parallel fabric: (C) Inclined fabric

Transverse fabrics have the $k1$ axes perpendicular to the current direction and have previously been interpreted to represent tractional processes (e.g. Hand, 1961; Ort 1993). Particles orientate themselves with their long axes aligned normal to the current direction, via particle interaction, to minimise energy dissipation. Transverse fabrics have been reported in the Upper Laacher See Tephra, Germany (Hughes & Druitt, 1998), the Cerro Panizos ignimbrite in the central Andes (Ort, 1998) and Rees (1983) produced them during experimental work. Transverse fabrics suggest more dilute flow-boundary conditions with lower levels of particle interaction, promoting turbulent conditions, producing a traction-influenced flow-boundary. These types of fabric were seen in the samples that exhibited girdle distributions.

Flume experiments found that relatively low concentration currents, with grains suspended in a shearing fluid, will orientate themselves into the most energetically favourable and stable position with the $k1$ axis parallel to the current direction (Rees, 1979). The flow-boundary zone of a fully dilute current would be influenced by either direct-fallout, at lower shear rates, or tractional processes at higher shear rates (Branney and Kokelaar 2002). These types of fabric were seen in the samples that produced well-grouped distributions or girdle distributions that had an element of grouping of the $k1$ and $k2$ axes (e.g. Fas1, Fas2, FAS18 and FL10; Fig 3.13A), suggesting that there may have been an element of granular shear as a result of the development of a small granular-fluid base at the bottom of the pyroclastic density current. This is discussed further in Chapter 4.

At higher concentration there is continual collision of individual particles within the current maintaining their orientation (Rees, 1968). To minimise energy transfer, collisions need to be distributed symmetrically with respect to their principle axes. This is achieved by the tilting of the long axes of the particles away from the current direction (Fig. 3.18; Rees 1979), resulting in a deviation of kI from the current direction. For example FL8 and FL10(2) display inclined fabrics. A granular-fluid base would suppress tractional processes and enhance granular shear. At lower shear rates, fluid escape would be dominant (Branney and Kokelaar, 2002), disrupting any fabrics, resulting in a greater degree of scatter of the susceptibility axes (e.g. samples FL8, FL10(2) and FL10(2i) Fig.3.13A)

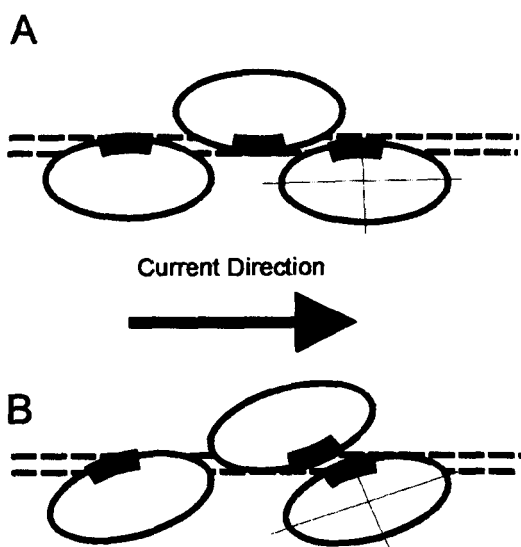


Figure 3.18: Two-dimensional representation of collisions between particles (plan view). The symmetrical distribution of collisions, with respect to the principle axes, can only occur if the particles are inclined away from the current direction (see b). Modified from Rees (1968, 1979)

3.5 Summary and conclusions

Although AMS has been used to investigate depositional mechanism, it has never been used to distinguish between fine ash layers emplaced by fallout and pyroclastic density currents. AMS provides a relatively quick and cost-effective means of investigating fine-scale, three-dimensional fabrics, and can be used on lithified deposits that cannot be subject to granulometric studies.

The ashfall deposits all have oblate fabrics with circular distributions, with a numerical mean lineation of $<0.5^\circ$ and a mean $k1/k2$ foliation dipping $<10^\circ$. Some variability between different fallout deposits exists with regards to the strength of the fabric and the degree of scatter; possibly due to varying amounts of fluid escape through the deposit. The unexpected imbrication of the AMS fabric ($<10^\circ$), may be due to slight imperfections in the sample orientation, to fluid escape, to the presence of air currents during deposition, or post-deposition modification.

The variability of the AMS fabric of fine ash current deposits is a reflection of natural current variability. The fabrics are less oblate than ashfall deposits and border on being triaxial and prolate, this, along with the higher mean imbrication angles of the AMS fabric and the higher numerical mean lineations, reflects the lateral shear found in a pyroclastic density current. The different types of distribution of the susceptibility axes (girdle distributions, girdle distributions with an element of grouping of the $k1$ and $k2$ axes and well grouped distributions) can be used to infer relative flow-boundary conditions (concentration, shear rate, and rate of deposition).

The distinction between ashfall and fine ash pyroclastic density current deposits using the traditional AMS plots can be equivocal, so a new discriminant plot using the numerical mean lineation and the imbrication angle of the mean $k1/k2$ foliation has been constructed, with the ashfall and pyroclastic density current deposits plotting in separate fields.

Like all natural processes there will be intermediate processes between pure fallout and pyroclastic density currents. For example, many of the co-ignimbrite fallout layers in the La Caleta Formation have been interpreted as wake deposits, produced by ashfall interacting with and being influenced by the wake of the preceding pyroclastic current (Chapter 2). It would therefore not be unreasonable to expect to find some overlap in the data. This overlap may provide a means of identifying wake deposits, which is important when considering the volcanic hazards of future eruptions. If overlap was found to exist, AMS studies could be run alongside image analysis studies of SEM images and analysis of the main petrographic and textural components of the fine ash layers to help differentiate the dominant process.

Volcanic fallout and pyroclastic density currents are both highly hazardous, but the latter present a far greater threat to human populations. Since both of these mechanisms can emplace fine ash

layers, the ability to distinguish between fine ash fallout and fine ash pyroclastic density current deposits is vital. The methodology outlined in this study can be used to distinguish between these two types of deposit and therefore enable more accurate hazard assessments minimising the threat to human populations.

Chapter 4: Fabric-characterisation of ignimbrite lithofacies: constraints on depositional mechanisms

Abstract: The opaque and highly hazardous nature of pyroclastic density currents makes observing their depositional mechanisms impossible and the deposits are the only means of interpreting them. The interpretation of lithofacies containing sedimentary structures is relatively straightforward, but massive lithofacies are more problematic. A variety of lithofacies (cross-stratified, stratified, diffusely-bedded and massive) have been sampled from ignimbrites and ash layers from the Bandas del Sur Group on Tenerife, Canary Islands, with the intention of studying their fabric using Anisotropy of Magnetic Susceptibility (AMS), and interpreting them in terms of flow-boundary conditions and depositional processes. The lithofacies have been subdivided into sub-categories on the basis of variations in the distribution of the magnetic susceptibility axes on the stereonet. Girdle-distributions are interpreted to infer traction-dominated flow-boundaries in cross-stratified and stratified lithofacies and where there is an element of grouping/ clustering on the girdle, granular shear is interpreted to have influenced the flow-boundary. Diffusely bedded lithofacies are interpreted to be a result of granular flow-dominated flow-boundaries and can be subdivided into those that are influenced by traction, with the periodic sweeping away of the granular-fluid base (girdle distribution with grouping) and those that are formed by periodic shear exerted on the top of the granular-fluid base by the overriding turbulent eddies in the more dilute part of the current (well grouped distributions). Three types of massive lapilli tuffs have been identified; those with random distributions, which are interpreted to represent end-member fluid escape dominated flow-boundaries; those with well grouped distributions, which are interpreted to represent granular flow-influenced, fluid escape flow-boundaries or deposition from a steady current with a granular flow-dominated flow-boundary. Finally there are those with girdle distributions, which are interpreted to represent traction-influenced fluid escape dominated flow-boundaries. Massive tuffs can be subdivided in a similar fashion and divided into ashfall deposits (circular distribution) and current deposits (girdle distributions and girdle distributions with an element of grouping), with the potential of having a separate category for wake deposits. The key outcome has been to develop a new categorisation for different lithofacies according to their AMS fabrics, which have been interpreted for the first time in terms of flow-boundary zone conditions. This has identified different types of massive deposit, each of which has been emplaced by subtly different mechanisms, refuting the concept that all massive deposits are emplaced in the same way.

4.1 Introduction

Because of the opaque and highly hazardous nature of pyroclastic density currents, it is impossible to directly observe the depositional mechanisms. The deposits are therefore an essential record for understanding them.

Pyroclastic density currents produce deposits with a wide variety of lithofacies, which is evidence of their heterogeneous nature. The resulting lithofacies depends on the concentration

and turbulence within the lower parts on the current, the source material, the mass flux, and current interactions with topography. The interpretation of a lithofacies containing sedimentary structures is relatively straightforward, but the interpretation of diffuse and massive lithofacies is more problematic. Massive deposits have been interpreted to be a result of rapid deposition from a high concentration current (Sparks et al. 1973; Sparks 1976; Wright & Walker 1981; Carey, 1991). The causes of this rapid deposition have been debated (see page 11) but the mechanism of deposition was the same and unvaried. Despite the apparent homogenous appearance of such deposits, fabric data have the potential to highlight variability at the flow-boundary during the deposition of massive deposits and to shed more light on the depositional mechanisms.

This study has used Anisotropy of Magnetic Susceptibility (AMS: Chapter 2) to compare and contrast the AMS fabrics of cross-stratified, stratified, diffusely bedded and massive ignimbrite lithofacies, to provide data to be used to interpret flow-boundary conditions and depositional mechanisms. Particular attention is paid to AMS variations of massive lithofacies, as these are the most enigmatic and poorly understood. An aspect of this study is to investigate whether all massive beds have the same fabric characteristics or whether there is facies variability that would indicate a range of flow-boundary conditions and depositional mechanisms. The impact of the palaeotopographic context of the samples will be considered in the interpretations. Improved understanding of how pyroclastic density currents behave and evolve during an eruption, and of their interactions with topography, is important for hazard assessment of inhabited volcanically active regions.

This chapter reviews some work on depositional mechanisms of pyroclastic density currents and the use of AMS in interpreting ignimbrites. The method of sample collection, preparation, measurement and analysis is given in Chapter 3, but specific details relating to this chapter are briefly reviewed. New data on fabrics of ignimbrite lithofacies are presented and for the first time used to discriminate and interpret the different flow-boundary zone conditions and their depositional mechanisms, allowing the semi-quantification of the flow-boundary model proposed by Branney & Kokelaar (2002). The effects of palaeotopography on density currents and the resulting fabrics are also considered.

4.2 Previous Work

Transportation within a pyroclastic density current occurs via combinations of tractional and granular processes and from suspension. Turbulence is related to the concentration and velocity of the current. For example, currents of higher velocities and lower concentrations at the flow-boundary tend to be more turbulent; this enhances saltation of particles and increases the suspended load. With increasing particle mass the forces required to move a particle increase, which decreases the suspended load and inhibits saltation. The principal forces responsible for the movement of particles are frictional drag, which is how coarse material is moved as the rolling component, and the Bernoulli Effect (or lift), which is caused by pressure differences above and below particles. This is an important force during saltation of particles. Once-deposited, particles can still be entrained and transported further downcurrent.

As a result of the interaction of a current with the underlying topography, a variety of bedforms can be produced. These bedforms are often found preserved in cross-section as sedimentary structures. Sedimentary structures have long been used as palaeocurrent indicators, and provide information of conditions at the base of the current (e.g McKee, 1957; Middleton, 1965).

The four types of flow-boundary zone (direct fallout-dominated, traction-dominated, granular flow-dominated and fluid escape-dominated), proposed by Branney and Kokelaar (2002), are conceptualised end-members in a continuum of current conditions. In fully-dilute, low velocity currents, direct fallout at the flow-boundary may occur. At higher velocities more vigorous turbulence causes tractional process to dominate at the flow-boundary. Granular-fluid based currents have flow-boundaries dominated by granular flow processes or, at higher rates of deposition, fluid escape may dominate the flow-boundary. How these different flow-boundary conditions may be reflected in AMS fabrics will be discussed.

AMS studies on ignimbrites have focussed on identifying palaeocurrent directions (e.g. Knight et al. 1986; MacDonald and Palmer, 1990; Hillhouse and Wells, 1991; Seaman et al. 1991; Wang et al. 2001), locating source vents (e.g. Hillhouse and Wells, 1991; Palmer and Macdonald, 1999; Ort et al. 2003), the effects of welding (Ellwood, 1982), and how AMS fabrics vary spatially and/or temporally to establish how pyroclastic density currents evolve (Hillhouse and Wells, 1991; Ort et al. 1999, 2002). AMS fabrics in ignimbrites are

predominately oblate, with the exception of rheomorphic ignimbrites, which yield more prolate fabrics as a result of ductile shear (Ellwood, 1982).

An AMS classification scheme by Knight et al. (1986), devised from the welded Toba Tuffs, was modified by Seamann et al. (1991) who categorised AMS fabrics in the Bloodgood Canyon and Shelley Park tuffs. Five different AMS fabrics were described, though it is not always clearly stated if the samples were from massive ignimbrites (Table 1). These studies focussed on identifying reliable k1 lineations to identify palaeocurrent directions, not depositional mechanism. Knight et al. (1986) alluded to the possibility that category 1 is a ‘flow feature’ and category 3 may be a result of turbulent conditions or of low anisotropies, but no further explanations with regard to the formation of these fabrics were offered. All five categories in Table 1 have been observed within this study and have been interpreted in terms of flow-boundary conditions and depositional mechanism.

Category	Knight et al. (1986)	Seamann et al. (1999)
1	Good clustering of k3 near vertical and good clustering of k1 and k2	Good clustering of k3 near vertical and good clustering of k1 and k2
1a	N/A	Good clustering of k1 and k2 on a great circle near the horizontal. k2 is within 10° of horizontal. Poor clustering of k3 near the vertical
2	Good clustering of k3 near the vertical. K1 and k2 are distributed along a great circle near horizontal, but are not clustered	Good clustering of k3 near the vertical. k1 and k2 are distributed along a great circle near horizontal, with no clustering
3	Random orientations of k1, k2, and k3	Random orientations of k1, k2, and k3
4	Good clustering of k1 and k2, with k3 inclined at an angle (<30°)	N/A

Table 1: Classification schemes of AMS fabrics of Knight et al. (1986) and Seamann et al. (1999).

Recently, AMS has been used to provide information about depositional processes within pyroclastic density currents. Cagnoli and Tarling (1997) recognised two fabrics: a girdle distribution, as defined by the k1 and k2 axes, and a well-grouped distribution of the principal susceptibility axes. The fabrics with a girdle distribution were from planar-laminated surge deposits, which were interpreted to have been deposited under turbulent conditions, whereas the well-grouped distributions were from the basal layer of the Pitigliano ignimbrite (assumed to be massive) and interpreted to have been deposited from laminar conditions. It would be

incorrect to assume that all ignimbrites are deposited under such conditions and this point will be discussed later in this chapter.

Similar AMS fabric types in the Campanian ignimbrite, Italy have been recorded (Ort et al. 1999). Proximal regions have scattered and girdle distributions with weaker lineations, were interpreted to represent more turbulent conditions close to source, whereas more distal deposits were characterised by better-grouped susceptibility axes and a stronger lineation, and interpreted to record increasing laminar conditions and shear (presumably laminar). Ort et al. (1999) attempted to distinguish fabrics generated by tractional processes from those generated by laminar shear. Where the k_1/k_2 foliation plane was inclined towards the k_1 direction, laminar shear was interpreted to be the dominant factor, whereas k_3 axes inclined towards k_2 axes were interpreted to represent more tractional processes.

The degree of scatter of the susceptibility axes has been interpreted to represent the level of shear during deposition; well-grouped axes represent higher laminar shear and more scattered or girdle distributions represent lower laminar shear (Cagnoli & Tarling, 1997). This interpretation was also used in the analysis of the orientation of lithic fragments in ignimbrites (Hughes & Druitt, 1998). Baer et al. (1997) suggested that turbulent systems were responsible for the Ito ignimbrite, based on the greater degree of scatter than expected as a result of analytical error alone.

Although others have sampled different lithofacies, there have been no detailed lithofacies studies using AMS, where AMS signatures of different lithofacies are compared and interpreted in terms of depositional mechanisms. The aim of this study was to characterise the different lithofacies according to their AMS fabric, with a view to better understanding depositional mechanisms. Of particular interest are the depositional mechanisms responsible for massive lithofacies, which are the most enigmatic and most poorly understood deposits. The intention is to distinguish between different types of massive lithofacies on the bases of their AMS fabric, and to interpret them in terms of depositional mechanism.

4.3 Methodology

Samples have been collected from formations throughout the Upper Bandas del Sur Group (Fig 4.1). The methods used in the collection, preparation, measurement and analysis of data for this chapter are identical to those used in Chapter 5 and full details can be found in Chapter 3. The majority of the samples were collected using a petrol-operated drill, but some sets of data were from orientated block samples, which were subsequently drilled in the laboratory: This allows very precise drilling in more controlled conditions.

Each of the lithofacies was described, photographed and sketched, with sedimentary logs as appropriate, and the positions of samples in relation to palaeotopography were noted wherever possible. Samples were selected from previously well-studied ignimbrites wherever possible so that the depositional context was known.

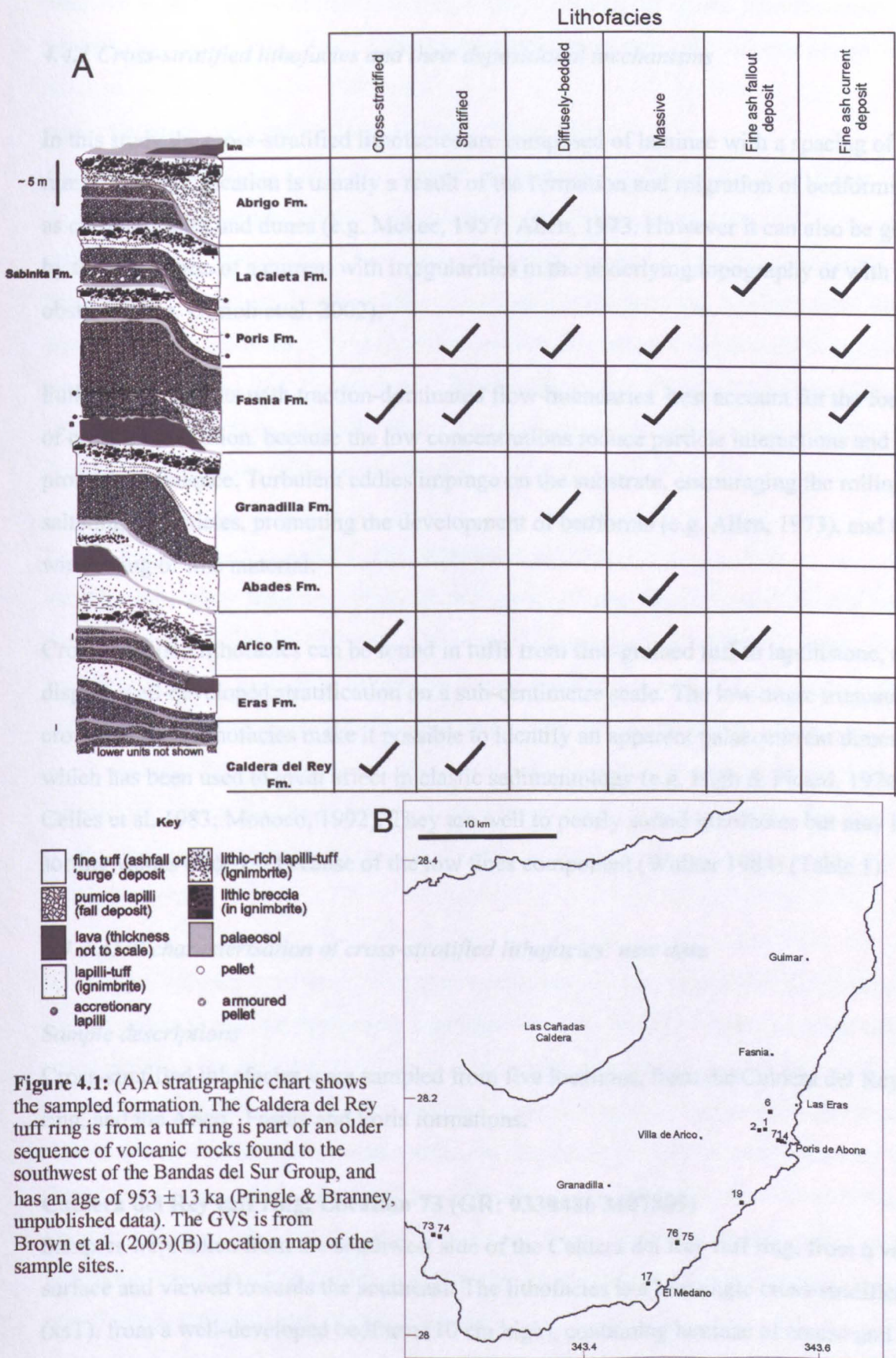


Figure 4.1: (A) A stratigraphic chart shows the sampled formation. The Caldera del Rey tuff ring is from a tuff ring is part of an older sequence of volcanic rocks found to the southwest of the Bandas del Sur Group, and has an age of 953 ± 13 ka (Pringle & Branney, unpublished data). The GVS is from Brown et al. (2003) (B) Location map of the sample sites..

4.4 Cross-stratified tuff lithofacies

4.4.1 Cross-stratified lithofacies and their depositional mechanisms

In this study the cross-stratified lithofacies are composed of laminae with a spacing of <10 mm. Cross-stratification is usually a result of the formation and migration of bedforms such as current ripples and dunes (e.g. McKee, 1957; Allen, 1973). However it can also be generated by the interaction of a current with irregularities in the underlying topography or with obstacles (e.g. Gurioli et al. 2002).

Fully dilute currents with traction-dominated flow-boundaries best account for the formation of cross-stratification, because the low concentrations reduce particle interactions and promote turbulence. Turbulent eddies impinge on the substrate, encouraging the rolling and saltating of particles, promoting the development of bedforms (e.g. Allen, 1973), and the winnowing of fine material.

Cross-stratified lithofacies can be found in tuffs from fine-grained tuff to lapillistone, and display well-developed stratification on a sub-centimetre scale. The low-angle truncations of cross-stratified lithofacies make it possible to identify an apparent palaeocurrent direction, which has been used to great affect in clastic sedimentology (e.g. High & Picard, 1974; De Celles et al. 1983; Monaco, 1992). They are well to poorly sorted lithofacies but may have sorting values of $\phi=1-3$ because of the low fines component (Walker 1984) (Table 1).

4.4.2 AMS characterisation of cross-stratified lithofacies: new data

Sample descriptions

Cross-stratified lithofacies were sampled from five locations, from the Caldera del Rey tuff ring, and the Arico, Fasnía and Poris formations.

Caldera del Rey tuff ring: Location 73 (GR: 0330486 3107809)

Samples were taken from the southwest side of the Caldera del Rey tuff ring, from a vertical surface and viewed towards the southeast. The lithofacies is a low-angle cross-stratified tuff (xsT), from a well-developed bedform (10 cm high), containing laminae of coarse and very coarse sand with a small amount of fine ash matrix. Subangular to subrounded lithics can be

observed with occasional altered pumice lapilli. The laminae had an apparent dip of 5° to the west. An apparent palaeocurrent direction to the southwest is inferred from the cross-stratification (Fig 4.2A). There were no apparent palaeotopographic features nearby.

Arico Formation: Location 71 (GR: 0358979 3116216)

Samples were taken from a vertical surface of the Arico Formation in a road section on the Poris-Arico road looking towards the northeast. The lithofacies is a low-angle cross-stratified tuff (xsT), and is interpreted to be a result of interactions with slight irregularities in topography, rather than the migration of a well-developed bedform. It is composed of fine ash and the laminae are defined by preferential erosion. An apparent palaeocurrent direction to the southeast is inferred from the cross-stratification (Fig 4.2B). There were no apparent palaeotopographic features nearby and the tuff appeared to be part of a relatively thin veneer deposit. Samples were drilled in the field.

Fasnia Formation: Location 1 (GR: 0380000 3117190)

Samples were taken from a quarry north of Poris de Abona, from a vertical surface viewed towards the south. The lithofacies is a low-angle, cross-stratified tuff (xsT), from small bedforms (≤ 6.5 cm high). The lithofacies is composed of fine ash, with the individual laminae with an apparent dip direction to the west, defined by sand-sized lithics. There were only occasional pumice lapilli present. An apparent palaeocurrent direction to the east may be inferred from the cross-stratification. There were no apparent palaeotopographic features nearby and the tuff appeared to be part of a relatively thin veneer deposit. Samples were drilled in the field.

In addition, samples were taken from a previously undocumented cross-stratified reworked deposit within the Fasnia Formation, near Tajao (Fig. 4.2D). The lithofacies is a low-angle, cross-stratified fine lapilli tuff (xsLT). It is very well sorted, consisting of sub-rounded pumice lapilli with minimal matrix, and was found with ignimbrite and ash layers above and below. Because of the exceptional sorting, this deposit is interpreted as reworked by flash floods that occurred during the Fasnia eruption. If a storm did occur, the excessive moisture in the atmosphere could account for the accretionary lapilli fallout layers within the Fasnia Formation. An apparent palaeocurrent direction to the east may be inferred from the cross-stratification. Samples were drilled in the field.

Poris Formation: Location 6 (GR: 0358346 3118754)

Samples were taken from a valley-fill deposit near to Mt Magua, from a vertical surface viewed towards the SW. The lithofacies was a diffuse, low-angle, splay-and fade cross-stratified tuff (xsT), which overlies, and is overlain by, massive lapilli tuff. The lithofacies is composed of fine ash, with the individual laminae defined by subtle changes in grain size. An apparent palaeocurrent direction to the SSE is inferred from the orientation of the valley axis. Samples were drilled in the field (Fig 4.2C).

Results

All the AMS data sets plotted as a girdle-distribution of the k_1 and k_2 susceptibility axes on the stereonets (Fig. 4.2A). These are particularly well defined in the data sets from the Caldera del Rey tuff ring and the Arico and Fasnía formations. The girdle distributions define a foliation, which is inclined between 8.2° and 32.6° relative to bedding (Fig. 4.2C). The data from the Poris Formation have less well-defined girdle distributions, with a greater degree of scatter. The mean susceptibility ranges from $8567.24 \text{ E } 10^{-6}$ and $1629.25 \text{ E } 10^{-6} \text{ SI}$ (Fig. 4.3). The girdle distributions seen in this study are comparable to a cross-stratified tuff sampled from the Campanian Ignimbrite by Ort et al. (2003), which also produced a girdle distribution.

Cross-stratified lithofacies in the Caldera del Rey tuff ring and Arico Formation have a tightly grouped oblate AMS fabric. Those in the Fasnía Formation are also characterised by an oblate AMS fabric, but have a greater degree of scatter. The splay-and-fade cross-stratification in the Poris Formation has a more triaxial to prolate fabric and has a larger scatter than the other formations, and this is consistent with the more diffuse nature of the lithofacies as viewed in the field. The mean strength of anisotropy varies from 1.27% and 4.06%. The Caldera del Rey tuff ring and the Arico Formation have the weakest fabrics (1.27% & 1.69% respectively), whilst the splay-and-fade cross-stratified fabric yields H values of 2.25% and 2.87%. The cross-stratified lithofacies from the Fasnía Formation has the strongest fabric with a mean value of 4.06% (Fig. 4.2B).

The AMS fabric from the reworked deposit from the Fasnía Formation produced a poorly defined circular distribution, with poorly grouped k_3 axes near to vertical. In all the other data sets the k_3 axes are very well-grouped. This difference may be a result of reworking and deposition from water. The strength of the mean anisotropy is 1.66% with the mean foliation

(1.5%) significantly greater than the mean lineation (0.16%). The mean imbrication angle of the foliation plane as defined by k1 and k2 is 5.6.

Interpretation

The formation of cross-stratified lithofacies is the simplest to interpret, because their formation can be directly observed from experimental studies in flume tanks (Mckee, 1957; Allen, 1973; Cheel, 1990) and observations from modern fluvial and aeolian systems (e.g. Mckee, 1957). Cross-stratified lithofacies are produced from fully dilute currents as turbulent eddies interact with the substrate (Allen, 1984; Burgisser & Bergantz, 2002; Baas et al. 2004), encouraging traction at the flow-boundary (Fig. 4.5A).

The processes by which cross-stratification form are well understood (e.g Allen, 1973), so the girdle-distributions are interpreted to indicate tractional processes at the flow-boundary. Turbulence arranges particles upon a plane creating the girdle-distribution, which is accentuated if maximum and intermediate susceptibility values are similar, meaning that their orientations become interchangeable. How well defined the girdle-distribution will be and how strong the anisotropy is, may be determined by the turbulence intensity; the more turbulence, the better defined the girdle-distribution. Cross-stratified tuffs with a girdle distribution will now be referred to as xsT Type 1 deposits (Fig. 4.3A).

Some cross-stratified tuffs (e.g. Arico Formation) display an element of grouping on the girdle, which is interpreted to represent an increase in the influence of granular shear, perhaps due to slightly higher concentrations and rates of shear at the flow-boundary, resulting in more lineated fabrics. These fabrics will now be referred to as xsT Type 2 deposit; Fig. 4.5A).

The splay-and-fade in the Poris Formation is very diffuse and unsurprisingly has a poorly developed girdle-distribution (e.g. sample SF12; Fig. 4.3A). It was sampled within a palaeovalley, where the concentration of the flow-boundary zone is likely to have been higher due to density stratification of the current. This may have partly suppressed turbulence and promoted fluid escape (Fig. 4.5B), preventing the development of more distinct cross-stratification. Channeling of the current along the palaeovalley may account for the more triaxial/prolate fabric seen on the F/L plots of sample SF12 (Fig. 4.3A).



(A) Cross-stratified tuff in the Caldera de Rey tuff ring.

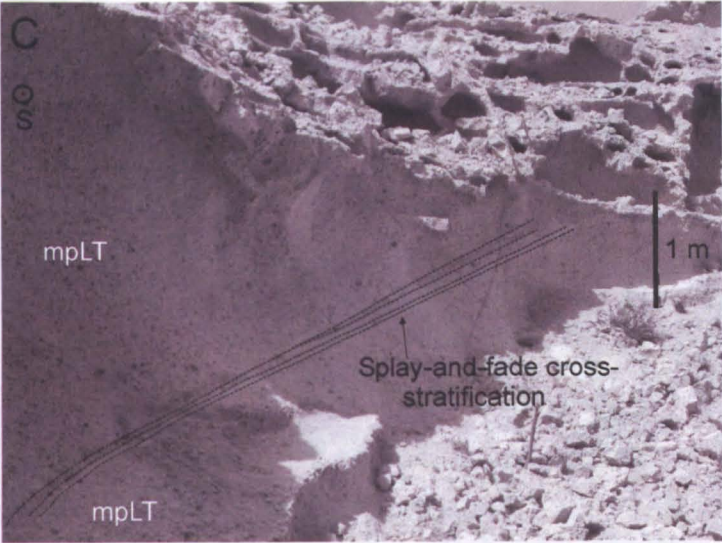
An apparent palaeocurrent direction to the west. Photo was taken of a vertical surface, on the southwest side of the tuff ring looking to the south
GR:0330486 3107809.



(B) Cross-stratified tuff in the Arico Formation. An apparent palaeocurrent direction to the southeast. Photo taken of a vertical surface looking to the NE Near Poris de Abona
GR:0358979 3116216.

(C) Cross-stratified tuff in reworked sediments within the El Pozo Tuff Ring. An apparent palaeocurrent direction to the south.

Figure 4.2: Examples of cross-stratified lithofacies sampled in this study.



(C) Splay-and-fade cross-stratified tuff overlying and overlain by massive lapilli tuff in the valley fill facies of the Poris Formation. The palaeocurrent direction is towards the south (out of the photo towards the reader). Near Mt Magua GR: 0358333 3118874.



(D) Cross-stratified tuff in reworked sediments within the Fasnja Formation. An apparent palaeocurrent direction to the east. Near Tajao GR: 0355826 3118380. Scale 1m.

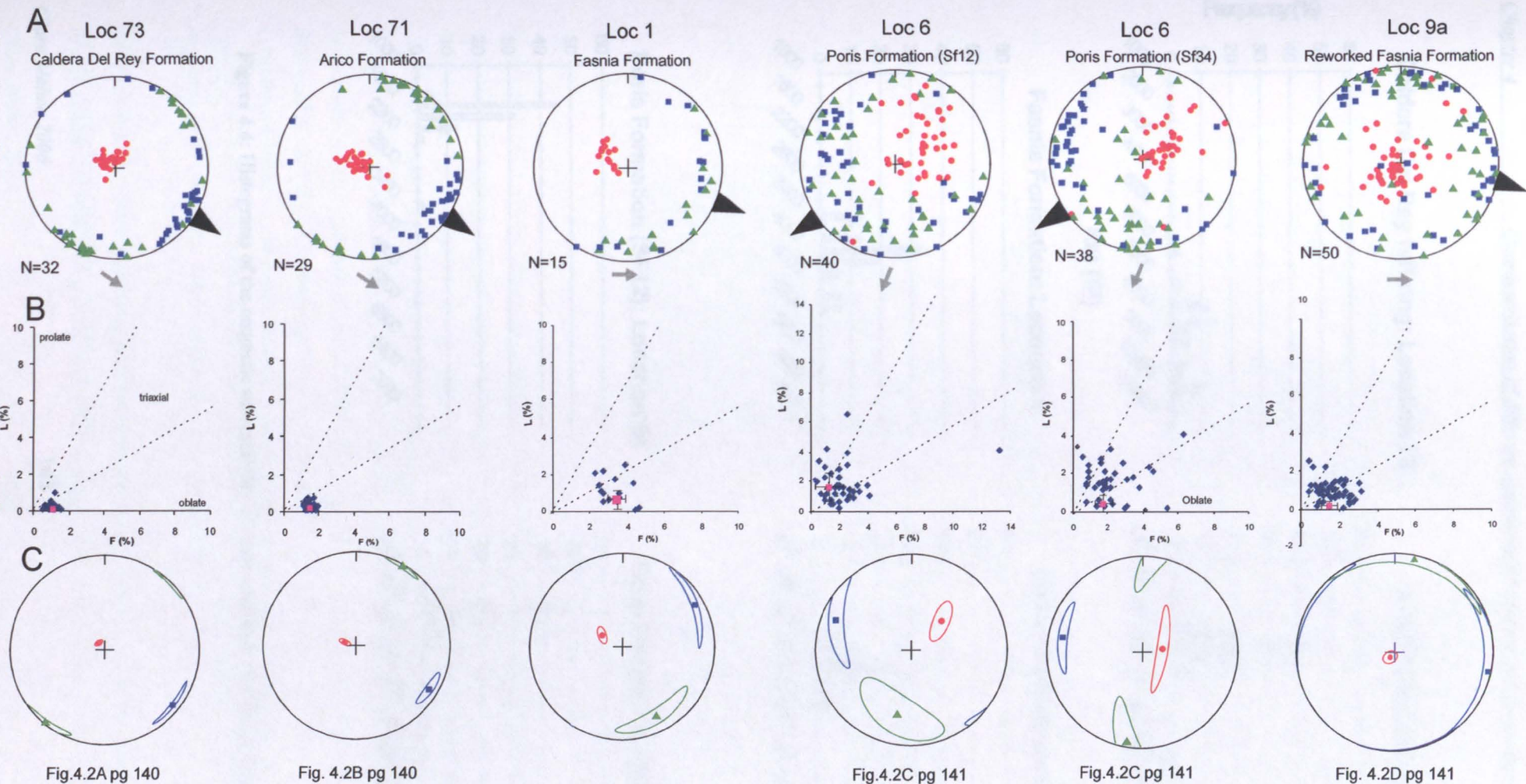


Figure 4.3: AMS data from the cross-stratified lithofacies including (A) stereonet of the orientation of the susceptibility axes; (B) foliation - lineation plot demonstrating the shape and strength of anisotropy of individual plugs and the **tensor** mean with error bars (where error bars appear to be absent, they are smaller than the actual data point); (C) stereonet of the mean orientation of the susceptibility axes with 95% confidence ellipses for the position of the mean. Corrected for bedding. See Fig.4.1B for a map of sample locations.

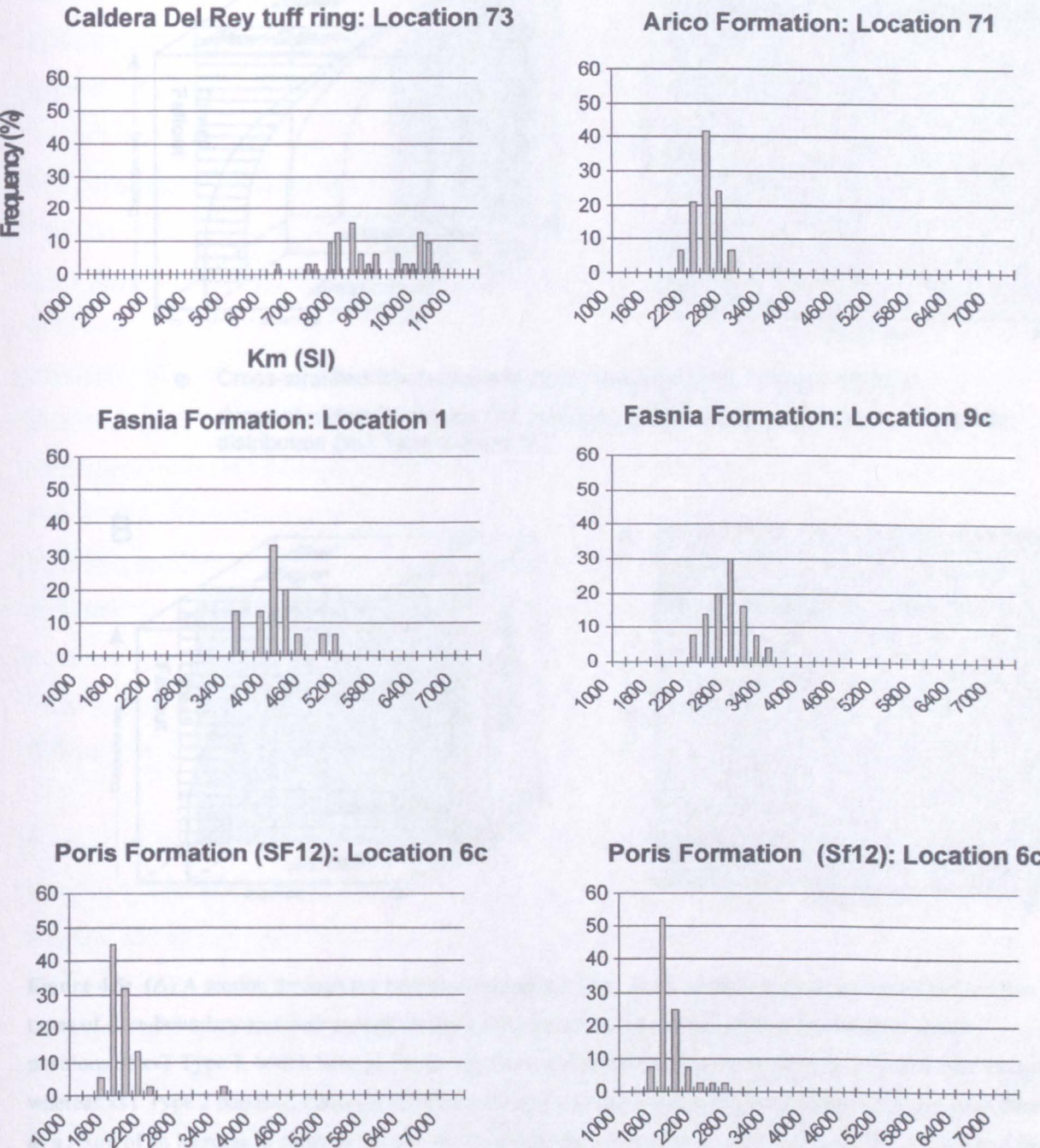


Figure 4.4: Histograms of the magnetic susceptibility of cross-stratified lithofacies from a variety of formations.

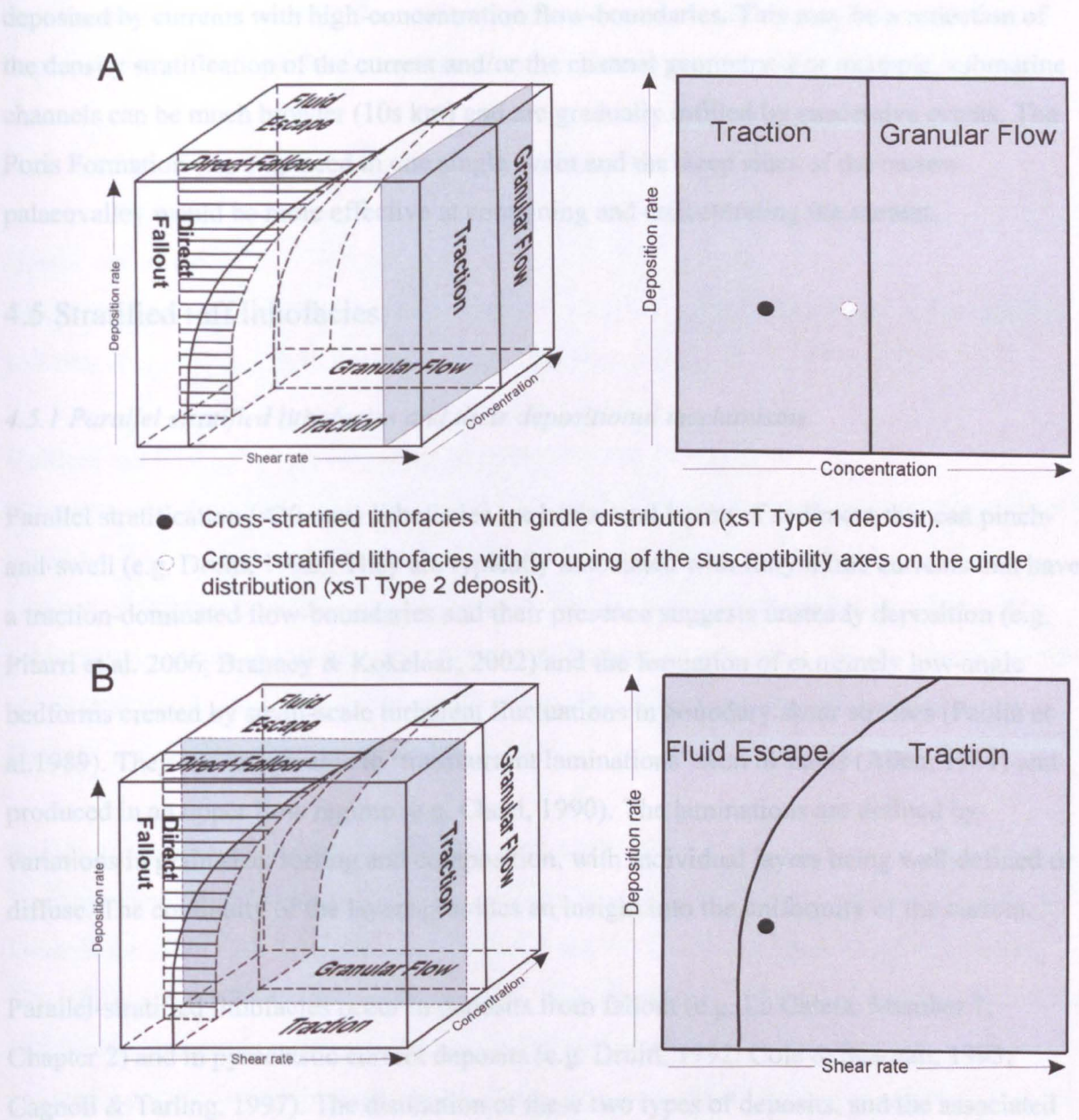


Figure 4.5: (A) A section through the traction and granular flow fields of the 3-dimensional model of the four types of flow-boundary and their controls proposed by Branney & Kokelaar (2002), showing the relative positions of xsT Type 1, which have girdle distributions and are interpreted to be strongly influenced by traction, whereas xsT Type 2 deposits, although still dominated by tractional processes, are influenced by granular shear, as a result of an increase in concentration in the flow-boundary zone; (B) A section through the traction and fluid escape fields of the 3-dimensional model of the four types of flow-boundary and their controls proposed by Branney & Kokelaar (2002), showing the relative position of the diffuse splay-and-fade cross stratification found in the Poris Formation. The poorly defined girdle distribution and the diffuse nature of the lithofacies suggest that the tractional processes were not as strong and that an increase in fluid escape due to higher concentrations and lower shear rates at the flow boundary may have inhibited the formation of cross-stratification.

Well-developed cross-bedding and cross-stratification has been documented within channelised turbidites (e.g McCabe, 1977), suggesting that not all channel deposits are

deposited by currents with high-concentration flow-boundaries. This may be a reflection of the density stratification of the current and/or the channel geometry. For example, submarine channels can be much broader (10s km) and are gradually infilled by successive events. The Poris Formation was emplaced in one single event and the steep sides of the narrow palaeovalley would be more effective at containing and concentrating the current.

4.5 Stratified tuff lithofacies

4.5.1 Parallel stratified lithofacies and their depositional mechanisms

Parallel stratification (<30 mm) lithofacies are horizontal layers of sediment that can pinch-and-swell (e.g. Druitt, 1992). They are typically associated with fully dilute currents that have a traction-dominated flow-boundaries and their presence suggests unsteady deposition (e.g. Pitarri et al. 2006; Branney & Kokelaar, 2002) and the formation of extremely low-angle bedforms created by small-scale turbulent fluctuations in boundary shear stresses (Paolia et al. 1989). They are comparable to 'transcurrent laminations' seen in sands (Allen, 1984) and produced in an upper flow regime (e.g. Cheel, 1990). The laminations are defined by variations in grain size, sorting and composition, with individual layers being well defined or diffuse. The continuity of the layers provides an insight into the uniformity of the current.

Parallel-stratified lithofacies occur in deposits from fallout (e.g. La Caleta, Member 1; Chapter 2) and in pyroclastic current deposits (e.g. Druitt, 1992; Cole & Scarpati, 1993; Cagnoli & Tarling, 1997). The distinction of these two types of deposits, and the associated problems when dealing with very fine grain sizes, are considered in Chapter 4. Pyroclastic currents can deposit parallel-stratified deposits by a number of means. In fully dilute currents of sufficiently low velocities, there may be virtually no traction. Consequently, particles must be deposited from a direct fallout-dominated flow-boundary zone (Branney & Kokelaar, 2002), in which particles simply fallout from the current, with negligible lateral movement and without rolling or saltating.

The layering is defined by gradational and subtle variations in grain size. The layering is sub-parallel and may or may not exhibit pinch-and-swell structures. Individual layers are laterally discontinuous and commonly grade laterally and vertically into massive lithofacies. They have been inferred to result from subtle unsteadiness at the flow-boundary of the depositing

current, possibly as a result of fluctuations within a sustained current and periodic impingement of turbulent eddies on the substrate (Branney & Kokelaar, 2002).

4.5.2 AMS characterisation of stratified lithofacies: new data

Sample descriptions

Samples of stratified lithofacies were sampled from three locations from the Caldera del Rey tuff ring (Fig. 4.6) and from the Fasnía and Poris formations.

Caldera del Rey tuff ring: Location 74 (GR:0331030 3107651)

Samples were taken from the southwest side of the Caldera del Rey tuff ring, from a vertical surface and viewed towards the south. The lithofacies is a stratified tuff (sT), containing laminae of coarse sand with a small amount of fine ash matrix. Subangular to subrounded lithics occur with occasional altered pumice lapilli. An apparent palaeocurrent direction to the west is inferred from near by cross-stratification. There were no apparent palaeotopographic features nearby. Samples were drilled in the field.

Fasnía Formation: Location 1 (GR: 0380000 3117190)

Samples were taken from a quarry north of Poris de Abona, from a vertical surface viewed towards the south. The lithofacies is a stratified tuff (sT), with near-horizontal laminations. The lithofacies is predominantly composed of fine ash, with the individual laminae defined by variations in clast size and populations. An apparent palaeocurrent direction to the east is inferred from nearby cross-stratification. There were no apparent palaeotopographic features nearby and this appeared to be part of a relatively thin veneer deposit. Samples were drilled in the field.

Poris Formation: Location 4 (GR:03592500 3116125)

Samples were taken from the Poris Formation type location (Bryan et al. 1998), just outside of Poris de Abona on the Arico road, from a vertical surface viewed towards the northeast. The lithofacies is a diffusely stratified tuff (dsT), with near-horizontal laminations. The lithofacies is predominantly composed of fine ash and occasional pumice and lithic lapilli, with the individual laminae defined by variations in grain size. There are no palaeocurrent indicators, so it is assumed to have been towards the coast (south to south-east). There were

no apparent palaeotopographic features nearby and this appeared to be part of a relatively thin veneer deposit. Samples were drilled from a block sample.

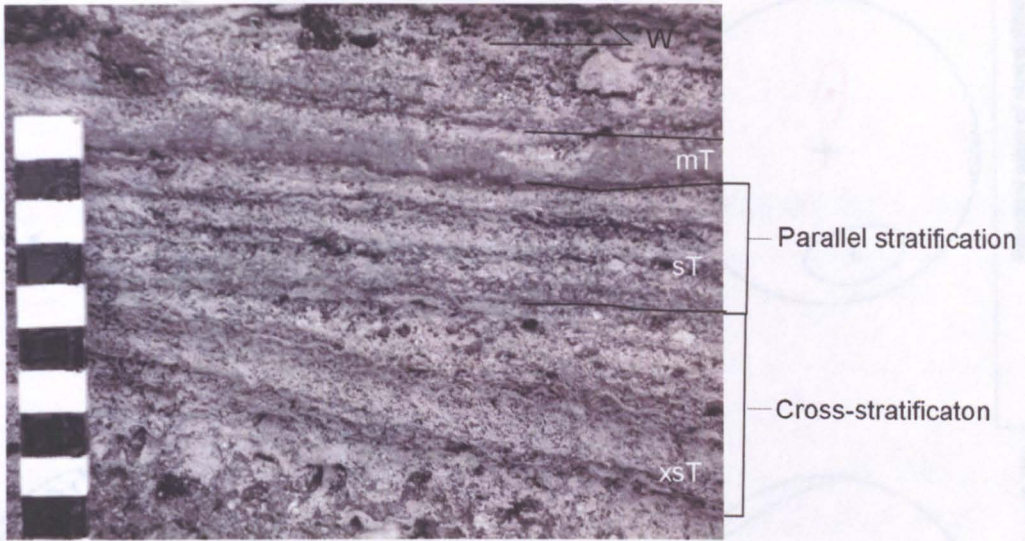


Figure 4.6: Parallel-stratified tuff in the Caldera del Rey tuff ring on the south -west side. An apparent palaeocurrent direction to the west.GR:0331030 3107651.

Results

Stratified lithofacies from the Fasnja and Poris formations produced girdle distributions, but not as well-defined as those seen in cross-stratified lithofacies (Fig. 4.7A), whereas the stratified lithofacies from the Caldera del Rey tuff ring produced discrete groups of the susceptibility axes that display very clear and well defined orientations of the susceptibility axes. The mean foliation as defined by k_1 and k_2 ranges from $16.4\text{--}31^\circ$ (Fig. 4.7C), and the susceptibility values vary from $10910.4 \text{ E}10^{-6}$ - $3042.35 \text{ E}10^{-6}$ (Fig. 4.8). The stratified lithofacies data produce moderate scatter on the F/L plots, with the exception being sample FS2, which is well grouped. They fall in the oblate to triaxial region, with the mean strength of anisotropy ranging from 1.26% to 3.03% (Fig. 4.7C).

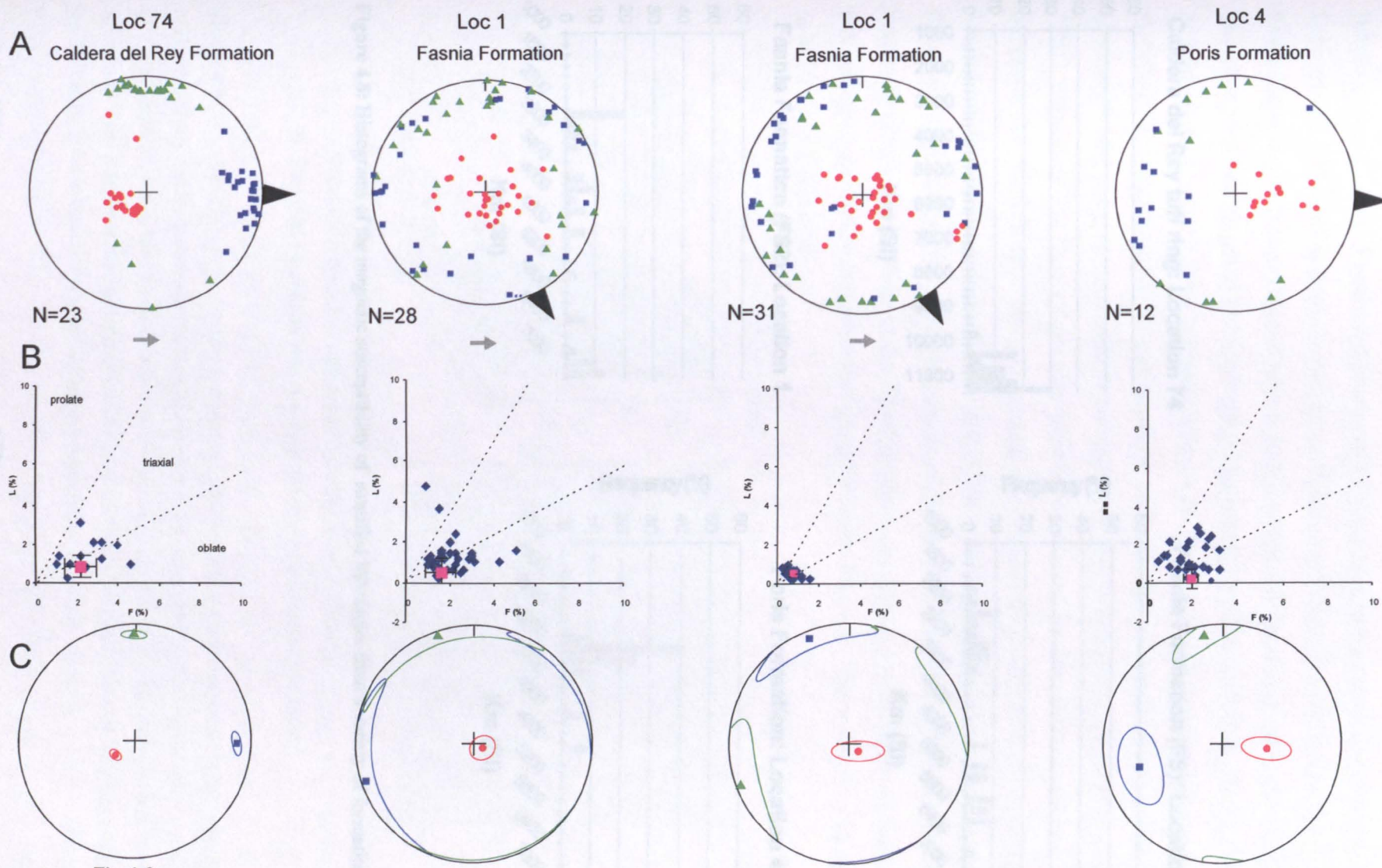


Figure 4.7: AMS data from the stratified lithofacies including (a) equal area stereonet of the orientation of the susceptibility axes; (b) foliation - lineation plot demonstrating the shape and strength of anisotropy of individual plugs and the tensor mean (pink square)(the errors on Fasnja Formation are smaller than the symbol); (c) equal area stereonet of the mean orientation of the susceptibility axes with 95% confidence ellipses for the position of the mean. Corrected for bedding. See Fig.4.1B for a map of sample locations.

Stratified lithofacies produced girdle-distributions, supporting the concept that stratified lithofacies are a result of tractional processes. This distribution agrees well with AMS fabrics from stratified lithofacies from the Solihull Volcano tuff ring (Proveda Island, Italy) and the Fossa Cappelana tuff cone (Linosa Island, Italy), which also produced girdle distributions and had have been interpreted as turbulent surge deposits (Caprio and Talling, 1997). These will

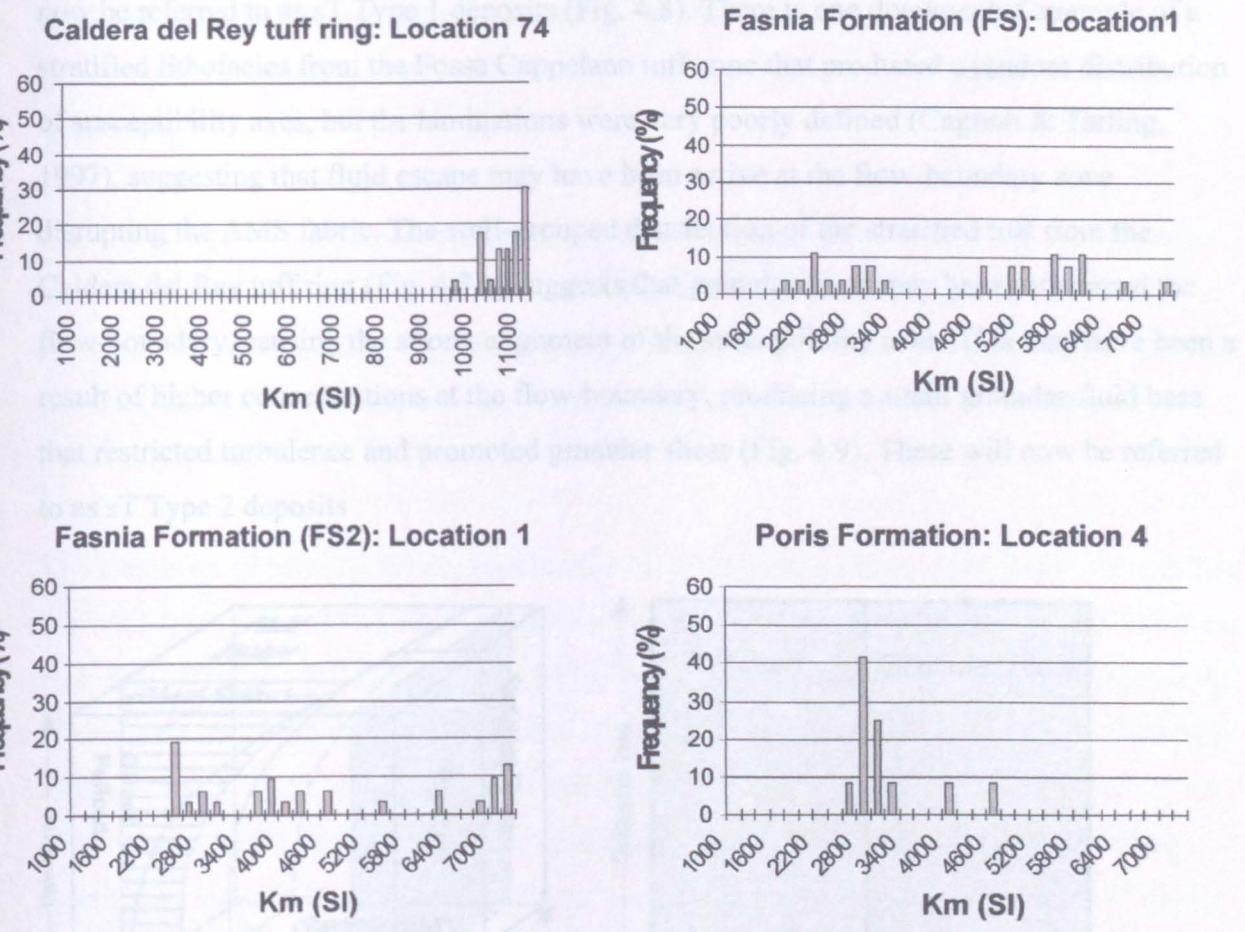


Figure 4.8: Histograms of the magnetic susceptibility of stratified lithofacies from a variety of formations.

- Stratified lithofacies with a girdle distribution (ST Type 1)
- Stratified lithofacies with a wing-shaped distribution (ST Type 2)

Figure 4.9: A section through the traction and granular flow fields of the 3-dimensional model of the four types of flow-boundary and their controls proposed by Branney & Burchfiel (1997), showing the relative positions of ST Type 1 deposits, which have girdle fabrications and are interpreted to be strongly influenced by traction, whereas ST Type 2 deposits, although deposited by tractional processes, are influenced by granular shear, as a result of an increase in concentration in the flow-boundary zone.

Interpretation

Stratified lithofacies produced girdle-distributions, supporting the concept that stratified lithofacies are a result of tractional processes. This data compares well with AMS fabrics from stratified lithofacies from the Solchiaro Volcano tuff ring (Procida island, Italy) and the Fossa Cappelano tuff cone (Linosa island, Italy), which also produced girdle-distributions and had have been interpreted as turbulent surge deposits (Cagnoli and Tarling, 1997). These will now be referred to as sT Type 1 deposits (Fig. 4.8). There is one documented example of a stratified lithofacies from the Fossa Cappelano tuff cone that produced a random distribution of susceptibility axes, but the laminations were very poorly defined (Cagnoli & Tarling, 1997), suggesting that fluid escape may have been active at the flow-boundary zone, disrupting the AMS fabric. The well-grouped distribution of the stratified tuff from the Caldera del Rey tuff ring (Fig. 4.7A) suggests that granular shear may have influenced the flow-boundary, causing the strong alignment of the susceptibility axes. This may have been a result of higher concentrations at the flow-boundary, producing a small granular-fluid base that restricted turbulence and promoted granular shear (Fig. 4.9). These will now be referred to as sT Type 2 deposits

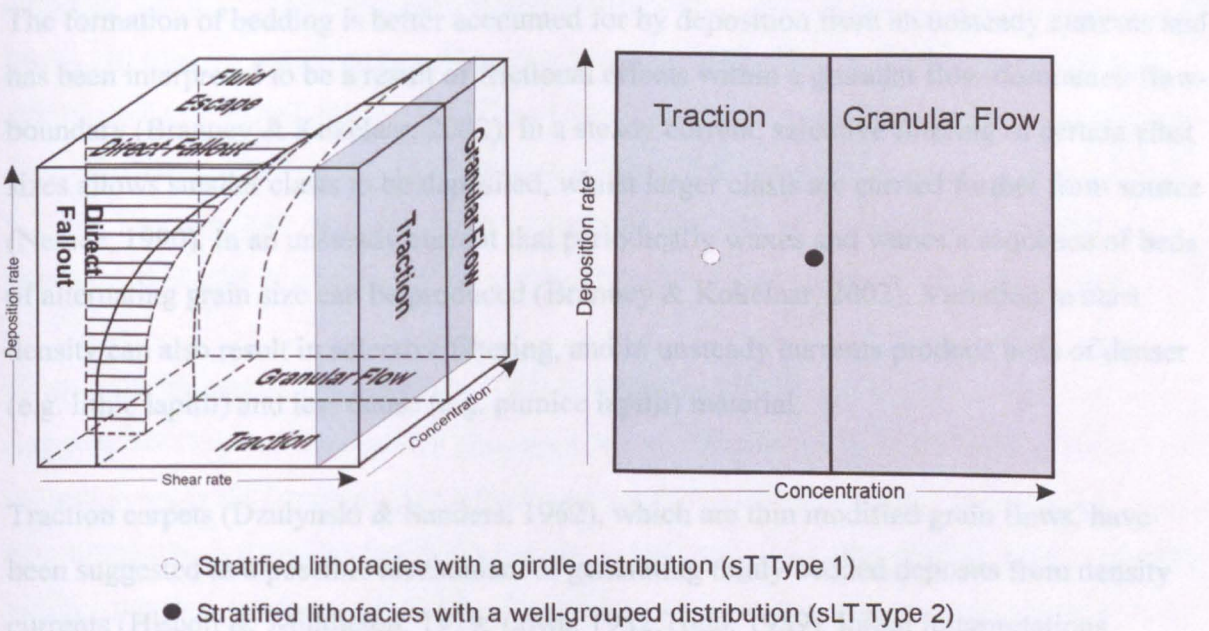


Figure 4.9: A section through the traction and granular flow fields of the 3-dimensional model of the four types of flow-boundary and their controls proposed by Branney & Kokelaar (2002), showing the relative positions of sT Type 1 deposits, which have girdle distributions and are interpreted to be strongly influenced by traction, whereas sT Type 2 deposits, although dominated by tractional processes, are influenced by granular shear, as a result of an increase in concentration in the flow-boundary zone.

4.6 Diffusely-bedded lapilli-tuff lithofacies

4.6.1 Diffusely-bedded lithofacies and their depositional mechanisms

Diffusely bedded lithofacies consist of internally massive, horizontal beds that can pinch and swell and, in this study, are >30mm. Diffuse bedded lithofacies are common and are documented in the Minoan ignimbrite (Sparks, 1976; Branney & Kokelaar, 1992), Taupo ignimbrite (Walker et al. 1981b; Wilson, 1985) and the Valley of Ten Thousand Smokes ignimbrite (Fierstein & Hildreth, 1992)

The ‘plug-flow’ model accounted for the presence of bedding by interpreting each bed as a separate flow unit (Sparks, 1976) and in the case of diffuse bedding was interpreted to represent the rapid stacking and partial amalgamation of flow units (Kuno, 1941). Although possible, evidence indicating a pause in the passage of pyroclastic density currents is frequently absent.

The formation of bedding is better accounted for by deposition from an unsteady currents and has been interpreted to be a result of frictional effects within a granular flow-dominated flow-boundary (Branney & Kokelaar, 2002). In a steady current, selective filtering of certain clast sizes allows smaller clasts to be deposited, whilst larger clasts are carried further from source (Nemec, 1990). In an unsteady current that periodically waxes and wanes a sequence of beds of alternating grain size can be produced (Branney & Kokelaar, 2002). Variation in clast density can also result in selective filtering, and in unsteady currents produce beds of denser (e.g. lithic lapilli) and less dense (e.g. pumice lapilli) material.

Traction carpets (Dzulynski & Sanders, 1962), which are thin modified grain flows, have been suggested as a possible mechanism of generating thinly bedded deposits from density currents (Hiscott & Middleton, 1979; Lowe, 1982; Todd, 1989). Initial interpretations suggested that the modified grain flows deposited en masse via ‘frictional freezing’ after reaching a critical thickness (Hiscott & Middleton, 1979; Lowe, 1982). Later interpretations invoked progressive aggradation from the base of the modified grain flows where the thickness of the individual beds does not necessarily reflect the thickness of the modified grain flow (Hein, 1982; Sohn, 1997). The bedding could result from the periodic impingement of powerful turbulent eddies, causing the flow-boundary, for a brief moment, to be dominated

by other processes (e.g. direct fallout or traction), before the modified grain flow re-establishes itself (Branney & Kokelaar 2002 pg 44). In density currents that have a thicker granular-fluid base and/or not has vigorous turbulence, turbulent eddies may be unable to penetrate to the flow-boundary, but exert fluctuating shear upon the top of the modified grain flow, which is undergoing stepwise aggradation and frequent frictional locking (Branney & Kokelaar, 2002 pg 44). Where the bedding planes are poorly defined, intermediate flow-boundary conditions have been interpreted (Branney & Kokelaar, 2002).

4.6.2 AMS characterisation of diffusely-bedded lithofacies: new data

Sample descriptions

Diffusely bedded lithofacies were sampled from four locations, from the Arico, Granadilla, Poris and Abrigo formations (Fig. 4.10).

Arico Formation: Location 75 (GR: 0350547 3106677)

Samples were taken from a vertical surface, and viewed towards the southeast, south of the autopista that lies west of the Granadilla industrial estate. The lithofacies is a diffusely bedded lapilli tuff (dbLT), containing small rounded pumice lapilli (frequently weathered) and subrounded to subangular lithic lapilli contained within an ash matrix. The beds were defined by variations in grainsize and small pumice cavities. Individual beds were 6-7 cm thick (Fig. 4.10A). There were no apparent palaeotopographic features nearby and the ignimbrite appeared to be part of a relatively thin veneer deposit. Samples were drilled in the field.

Granadilla Formation: Location 1 (GR: 0358250 3117350)

Samples were taken from a quarry northwest of Poris de Abona, from a vertical surface, viewed towards the northeast. The lithofacies is a diffusely bedded lapilli tuff (dbLT), containing rounded pumice lapilli (frequently weathered) and subrounded to subangular lithic lapilli contained within an ash matrix. The beds were defined by variations in grainsize and clast populations. Individual beds are 25 cm thick. Palaeocurrent direction is assumed to be in south to south eastly direction, towards the coastline. There were no apparent palaeotopographic features nearby. Samples were drilled in the field.

Poris Formation : Location 6

Samples were taken from northwest of Poris de Abona (GR: 0358333 318874), from an overbank facies, from a vertical surface, viewed towards the south. It is a diffusely-bedded lapilli tuff (dbLT), ~9 m thick, containing small to medium, rounded pumice lapilli and small, subrounded to subangular lithic lapilli within an ash matrix from an overbank deposit (Member 7: Brown et al. 2004). The beds (10 cm thick) are defined by changes in pumice concentrations and fine material. An apparent easterly palaeocurrent direction is inferred from nearby imbrication of clasts (Fig. 4.10B). The sample was taken 1.5 m from the base of the formation. This overbank facies can be traced into a large NNE-trending palaeovalley infilled by the Poris Formation (~25m thick), from which a diffusely bedded lapilli tuff (dbLT) from Member 6 (Brown et al. 2004) was sampled (GR: 0358346 3118754). It contains rounded pumice lapilli, subordinate subrounded to angular lithic lapilli, rare accretionary lapilli and carbonate concretions. Each bed is ~10 cm thick and defined by layers of pumice cavities, and changes in the size of the pumice lapilli. The orientation of the palaeovalley axis suggests a palaeocurrent direction to the south. These samples were taken from 1.25 m above the base of the formation. All samples were drilled in the field. Further samples were taken from a diffusely bedded tuff (TB), near Mt Magua (GR:0358267 3118268) from a vertical surface viewed towards the south (possibly Member 7: Brown et al. 2004). It is predominately fine ash with individual beds defined by layers of coarse sand and granule-sized lithic clasts. Individual beds are approximately 8-10 cm thick. Samples were drilled in the field.

Abrigo Formation: Location 76 (GR:0350549 3106754)

Samples were taken from a vertical surface, and looking towards the west just south of the autopista west of the Granadilla industrial estate. It is a diffusely bedded lapilli tuff (dbLT), containing small subrounded to subangular lithic lapilli and subordinate pumice lapilli contained within an ash matrix. The beds are defined by small lithic lapilli and were 10 cm thick (Fig. 4.10C). There were no palaeocurrent indicators, so the palaeocurrent direction is assumed to have been towards the south to southeast. There were no apparent palaeotopographic features nearby and the ignimbrite appeared to be part of a relatively thin veneer deposit. Samples were drilled in the field.

Results

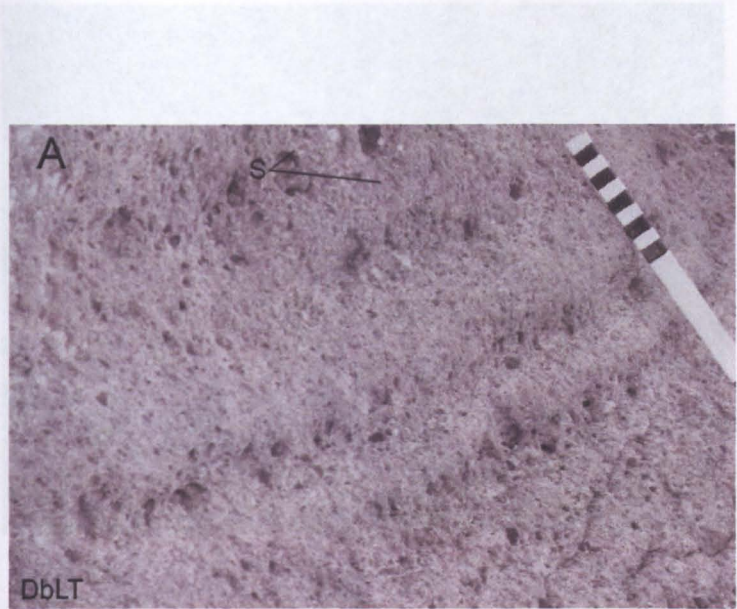
The distribution of the susceptibility axes fall into two groups: Those that display girdle distributions between k_1 and k_2 , which do display an element of clustering, and those that

display more discrete grouping of the susceptibility axes on the foliation e.g. Poris Formation bedform and valley-fill facies (Fig. 4.11A). The data set from the Abrigo Formation produces a girdle distribution, but it is between the k_2 and k_3 susceptibility axes indicating a triaxial/prolate fabric with a greater linear component. This is different compared to the other data sets, but is supported by its F/L plot which has a tensor mean that plots on the boundary between triaxial and prolate fabrics (Fig. 4.11B). The mean imbrication of the foliation as defined by the k_1 and k_2 axes for diffusely bedded lithofacies ranges from $13 - 47.7^\circ$, although they are predominantly $<20^\circ$ (Fig. 6.7c). The mean susceptibility values range between $1389.02 \text{ E } 10^{-6}$ and $6229.11 \text{ E } 10^{-6}$ (Fig. 4.12). The F/L diagrams (Fig. 4.11B) indicate an oblate to triaxial fabric, with a moderate scattering of data and strength of anisotropy ranging between 1.7 and 5.81%. Data that form discrete groups of susceptibility axes have a greater degree of anisotropy (e.g. the Poris Formation bedform and the valley-fill facies (5.81 and 3.76% respectively).

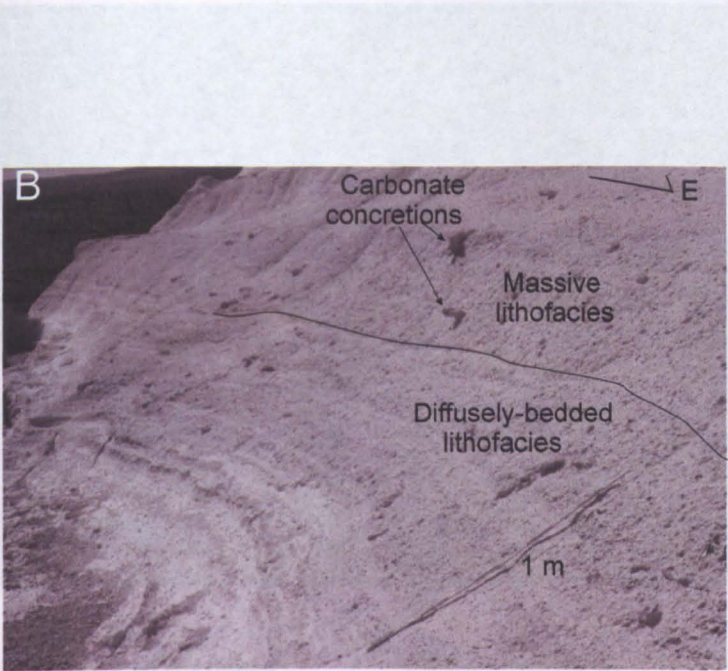
Interpretation

The presence of girdle-distributions, although less well-defined than those in cross-stratified and stratified lithofacies, and the well-grouped distributions, suggest similar depositional processes to stratified lithofacies. The girdle-distributions are interpreted to indicate the influence of traction within the flow-boundary zone, but the crude clustering of the susceptibility axes (lineation) on the foliation suggests that granular shear was operating within the flow-boundary zone (Fig. 4.13). However, the granular-fluid part of the current was insufficiently developed to totally inhibit the effects of turbulence and traction, and the bedding surfaces are interpreted to be a result of turbulent eddies periodically impinging upon the flow-boundary (see Branney & Kokelaar, 2002), hence the overall girdle distribution (Fig. 4.10A). These will now be referred to as dbLT Type 1 deposits.

The data sets with very well-grouped (lineated) distributions (e.g. within the Poris Formation bedform and the Poris valley-fill facies) are interpreted to have been emplaced at a granular flow-dominated flow-boundary zone (Fig. 4.13) at the base of a granular-fluid that was sufficiently thick and concentrated to prevent turbulent eddies influencing the internal fabric within individual beds. The bedding planes in this instance are interpreted to be a result of unsteady turbulent shear acting on to the top of the granular-fluid base of the current. These will now be referred to as dbLT Type 2 deposits.



(A) Diffusely bedded lapilli-tuff in the Arico Formation. The photo was taken looking approximately to the east. Palaeocurrent direction is assumed to be to the south (to the left and into the photo). Near El Medano GR:0350547 3106677.

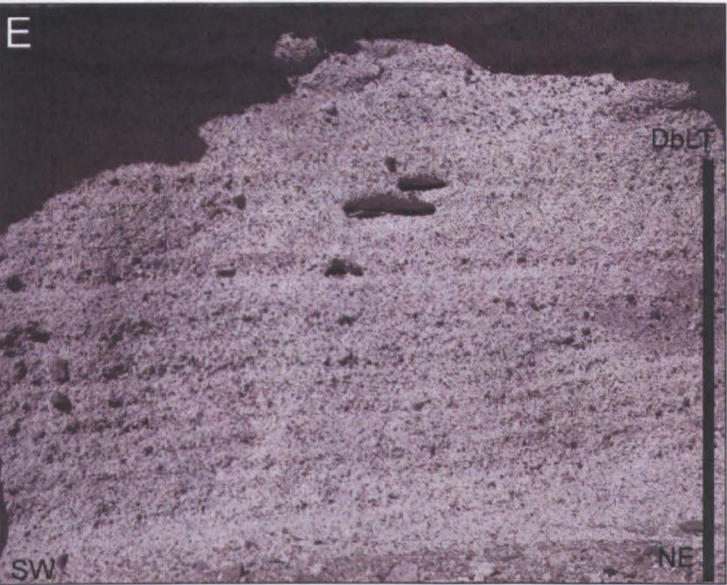


(B) Diffusely-bedded lapilli-tuff overlain by a massive lapilli-tuff in the overbank facies of the Poris Formation. An apparent palaeocurrent direction to the east. Near Mt Magua GR:0358346 3118754.

Figure 4.10: Examples of diffusely-bedded lithofacies sampled in this study.



(D) Diffusely bedded tuff in the Poris Formation. Thin overbank deposit. Apparent palaeocurrent direction to the east. Near Mt Magua GR:0358267 3118268..



(E) Diffusely bedded lapilli tuff in the Abrigo Formation. Scale bar 1 m. An apparent palaeocurrent is assumed to be in a southly direction. Near El Medano. GR:0350549 3106754.

Figure 4.10 continued:

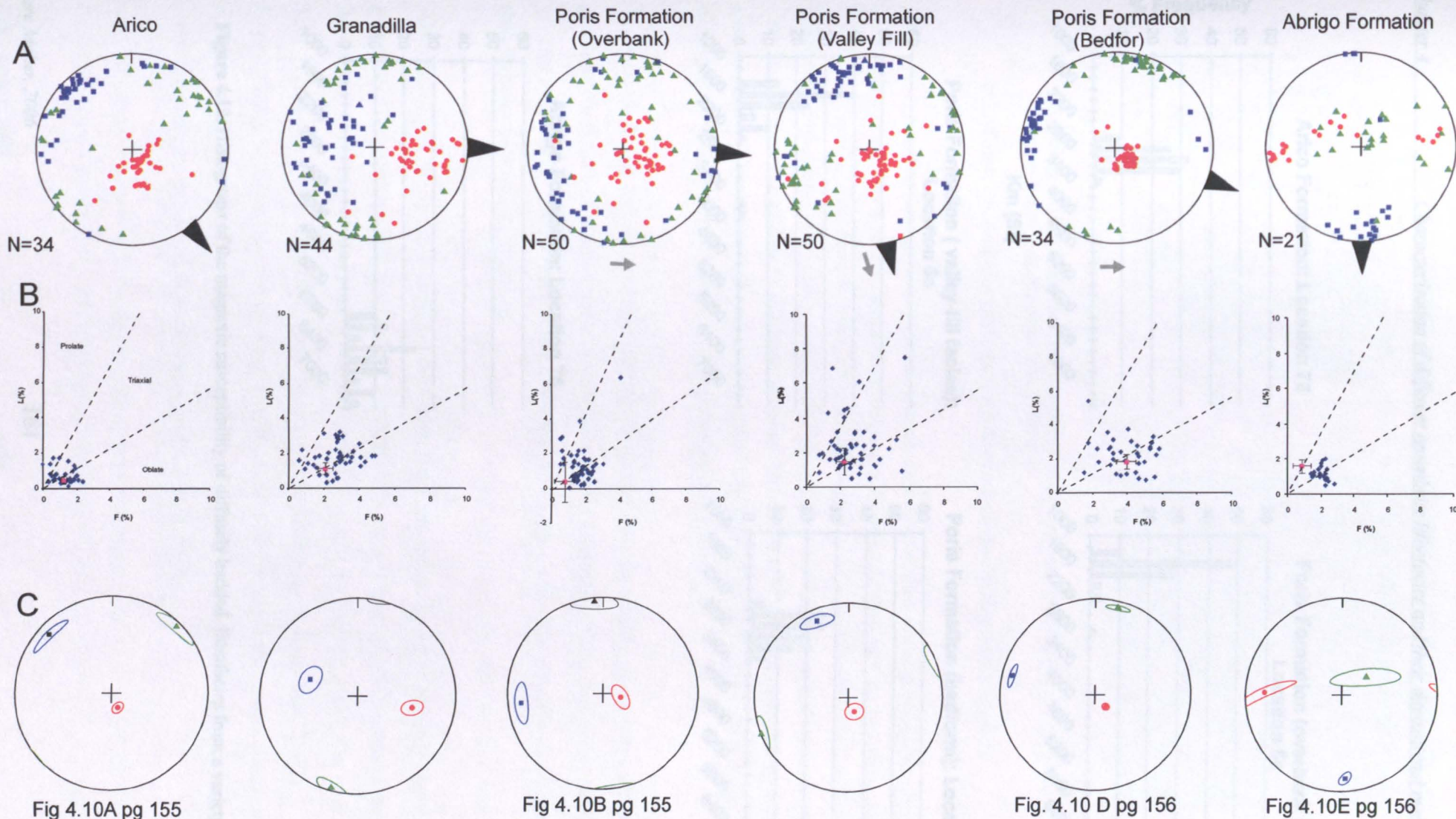
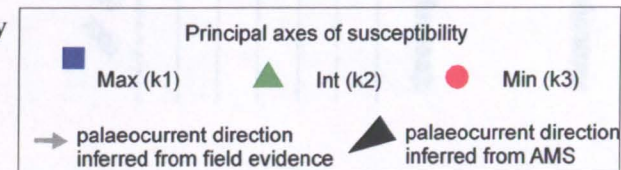


Figure 4.11: AMS data from the diffusely bedded lithofacies including (a) a stereonet of the orientation of the susceptibility axes; (b) foliation - lineation plot demonstrating the shape and strength of anisotropy, of individual plugs and the tensor mean (pink square) with error bars (where error bars appear to be absent, they are smaller than the actual data point); (c) Stereonet of the mean orientation of the susceptibility axes with 95% confidence ellipses for the position of the mean. Corrected for bedding. See Fig.4.1B for a map of sample locations.



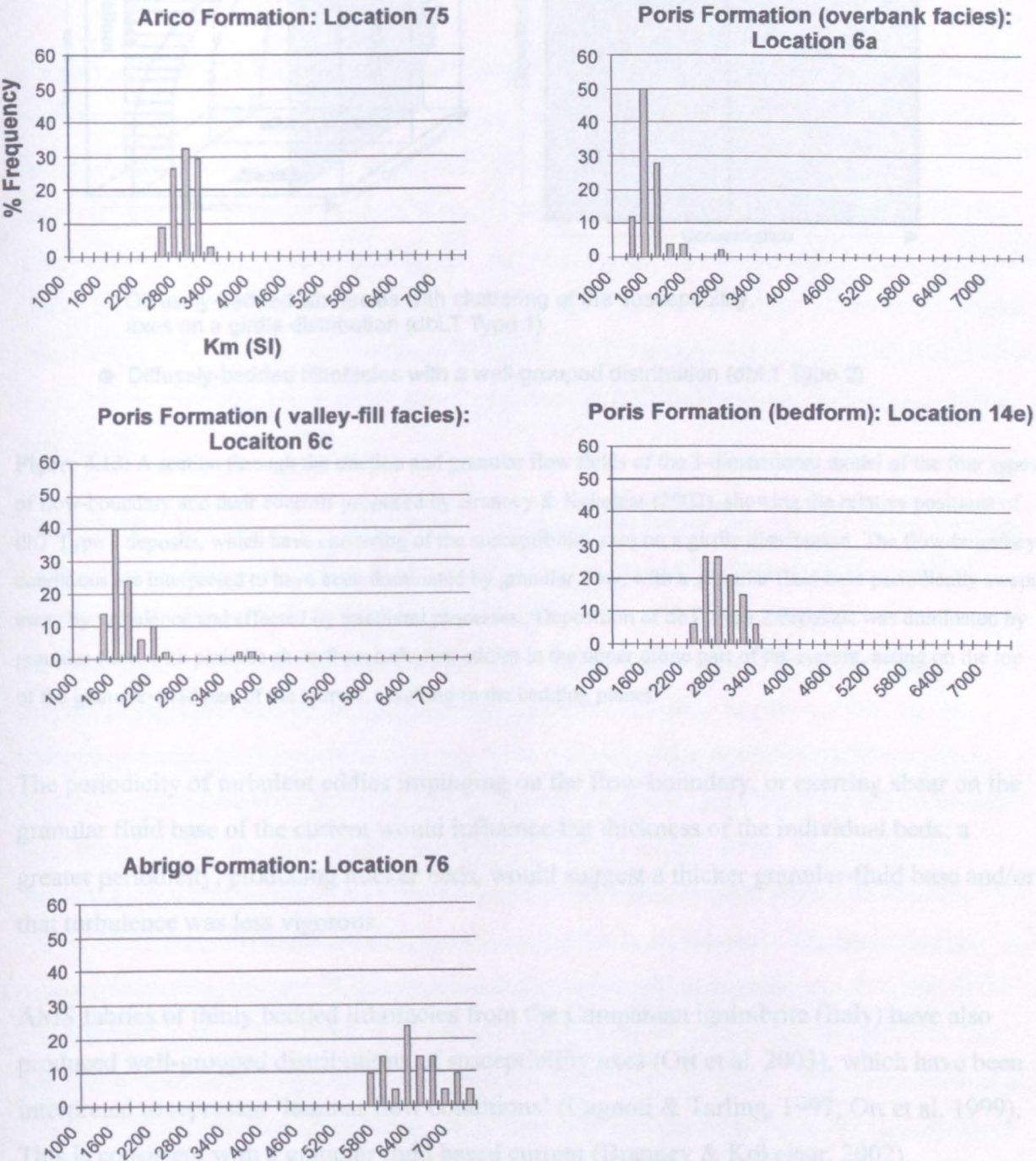
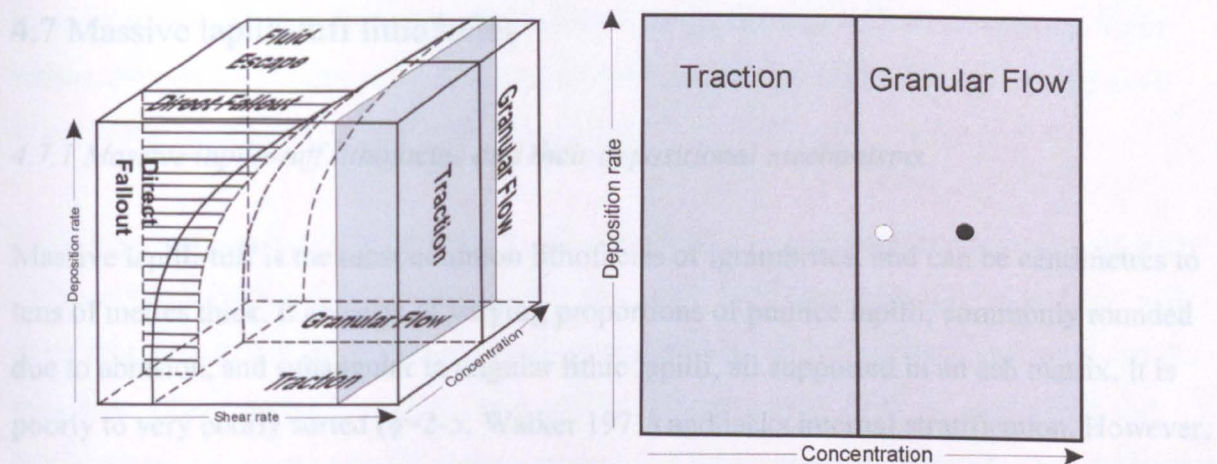


Figure 4.12: Histograms of the magnetic susceptibility of diffusely bedded lithofacies from a variety of formations.



- Diffusely-bedded lithofacies with clustering of the susceptibility axes on a girdle distribution (dbLT Type 1)
- Diffusely-bedded lithofacies with a well-grouped distribution (dbLT Type 2)

Figure 4.13: A section through the traction and granular flow fields of the 3-dimensional model of the four types of flow-boundary and their controls proposed by Branney & Kokelaar (2002), showing the relative positions of dbT Type 1 deposits, which have clustering of the susceptibility axes on a girdle distribution. The flow-boundary conditions are interpreted to have been dominated by granular flow, with a granular fluid base periodically swept away by turbulence and affected by tractional processes. Deposition of dbT Type 2 deposits, was dominated by granular flow, with periodic shear from turbulent eddies in the upper dilute part of the current, acting on the top of the granular-fluid part of the current, resulting in the bedding planes.

The periodicity of turbulent eddies impinging on the flow-boundary, or exerting shear on the granular fluid base of the current would influence the thickness of the individual beds; a greater periodicity, producing thicker beds, would suggest a thicker granular-fluid base and/or that turbulence was less vigorous.

AMS fabrics of thinly bedded lithofacies from the Campanian ignimbrite (Italy) have also produced well-grouped distributions of susceptibility axes (Ort et al. 2003), which have been interpreted to represent 'laminar flow conditions' (Cagnoli & Tarling, 1997; Ort et al. 1999). This is consistent with a granular fluid based current (Branney & Kokelaar, 2002).

Experimental work carried out by Rees and Woodall (1975) found that more concentrated currents produce well-grouped distributions of susceptibility axes, whereas more dilute turbulent currents produced deposits with girdle-distributions.

4.7 Massive lapilli-tuff lithofacies

4.7.1 Massive lapilli-tuff lithofacies and their depositional mechanisms

Massive lapilli-tuff is the most common lithofacies of ignimbrites, and can be centimetres to tens of metres thick. It consists of varying proportions of pumice lapilli, commonly rounded due to abrasion, and subangular to angular lithic lapilli, all supported in an ash matrix. It is poorly to very poorly sorted ($\phi=2-5$; Walker 1971) and lacks internal stratification. However, it may exhibit various types of grading, as well as grain fabrics such as imbrication. The grain fabrics can vary in orientation and intensity, both laterally and vertically within an ignimbrite (MacDonald & Palmer, 1990; Hillhouse & Wells, 1991; Hughes and Druitt, 1998; Capaccioni et al., 2001), providing information about variations at the flow-boundary conditions during deposition.

Massive lithofacies have been interpreted to be deposited from granular-fluid based currents at high rates of deposition. This in turn is influenced by the rate of supply of pyroclasts (Branney & Kokelaar, 2002). A high rate of supply that exceeds the rate of deposition causes the basal layer to thicken, and the flow-boundary becomes dominated by fluid-escape. Tractional processes and turbulence becomes inhibited, resulting in poor sorting and an absence of sedimentary structures. The rapid deposition causes interstitial fluid to rise up through the flow-boundary zone and hinder deposition, generating a fluid escape-dominated flow-boundary lacking intense granular shear at the base of the current. Some massive deposits have a crystal -enriched matrix relative to the juvenile clasts (Spark & Walker, 1977), which suggests elutriation of fine ash by fluid escape. However, abundant fine ash remains suggesting that the fluid-escape process was not efficient enough to elutriate all the ash. Elutriation could be inhibited by particle interlocking and/or the agglomeration of fine ash due to electrostatic attraction or the presence of moisture (Simons, 1996; Schaafsma et al. 1998). Where there is no grain fabric, deposition may have been from an end-member fluid escape-dominated flow-boundary, in which granular shear was minimal and deposition was predominantly by hindered settling (Branney & Kokelaar, 2002). Where massive lapilli-tuff facies exhibit grain fabrics, there may have been some granular shear in the flow-boundary zone, causing the orientation of the clasts. The strength of such directional fabrics would be dependent upon the shear intensity (e.g. Kneller & Branney, 1995), the residence time of the clasts within the shear zone, and the shape and size of the clasts (Branney & Kokelaar, 2002).

In addition, any forming fabrics could be destroyed by subsequent fluid escape (e.g. in the uppermost parts of the decompacting deposit, and maybe modified or overprinted by post-depositional compaction and (if present) welding.

It has been proposed that the orientation of long axes of clasts may indicate conditions at the flow-boundary (Branney & Kokelaar, 2002; Ort et al., 1993). For example, by analogy with grain fabrics or debris flow deposits, clasts with their long-axes transverse to current direction may have rolled into position (e.g. Ort et al. 1993; Bertran et al. 1997; Jo et al. 1997) and would perhaps suggest more dilute conditions at the flow-boundary, whereas clasts with their long-axis parallel to the current direction may result from shearing of high concentration dispersions without rolling (e.g. Rees, 1966; Postma et al., 1988).

4.7.2 AMS characterisation of massive lapilli-tuffs lithofacies: new data

Sample descriptions

Massive lithofacies were sampled from ignimbrites at six locations, from the Arico, Abades Granadilla, Fasnía and Poris formations (Fig. 4.14).

Arico Formation: Location 17 (GR: 0348125 3102967)

Samples were taken from a vertical surface, viewed towards the east in El Medano. The lithofacies is a massive lapilli tuff (mLT), containing medium-sized, rounded pumice lapilli and subrounded to subangular lithic lapilli contained within an ash matrix. The lithic lapilli coarsen upwards and are imbricated at 6-20° indicating an apparent palaeocurrent direction to the south (Fig. 4.14A), which is supported by the presence of cross stratification indicating a palaeocurrent direction to the south. Samples were drilled in the field.

Abades Formation: Location 19 (GR: 0355869 3110392)

Samples were taken from a vertical surface, viewed towards the NNE near Tajao. The lithofacies is a massive lapilli tuff (mLT), containing small to medium-sized, rounded pumice lapilli and subrounded to subangular lithic lapilli contained within an ash matrix. The lithic and pumice lapilli are imbricated by 20° indicating an apparent palaeocurrent direction to the southeast (Fig. 4.14B). Samples were drilled in the field.

Granadilla Formation: Location 1 (GR: 03579250 3117225)

Samples were taken from a vertical surface, viewed towards the west, in a quarry northwest of Poris de Abona. The lithofacies is a massive lapilli tuff (mLT), containing abundant medium, rounded pumice lapilli, and few lithic lapilli, contained within an ash matrix. There were no palaeocurrent indicators but this is assumed to have been towards the south to southeast, towards the coast (Fig. 4.14C). Samples were drilled in the field.

Fasnía Formation: Location 2 (GR: 0357400 3117025)

Samples were taken from a vertical surface, viewed towards the east in a quarry northwest of Poris de Abona. The lithofacies is a massive lapilli tuff (mLT), containing abundant medium, subrounded to angular lithic lapilli, and some rounded pumice lapilli, contained within an ash matrix. There were no palaeocurrent indicators, but it is assumed to have been towards the south to southeast, towards the coast. Samples were drilled in the field.

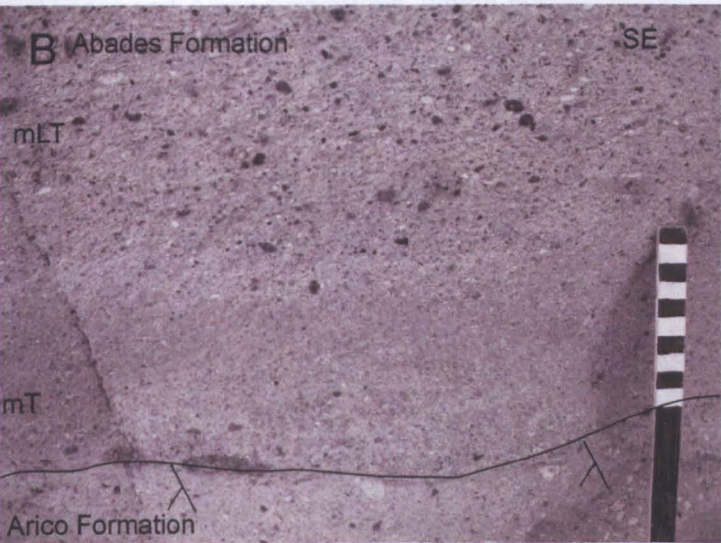
Poris Formation: Location 6

Samples were also taken from near Mt Magua from a vertical surface, looking towards the north from overbank deposits (OB; GR:0358333 3188740). The lithofacies is a poorly sorted massive lapilli tuff (mLT), which is 1.3m thick, containing medium to large, rounded pumice lapilli and subrounded to angular lithic lapilli, contained within an ash matrix. Carbonate concretions are also present (Fig. 4.10B). It is between 2.35 and 3.65cm from the base of the deposit and is Member 7 (Brown et al. 2004). The same lithofacies was also sampled 10 m away from the palaeovalley side (VS; GR:0358564 3118667) and from within the palaeovalley at two heights (VF=2.5m & VF2= 5m VF2; GR:0358346 3118754), where rare accretionary lapilli occur (Member 6: Brown et al. 2004). The orientation of the palaeovalley axis suggests a palaeocurrent direction towards the south.

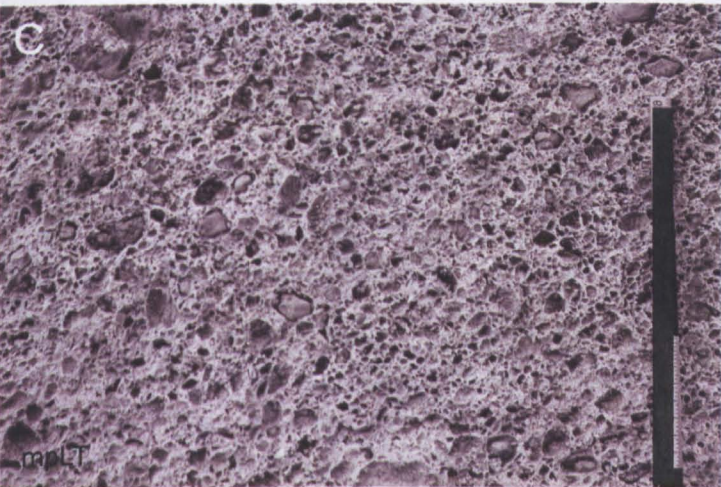
Samples were also taken from near Tajao (GR:0355960 3110925) from a vertical surface, viewed towards the east. The lithofacies is a massive lapilli tuff (mLT), containing medium, rounded pumice lapilli and subrounded to angular lithic lapilli, contained within an ash matrix. Giant flute casts nearby suggest a palaeocurrent direction to the south. Samples were drilled in the field.



(A) Massive lapilli tuff in the Arico Formation, with imbrication of lithic and pumice lapilli (as highlighted) indicating a palaeocurrent direction to the SSE. Near El Medano. GR:0348125 3102967.



(B) Massive lapilli tuff in the Abades Formation. An apparent palaeocurrent direction to the SE. Near Tajao: GR:0355869 3110392.



(C) Massive pumice lapilli tuff in the Granadilla Formation. Scale 30 cm. Near Mt del Puerto. GR: 0357950 3117250

Figure 4.14: Examples of massive lithofacies, sampled in this study.

Results

The distribution of the magnetic susceptibility axes of massive lapilli-tuffs can be divided into three groups (Fig. 4.15A): (1) well-scattered or random distribution of susceptibility axes (mLT Type 1; Knight et al. 1986, Category 3); (2) well-grouped distributions of the susceptibility axes (mLT Type 2; Knight et al. 1986, Category 1); (3) girdle-distributions of the k1 and k2 susceptibility axes (mLT Type 3; Knight et al. 1986, Category 2). The mean imbrication angle of the foliation, as defined by k1 and k2, ranges between 5 to 34° and is typically greater than 20° (Fig. 4.15C). The mean susceptibility ranges between 1352 E10⁻⁶ and 6570 E10⁻⁶ SI (Fig 4.16) and the F/L diagrams suggest triaxial to prolate fabrics in general, although data sets displaying girdle-distributions have a higher percentage of data points in the oblate field (Fig. 4.15B). The mean strength of anisotropy ranges from 0.79 - 6.44%. The data displaying the greatest degree of anisotropy are the massive lithofacies of the Abades and Arico formations, which possess discrete groups of susceptibility axes.

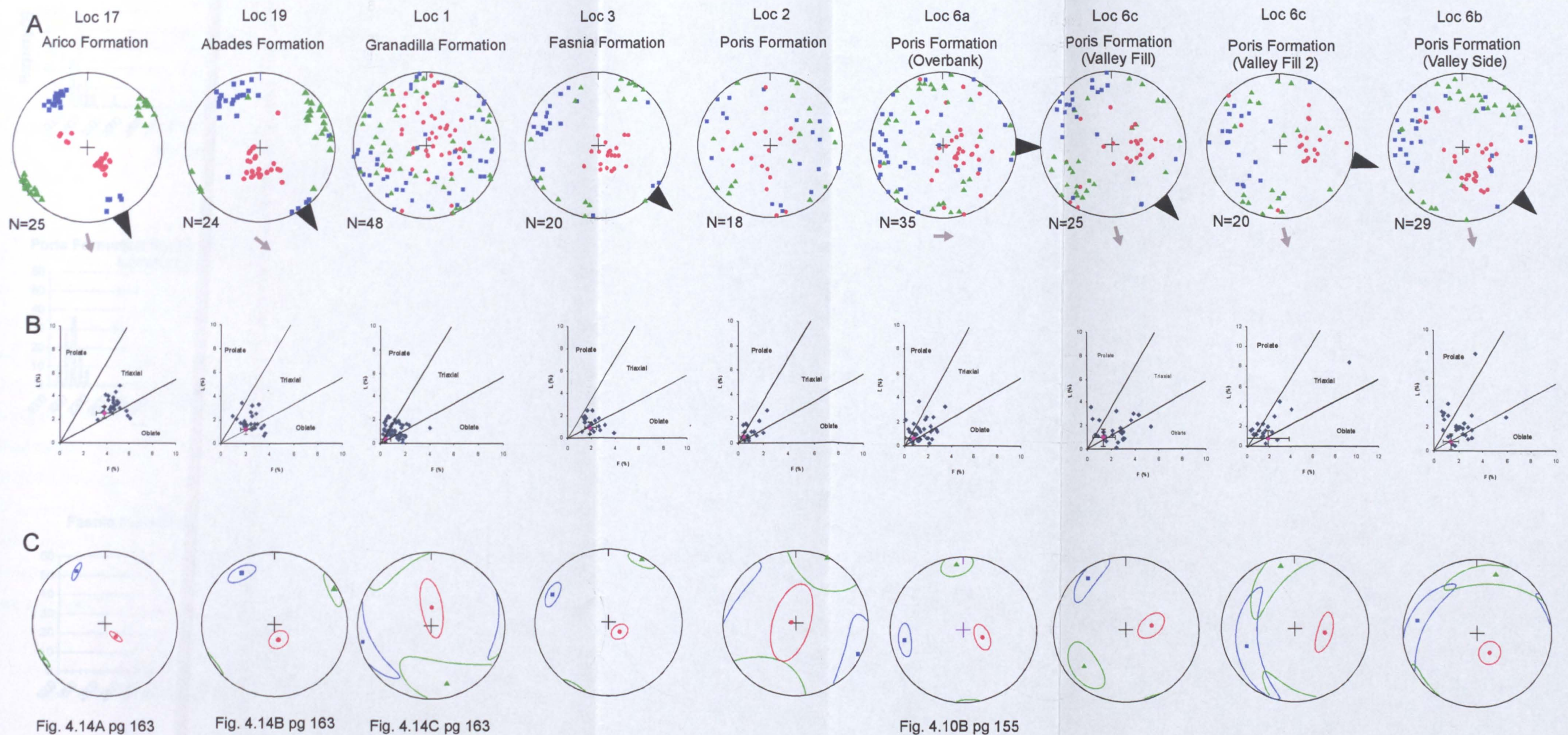
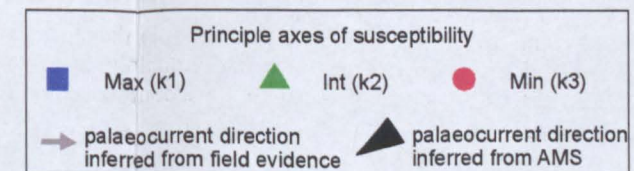


Figure 4.15: AMS data from the massive lithofacies including (a) a stereonet of the orientation of the susceptibility axes; (b) foliation - lineation plot demonstrating the shape and strength of anisotropy of individual plugs and the **tensor** mean with error bars; (c) stereonet of the mean orientation of the susceptibility axes with 95% confidence ellipses for the position of the mean. Corrected for bedding. See Fig.4.1B for a map of sample locations.



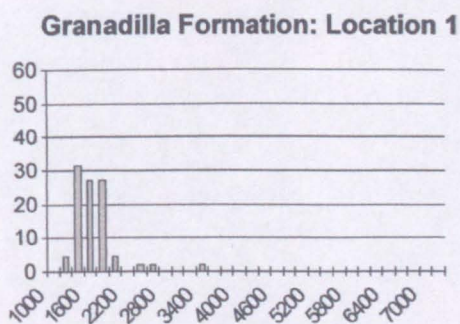
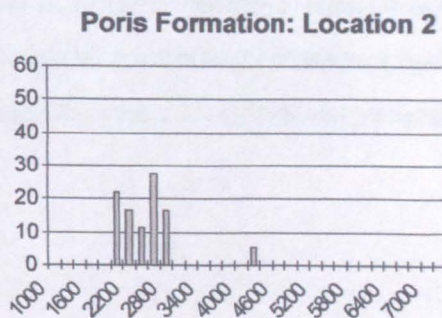
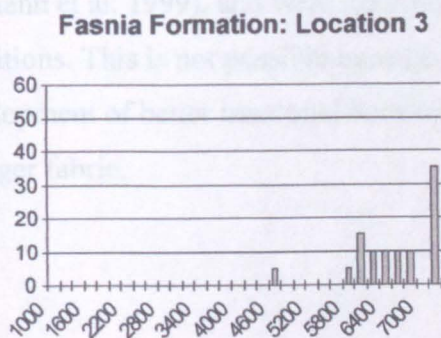
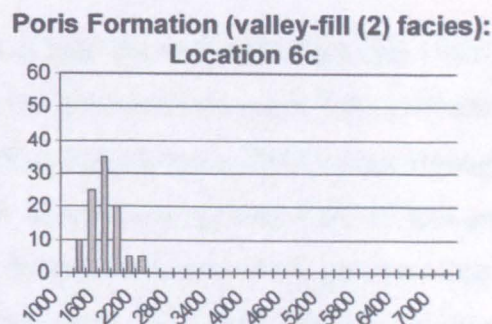
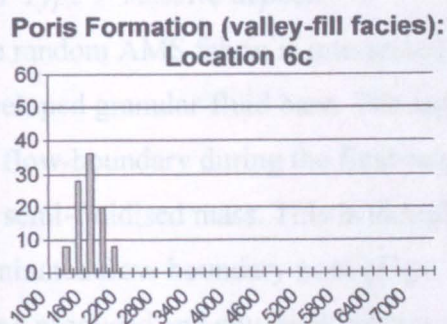
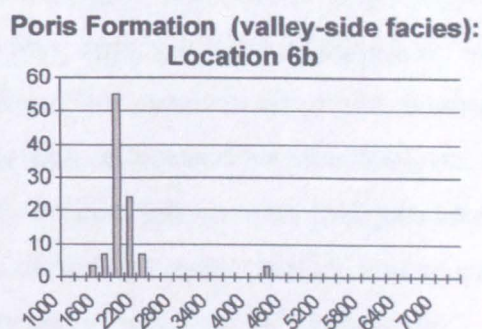
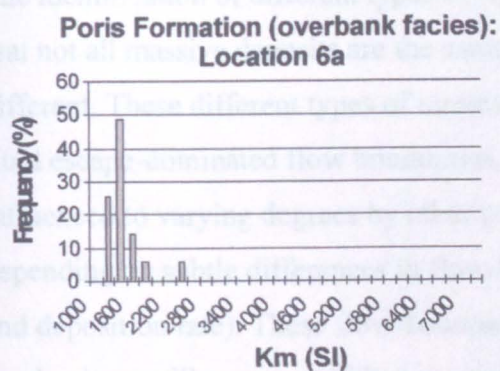


Figure 4.16: Histograms of the magnetic susceptibility of massive lithofacies from a variety of formations.

Interpretation

The identification of different types of AMS fabric in massive lapilli-tuffs (Fig 4.17) indicates that not all massive deposits are the same and that their depositional mechanisms are subtly different. These different types of massive deposits are interpreted to have been deposited at fluid escape-dominated flow boundaries, hence the lack of sedimentary structures, but were influenced to varying degrees by other processes (i.e. direct fallout, tractional, granular) depending on subtle differences in flow-boundary conditions (concentration, current velocity, and deposition rate). These flow-boundary conditions and therefore the depositional mechanisms will operate within a continuum.

mLT Type 1 massive deposit

The random AMS fabric is interpreted to be a result of high rates of supply causing a well-developed granular-fluid base. The rapid deposition prevents granular shear from influencing the flow-boundary during the final stages of deposition, and promotes fluid-escape through the semi-fluidised mass. This is thought to represent the near end-member type of fluid escape dominated flow-boundary zone (Figs. 4.18 & 4.19). Minimal granular shear prevents fabrics being produced and any weak fabrics that may develop are subsequently destroyed by the fluid escape, resulting in weak anisotropies. Random distributions of susceptibility axes have been documented from massive lapilli-tuff (Knight et al. 1986; Cagnoli & Tarling, 1997; Seaman et al. 1999), and were interpreted by Knight et al. (1986) to be a result of turbulent conditions. This is not possible because this would result in tractional processes, causing the development of better tractional bedforms, and sorting and particle orientation, creating a stronger fabric.

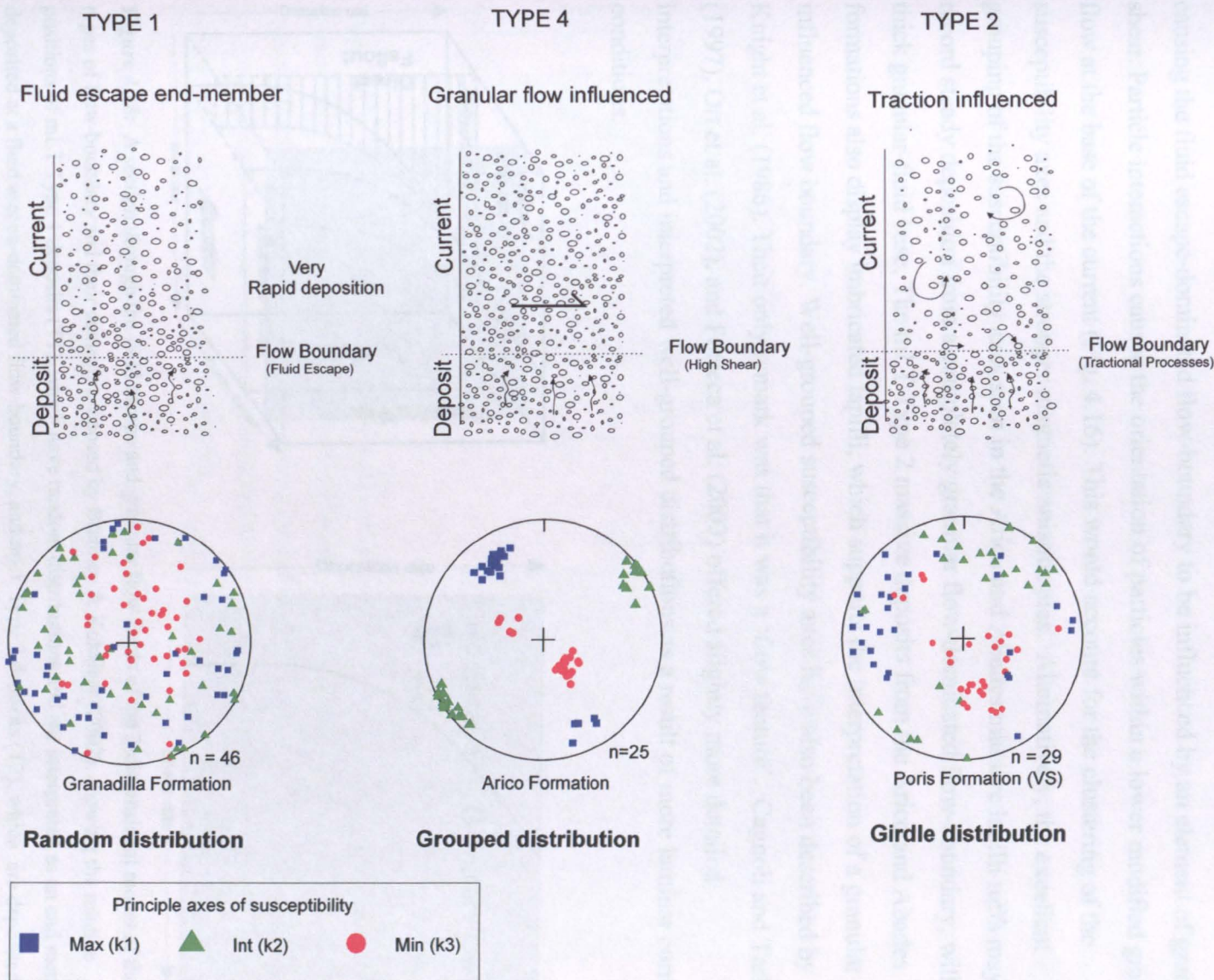


Figure 4.17: The flow-boundary conditions and the resulting AMS fabric of the different types of massive lapilli tuff deposits.

mLT Type 2 massive deposit

The well-grouped distributions of Type 2 massive lapilli tuffs are interpreted to be a result of deposition from a granular-fluid based current where the rate of supply was significant enough to establish a granular-fluid base, but the rate of deposition was less rapid than that of mLT Type 1 massive deposits, allowing lateral shear to develop at the flow-boundary causing the fluid escape-dominated flow-boundary to be influenced by an element of granular shear. Particle interactions caused the orientation of particles within a lower modified grain flow at the base of the current (Fig. 4.16). This would account for the clustering of the susceptibility axes and the stronger magnetic anisotropies. Alternatively, the excellent grouping of the susceptibility axes seen in the Arico and Abades massive lapilli tuffs may record steady deposition from a completely granular flow-dominated flow-boundary, with a thick granular-fluid base. The mLT Type 2 massive deposits from the Arico and Abades formations also display imbricated lapilli, which supports the interpretation of a granular influenced flow boundary. Well-grouped susceptibility axes have also been described by Knight et al. (1986). Their only remark was that it was a 'flow feature'. Cagnoli and Tarling (1997), Ort et al. (2002), and Porreca et al. (2003) offered slightly more detailed interpretations and interpreted well-grouped distributions as a result of more laminar current conditions.

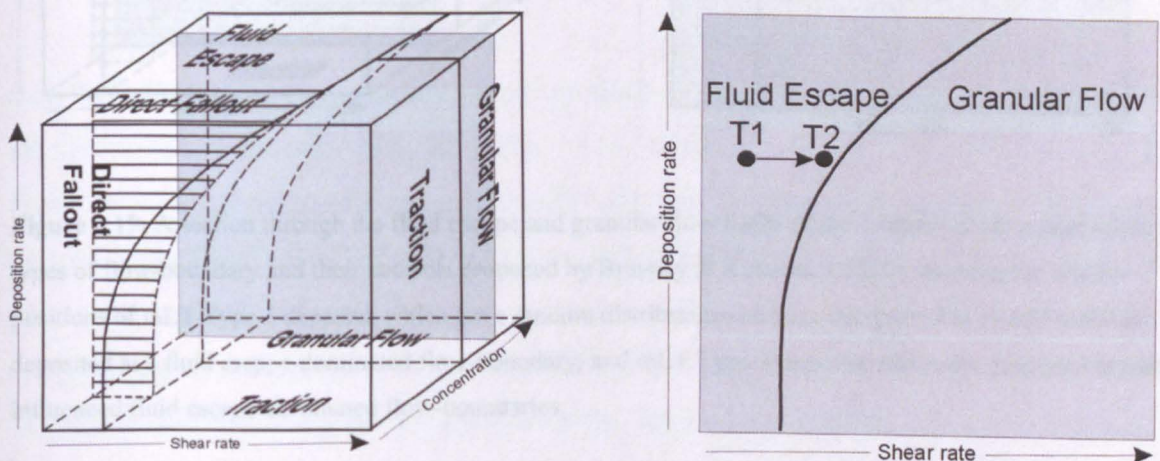


Figure 4.18: A section through the fluid escape and granular flow fields of the 3-dimensional model of the four types of flow-boundary and their controls proposed by Branney & Kokelaar (2002), showing the relative positions of mLT Type 1 deposits (T1), which have random distributions and are interpreted as an end member deposited at a fluid escape-dominated flow-boundary, and mLT Type 2 deposits (T2), which are deposited at granular flow influenced fluid escape-dominated flow-boundaries.

mLT Type 3 massive deposit

The poorly developed girdle distributions that characterise mLT Type 3 massive deposits are interpreted to reflect the influence of minor turbulence. It is inferred that the granular-fluid base was relatively thin as a result of lower rates of supply and that turbulence was able to cause traction to influence the fluid-escape dominated flow-boundary, generating some alignment and sorting, but was insufficient to generate any sedimentary structures. The inference of limited/weak turbulence is further supported by the poorly defined nature of the girdle distribution (e.g. Fig. 4.17). Girdle-distributions from massive deposits have been described by Knight et al. (1986), and Seaman et al. (1991), who made no interpretations with regards to depositional mechanism, and Ort et al. (2002) and Porreca et al. (2003), who inferred more dilute, turbulent conditions to be responsible for the formation of girdle distributions.

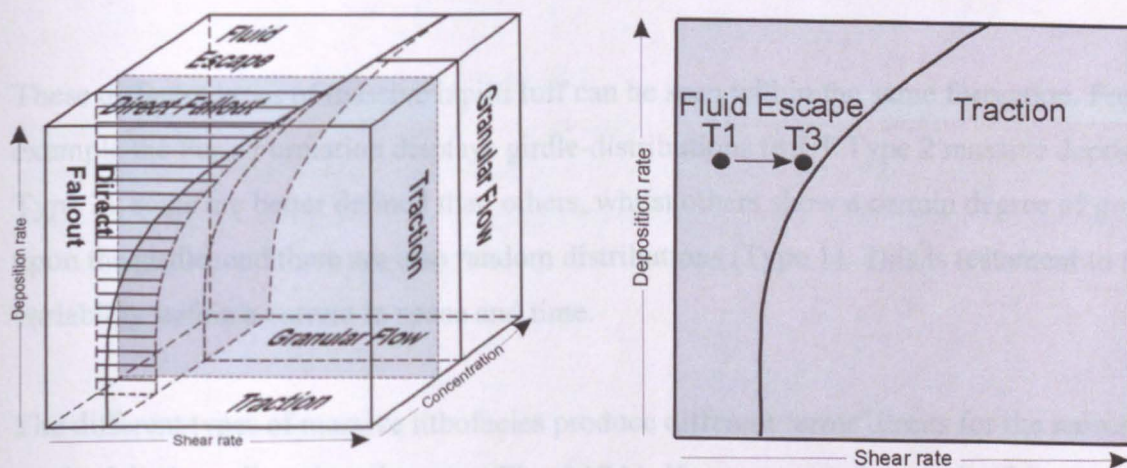


Figure 4.19: A section through the fluid escape and granular flow fields of the 3-dimensional model of the four types of flow-boundary and their controls proposed by Branney & Kokelaar (2002), showing the relative positions of mLT Type 1 deposits, which have random distributions and are interpreted as an end member deposited at a fluid escape-dominated flow-boundary, and mLT Type 3 deposits which are deposited at traction-influenced fluid escape-dominated flow-boundaries.

The term ‘surge’ was traditionally used to refer to turbulent conditions and tractional processes, whereas the term ‘pyroclastic flow’ was used to refer to laminar flows thought to be responsible for the emplacement of massive lithofacies (e.g. Sparks, 1976; Cole & Scarpati, 1993). Therefore, turbulence has not generally been associated with the formation of massive lithofacies, due to the absence of tractional sedimentary structures. The new data (Fig. 4.13) suggest turbulence and tractional processes do play some role in the deposition of massive deposits, and this reinforces the idea that there is a continuum between flows with

laminar and turbulent basal parts so that the terms ‘surge’ and ‘flow’ are no longer appropriate and should be made obsolete.

Type of massive lapilli-tuff deposit	AMS Fabric	Description of the current conditions at the flow-boundary
mLT Type 1	Random distribution	Fluid escape-dominated flow-boundary: Thick granular flow –fluid base. Rapid deposition.
mLT Type 2	Well-grouped distribution	Fluid escape dominated flow-boundary influenced by granular flow processes. Well-developed granular-fluid base. Lower rates of deposition and/or increased granular shear.
mLT Type 3	Girdle distribution	Fluid escape dominated flow-boundary influenced by tractional processes. Relatively thin granular-fluid base. mLT

Table 2: A table listing the different types of massive lapilli tuff deposits, their AMS fabrics and the relative flow-boundary conditions.

These different types of massive lapilli tuff can be seen within the same formation. For example the Poris Formation displays girdle-distributions (mLT Type 2 massive deposits Type 3), some are better defined than others, whilst others show a certain degree of grouping upon the girdle, and there are also random distributions (Type 1). This is testament to the variability within a current in space and time.

The different types of massive lithofacies produce different ‘error’ limits for the tensor mean on the foliation – lineation diagrams (Fig. 4.18A). However, this is a result of the natural variation within the deposits and is not analytical error. Type 1 massive deposits have small ‘error’ limits of 0.31-0.41% for the foliation and 0.28-0.36% for the lineation. This is somewhat surprising given the random orientation of the data. Type 2 massive deposits have intermediate error limits of 0.44-0.73% for the foliation and 0.47-0.56% for the lineation.

Type 3 massive deposits had the greatest ‘error’ limits varying from 0.6-1.87% for the foliation and 0.47-0.81% for the lineation, but were predominately greater than 0.6% overall.

When the tensor means are calculated, the orientation of the data is taken into account and has an impact on the ‘error’ limits. The reason for mLT Type 1 deposits having the weakest anisotropy may be due to the very weak anisotropies and the tensor mean plotting close to zero. Because mLT Type 2 deposits have well-grouped k1 and k2 axes the ‘error’ limits will naturally be smaller than mLT Type 3 deposits, whose k1 and k2 values are orientated across

a girdle-distribution spanning 180°. This variety of orientations is reflected in slightly larger error limits for mLT Type 3 deposits.

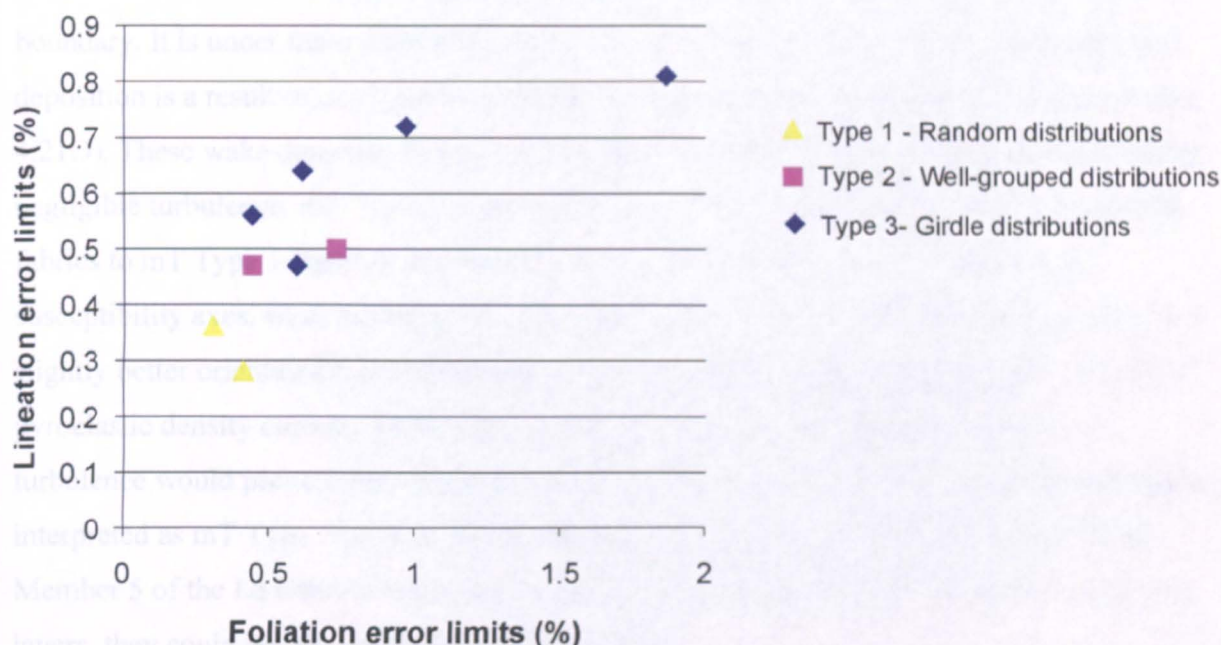


Figure 4.20: The error limits of the foliation and lineation values for the tensor means of the different types of massive lapilli tuff. These ‘errors’ are a reflection of the natural scatter of the susceptibility axes of the different types of massive lithofacies. mLT Type 3 deposits have the greatest ‘error’ because the k_1 and k_2 axes are scattered along a girdle, defining the magnetic foliation. mLT Type 2 have better grouping of the susceptibility axes and therefore have a smaller ‘error’.

4.8 Massive tuff lithofacies

Massive tuffs that lack pumice and lithic lapilli are common in modern and ancient volcanic successions (e.g. La Caleta Formation, Tenerife, Chapter 2; Poris Formation, Tenerife, Brown et al. 2004; the 1991 eruption Mount Pinatubo, Rosi et al. 2001) and can be fallout deposits, pyroclastic density current deposits or wake deposits (Chapters 2 and 3). Chapter 3 describes in detail the differences in AMS fabric between fallout and current deposits, which are the two end members. Massive tuff fallout deposits (mT Type 1; Fig. 4.21A) produce a circular distribution of susceptibility axes, whereas massive tuff current deposits (mT Type 2a; Fig. 4.21B), well-grouped distributions (mT Type 2b; Fig. 4.21C) and random distributions (mT Type 2c; Fig. 4.21D). The girdle distributions represent a traction-influenced fluid escape flow-boundary and well-grouped (lineated) distributions indicate a granular shear-influenced fluid escape flow-boundary (Fig. 4.21). The random distributions would best represent a pure fluid-escape flow-boundary.

Because depositional mechanisms operate on a continuum, it is inevitable that some deposits are a result of a combination of processes. For example, the wake of larger pyroclastic density currents will be dilute and travel at low velocities with very little lateral shear at the flow-boundary. It is under these conditions that direct-fallout can occur at the flow-boundary and deposition is a result of a combination of fallout influenced by minor amount turbulence (Fig. 4.21D). These wake deposits are here after referred to as mT Type 3 deposits. Because of the negligible turbulence, mT Type 3 (wake) deposits are anticipated to have very similar AMS fabrics to mT Type 1 (fallout) deposits, with near-horizontal circular distributions of susceptibility axes, weak anisotropies and oblate fabrics. The only slight difference may be a slightly better orientated fabric reflecting the weak turbulence associated with the wake of a pyroclastic density current. This is anticipated to be minor as any significant levels of turbulence would prevent deposition and even cause erosion. Examples of massive ash layers interpreted as mT Type 3 (wake) deposits include Member 4b and Couplets 1b and 5b of Member 5 of the La Caleta Formation (Chapter 2), but due to poor preservation of these ash layers, they could not be sampled for AMS analysis.

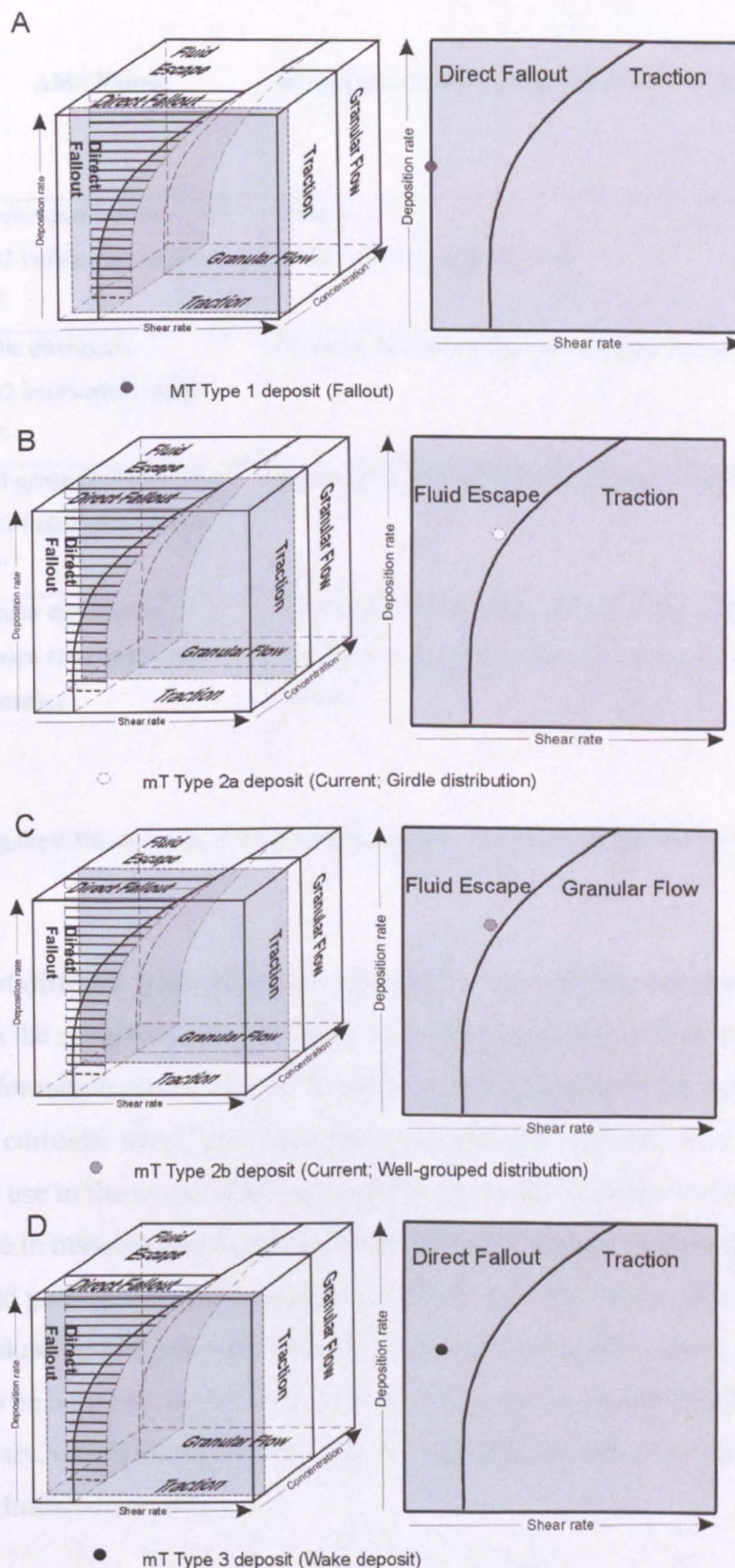


Figure 4.21: The proposed flow-boundary conditions for the different types of massive tuff; (A) Fallout would have very low concentrations and no lateral shear. Current deposits can have a fluid escape-dominated flow boundary influenced by (B) traction, forming a girdle distribution, or (C) granular flow, forming a well grouped distribution. Wake deposits are interpreted to be fallout deposits influenced by the wake of the preceding pyroclastic density current and are inferred to be deposited from a direct fallout-dominated flow-boundary (D).

Type of massive tuff deposit	AMS Fabric	Description of the current conditions at the flow-boundary
mT Type 1	Circular distribution k1/k2 imbrication angle <10°	Fallout k1/k2 imbrication angle <10°
mT Type 2a	Girdle distribution k1/k2 imbrication angle >10°	Traction influenced fluid escape flow-boundary
mT Type 2b	Well-grouped distribution k1/k2 imbrication angle >10°	Granular flow influenced fluid escape flow-boundary
mT Type 3	Circular distribution? Perhaps some preferred orientation	Direct fallout flow-boundary. Fully dilute current travelling at low velocities. Possibly the wake of a pyroclastic density current.

Table 3: A table listing the different types of massive tuff deposits, their AMS fabrics and the relative flow-boundary conditions.

The identification of different types of massive deposit has revealed that all massive deposits are not emplaced in the same way, and that there are subtle variations in flow-boundary conditions. This information can be used to further our understanding of the behaviour of pyroclastic density currents, which has important implications for hazard assessment. It could also be of potential use in the hydrocarbon industry, as the majority of the world’s hydrocarbons reside in massive sands deposited by turbidity currents. By investigating their sorting, porosity and permeability characteristics it may be possible to establish which type of massive deposit makes the best reservoir rock. For example, you might expect mLT Type 2 massive deposits to be better sorted because of being emplaced at a traction-influenced fluid-escape flow-boundary, which means that their porosity and permeability would be higher, making a better hydrocarbon reservoir.

To attempt to quantify the different AMS distributions in the different lithofacies, the standard deviation of the foliation and lineation data were plotted against one another to identify if different lithofacies had different standard deviations. However, no distinguishable groups were identifiable, and the different lithofacies overlap (Fig. 4.22).

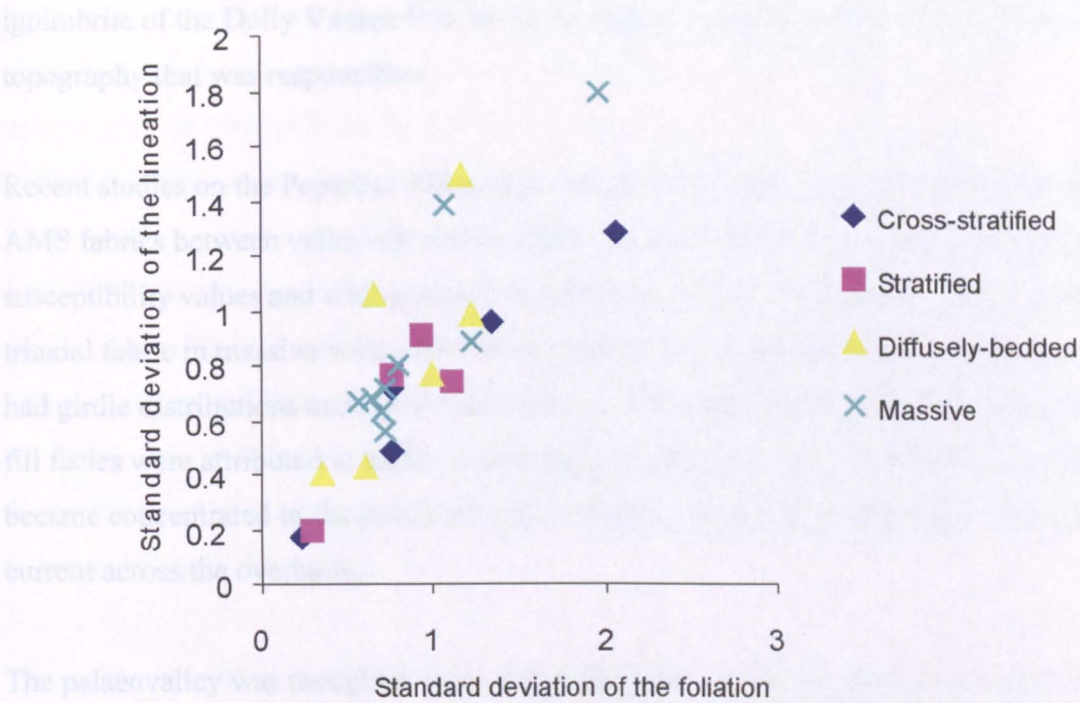


Figure 4.22: The variation in the standard deviation of the foliation-lineation data for the different lithofacies. It is not possible to characterise the different lithofacies in this way due to the substantial overlap.

4.9 The impact of topography on AMS fabrics in massive and diffuse bedded lapilli-tuffs.

The way a current behaves around topography is complex and depends on the relative height of the topography in relation to the current and on the current's properties. Pyroclastic currents are density-stratified, therefore the flow-boundary conditions will vary according to the height of the topography in the current. For example, flow-boundary conditions in a valley axis will be more concentrated and therefore less turbulent, because it is the bottom denser part of the current that is interacting with the topography. Flow-boundary conditions up the valley sides and onto the overbank will become progressively more dilute and therefore turbulent because the position in the current is higher (Fig. 2.24). This explains why massive deposits dominate valley-fill deposits (less turbulence), whereas overbank deposits are dominated by stratified and cross-stratified lithofacies (e.g. Pitarri et al. 2006). Pre-existing topography, therefore, plays a fundamental role in the distribution of deposits, the transport and depositional mechanisms of density currents, and influences the lithofacies and their fabrics. For example, a greater degree of scatter in k_1 directions in less channelised zones has also been documented by Palmer and MacDonald (1999) in the Peach Springs Tuff and the

ignimbrite of the Dolly Varden Formation, and they concluded that it was the pre-existing topography that was responsible.

Recent studies on the Peperino Albana ignimbrite (Italy) have found notable differences of AMS fabrics between valley-fill and overbank facies (Porreca et al. 2003), including higher susceptibility values and well-grouped distributions of the susceptibility axes, forming a triaxial fabric in massive valley-fill facies, whereas the overbank facies (variably stratified) had girdle distributions and more oblate fabrics. The higher susceptibility values in the valley-fill facies were attributed to higher concentrations of denser clasts, such as magnetite, which became concentrated in the palaeovalley, decreasing upwards into the upper dilute part of the current across the overbank.

The palaeovalley was thought to have channelled the current, resulting in the well-defined lineation parallel to the flow direction and the triaxial fabrics (Porreca et al. 2003), whereas the current passing over the overbank was interpreted to have been more dilute and turbulent, resulting in more tractional processes, creating a girdle distribution of k_1 and k_2 along the foliation plane. However, Porreca et al. (2003) compared different lithofacies with one another, so the flow-boundary conditions and depositional mechanisms would be different regardless of topography, restricting the investigation of the effects of topography on depositional mechanism to a large scale.

Description

In this study, massive and diffusely bedded lapilli-tuffs lithofacies were sampled from a valley-fill facies and overbank facies within the Poris Formation (Fig. 4.23). The different lithofacies from the same topographic setting were compared with another and like lithofacies compared between the different topographic settings.

The massive lapilli-tuff and the diffuse bedded lapilli-tuff from the overbank facies both have girdle-distributions that have k_1 axes 90° to the palaeocurrent direction (Figs. 4.11A & 4.15A), as indicated by the giant regressive bedform documented by Brown and Branney (2004), where diffuse inclined strata dip towards the NNW, defining a transverse fabric. The girdle distribution of diffuse bedded lithofacies does display some crude preferential grouping of the susceptibility axes and has an oblate to triaxial fabric

The massive lapilli-tuff (VF) and diffuse bedded lapilli-tuff (VF6E) in the valley-fill facies (Figs 4.11A & 4.15A) has a crude girdle-distribution upon which there is an element of grouping of the susceptibility axes (Fig. 4.24). This grouping is much stronger in the diffuse bedded lithofacies. The k_1 axes have a NW to NNW orientation, which corresponds well with the orientation of the palaeovalley axis (Fig. 4.24) and they have triaxial fabrics. Massive lapilli-tuff sampled higher in the valley-fill deposit (VF2, 5 m above the base; Fig. 4.23) has a girdle distribution highlighting a transverse fabric that is approximately perpendicular to the palaeovalley axis. Massive lapilli-tuff was also sampled approximately 10-15 m away from the valley side 10 m from the base of the palaeovalley floor. This produced a girdle distribution defining a foliation that dips to the WNW to NW. Samples VF2 and VS both had oblate to triaxial fabrics (Figs. 4.15B).

The diffusely-bedded lapilli tuffs in both palaeotopographic settings have stronger anisotropies compared to the massive lapilli-tuffs, and have lower angles of imbrication with respect to bedding (valley-fill 13° and overbank 15.8° respectively) than the massive lithofacies (valley-fill 22.9° and overbank 34°). Valley-fill facies have higher magnetic susceptibilities (Figs. 4.12 & 4.16) and stronger anisotropies, with a better-developed foliation and lineation, and lower angles of imbrication, compared to the overbank facies (Figs 4.11 & 4.15)

Interpretation

The girdle-distribution and transverse fabrics in the massive lapilli tuff from the overbank facies suggests a fluid escape-dominated flow-boundary influenced by tractional processes. The slight grouping of susceptibility axes on the girdle distribution from the diffuse bedded lapilli-tuff belonging to the overbank facies suggests that increased granular shear was influencing the flow boundary with an element of traction (dbLT Type 1; Section 4.6.2), which would account for the lower angles of imbrication of the magnetic foliation in relation to bedding. It may also help account for their stronger anisotropies compared with the massive lithofacies. The overbank setting would have been exposed only to the higher more dilute parts of the pyroclastic current and consequently the flow-boundary zone would have been less concentrated, promoting turbulence and traction, resulting in girdle-distributions and weaker anisotropies (Fig. 4.24). The change from diffusely-bedded lapilli-tuff to massive lapilli-tuff in the overbank suggests that the flow-boundary conditions became relatively more

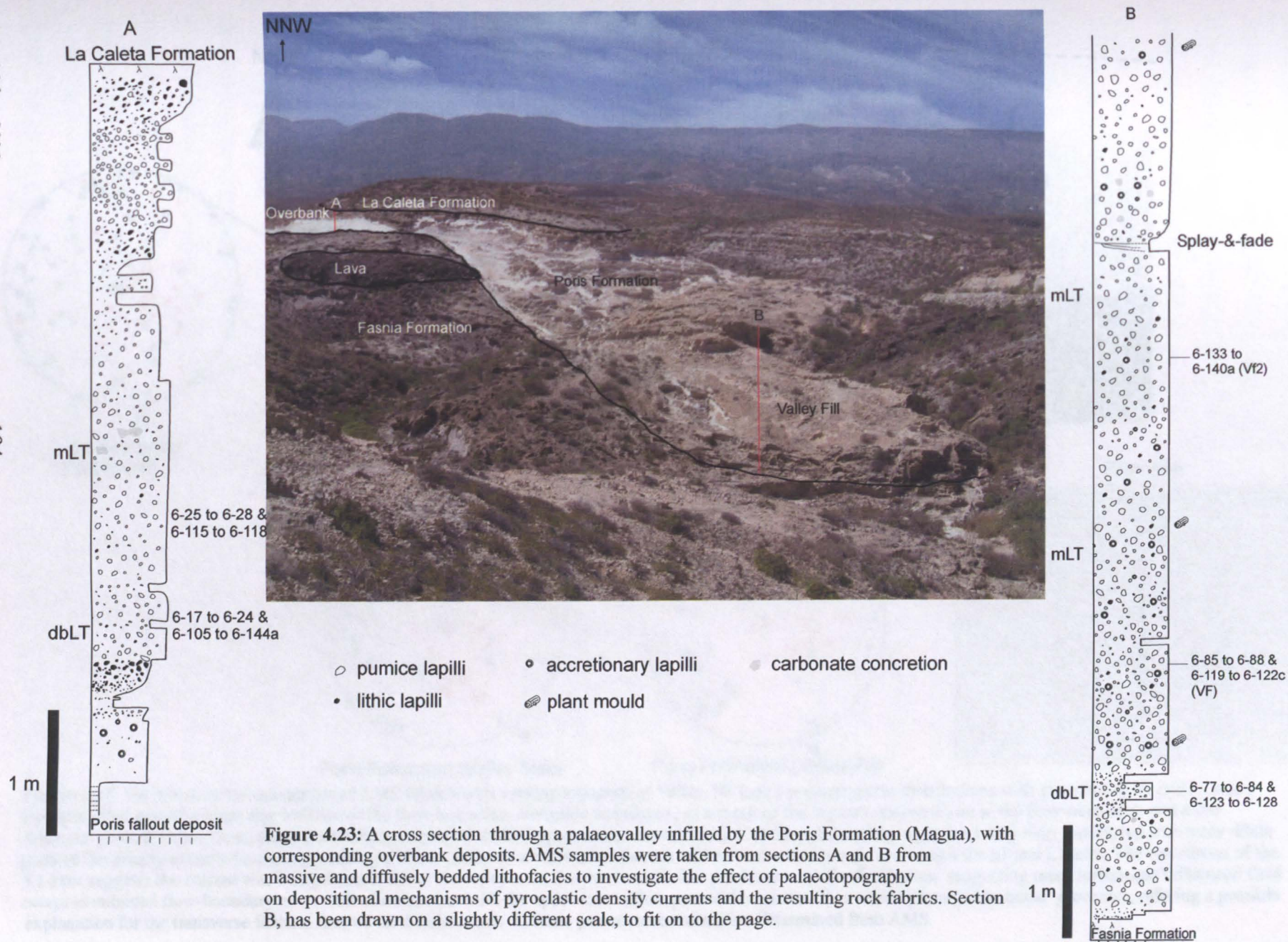
concentrated, with an increase in deposition rate, which would have enhanced fluid escape and hindered settling, resulting in a massive lithofacies.

The girdle distributions in all the massive deposits within the valley-fill indicate that although the flow-boundary was dominated by fluid-escape, traction and granular flow processes were able to influence the flow boundary (mLT Type 3a deposits; Section 4.7). The grouping of the susceptibility axes seen in sample VF suggests that granular shear was also influencing the flow boundary (mLT Type 3b deposits). This is because the densest part of the pyroclastic current is found in the valley axis, and consequently the flow-boundary conditions are more concentrated promoting granular shear. The parallel orientation of the k_1 axes with the valley axes is evidence of the effect topography had on the depositional mechanisms and can help to account for the better clustering of susceptibility axes, stronger anisotropies, and the a more prominent lineation. A greater element of granular shear would also explain why the imbrication angle of the AMS foliation is less in the valley-fill deposits. The transverse fabric (k_1 perpendicular to current direction) in sample VF2, suggests lower concentrations at the flow-boundary zone and a greater influence from tractional processes. The girdle-distribution becomes much better defined in the sample taken from the valley-side, suggesting a further decrease in concentration of the flow-boundary and a stronger influence from tractional processes, due to density stratification in the current (Fig. 4.24). The change in orientation of the k_1 axes in the massive lapilli tuff sampled from the valley-side suggests that the current was being channelled into the valley axis (Fig 4.24).

The diffusely bedded lithofacies sampled within the valley-fill facies produced a much stronger anisotropy compared to the massive deposits in the valley facies, and these were oblate to triaxial with relatively well-grouped k_1 and k_2 axes along the magnetic foliation suggesting a granular flow-dominated flow-boundary (Section 4.6). Lower imbrication angles compared to the massive deposits within the valley-fill facies, result from increased granular shear. The change from diffusely bedded lithofacies to massive lithofacies in the valley-fill deposits is interpreted to represent an increase in concentration and rate of deposition at the flow boundary. This would have the effect of suppressing turbulence and granular shear and enhancing fluid escape, resulting in the formation of a massive deposit.

Fabrics from experimentally deposited sediments (e.g. Rees & Woodall, 1974) reveal that deposits derived from higher concentration currents produce a foliation with a high angle of

imbrication (e.g. 11-22°). Granular flow-fluid based pyroclastic density currents undergoing rapid deposition (Fluid-escape dominated) may produce higher imbrication angles as hindered settling prevents the development of granular shear (i.e. valley-fill facies). Currents undergoing less rapid deposition (i.e. overbank facies) will be able to exert a greater amount of shear, resulting in lower imbrication angles. This may account for the lower imbrication angle in the overbank facies, which increases down the palaeovalley side, and into the valley-fill facies, downwards to where the concentration of the current would have been greater.



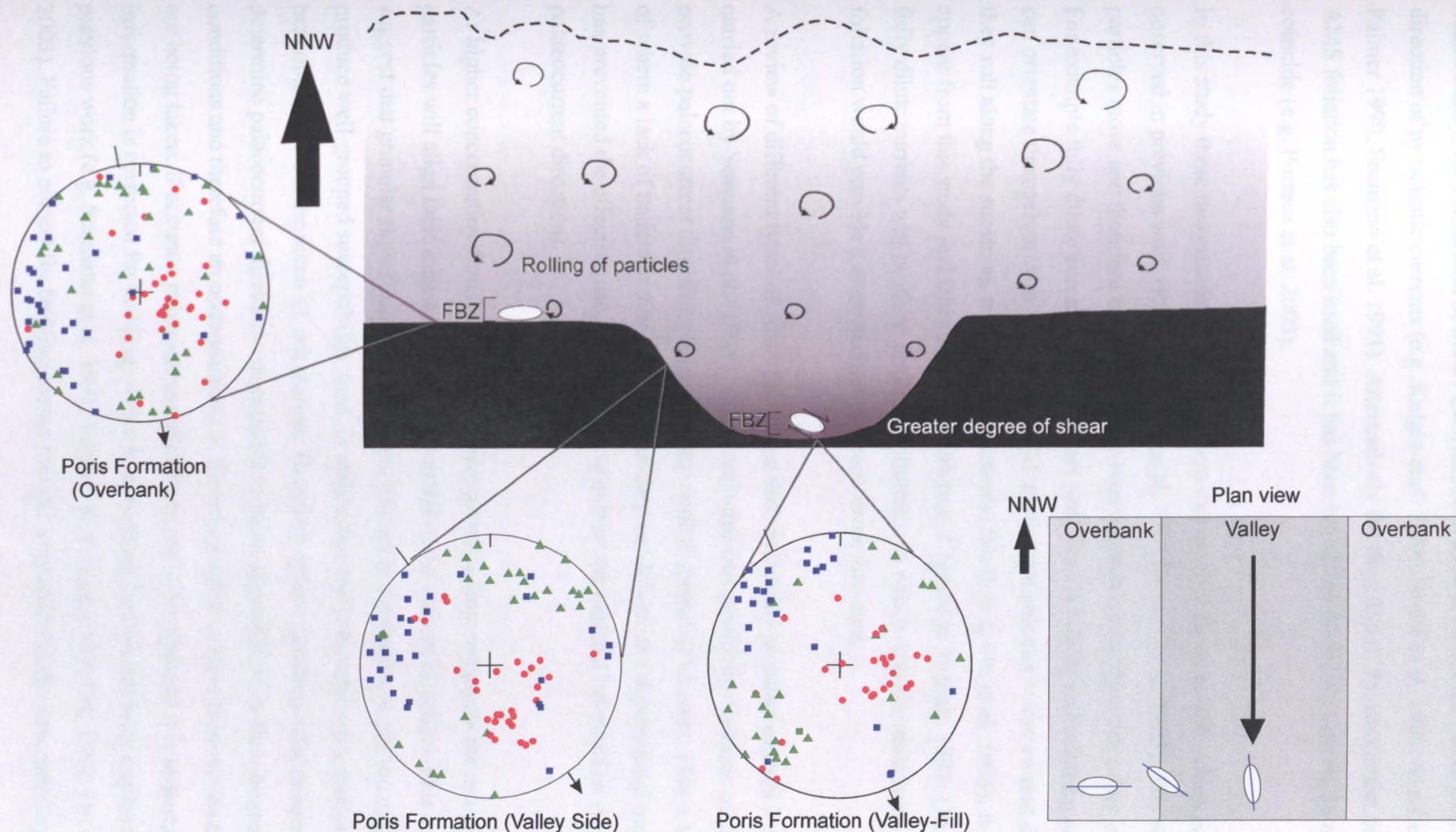


Figure 4.24: Variations of the orientation of AMS fabrics with varying topography. Valley-fill facies produce girdle distributions with grouping of k_1 and k_2 axes, indicating that granular shear also influenced the flow-boundary, alongside turbulence, as a result of the higher concentrations at the flow-boundary and more frequent particle interactions, forcing a stronger alignment which approximates the orientation of the palaeovalley axis; the valley side, interacted with more dilute parts of the density-stratified current producing a better girdle distribution, but there is still an element of grouping amongst the k_1 and k_2 axes. The orientation of the k_1 axes suggests the current was being funnelled into the valley axis; the overbank facies produces a girdle distribution suggesting more turbulence influenced fluid escape-dominated flow-boundary as a result of interaction with the upper more dilute part of the current. This would promote tractional processes, offering a possible explanation for the transverse fabrics. Arrows on the stereonet indicate palaeocurrent direction determined from AMS.

Traditionally, the orientation of the k_1 axes has been used to define the palaeocurrent direction of pyroclastic currents (e.g. Knight et al. 1986; Wolff et al. 1989; MacDonald & Palmer 1990; Seaman et al. 1991). Alternatively the direction of the maximum dip of the AMS foliation has also been used and it has been noted that these two criteria do not always coincide (e.g. Porreca et al. 2003).

In this study these two criteria can deviate from one another by up to 90° , which has also been observed in previous work (Rees, 1979; Ort et al. 1993 Porreca et al. 2003). The way in which particles move and therefore orientate themselves depends on the flow-boundary conditions. For example fully dilute currents will transport particles via rolling and saltating and particles can orientate themselves with the long axis (k_1 axis) perpendicular to the current direction as they roll along the substrate, producing a transverse fabric (e.g. Ort et al. 1993). It would appear from this study and from previous work (e.g. Cagnoli & Tarling, 1997; Ort, 1999) that fully dilute currents will produce girdle distributions, in which case the maximum dip of the foliation would provide a more accurate palaeocurrent direction.

A review of different types of AMS fabric and their suitability as palaeocurrent indicators was carried out by Seaman et al. (1991). They concluded that girdle distributions could not provide palaeocurrent directions because of the wide dispersal of k_1 axes. This is an example of where a lack of understanding of flow-boundary conditions and depositional mechanisms has prevented the effective use of AMS data to extract meaningful information (i.e. palaeocurrent direction).

At higher concentration flow-boundaries, where granular flow processes are more dominant, particles will align their long axis (k_1 axis) parallel to the current direction. This study would suggest that granular flow-fluid based currents, providing deposition is not too rapid, will produce well-grouped susceptibility axes, in which case the palaeocurrent direction would be best obtained from the mean k_1 orientation. Therefore before deciding what criteria to use to determine palaeocurrent directions there needs to be an appreciation of flow-boundary conditions and therefore an understanding of the topographic context from which the samples are being taken. If accurate palaeocurrent directions are to be obtained it is important that the information is corrected for bedding, which is something that has not been implemented in previous work (e.g. Seaman et al. 1991; Cagnoli & Tarling, 1997; Ort, 1999; Ort et al. 2003). Failure to correct for bedding means that the orientation of the susceptibility axes

could be inaccurate and the resulting imbrication, as defined by the AMS foliation, may be meaningless.

4.10 Summary and conclusions

For the first time, AMS has been used to recognise and interpret variations in flow-boundary zone conditions and depositional mechanisms, and different lithofacies have been characterised by their AMS fabrics. The four fabric types (girdle distribution, well-grouped distributions, random distributions and circular distributions) have been interpreted in terms of the four end-member flow boundary zones presented by Branney & Kokelaar (2002) allowing a semi-quantification of the flow-boundary model.

Although one type of flow-boundary zone dominates, each of these end members (direct fallout, traction, fluid escape, and granular shear) operates on a continuum and a combination of processes can occur simultaneously depending on the concentration of the flow-boundary zone, shear rate, and the deposition rate.

Cross-stratified lithofacies were characterised by girdle-distributions. Since traction is the known cause for cross-stratified lithofacies the girdle distribution was interpreted to signify the presence of turbulence and tractional processes. Where the cross-stratification was not as well developed, resulting in a less well developed girdle distribution, turbulence was interpreted to be restricted, perhaps due to an increase in concentration and rates of deposition, causing fluid escape to play a greater role in the flow-boundary zone, preventing the development of well-defined cross-stratification and girdle distributions (Table 3).

Stratified lithofacies also had girdle distributions suggesting the occurrence of turbulence and traction at the flow boundary, although there was an example of well grouped (lineated) distributions, which were interpreted to indicate an increase in granular shear at the flow boundary as a result of increased concentrations at the base of the current (Table 3).

Diffusely-bedded lithofacies had well-grouped (lineated) distributions, which are interpreted to indicate granular-fluid based current, where granular shear dominates at the flow-boundary zone. They also have girdle distributions that displayed an element of grouping of the susceptibility axes. This is interpreted to represent a less well-developed granular-fluid based

current, where turbulence is still able to influence the granular flow-dominated flow boundary (Table 3). The diffuse bedding is a result of the passage of an unsteady pyroclastic density currents with periodic turbulent eddies sweeping away the granular-fluid base (grouping of susceptibility axes on the girdle distribution) or periodic shear exerted on the granular-fluid base by overriding turbulent eddies (well-grouped distribution).

Massive lapilli tuffs can be subdivided into three types: (1) those that produce a random distribution of susceptibility axes (mLT Type 1) and represent near end-member fluid escape dominated flow boundaries; (2) well grouped distributions of susceptibility axes (mLT Type 2), which represent granular flow influenced fluid escape flow boundaries or granular flow-dominated flow-boundaries of steady currents; and (3) girdle distributions which represent traction-influenced fluid escape flow-boundaries. The presence of crude grouping on these girdles would suggest an element of granular shear was acting within the flow-boundary zone (Table 3).

Massive tuffs (Table 3) can be subdivided into three types: (1) fallout deposits, which have circular distributions of susceptibility axes (mT Type 1); (2) pyroclastic current deposits, which have a variety of fabric types including girdle distributions (mT Type 2a), interpreted to represent traction-influenced fluid escape flow-boundaries, and well-grouped distributions (mT Type 2b), which are interpreted to represent granular flow-influenced fluid escape flow-boundaries; (3) wake deposits (mT Type 3), deposited from a direct fallout flow-boundary of the wake of a preceeding pyroclastic current. This type of massive tuff is anticipated to form at a direct fallout-dominated flow boundary and to have a very similar AMS fabric to mT Type 1 (fallout) deposits, but may have a slightly better orientated fabric. The identification of different types of massive deposits confirms that massive deposits do not all share identical flow-boundary conditions and depositional mechanisms, but are a result of subtle variations, within a continuum, dependent upon rates of deposition, rate of shear and concentration of the flow-boundary zone. This idea is supported by the presence of intermediate fabrics.

The massive lapilli-tuff samples from the valley-fill facies (mLT) are interpreted to have been deposited from a (relatively) higher concentration flow-boundary, dominated by fluid-escape, but influenced by tractional and granular processes, as indicated by an element grouping of the susceptibility axes along a girdle distribution. The flow-boundary became more dilute with time causing transverse fabrics. The massive lapilli-tuff from the overbank facies is

interpreted as an mLT Type 2 deposit emplaced from a fluid escape-dominated flow-boundary influenced by traction

The diffusely-bedded lapilli tuff from the valley-fill facies had a strong grouping on the girdle distribution and was interpreted as dbLT Type 2 deposit emplaced at a granular flow-dominated flow-boundary influenced by a certain amount of traction. The diffusely bedded lapilli tuff from the overbank facies did not have such a strong grouping of axes on the girdle distribution and was interpreted to have been emplaced at a granular flow-dominated flow boundary, but with a greater tractional influence than the diffusely-bedded lithofacies in the valley-fill deposits. Overall the valley-fill deposits have greater magnetic susceptibilities, a greater linear component and lower angles of imbrication compared to the corresponding overbank facies (mLT and dbLT). The AMS fabrics of massive and diffusely bedded lapilli tuffs from different topographic settings have been interpreted to be a result of a density-stratified current interacting with topography. This controlled the flow-boundary conditions according to the position of the topography in relation to the height within the current. As the topography is infilled the denser more concentrated base of the current starts to interact more with the valley sides and the overbank. Therefore one might expect to see more mLT Type 1 or 2 deposits higher up in the sequence.


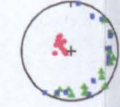

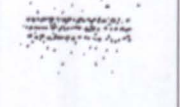
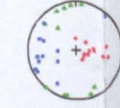


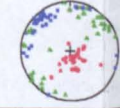

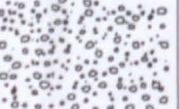
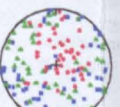

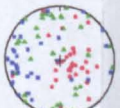
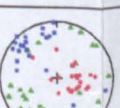

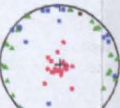
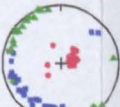


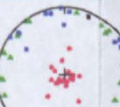
Lithofacies	Appearance	Description	Interpretation	AMS Fabric	Flow-boundary conditions
Cross-stratified tuff (xsT)		Lithology: Ash to fine pumice/lithic lapilli. Structure: Low angle cross-stratification dipping up- or down stream at 5-15°; defined by horizons of fines, lithic- and pumice lapilli <10 mm. Occurrence: Isolated bedforms within variably massive and stratified lithofacies from 8-30 cm in height. The Caldera del Rey xsT consists of large sequence of cross-stratified lithofacies separated by ash layers.	Deposited by pyroclastic density currents of sufficiently low concentration as to allow turbulent eddies to impinge on the flow boundary promoting sorting via tractional processes, producing ripple and dune bedforms.	(xsT Type 1 deposit) Girdle distribution k1 and k2 susceptibility axes define a girdle distribution (foliation). 	Fully dilute current Traction-dominated flow-boundary Relatively low rates of deposition
				Grouped on a girdle distribution (xsT Type 2 deposit) k1 and k2 susceptibility axes group on the girdle distribution. 	Dilute current with a thin granular fluid base Traction-dominated flow-boundary influenced by granular shear Relatively low rates of deposition
Stratified tuff (sT)		Lithology: Predominantly ash grade material, occasionally supporting coarser pumice and lithic lapilli. Structure: Thin tractional sub-parallel boundaries (<10 mm) defined by fluctuations in grain size. Individual strata may pinch and swell slightly. Occurrence: Can be laterally persistent or fade laterally into massive lithofacies. Frequently found in multiple sets, which can be up to 1-2 m thick.	Progressive aggradation from an unsteady current with a degree of turbulence, promoting sorting, and therefore defining individual strata.	Girdle (sT Type 1 deposit) 	Fully dilute current Traction-dominated flow-boundary Relatively low rates of deposition
				Well-grouped (sT Type 2 deposit) 	Dilute current with a thin granular-fluid base Traction-dominated flow-boundary influenced by granular shear. Relatively low rates of deposition
Diffusely-bedded lapilli tuff (dbLT)		Lithology: Varying proportion of sub-rounded to rounded pumice lapilli and subrounded to angular lithic lapilli contained within an ash matrix. Structure: Individual beds are massive and are on a decimetre scale. Individual beds are defined by subtle and gradual changes in grain size. Occurrence: Typically in multiple units. Laterally persistent. Can transform laterally into massive lithofacies. Often found near palaeotopographic margins fading into valley-fill sections.	Progressive aggradation of internally massive beds, with periods of slower deposition and the presence of turbulent eddies at the flow boundary (current unsteadiness), causing definition of individual beds.	Grouped on a girdle distribution (dbLT Type 1 deposit) 	Well developed granular-fluid base Granular-dominated flow-boundary Bedding surfaces generated by shear exerted by overriding turbulence
				Well-grouped (dbLT Type 2 deposit) 	Less well developed granular-fluid base Granular-dominated flow-boundary, influenced by traction. Bedding surfaces generated by the periodical sweeping away of the granular fluid base by turbulent eddies.
Massive lapilli tuff (mLT)		Lithology: Varying proportion of sub-rounded to rounded pumice lapilli and subrounded to angular lithic lapilli contained within an ash matrix. Poorly sorted. Structure: Massive. Lacks internal stratification and bedding. May exhibit imbrication of pumice and lithic lapilli and/or grading patterns. Occurrence: Pinch and swell, infilling palaeotopography. May laterally diversify into variably stratified and diffusely bedded lithofacies.	Rapid progressive aggradation from a concentrated current. Branney and Kokelaar (2002) proposed that fluid escape is dominant at the flow-boundary.	Random (mLT Type 1 deposit) 	Well developed granular-fluid base Fluid escape-dominated flow-boundary Rapid deposition
				Well-grouped (mLT Type 2 deposit) 	Well developed granular-fluid base Fluid escape-dominated flow-boundary, influenced by granular flow, suggesting slower rates of deposition. Or Granular dominated flow-boundary zone at the base of a steady current.
				Girdle distribution (mLT Type 3a deposit) 	Thinner granular-fluid base Fluid escape dominated flow-boundary, influenced by traction, suggest slower rates of deposition and lower concentrations at the flow boundary
				Grouped on a girdle distribution (mLT Type 3b deposit) 	
Massive tuff (mT)		Lithology: Typically a fine ash. Not possible to observe clast shape or sorting. May contain pellets, coated pellets and accretionary lapilli. Can coarsen and thicken laterally into lapilli-tuffs or pumice lapilli. Structure: Massive. Lacks internal stratification and bedding. May display subtle grading patterns. Occurrence: Common in modern and ancient volcanic successions. They can drape topography remaining a uniform thickness (ashfall deposits) or they can infill topography; thickening into topographic lows and thinning over topographic highs (pyroclastic density current deposits).	Depending on the field relations, massive tuff can be ashfall deposits (Plinian or co-ignimbrite), pyroclastic density current deposits or wake deposits.	Circular distribution (mT Type 1 deposit) 	Fallout. This can be from a Plinian eruption, in which case there would be systematic and regional variations in grain size and thickness, or co-ignimbrite ash fall, in which case the thickness would remain fairly constant and there would be no change in grain size
				Girdle distribution (mT Type 2a deposit) 	Pyroclastic density current deposits Traction-influenced fluid escape flow boundary. Poorly developed granular-fluid based current.
				Well-grouped distribution (mT Type 2b deposit) 	Pyroclastic density current deposit. Granular influenced fluid escape flow boundary. Thin granular fluid based current. Exceptionally well grouped fabric might suggest deposition from a steady current from a granular-dominated flow-boundary
				Random distribution (mT Type 2c deposit) 	Granular-fluid based. Pyroclastic density current. Pure fluid escape dominated flow-boundary.
				(mT Type 3 deposit) Predicted to have a circular distribution 	Wake deposit: Direct fallout flow boundary. Fully dilute current travelling at low velocities. Fallout influenced by the wake of a pyroclastic density current.

Table 3: A new categorisation of the sampled lithofacies, documenting their physical appearance, their AMS fabrics and interpretations of the flow-boundary conditions and depositional mechanisms.

Understanding previous eruptions by examining their deposits is an important way of anticipating potential future hazards. Different flow-boundary conditions affect the way in which pyroclastic density currents behave, therefore the recognition of different flow-boundaries from AMS fabrics and how they evolve with time may provide information about the mobility and palaeocurrent directions of past pyroclastic currents. Information about relative rates of deposition could give an indication of how quickly a current was being depleted, which would affect its mobility and distance travelled from source, which is an important considerations when making hazard assessments.

The identification of different massive ignimbrites has filled a gap in the understanding regarding their formation, and there is now the potential to extract more information about flow-boundary conditions and depositional mechanism, even in the absence of sedimentary structures. The identification of different types of massive deposits may also be possible in massive sands deposited by turbidity currents. It is feasible that some massive types may make better oil and gas reservoirs, and if these different types of massive deposit can be constrained to certain topographic settings, this information could be useful in oil and gas exploration.

Chapter 5: Conclusions

5.1 The event history of the La Caleta eruption.

This thesis presents the first detailed stratigraphic study and interpretation of the La Caleta Formation, Tenerife. The 221ka La Caleta eruption resulted in the deposition of $> 15 \text{ km}^3$ of phonolitic ignimbrites and fallout deposits across the Bandas del Sur Region of Tenerife, potentially covering an area of 533 km^2 . The eruption produced an eruption column that reached heights of 36 km, which deposited Plinian fallout (members 1 & 2). The eruption column then became unstable and collapsed causing periodic fountaining, generating a series of pyroclastic density currents. Between the pyroclastic density currents, co-ignimbrite ash fall was able to deposit over a large area, which locally may have interacted with the wake of preceding pyroclastic density currents (members 3-5). The injection of a secondary magma type (tephriphonolite), may have triggered a waxing of the eruption, causing more sustained pyroclastic density currents, resulting in the deposition of Member 6 and culminating in caldera collapse and the emplacement of inversely graded lithic breccias.

This study of the La Caleta Formation has highlighted the importance of correctly identifying the presence of co-ignimbrite fallout deposits, as they signify a hiatus in the passage of pyroclastic density currents and, more importantly, they signify the passage of a pyroclastic density current even when there is no pyroclastic current deposit. This is an important consideration for hazard assessment of populated volcanically active regions.

5.2 Discrimination of fine ash fallout and fine ash current deposits, using AMS.

Volcanic fallout and pyroclastic density currents are both highly hazardous, but the latter presents a far greater threat to human populations. Since both of these phenomena can emplace fine ash layers, the ability to distinguish between fine ash fallout and fine ash pyroclastic density current deposits is vital.

A new methodology for distinguishing between ashfall and fine ash pyroclastic current deposits, using Anisotropy of Magnetic Susceptibility (AMS), has been presented in this thesis and successfully applied to ash layers from Tenerife (Canary Islands) and Arizona (USA). The methodology is a relatively quick and cost-effective means of investigating fine scale, three-dimensional fabrics, and can be used on lithified deposits that cannot be subject to granulometric studies.

The ashfall deposits were found to have oblate fabrics with circular distributions, with a numerical mean lineation of $<0.5\%$ and a mean $k1/k2$ foliation dipping $<10^\circ$, whereas the fine ash current deposits displayed greater variability with regards to their AMS fabric, reflecting the natural current variability. The fabrics were less oblate than ashfall deposits and border on being triaxial and prolate. They have higher mean imbrication angles of the magnetic foliation and higher numerical mean lineations, reflecting the lateral shear generated by pyroclastic density currents. The different types of distribution of the susceptibility axes (girdle distributions, girdle distributions with an element of grouping of the $k1$ and $k2$ axes and well grouped distributions) have been used to infer relative flow-boundary conditions (concentration, shear rate, and rate of deposition).

The distinction between ashfall and fine ash pyroclastic density current deposits using the traditional AMS plots can be equivocal, so a new discriminant plot using the numerical mean lineation and the imbrication angle of the mean $k1/k2$ foliation has been constructed, with the ashfall and pyroclastic density current deposits plotting in separate fields. It is anticipated that further sampling may result in an overlap, which may provide a useful means of identifying wake deposits, resulting from the interaction of co-ignimbrite ashfall with the wake of a preceding pyroclastic density current.

5.3 Characterisation of different ignimbrite lithofacies and their depositional mechanisms.

This thesis presents a new categorisation for lithofacies based on their AMS fabrics, which have been interpreted in terms of the flow-boundary model presented by Branney and Kokelaar (2002) for the first time. Although one type of flow-boundary zone dominates, each of these end

members (direct fallout, traction, fluid escape, and granular shear) operates in a continuum and a combination of processes can occur simultaneously depending on the concentration of the flow-boundary zone, shear rate, the deposition rate and the rate of supply of pyroclastic material.

Girdle distributions found in cross-stratified and parallel-stratified lithofacies have been interpreted to represent traction dominated flow-boundary conditions in a fully dilute current. Where there is any clustering of susceptibility axes on the girdle, granular shear is interpreted to be influencing the flow-boundary zone.

Diffusely-bedded lithofacies were found not to produce such well-defined girdle distributions, and there is an element of clustering of the susceptibility axes. Alternatively they have very well-grouped distributions of susceptibility axes. Diffusely-bedded lithofacies are interpreted to have been deposited at a granular flow dominated flow-boundary zones. The diffuse bedding is a result of the passage of unsteady pyroclastic density currents, with periodic turbulent eddies sweeping away the granular-fluid base (grouping of susceptibility axes on the girdle distribution) or periodic shear exerted on the granular-fluid base by overriding turbulent eddies (well-grouped distribution).

Massive lapilli tuffs have been subdivided into three types: (1) those that produce a random distribution of susceptibility axes (mLT Type 1) and represent near end-member fluid escape dominated flow-boundaries, (2) well-grouped distributions of susceptibility axes (mLT Type 2), which represent granular flow influenced fluid escape flow-boundaries, or granular flow dominated flow-boundaries of steady currents, and (3) girdle distributions, which represent traction-influenced fluid escape flow-boundaries. The presence of crude grouping on these girdles suggests an element of granular shear was also influencing the flow-boundary zone. Massive tuffs (Table 3) can be subdivided into three types: (1) fallout deposits, which have circular distributions of susceptibility axes (mT Type 1); (2) pyroclastic current deposits, which have a variety of fabric types including girdle distributions (mT Type 2a), interpreted to represent traction influenced fluid escape flow-boundaries, and well-grouped distributions (mT Type 2b), which are interpreted to represent granular flow influenced fluid escape flow boundaries; (3) wake deposits (mT Type 3), which are anticipated to have a circular distribution and be deposited from a direct fallout dominated flow-boundary. The identification of different massive ignimbrites has filled a gap in the understanding of their formation and confirms that massive

deposits are not identical, rather they are a result of subtle variations within a continuum, depending on rates of deposition, rate of shear and concentration of the flow-boundary zone. There is now the potential to extract far more information about flow-boundary conditions and depositional mechanism, even in the absence of sedimentary structures.

The comparison of massive and diffusely-bedded lithofacies from different topographic settings (valley-fill and overbank) reveals variations in AMS fabric that are interpreted to be a result of subtle variations in flow-boundary zone conditions, due to a density-stratified current interacting with topography. The flow-boundary zone conditions are determined according to the position of the topography in relation to the height within the current (i.e. the more concentrated flow-boundary zones are found in topographic lows, where the pyroclastic density current is its most concentrated and the upper more dilute part of the current interacts with the topographic highs).

5.4 Suggestions for further work

5.4.1 *The event history of the La Caleta eruption*

The isopach and isopleth data for members 1 and 2 could be extended and the internal stratigraphy of Member 1 could be documented in more detail (i.e. internal isopach and isopleth data) and correlated over a larger area. This has the potential to reveal how the initial phase of the eruption evolved and would constrain variations in eruption column height and distribution. It would be beneficial to trace the La Caleta Formation upslope towards the source and attempt to correlate it with members observed in the wall of the Las Cañas caldera. This would further constrain the depositional limits and source of the La Caleta eruption.

A more detailed geochemical and petrological study of the La Caleta Formation would provide information about the magma source and how it evolved during the eruption. Better comparisons could then be made with other formations within the Upper Bandas del Sur Group, which would provide an insight into how the magma source for the Upper Bandas del Sur Group has varied with time, and whether there has been a common source or multiple sources.

5.4.2 Discrimination of fine ash fallout and fine ash current deposits

The discrimination of fine ash fallout and current deposits could be built upon by applying the same methodology to fine ash layers from around the world to remove ambiguities about the origin of fine ash layers. The same methodology could also be applied to hybrid fallout deposits (Wilson & Hildreth, 1998) to see if they have a distinct AMS signature. This would aid in the recognition of previously unrecognised hybrid deposits and further our understanding of the depositional processes involved in their emplacement.

The AMS work carried out on fine ash layers could be supplemented with image analysis of SEM images taken from three orientated, mutually perpendicular surfaces and analysis of the main petrographic and textural components of the fine ash layers to help differentiate the dominant process. This may provide further means of discriminating between fine ash layers of different depositional origin, on the basis of the shape of the fabric and the microscopic imbrication of ash particles. One would anticipate current deposits to have a stronger linear component with a greater degree of imbrication than fallout deposits. It would also provide an opportunity to establish if there is any discrepancy in palaeocurrent direction obtained from AMS and petrological fabrics.

5.4.3 Characterisation of different types of massive deposits and its application to the oil industry

Since a vast amount of the world's hydrocarbons are found in massive sands, and having established that there are different types of massive deposit in pyroclastic current deposits, it would be useful to establish if these different types of massive lithofacies exist in massive sands deposited by turbidity currents. If they do exist, it would be of interest to establish if one particular massive type makes a better hydrocarbon reservoir than another. This would involve investigating the porosity and permeability of the different massive types. Good reservoirs would require good porosity and a high level of permeability, which is best accommodated in well-sorted deposits. Therefore Type 2 massive sands deposited at a traction-influenced flow-boundary might be expected to make the best hydrocarbon reservoirs.

References

- Ablay, G.J., Ernst, G.G.J., Martí, J., & Sparks, R.S.J., 1995, The ~ 2 ka subplinian eruption of Montaña Blanca, Tenerife: *Bulletin of Volcanology*, **57**, 337–355.
- Ablay, G. & Hürlimann, M. 2000. Evolution of the north flank of Tenerife. *Journal of Volcanology and Geothermal Research*, **103**, 135-159
- Allen, J. R. L. (1963). The classification of cross-stratified units with notes on their origin. *Sedimentology*, **2**, 93
- Allen, J. R. L. (1979). Features of cross-stratified units due to random and other changes in bedforms. *Sedimentology*, **20**, 189
- Allen, J. R. L. (1994). Fundamental properties of fluids and their relation to sediment transport processes. Sediment transport and depositional process, K. Pye, Blackwell Scientific Publications
- Alonso, J. J. (1989). Estudio volcanoe stratigrafico y volcanologico de los piroclastos salicos del sur de Tenerife, PhD Thesis, University of La Laguna.
- Alonso, J. J., V. Arana, et al. (1988). La ignimbrita de Arico (Tenerife). Mecanismos de emision y emplazamiento. *Revista de la Sociedad Geologica de Espana*, **1**, 15-25.
- Amy, L. A., Peakall, J. & Talling, P. J. 2005. Density- and viscosity-stratified gravity currents: Insight from laboratory experiments and implications for submarine flow deposits. *Sedimentary Geology*, **179**, 5-29.
- Ancochea, E., Huertas, M. J., Catagrel, J. M., Coello, J., Fuster, J. M., Arnaud, N. & Ibarrola, E. 1999. Evolution of the Canadas edifice and its implications for the origin of the Canadas Caldera (Tenerife, Canary Islands), *Journal of Volcanology and Geothermal Research*, **88**, 177-199
- Baas, J. H. (2004). Conditions for formation of massive turbiditic sandstones by primary depositional processes. *Sedimentary Geology*, **166**, 293-310.
- Baas, J. H., V. K. W, et al. (2004). Deposits of depletive high-density turbidity currents: a flume analogue of bed geometry, structure and texture. *Sedimentology* **51**: 1053-1088.
- Baer, E. M., Fisher, R. V., Fuller, M. & Valentine, G. 1997. Turbulent transport and deposition of the Ito pyroclastic flow: determinations using anisotropy of magnetic susceptibility. *Journal of Geophysical Research*, **B102**, 22 565-22 586.
- Bagnold, R. A. 1954. Experiments on gravity-free dispersions of large solid spheres in Newtonian fluid under shear. *Proceedings of the Royal Society, London*, **A225**, 49-63.
- Bagnold, R. A. 1956. The flow of cohesionless grains in fluids. *Philosophical Transactions of the Royal Society, London*, **A249**, 235-297.
- Bagnold, R. A. 1973. The nature of saltation and of 'bed-load' transport in water. *Philosophical Transactions of the Royal Society, London*, **A332**, 473-504.

- Barberi, F., Cioni, R., Rosi, M. Santacroce, R. Sbrana. A. & Vecchi, R. 1989. Magmatic and phreatomagmatic phases in explosive eruptions of Vesuvius as deduced by grainsize and component analysis of the pyroclastic rocks. *Journal of Volcanology and Geothermal Research*, **38**, 287-307.
- Bertran, P., Hétu, B., Texier, J.P. & van Steijn, H. 1997. Fabric characteristics of subaerial slope deposits, *Sedimentology*. **44**, 1-16.
- Best, M. G. and E. H. Christiansen. 2001. *Igneous Petrology*, Blackwell Science.
- Blanchette, F & Bush, J. W. M. 2005. Particle concentration evolution and sedimentation-induced instabilities in a stably stratified environment. *Physics of Fluids*, **17**,
- Bogaard, P. V. D. & Schmincke, H. -U. 1984. The eruptive centre of the Late Quaternary Laacher See Tephra. *Geol. Rundsch.* **73**, 93-980.
- Booth, B. 1973. The Granadilla Pumice deposit of southern Tenerife, Canary Islands. *Proceedings of the Geological Association*. **84**, 353-370.
- Bridgewater, J., Foo, W. S. & Stephens, D. J. 1985. Particle mixing and segregation in failure zones -theory and experiment. *Powder Technology*, **41**, 147-158.
- Booth, B., Croasdale, R. et al. (1978). A quantitative study of five thousand years of volcanism on Sao Miguel, Azores. *Philosophical Transactions of the Royal Society*, **A288**, 271-319.
- Botterill, J. S. M. & Halim, B. H. 1978. The flow of fluidized solids. In: Davidson, J. F. & Keairns, D. L. (eds) *Fluidization. Proceedings of the 2nd Engineering Foundation Conference, Trinity College, Cambridge England, 2-6 April 1978*. 122-127, Cambridge University Press, Cambridge.
- Bouillin, J-P., Bouchez, J-L., Lespinasse, P. & Pêcher, A. 1993. Granite emplacement in extensional settings: an AMS study of the magmatic structures of Monte Capanne (Elba, Italy). *Earth and Planetary Science Letters*, **118**, 263-279.
- Bouma, A. H. (1962). *Sedimentology of some flysch deposits: a graphic approach to facies interpretation.*, Elsevier Amsterdam.
- Bouma, A. H. (1969). *Methods for the study of sedimentary structures*. John Wiley & Sons.
- Branney, M. J. & Kokelaar, P. (1992). A reappraisal of ignimbrite emplacement: progressive aggradation and changes from particulate to non-particulate flow during emplacement of high-grade ignimbrite. *Bulletin of Volcanology*, **54**, 504-520.
- Branney, M. J. & Kokelaar, P. 1997. Giant bed from a sustained catastrophic density current flowing over topography: Acatlán ignimbrite, Mexico. *Geology*, **25**, 115-118.
- Branney, M. J. & Kokelaar, P. (2002). *Pyroclastic density currents and the sedimentation of ignimbrites*, The Geological Society of London. Memoir 27.

- Brown, R. J. 2001. *Eruption history and depositional processes of the Poris ignimbrite of Tenerife and the Glaramara Tuff of the English Lake District*. PhD Thesis, Department of Geology, University of Leicester.
- Brown, R. J., Barry T. L., Branney, M. J. Pringle, M. S. & Bryan, S. E. (2003). The Quaternary pyroclastic succession of southeast Tenerife, Canary Islands: explosive eruptions, related caldera subsidence, and sector collapse. *Geological Magazine*, **140**(1),1-24.
- Brown, R. J. & Branney, M. J. 2004a.Event-stratigraphy of a caldera-forming ignimbrite eruption on Tenerife: the 273 ka Poris Formation. *Bulletin of Volcanology*, **66**, 392-416.
- Brown, R. J. & Branney, M. J. 2004b.Bypassing and diachronous deposition from density currents: Evidence from a giant regressive bed form in the Poris ignimbrite, Tenerife, Canary Islands. *Geology*, **32**, 445-448.
- Bryan, S. E. 1998. Volcanology and Petrology of the Granadilla Member, Tenerife (Canary Islands: Constraints on the eruption dynamics, ignimbrite emplacement and caldera evolution. Unpubl. PhD Thesis, Monash University, Australia.
- Bryan, S. E., Cas, R. A. F. & Marti, J. 1998. Stratigraphy of the Bandas del Sur Formation: an extracaldera record of Quaternary phonolitic explosive eruptions from the Las Canadas edifice, Tenerife (Canary Islands). *Geological Magazine*, **135**(5), 605-636.
- Bryan, S. E., Marti, J. & Cas, R. A. F. 1998b.Lithic breccias in intermediate volume phonolitic ignimbrites from Tenerife (Canary Islands): Constraints on pyroclastic flow and depositional processes. *Journal of Volcanology and Geothermal Research*, **81**, 269-296.
- Bryan, S. E., Cas, R. A. F. & Marti, J. 2000. The 0.57 Ma Plinian eruption of the Granadilla Member, Tenerife (Canary Islands): an example of complexity in eruption dynamics and evolution. *Journal of Volcanology and Geothermal Research*, **103**, 209-238.
- Bryan, S. E., J. Marti, et al. 2002. Petrology and geochemistry of the Bañdas del Sur Formation Las Cañadas edifice, Tenerife (Canary Islands). *Journal of Petrology*, **43**, 1815-56.
- Bryan, S. E. 2006. Petrology and Geochemistry of the Quaternary Caldera-forming, Phonolitic Granadilla Eruption, Tenerife (Canary Islands). *Journal of Petrology*, **47**, 1557-1589.
- Buesch, D. C. 1993. Feldspar geochemistry of four Miocene ignimbrites in south eastern California and western Arizona:. *Tertiary stratigraphy of highly extended terrenes, California, Arizona, and Nevada*:. D. R. Sherrod and J. E. Nielson (eds), U.S. *Geological Bulletin*, **2053**, 55-85.
- Buesch, D. C. & Valentine G. A. 1986. Peach Springs Tuff and the volcanic stratigraphy of the southern Cerbat Mtns, Kingman, Arizona:. *Geological Society of America Cordilleran Section Field Trip Guide and Volume: Field Trip Number 5*, 7-14.
- Burgisser, A. & Bergantz G. W..2002. Reconciling pyroclastic flow and surge: the multiphase physics of pyroclastic density currents. *Earth and Planetary Science Letters*, **202**, 405-418.
- Bursik, M. I., Kurbatov, A. V., Sheridan, M. F. & Woods, A. W. 1998. Transport and deposition in the May 18, 1980, Mount St Helens blast flow, *Geology*, **26**, 155-158.

- Butler, R. F. 1992. Paleomagnetism. Boston, Blackwell Scientific Publications.
- Cas, R. A. F. & Wright, J. V. 1987 Volcanic successions: modern and ancient. Allen and Unwin, London.
- Cagnoli, B. & Manga, M. 2005. Vertical segregation in granular mass flows: A shear cell study. *Geophysical Research Letters*, **32**.
- Cagnoli, B. & Tarling, D. H. 1997. The reliability of anisotropy of magnetic susceptibility (AMS) data as flow direction indicators in friable base surges and ignimbrite deposits: Italian examples. *Journal of Volcanology and Geothermal Research*, **75**, 309-320.
- Calder, E. S., R. S. J. Sparks, et al. 2000. Erosion, transport and segregation of pumice and lithic clasts in pyroclastic flows inferred from ignimbrite at Lascar Volcano, Chile. *Journal of Volcanology and Geothermal Research*, **104**, 201-235.
- Campbell, C. S. & Brennen, C. E. 1983. Computer simulations of shear flows of granular material. In: Jenkins, J. T. & Satake, M. (eds) *Mechanics of Granular Materials: New Models and Constitutive Relations* Elsevier, Amsterdam.
- Campbell, C. S. 1990. Rapid Granular Flows. *Annual Review of Fluid Mechanics*, **22**, 57-92.
- Capaccioni, B., G. Nappi, et al. 2001. Directional fabric measurements: an investigative approach to transport and depositional mechanisms in pyroclastic flows. *Journal of Volcanology and Geothermal Research*, **107**, 275-292.
- Capaccioni, B. & Sarocchi D. 1996. Computer-assisted image analysis on clast shape fabric from the Orvieto-Bagnoregio ignimbrite (Vulsini District, central Italy): implications on the emplacement mechanisms. *Journal of Volcanology and Geothermal Research*, **70**, 75-90.
- Carey, S. N. 1991. Transport and deposition of tephra by pyroclastic flows and surges. *Sedimentation in Volcanic Settings*, SEPM Special Publication **45**
- Carey, S. N. & Sigurdsson, H. 1982. Influence of particle aggregation on deposition of distal tephra from May 18, 1980 eruption of Mount St Helens volcano. *Journal of Geophysical Research*, **87** B8, 7061-7072.
- Carey, S. N. & Sparks, R. S. J. 1986. Quantitative models of the fallout and dispersal of tephra from volcanic eruption columns. *Bulletin of Volcanology*, **48**, 109-125.
- Carrasco-Nunez, G. & Branney, M. J. 2005. Progressive assembly of a double-zoned massive ignimbrite: the Zaragoza ignimbrite, Mexico. *Bulletin of Volcanology*, **68**, 3-20.
- Cas, R. A. F. & Wright, J. V. (1987). *Volcanic successions: modern and ancient*. London, Allen & Unwin.
- Cheel, R. J. 1990. Horizontal lamination and the sequence of bed phases and stratification under upper-flow-regime conditions. *Sedimentology*, **37**, 517.
- Cole, P. D. & Scarpati, C. 1993. A facies interpretation of the eruption and emplacement mechanisms of the upper part of the Neapolitan Yellow Tuff, Campi Flegrei, southern Italy. *Bulletin of Volcanology*, **55**, 311-326.

- Colella, A. & Hiscott, R. N. 1997. Pyroclastic surges of the Pleistocene Monte Guardia sequence (Lipari island, Italy): depositional processes. *Sedimentology*, **44**, 47-66.
- Crowell, J. C. 1955. Directional-current structures from the Prealpine Flysch, Switzerland. *GSA Bulletin*, **66**, 1351-1384.
- Dapples, E. C. & Rominger, J. F. 1945. Orientation analysis of fine-grained clastic sediments. *Journal of Geology*, **53**, 246-261.
- De Celles, P. G., Langford, R. P. & Schwartz, R. K. 1983. Two new methods of palaeocurrent determination from trough cross stratification. *Journal of Sedimentary Research*, **53**, 629-642.
- De Rita, D., Giordano, G., Esposito, A., Fabbri, M. & Rodani, S. 2002. Large volume phreatomagmatic ignimbrites from the Colli Albani volcano (Middle Pleistocene, Italy) > *Journal of Volcanology and Geothermal Research*, **118**, 77-98.
- De Rosa, R. 1999. Compositional models in the ash fraction of some modern pyroclastic deposits: their determination and significance. *Bulletin of Volcanology*, **61**, 162-173.
- Dobran, F., Neri, A. & Macedonio, G. 1993. Numerical simulations of collapsing volcanic columns. *Journal of Geophysical Research*, **B98**, 4231-4259.
- Druitt, T. H. 1992. Emplacement of 18 May 1980 lateral blast deposit ENE of Mount St Helens, Washington. *Bulletin of Volcanology*, **54**, 554-572.
- Druitt, T. H. 1995. Settling behaviour of concentrated dispersions and some volcanological applications. *Journal of Volcanology and Geothermal Research*, **65**, 27-39.
- Druitt, T. H., Calder, E. S., Cole, P. D., Hoblitt, R. P., Norton, G. E., Ritchie, L. J., Sparks, R. S. J. & Voight, B. 2002. Small-volume, highly mobile pyroclastic flows formed by rapid sedimentation from pyroclastic surges at Soufrière Hills Volcano, Montserrat: an important volcanic hazard. In: Druitt, T. H. & Kokelaar, B. P. (eds) *The eruption of Soufrière Hills Volcano, Montserrat, from 1995 to 1999*. Geological Society, London, Memoirs, **21**, 263-280.
- Druitt, T. H. & Sparks, R. S. J. 1982. A proximal ignimbrite breccia facies on Santorini volcano, Greece. *Journal of Volcanology and Geothermal Research*, **13**, 147-171.
- Dzulynski, S. & Sanders, J. E. 1962. Current marks on firm mud bottoms. *Proceedings of the Connecticut Academy of Arts and Science*, **42**, 57-96.
- Edgar, C. J., Wolff, J. A. et al. 2002. A complex quaternary ignimbrite-forming phonolite eruption: the Poris Member of the Diego Hernandez Formation (Tenerife, Canary Islands). *Journal of Volcanology and Geothermal Research*, **118**, 99-130.
- Edgar, C. J., Wolff, J. A., Olin, P. H., Nichols, H. J., Pittari, A., Cas, R. A. F., Reiners, P. W., Spell, T. L. & Marti, J. 2006. The late Quaternary Diego Hernandez Formation, Tenerife: volcanology of a complex cycle of voluminous explosive phonolitic eruptions. *Journal of Volcanology and Geothermal Research*. In Press.
- Ellwood, B. B. 1978. Flow and emplacement directions determined for basaltic bodies using magnetic susceptibility measurements. *Earth Planet Science Letters*, **41**, 254-264.

- Ellwood, B. B. 1979. Anisotropy of magnetic susceptibility variations in Icelandic columnar basalts. *Earth Planet Science Letters*, **42**, 209-212.
- Ellwood, B. B. 1982. Estimates of flow direction for calc-alkaline welded tuffs and paleomagnetic data reliability from anisotropy of magnetic susceptibility measurements: central San Juan Mountains, southwest Colorado. *Earth and Planetary Science Letters*, **59** 303-314.
- Ellwood, B. B. & Howard, J. H. III. 1981. Magnetic fabric development in an experimentally produced barchan dune. *Journal of Sedimentary Petrology*, **51**, 97-100.
- Elston, W. E. and E. I. Smith (1970). Determination of flow direction of rhyolitic ash-flow tuffs from fluidal textures. *Geological Society of America Bulletin*, **81**, 3393-3406.
- Felix, M. 2001. A two-dimensional numerical model for a turbidity current. *Particulate Gravity Currents*. W. D. McCaffrey, B. Kneller and J. Peakall, IAS Special Publication, **31**, 71-81.
- Felix, M. 2002. Flow structure of turbidity currents. *Sedimentology*, **49**, 397-419.
- Fierstein, J. & Hildreth, W. 1992. The Plinian eruptions of 1912 at Novarupta, Katmai National Park, Alaska. *Bulletin of Volcanology*, **54**, 646-684.
- Fisher, R. V. 1966. Mechanisms of deposition from pyroclastic flows. *American Journal of Science*, **264**, 350-363.
- Fisher, R. V. 1983. Flow transformations in sediment gravity flows, *Geology*, **11**, 273-274.
- Fisher, R. V. 1995. Decoupling of pyroclastic currents: hazards assessments. *Journal of Volcanology and Geothermal Research*, **66**, 257-263.
- Florel, F. 1885. Les ravins sous-lacustres des fleuves glaciaires. *C. R. Acad. Sci. Paris*, **101**, 725-728.
- Fritsch, K. V. & Reiss, W. 1868. Geologische Beschreibung der Insel Tenerife, Winterhur: Wurster & Co.
- Gladstone, C. & Sparks, R. S. J. 2002. The significance of grainsize breaks in turbidites and pyroclastic density currents. *Journal of Sedimentary Research*, **72**, 182-196.
- Gladstone, C., Ritchie, L. J., Sparks, R. S. J. & Woods, A. W. 2004. An experimental investigation of density-stratified inertial gravity currents. *Sedimentology*, **51**, 767-789.
- Gómez-Tuena, A. & Carrasco-Núñez, G. 1999. Fragmentation, transport and deposition of a low-grade ignimbrite: The Citlaltépetl Ignimbrite, Eastern Mexico. *Bulletin of Volcanology*, **60**, 448-464.
- Gurioli, L., Cioni, R., Sbrana, A. & Zanello, E. 2002. Transport and deposition of a pyroclastic density currents over an inhabited area: the deposits of the AD 79 eruption of Vesuvius at Herculaneum, Italy. *Sedimentology*, **49**, 929.
- Haff, P. K. 1983. Grain flow as a fluid-mechanical phenomenon. *Journal of Fluid Mechanics*, **134**, 401-430.

- Hailwood, E., F. Ding, et al. 2000. Determining sediment transport directions in deepwater depositional systems using magnetic anisotropy: an example from the Upper Jurassic Claymore Sandstone member, Claymore field, Northern North Sea. *Petroleum Geoscience* **6**: 369-379.
- Halvorsen, E. 1974. The magnetic fabric of some Dolerite intrusions, NE Spitsbergen: Implications for their mode of emplacement. *Earth Planet. Sci. Lett.* **21**, 121-133
- Hamblin, W. H. 1962. X-ray radiography in the study of structures in homogeneous sediments. *Journal of Sedimentary Petrology* **32**: 201-210.
- Hamblin, W. H. 1965. Internal structures of "homogeneous" sandstones. *State Geological Survey of Kansas* **175**.
- Hamilton, N., Owens, W. H. & Rees, A. I. 1968. Laboratory experiments on the production of grain orientation in shearing sands. *Journal of Geology* **76**: 465-472.
- Hand, B. M. 1961. Grain orientation in turbidites. *Compass.* **28**, 133-144.
- Hannes, D. M. & Bowen, A. J. 1985. A granular-fluid model for steady intense bed-load transport. *Journal of Sedimentary Research*, **B90**, 9149-9158.
- Hein, F. J. 1982. Depositional mechanisms of deep-sea coarse clastic sediments, Cap Enragé Formation, Quebec. *Canada Journal of Earth Sciences* **19**: 267-287.
- Herrero-Bervera, E., Cañon-Tapia, E., Walker, G. P. L. & Tanaka, H. 2002. Magnetic fabrics study and inferred flow directions of lavas of the Old Pali Road, O'ahu, Hawaii. *Journal of Volcanology and Geothermal Research*, **118**, 161-171.
- High, L. R. & Picard, M. D. 1974. Reliability of cross-stratification types as palaeocurrent indicators in fluvial rocks. *Journal of Sedimentary Research*, **44**, 158-168.
- Hillhouse, J. W. & Wells R. E. 1991. Magnetic fabric, flow directions, and source area of the lower Miocene Peach Springs Tuff in Arizona, California, and Nevada. *Journal of Geophysical Research*, **96**, 12,443-12,460.
- Hiscott R. N., Pickering, K. T., Bouma, A. H., Hand, B. M., Kneller, B. C., Postma, G. & Soh, W. 1997. Basin-floor fans in the North Sea: sequence stratigraphic models vs sedimentary facies: discussion. *Am. Ass. Petrol. Geol. Bull.*, **81**, 662-665.
- Hiscott, R. N. & Middleton, G. V. 1979. Depositional mechanics of thick-bedded sandstones at the base of a submarine slope, Tourelle Formation (Lower Ordovician), Quebec, Canada. In: *Geology of the continental slopes*. Doyle, L. J. Pilkey, O.H. Jr., *Spec. Publ. Soc. econ. Paleont. Miner.*, **27**, 307-326.
- Hiscott, R. N. and G. V. Middleton (1980). Fabric of coarse deep-water sandstones, Tourelle formation, Quebec, Canada. *Journal of Sedimentary Petrology*, **50**, 0703-0722.
- Houghton, B. F., Hobden, B. J., Cashman, K. V., Wilson, C. J. N. & Smith, R. T. 2003. Large scale interaction of lake water and rhyolitic magma during the 1.8ka Taupo eruption, New Zealand. *Geophysical Monograph*, **140**, 97-109.

- Hughes, S. R. & Druitt, T. H. 1998. Particle fabric in a small, type-2 ignimbrite flow unit (Laacher See, Germany) and implications for emplacement dynamics. *Bulletin of Volcanology*, **60**, 125-136.
- Huppert, H. E., Turner, J. S., Carey, S. N., Sparks, R. S. J. & Hallworth, M. A. 1986. A laboratory study of pyroclastic flows down slopes. *Journal of Volcanology and Geothermal Research*, **30**, 179-199.
- Hürlimann, M., Garcia-Piera, J. O. & Ledesma, A. 2000. *Journal of Volcanology and Geothermal Research*, **103**, 121-134.
- Ishida, M. & Hatano, H. 1983. The flow of solid particles in an aerated inclined channel. In: *Advances in the Mechanics and Flow of Granular Materials, Volume 2*. Trans. Tech Publications, Houston, TX, 565-575.
- Iverson, R. M., M. E. Reid, et al. 1997. Debris-flow mobilisation from landslides. *Annual Reviews of Earth and Planetary Sciences*, **25**, 85-138.
- Iverson, R. M. & Valance, J. M. 2001. New views of granular mass flows. *Geology*, **29**, 115-118.
- Jiang, Z. 1995. The motion of sediment-water mixtures during intense bedload transport: computer simulations. *Sedimentology*, **42**, 935-945.
- Jo, H. R., Rhee, C. W. & Chough, S. K. 1997. Distinctive characteristics of streamflow-dominated alluvial fan deposit: Sanghori fan, Kyongsang Basin (Early Cretaceous), southeastern Korea. *Sedimentary Geology*, **110**, 51-70.
- Johnson, A. M. 1970. *Physical Processes in Geology*. San Francisco, CA, Freeman.
- Karátson, D., O. Sztanó, et al. 2002. Preferred clast orientation in volcanoclastic mass-flow deposits: application of a new photo-statistical method. *Journal of Sedimentological Research*, **72**(6), 823-835.
- Khan, M. A. 1962. Anisotropy of magnetic susceptibility of igneous and metamorphic rocks. *Journal of Geophysical Research*, **67**, 2873-2885.
- Kneller, B. 1995. Beyond the turbidite paradigm: physical models for deposition of turbidites and their implications for reservoir prediction. Characterisation of deep-marine clastic systems. A. J. Hartley and D. J. Prosser, Geological Society, **Special Publication 12**, 21-49.
- Kneller, B. & Buckee, C. 2000. The structure and fluid mechanics of turbidity currents approaching a bounding slope: deflection, reflection and facies variations. *Journal of Sedimentary Research*, **47**, 62-94.
- Knight, M. D., Walker, G. P. L., Ellwood, B. B. & Diehl, J. F. 1986. Stratigraphy, paleomagnetism, and magnetic fabric of the Toba Tuffs - constraints on the sources and eruptive styles. *Journal of Geophysical Research*, **B91**, 10 355-10 382.
- Knight, M. D. & Walker, G. P. L. 1988. Magma flow directions in dikes of the Koolau complex, Oahu, determined from magnetic fabric studies. *Journal of Geophysical Research*, **93**, 4301-4319.

- Kuenen, Ph. H. 1951. Properties of turbidity currents of high density. In: *Turbidity currents and the transportation of coarse sediments to deep water*. Hough, J. L. (ed). *SEPM Spec. Publ.* **2**, 14-33.
- Kuno, H. 1941. Characteristics of deposits formed by pumice flows and those formed by ejected pumice. *Tokyo University Earthquake Research Institute Bulletin*, **19**, 144-1449.
- Le Pennec, J. L., Y. Chen, et al. 1998. Interpretation of anisotropy of magnetic susceptibility fabric of ignimbrites in terms of kinematic and sedimentological mechanisms: An Anatolian case-study. *Earth and Planetary Science Letters*, **157**, 105-127.
- Legros, F., Kelfoun, K. & Marti, J. (2000). The influence of conduit geometry on the dynamics of a caldera-forming eruptions. *Earth and Planetary Science Letters*, **179**, 53-61.
- Legros, F. & Kelfoun K. (2000). Sustained blasts during large volcanic eruptions, *Geology* **28**, 895-898.
- Lemarche, G. & Froggatt, P. C. 1993. New eruptive vents for the Whakamaru Ignimbrite (Taupo Volcanic Zone) identified from a magnetic fabric study. *NZ. Journal of Geology and Geophysics*, **36**, 2133-222.
- Lowe, D. R. 1982. Sediment Gravity Flows: II. Depositional models with special reference to the deposits of high-concentration turbidity currents. *Journal of Sedimentary Petrology*, **52**, 279-298.
- Lowe, D. R. 1988. Suspended-load fallout rate as an independent variable in the analysis of current structures. *Sedimentology*, **35**, 765-776.
- MacDonald, W. D. & Palmer, H. C. 1990. Flow directions in ash-flow tuffs: a comparison of geological and magnetic susceptibility measurements, Tshirege member (upper Bandelier Tuff), Valles caldera, New Mexico, USA. *Bulletin of Volcanology*, **53**, 45-59.
- Marstin, L. G. 1997. Evidence for water influx from a cladera lake during the explosive hydromagmatic eruption of 1790, Kilauea volcano, Hawaii. *Journal of Geophysical Research*, **102 B9**, 20,093.
- Marti, J., Ablay, G., et al. 1995. Part II: Description of field stops. *A field guide to the Central Volcanic Complex of Tenerife (Canary Islands)*. J. Marti and J. Mitjavila, Lanzarote: Cabildo Insular de Lanzarote, 93-156.
- Mart, J. & Gundmundsson, A. 2002. The Las Cañadas (Tenerife, Canary Islands): An overlapping collapse caldera generated by magma chamber migration. *Journal of Volcanology and Geothermal Research*, **103**, 161-173.
- Masson, D. G., Watts, A. B., Gee, M. J. R., Urgeles, R. & Mitchell, N. C., Le Bas, T. P. & Canels, M. 2002. Slope failures on the flanks of the western Canary Islands. *Earth-Science Reviews*, **57**, 1-35.
- McCabe, P. J. 1977. Deep distributary channels and giant bedforms in the upper Carboniferous of the central Pennines, northern England. *Sedimentology*, **24**, 271.
- McKee, E. D. 1957 Flume experiments on the production of stratification and cross-stratification. *Journal of Sedimentary Research*, **27(2)**, 129-134.

- Middleton, G. V. 1965 *Primary sedimentary structures and their hydrodynamic interpretation*, Society of Paleontologists and Mineralogists.
- Middleton, G. V. 1966a Experiments on density and turbidity currents I. Motion of the head. *Canadian Journal of Earth Science*, **3**, 523-546.
- Middleton, G. V. 1966b Experiments on density and turbidity currents. II. Uniform flow of density currents. *Canadian Journal of Earth Sciences*, **3**, 627-637.
- Middleton, G. V. 1967. Experiments of density and turbidity currents. III. Deposition of sediment. *Canadian Journal of Earth Science*, **4**, 475-505.
- Middleton, G. V. 1970. Experimental studies related to the problems of flysch sedimentation. *Geological Association of Canada Special Publication*, **7**, 253-272.
- Middleton, G. V. & Hampton, M. A. 1973. Sediment gravity flows: mechanics of flow and deposition. *Turbidites and deep-water sedimentation*, G. V. Middleton and A. H. Bouma, Section society of Economic Paleontologists and Mineralogists, Los Angeles, 1-38.
- Monaco, P. 1992. Hummocky cross-stratified deposits and turbidites in some sequences of the Umbria-Marche area (central Italy) during the Toarcian. *Sedimentary Geology*, **77**, 123-142.
- Nemec, W. 1990. Aspects of sediment movement on steep delta slopes. In: Colella, A. & Prior, D. B. (eds) *Coarse grained deltas*. International Association of Sedimentology, Special Publications, **10**, 29-73.
- Nichols, G. 1999. *Sedimentology and stratigraphy*, Blackwell Science.
- Nichols, H. I., Wolff, J. A., Larson, P. B., Pittari, A., Edgar, C.J., Cas, R. A. F. & Marti, J. 2001. The complex history of a caldera-forming magma: the El Abrigo ignimbrite, Tenerife, Canary Islands. *EOS*. **82** Fall Meeting Suppl., Abstract V42D-1059 p.F1380.
- Ogawa, S. 1978. Multi-temperature theory of granular materials. In: *Proceedings US-Japan Seminars on Continuum-Mechanics and Statistical Approaches to Mechanical Granular Materials*, gunkunjutsu bunken Fukyukai, Tokyo, 208-217.
- Ort, M. H. 1993. Eruptive processes and caldera formation in nested down-sag-collapse calderas: Cerro Panizos, central Andes Mountains. *Journal of Volcanology and Geothermal Research*, **56**, 221-252.
- Ort, M. H. 1999. Correlation of deposits and vent locations of the proximal Campanian Ignimbrite deposits, Campi Flegrei, Italy, based on natural remnant magnetization and anisotropy of magnetic susceptibility characteristics *Journal of Volcanology and Geothermal Research*, **91**:, 167-178.
- Ort, M. H., Orsi, G., et al. 2003. Anisotropy of magnetic susceptibility studies of depositional processes in the Campanian Ignimbrite, Italy. *Bulletin of Volcanology*, **64**.
- Palmer, H. C., MacDonald, W. D. Gromme, C. S. & Ellwood, B. B. (1996). Magnetic properties and emplacement of the Bishop tuff, California. *Bulletin of Volcanology*, **58**, 101-116.

- Palmer, H. C., MacDonald, W. D. (1999). Anisotropy of magnetic Susceptability in relation to source vents of ignimbrites: empirical observations. *Tectonophysics*, **307**, 207-218.
- Paola, C., Wiele, S. M. & Reinhart, M. A. 1989. Upper regime parallel laminationas the result of turbulent sediment transport and low amplitude bedforms. *Sedimentology*, **36**, 47
- Parés, J. M., van der Pluijm, B. A. & Dinares-Turell, J. 1999. Evolution of magnetic fabrics during incipient deformation of mudrocks (Pyrenees, northern Spain). *Tectonophysics*, **307**, 1-14
- Parés, J. M. & van der Pluijm, B. A. 2002. Phyllosilicate fabric characterization by Low-Temperature Anisotropy of Magnetic Susceptibility(LT-AMS). *Geophysical Research Letters*. **29**, 68-1 - 68-4.
- Parkash, B. & Middleton, G. V. 1970. Downcurrent textural changes in Ordovician turbidite grewackes. *Sedimentology*, **14**, 259-293.
- Pitarri, A. 2004. Eruption Dynamics and Emplacement Processes for the Climatic Abrigo Member, Tenerife, Canary Islands. PhD Thesis. Monash Unveristy, Clayton
- Pitarri, A. & Cas, R. A. F. 2004. Sole Marks at the base of the late Pleistocene Abrigo Ignimbrite, Tenerife: implications for transport and depositional processes at the base of pyroclastic flows. *Bulletin of Volcanology*, **66**, 356-363.
- Pittari, A., Cas, R. A. F. & Marti, J. (2005). "The occurrence and origin of prominent massive, pumice-rich ignimbrite lobes within the Late Pleistocene Abrigo Ignimbrite, Tenerife, Canary Islands." *Journal of Volcanology and Geothermal Research*, **139**, 271-293.
- Pittari, A., Cas, R. A. F. & Edgar, C. J., Nichols, J. A., Wolff, J. A. & Marti, J. (2006). The influence of palaeotopography on facies architecture and pyroclastic flow processes of a lithic-rich ignimbrite in a high gradient setting: The Abrigo Ignimbrite, Tenerife, Canary Islands. *Journal of Volcanology and Geothermal Research*, **152**, 273-315.
- Poliakov, A. S. 2002. Properties of granular media and transportation mechanism of subaqueous debris flows. *Lithology of mineral resources*, **37**, 25-38.
- Porreca, M., Mattei, M., Giordano, D., De Rita, D. & Funiciello, R. 2003. Magnetic fabric and implications for pyroclastic flow and lahar emplacement, Albano maar, Italy. *Journal of Geophysical Research*, **108 B5**, EPM 12-1 - EPM 12-14.
- Postma, G., Nemec, W. & Kleinspehn, K. L. 1988. Large loading clasts in turbidites - a mechanism for their emplacement. *Sedimentary Geology*, **58**, 47-61.
- Pyle, D. M. 1989. The thickness, volume and grainsize of tephra fall deposits. *Bulletin of Volcanology*, **51**, 1-15.
- Rees, A. I. 1968. The production of preferred orientation in a concentrated dispersion of elongated and flattened grains. *Journal of Geology*, **76**, 457-465.
- Rees, A. I. 1966. The affects of depositional slope on the anisotropy of magnetic susceptibility of laboratory deposited sands. *Journal of Geology*, **74**, 856-867.

- Rees, A. I. 1979. The orientation of grains in a sheared dispersion. *Tectonophysics*, **55**, 275-287.
- Rees, A. I. 1983. Experiments on the production of transverse grain alignment in a sheared dispersion. *Sedimentology*, **30**, 437-448.
- Rees, A. I. & Woodall, W. A. 1975. The magnetic fabric of some laboratory-deposited sediments. *Earth and Planetary Science Letters*, **25**, 121-130.
- Rhodes, R. C. & Smith, E. I. 1972. Distribution and directional fabric of ash-flow sheets in the northwestern Mogollon plateau, New Mexico. *Geological Society of America Bulletin*. **83**, 1863-1868.
- Rollinson, H. 1993. Using geochemical data: evaluation, presentation, interpretation, Longman Scientific & Technical.
- Roche, O., Gilbertson, M., Phillips, J. C. & Sparks, R. S. J. 2002, Experiments on deaerating granular flows and implications for pyroclastic flow mobility. *Geophysical Research Letters*, **29**, 40-1 to 40-4.
- Rose, W.I, Bluth, G. J. S., Schneider, D. J., Ernst, G. G. J. Riley, C. M., Henerson, J. & McGimsey, R. G. 2001. Observations of volcanic clouds in their first few days of atmospheric residence: The 1992 eruptions of Crater Peak, Mount Spurr volcano, Alaska. *The Journal of Geology*, **109**, 667-694.
- Rosi, M., Paladio-Melosantos, M., Di Muro, A. Leoni, R. & Bacolcol T. 2001. Fall vs flow activity during the 1991 climactic eruption of Pinatubo Volcano (Philippines). *Bulletin of Volcanology*, **62**, 549-566.
- Rusnak, G. A. 1957. Orientation of sand grains under conditions of unidirectional flow. *Journal of Geology*, **65**, 384-409.
- Savage, S. B. 1979. Granular flow of cohesionless granular materials in chutes and channels. *Journal of Fluid Mechanics*, **92**, 53-96.
- Savage, S. B. 1983. Granular flow down rough inclines - review and extension. In: Jenkins, J. T. & Satake, M. (eds) *Mechanics of Granular Materials: New Models and Constitutive Relations*. Elsevier, Amsterdam, 261-281.
- Savage, S. B. 1984. The mechanics of rapid granular flows. *Advances in Applied Mechanics*, **24**, 289-366.
- Savage, S. E. & Lun, C. K. K. 1988. Particle size segregation in inclined chute flow of dry cohesionless granular solids. *Journal of Fluid Mechanics*, **189**, 311-335.
- Schaafsma, S. H., Vonk, P., Segers, P. & Kossen, N. W. F. 1998. Description of agglomerate growth. *Powder Technology*, **97**, 183-190.
- Schmincke, H.-U. & Swanson, D. A. 1967. Ignimbrite origin of eutaxites from Tenerife. *Neues Jahrbuch für Geologie Paläontologie, Monatshefte*, **1**, 700-3.

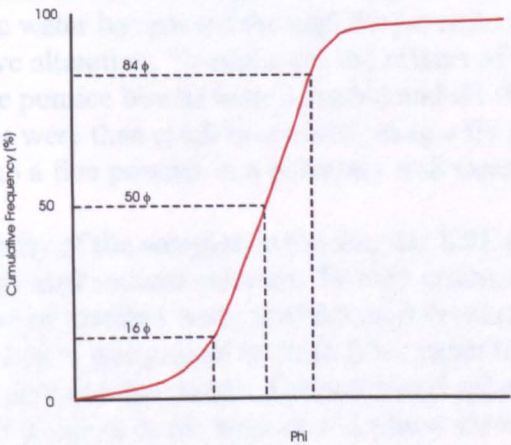
- Schumacher, R. & Schmincke, H-U. 1990. The lateral facies of ignimbrites at Laacher See Volcano. *Bulletin of Volcanology*, **52**, 271-283.
- Schumacher, R. & Schmincke, H-U. 1991. Internal structure and occurrence of accretionary lapilli — a case study at Laacher See Volcano. *Bulletin of Volcanology*, **53**, 612-634.
- Schumacher, R. & Schmincke, H-U. 1994. Models for the origin of accretionary lapilli. *Bulletin of Volcanology*, **56**, 626-639.
- Scott, A. M. & Bridgewater, J. 1975. Interparticle percolation: a fundamental solids mixing mechanism. *Industrial and Engineering Chemistry: Fundamentals*, **14**, 22-27.
- Seamann, S. J., McIntosh, W. C. Geissmann, J. W., Williams, M. L. & Wolfgang, E. E. 1991. Magnetic fabrics of the Bloodgood Canyon and Shelley Peak Tuffs, southwestern New Mexico: implications for emplacement and alteration processes. *Bulletin of Volcanology*, **53**, 460-476.
- Self, S., 1983. Large-scale phreatomagmatic silicic volcanism: a case study from New Zealand. *Journal of Volcanology and Geothermal Research*, **17**, 433-469.
- Sheridan, M. F. 1979. Emplacement of pyroclastic flows: a review. Ash-flow tuffs. C. E. Chapin and W. E. Elston, Geol Soc Am Spec Paper, **180**, 125-136.
- Sheridan, M. F. and D. M. Ragan (1976). Compaction of ash-flow tuffs: a review. *Compaction of coarse-grained sediments, II, Development in Sedimentology*. G. V. Chilingarian and K. A. Wolff. Amsterdam, Elsevier, 677-713.
- Sides, J. R. 1981. Geology of the Ketcherside Mountain area, southeastern Missouri and the source of the Grassy Mountain Ignimbrite. *Geol. Soc. Am. Bull.* **92**, 686-693.
- Simons, S. R. J. 1996. Modelling of agglomerating systems: from spheres to fractals. *Powder Technology*, **87**, 29-41.
- Sohn, Y. K. 1997. On traction-carpet sedimentation. *Journal of Sedimentary Research*, **67**, 502-509.
- Sparks, R. S. J. 1976. Grain size variations in ignimbrites and implications for the transport of pyroclastic flows. *Sedimentology*, **23**, 147-188.
- Sparks, R. S. J. 1986. The dimensions and dynamics of volcanic eruption columns. *Bulletin of Volcanology*, **48**, 3-15.
- Sparks, R. S. J., S. Self, et al. (1973). Products of ignimbrite eruptions. *Geology*, **1**, 115-118.
- Sparks, R. S. J. & Walker, G. P. L. 1977. The significance of vitric-enriched air-fall ashes associated with crystal-enriched ignimbrites. *Journal of Volcanology and Geothermal Research*, **2**, 329-341.
- Sparks, R. S. J., L. Wilson, et al. 1978. Theoretical modelling and the generation, movement, and emplacement of pyroclastic flows by column collapse. *Journal of Geophysical Research*, **83**, 1727-1739.

- Stix, J. 2001. Flow evolution of experimental gravity currents: Implications for pyroclastic flows at volcanoes. *Journal of Geology*, **109**, 381-398.
- Stow, D. A. V. 1994. Deep sea processes of sediment transport and deposition. *Sediment transport and Depositional processes*. K. Pye, Blackwell Scientific Publications.
- Tiara, A. & Scholle, P. A. 1979. Deposition of resedimented sandstone beds in the Pico Formation, Ventura basin, California, as interpreted from magnetic fabric measurements. *Geol. Soc. Am. Bull.*, **90**, 952-962.
- Talbot, J-Y., Chen, Y., Faure, M. & Lin, W. 2000. AMS study of the Pont-de-Montvert-Bourne porphyritic granite pluton (French Massif Central) and its tectonic implications. *Geophysical Journal International*, **140**, 677-686.
- Tarney, J., & Marsh, N.G. 1991. Major and trace element geochemistry of Holes CY-1 and CY-4 : Implications for petrogenetic models. In: Gibson, I.L., Malpas, J., Robinson, P.A. & Xenophontos, C. (eds). Initial Reports, Holes CY-1 and CY-1A, *Geological Survey of Canada, Paper*, 90-20.
- Tomkins, M. R., T. E. Baldock, et al. 2005. Hindered settling of sand grains. *Sedimentology*, **52**, 1425-1432.
- Turner, J. S. & Campbell, I. H. 1986. Convection and mixing in magma chambers. *Earth-Science Reviews*, **23**: 255-352.
- Valentine, G. H. & Wohletz, K. H. 1989. Numerical models of Plinian eruption columns and pyroclastic flows. *Journal of Geophysical Research*, **B94**, 1867-1887.
- Varekamp, J.C. 1993. Some remarks on volcanic vent evolution during Plinian eruptions. *Journal of Volcanology and Geothermal Research*, **54**, 309-318.
- Walker, G. P. L. 1971. Grainsize characteristics of pyroclastic deposits. *Journal of Geology*, **79**, 696-714.
- Walker, G. P. L. 1981. Plinian eruptions and their products. *Bulletin of Volcanology*, **44**, 223-240.
- Walker, G. P. L. 1983. Ignimbrite types and ignimbrite problems. *Journal of Volcanology and Geothermal Research*, **17**, 65-88.
- Walker, G. P. L. 1984. Characteristics of dune-bedded pyroclastic surge bedsets. *Journal of Volcanology and Geothermal Research*, **20**, 281-296.
- Walker, G. P. L. 1985. Origin of coarse lithics near ignimbrite source vents. *Journal of Volcanology and Geothermal Research*, **25**, 157-171.
- Walker, G. P. L. & McBroome, L. A. 1983. Mount St Helens 1980 and Mount Pelée 1902 - flow or surge? *Geology*, **11**, 571-574.
- Wang, X., J. Roberts, et al. 2001. Flow directions of Carboniferous ignimbrites, southern New England Oregon, Australia, using anisotropy of magnetic susceptibility. *Journal of Volcanology and Geothermal Research*, **110**, 1-25.

- Wennerström, M. & Airo, M-L. 1998. Magnetic fabric and emplacement of the post-collisional Pomovaara Granite Complex in northern Fennoscandia. *Lithos*, **45**, 131-145.
- Wentworth, C. K. 1922. A scale of grade and class terms for clastic sediments. *Journal of Geology*, **30**, 377-392.
- Wilson, C. J. N. 1980. The role of fluidisation in the emplacement of pyroclastic flows: An experimental approach. *Journal of Volcanology and Geothermal Research*, **8**, 231-249.
- Wilson, C. J. N. 1984. The role of fluidisation in the emplacement of pyroclastic flows 2. Experimental results and their interpretations. *Journal of Volcanology and Geothermal Research*, **20**, 54-84.
- Wilson, C. J. N. 1985. The Taupo eruption, New-Zealand: II. The Taupo ignimbrite. *Philosophical Transactions of the Royal Society of London Series A*, **314**, 229-310.
- Wilson, C. J. N. 1997. Emplacement of the Taupo ignimbrite. *Nature*, **385**, 306-307.
- Wilson, C. J. N. & Walker, G. P. L. 1982. Ignimbrite depositional facies: the anatomy of a pyroclastic flow. *Journal of the Geological Society of London*, **139**, 581-597.
- Wolff, J. A. 1985. Zonation, mixing and eruption of silica-undersaturated alkaline magma: a case study from Tenerife, Canary Islands. *Geological Magazine*, **122**, 623-40.
- Wolff, J. A. 1987. Crystallisation of nepheline syenite in a subvolcanic magma system: Tenerife, Canary Islands. *Lithos*, **20**, 207-223.
- Wolff, J. A., Ellwood, B. B. & Sachs, S. D. 1989. Anisotropy of magnetic susceptibility in welded tuffs: application to welded-tuff dyke in the Tertiary Trans-Pecos Texas Volcanic province, USA. *Bulletin of Volcanology*, **51**, 299-310.
- Wright, J. V. 1981. Rio Caliente ignimbrite: analyses of a compound intraplinian ignimbrite from a major Quaternary Mexican eruption. *Bulletin of Volcanology*, **44**, 189-212.
- Wright, J. V., Smith, A. L. et al. 1980. A working terminology of pyroclastic deposits. *Journal of Volcanology and Geothermal Research*, **8**, 315-336.
- Wright, J. V. and Walker, G. P. L. 1981. Eruption, transport and deposition of ignimbrite: a case study from Mexico. *Journal of Volcanology and Geothermal Research*, **9**, 111-131.
- Yamamoto, T. Takarada, S. & Suto, S. 1993. Pyroclastic flows from the 1991 eruption of Unzen volcano, Japan. *Bulletin of Volcanology*, **55**, 166-175.
- Yenes, M., Álvarez, F. & Gutiérrez-Alonso, G. 1999. Granite emplacement in orogenic compressional conditions: the La Alberca-Béjar granitic area (Spanish Central System, Variscan Iberian Belt). *Journal of Structural Geology*, **21**, 1419-1440.
- Zhu, R. & Shi, C. 2003. Anisotropy of magnetic susceptibility of Hannuoba basalt, northern China: Constraints on the vent position of the lava sequences. *Geophysical Research Letters*, **30**, 38-1 - 38-4

Appendix 1

The phi values are taken from where the cumulative frequency curve crosses the 16%, 50% and 84% levels



Mean size (ϕ)

$$M\phi = \frac{\phi_{16} + \phi_{50} + \phi_{84}}{3}$$

Median

$$Md\phi = \phi_{50}$$

Sorting

$$\sigma\phi = \frac{(\phi_{84} - \phi_{16})}{2}$$

Skewness

$$\alpha\phi = \frac{M\phi - Md\phi}{\sigma\phi}$$

Appendix 2: XRF Preparation

The juvenile material within the La Caleta Formation is frequently altered to clay around the edges, particularly in the ignimbrites. Their age and their porous and permeable nature mean that a great deal of meteoric water has passed through the juvenile material, and may have resulted in unseen, pervasive alteration. To minimise the effects of alteration on the geochemical analyses, large pumice blocks were sampled and all visible signs of alteration were removed. The samples were then crudely crushed using a fly press and dried for two days, before being ground to a fine powder in a planetary mill (agate).

Because of the close proximity of the samples to the sea, the XRF powders were thoroughly rinsed to remove any precipitated sodium chloride. Twenty grams of each sample were placed in a conical flask with 40 ml of distilled water and thoroughly mixed. The sediment was allowed to settle and the solution was passed through filter paper to ensure none of the sample was lost. This process was repeated five times. The combined solutions of the first four rinses was analysed using the ICP to quantify the amount of sodium chloride removed and the solution from the fifth rinse was analysed separately to ensure that all the sodium chloride had been removed. The powders were then dried overnight and milled for a final time to remove any aggregates that may have formed. These powders were then used to make XRF pellets and fusion beads.

The pellets were made using 7 g of rinsed and dried sample and mixed with 10 drops of adhesive and mixed until it reached the consistency of bread crumbs. This mixture was then placed into a mould, covered with Boric acid and pressed to 10 tonnes to make a pellet. The loss on ignition of each sample was calculated by weighing a quantity of sample before and after being heated in a furnace to ~950°C for 1.5 hours. This process oxidised the sample and removed any volatiles. From the loss on ignition the amount of flux required (20% lithiumtetraborate 80% lithiumborate) can be determined and added to 0.6g of the rinsed and dried sample. The sample and flux were then heated to 1200°C for ~10 minutes until melted and then cast into a platinum mould to make a fusion bead.

Appendix 3: Microprobe phenocryst analyses

Samples 81-1, 81-2 & 81-3 pg. 215-217

Samples 81-4, 81-6 & 55-1 pg. 218-219

Samples 46-1 & 46-3 pg. 220-221

Analysis	Sample	SiO2	TiO2	Al2O3	Cr2O3	FeO	MnO	MgO	CaO	Na2O	K2O	NiO	F	-O=F	Cl	-O=Cl	SO3	Total
1	81-2	0.04	15.14	3.60	0.00	72.32	0.99	4.44	0.06	0.00	0.01	0.00	0.00	0.00	0.01	0.00	0.00	96.61
2	81-2	50.76	1.45	3.16	0.00	6.93	0.29	14.10	22.54	0.66	0.01	0.02	0.00	0.00	0.00	0.00	0.01	99.96
3	81-2	0.10	14.80	3.44	0.00	71.29	0.94	4.39	0.13	0.06	0.04	0.00	0.00	0.00	0.01	0.00	0.01	95.20
4	81-2	66.29	0.04	19.04	0.00	0.30	0.00	0.00	0.54	6.94	6.42	0.00	0.09	0.04	0.00	0.00	0.01	96.63
5	81-2	64.96	0.06	18.59	0.00	0.32	0.00	0.00	0.58	6.99	6.03	0.00	0.05	0.02	0.02	0.00	0.02	97.59
6	81-2	65.77	0.11	19.45	0.00	0.34	0.04	0.00	1.03	7.18	5.49	0.02	0.00	0.00	0.01	0.00	0.02	99.46
7	81-2	66.08	0.10	19.20	0.00	0.31	0.00	0.00	0.80	7.26	5.73	0.00	0.02	0.01	0.02	0.00	0.00	99.52
8	81-2	66.21	0.07	19.24	0.00	0.36	0.00	0.00	0.74	6.94	5.70	0.00	0.09	0.04	0.00	0.00	0.00	96.31
9	81-2	39.06	6.40	12.36	0.01	11.52	0.23	12.37	11.80	2.77	0.84	0.02	0.14	0.06	0.02	0.01	0.04	97.50
10	81-2	36.59	6.37	12.06	0.00	11.84	0.24	12.12	11.63	2.72	0.85	0.00	0.20	0.08	0.03	0.01	0.05	96.60
11	81-2	0.01	14.39	3.17	0.00	73.68	1.11	4.21	0.02	0.00	0.02	0.00	0.00	0.00	0.01	0.00	0.00	96.82
12	81-2	5.01	0.13	1.42	0.02	1.09	0.14	0.28	40.18	0.95	0.84	0.00	1.84	0.77	0.23	0.05	0.86	51.90
13	81-2	0.58	0.00	0.05	0.00	0.16	0.08	0.15	50.99	0.26	0.02	0.01	2.32	0.98	0.14	0.03	0.85	54.43
14	81-2	21.25	0.31	5.75	0.01	1.65	0.06	0.40	2.12	1.44	2.07	0.00	0.00	0.00	0.00	0.00	0.00	95.87
15	81-2	29.77	0.34	9.74	0.00	1.87	0.06	0.75	1.94	2.59	1.88	0.00	0.14	0.06	0.36	0.06	0.48	49.79
16	81-2	51.82	0.84	1.35	0.01	6.66	0.95	12.06	20.64	1.82	0.01	0.00	0.00	0.00	0.02	0.00	0.00	99.41
17	81-2	52.68	0.60	1.24	0.02	6.17	0.95	12.33	21.53	1.83	0.01	0.04	0.00	0.00	0.00	0.00	0.00	100.40
18	81-2	52.33	0.72	1.23	0.01	6.18	0.99	12.21	21.68	1.78	0.01	0.00	0.00	0.00	0.02	0.00	0.00	100.14
19	81-2	0.02	12.19	0.75	0.01	77.19	2.89	1.67	0.17	0.03	0.00	0.05	0.00	0.00	0.00	0.00	0.00	94.97
20	81-2	37.19	7.65	13.04	0.00	11.64	0.32	15.55	0.04	1.11	8.41	0.02	0.54	0.23	0.01	0.00	0.06	95.36
21	81-2	37.16	7.69	13.04	0.04	11.58	0.35	15.96	0.00	1.14	8.55	0.03	0.58	0.24	0.01	0.00	0.06	95.83
22	81-2	1.55	0.08	0.00	0.00	0.45	0.11	0.14	49.50	0.17	0.07	0.04	0.00	0.00	0.00	0.00	0.00	95.42
23	81-2	0.05	0.00	0.02	0.00	85.24	0.21	0.00	0.02	0.00	0.03	0.00	0.00	0.00	0.00	0.01	94.35	179.84
24	81-2	53.16	0.92	16.63	0.00	14.23	0.16	0.85	1.35	3.31	4.29	0.00	0.08	0.04	0.09	0.02	0.00	95.87
25	81-2	0.00	46.33	0.13	0.00	45.25	3.07	3.73	0.01	0.04	0.00	0.00	0.00	0.00	0.00	0.00	0.00	96.30
26	81-2	0.81	46.74	0.35	0.02	44.51	3.09	3.71	0.01	0.16	0.08	0.00	0.00	0.00	0.00	0.00	0.00	96.67
27	81-2	42.10	5.30	10.36	0.01	11.32	0.42	13.47	11.33	3.12	1.04	0.00	0.29	0.12	0.01	0.00	0.03	96.87
28	81-2	41.69	5.15	10.16	0.01	10.87	0.46	13.27	11.00	3.05	1.06	0.00	0.32	0.13	0.02	0.01	0.04	96.97
29	81-2	42.20	5.24	10.24	0.02	11.46	0.48	13.38	10.99	3.13	1.04	0.00	0.34	0.14	0.03	0.01	0.05	96.42
30	81-2	42.19	5.45	10.32	0.00	11.15	0.41	13.52	10.96	3.13	0.99	0.03	0.30	0.13	0.01	0.00	0.02	96.35
31	81-2	0.02	11.73	0.76	0.01	79.07	3.01	1.45	0.00	0.03	0.01	0.00	0.00	0.00	0.01	0.00	0.02	96.11
32	81-2	0.04	11.82	0.77	0.05	78.28	2.99	1.43	0.02	0.01	0.00	0.00	0.00	0.00	0.00	0.00	0.02	95.40
33	81-3	8.23	0.07	2.43	0.00	0.32	0.00	0.22	0.40	1.81	0.50	0.02	0.01	0.00	0.12	0.03	0.83	14.74
34	81-3	15.02	0.13	4.30	0.02	0.59	0.05	0.34	1.01	1.02	0.56	0.01	0.09	0.04	0.06	0.01	0.04	95.94
35	81-3	1.07	0.04	0.32	0.00	0.54	0.62	0.01	0.32	0.17	0.13	0.53	0.02	0.01	0.03	0.01	0.04	3.82
36	81-3	0.08	0.00	0.00	0.00	0.32	0.00	0.04	0.01	0.35	0.01	0.05	0.00	0.00	0.00	0.00	0.00	1.50
37	81-3	10.08	0.10	2.56	0.00	0.64	0.03	0.25	0.57	1.28	0.59	0.03	0.12	0.05	0.17	0.04	0.24	16.57
38	81-3	9.74	0.12	3.16	0.01	0.48	0.04	0.23	0.40	1.57	0.77	0.00	0.04	0.02	0.10	0.02	0.14	16.76
39	81-3	58.64	0.03	0.34	0.00	0.06	0.00	0.26	3.26	5.47	0.40	0.00	0.04	0.02	0.00	0.00	0.00	17.96
40	81-3	66.82	0.04	18.83	0.02	0.27	0.00	0.00	0.23	6.86	6.52	0.00	0.00	0.00	0.01	0.00	0.01	96.61
41	81-3	66.68	0.06	18.85	0.02	0.29	0.00	0.00	0.35	6.92	6.56	0.00	0.05	0.02	0.00	0.00	0.00	96.75
42	81-3	10.90	0.07	2.96	0.00	0.24	0.01	0.12	0.34	1.16	0.43	0.03	2.26	0.95	0.10	0.02	1.53	19.10
43	81-3	0.28	0.01	0.07	0.00	0.51	0.00	0.00	0.04	0.07	0.01	0.00	0.07	0.03	0.07	0.02	0.02	1.11
44	81-3	37.70	5.48	12.19	0.01	14.04	0.78	15.47	0.00	0.95	8.71	0.00	0.98	0.41	0.04	0.01	0.04	95.94
45	81-3	60.85	0.94	18.82	0.02	3.55	0.29	0.90	0.58	2.06	5.31	0.04	0.16	0.07	0.21	0.05	0.12	93.73
46	81-3	36.01	5.64	12.28	0.02	14.18	0.65	15.43	0.00	0.93	8.78	0.03	1.02	0.43	0.04	0.01	0.04	96.61
47	81-3	54.26	1.50	16.92	0.00	4.82	0.24	2.59	0.59	1.64	5.43	0.03	0.31	0.13	0.19	0.04	0.10	98.45
48	81-3	0.17	0.02	0.11	0.46	0.00	0.01	0.00	0.03	0.00	0.02	0.00	1.24	0.52	0.01	0.00	0.20	1.73
49	81-3	2.51	0.03	0.48	0.00	0.15	0.02	0.11	0.39	0.26	0.05	0.03	1.31	0.55	0.01	0.00	0.19	4.97
50	81-3	22.69	0.27	4.87	0.00	1.22	0.11	0.41	1.33	1.62	1.56	0.00	0.03	0.01	0.24	0.05	0.32	34.61
51	81-3	17.34	0.27	5.34	0.05	1.51	0.06	0.67	1.83	2.79	1.22	0.01	0.18	0.07	0.22	0.05	0.55	31.73
52	81-3	1.53	0.00	0.00	0.00	13.02	0.02	0.02	0.01	6.46	0.01	0.00	0.00	0.00	0.03	0.01	0.00	21.07
53	81-1	67.62	0.05	18.91	0.00	0.34	0.00	0.00	0.20	7.08	6.33	0.00	0.04	0.02	0.00	0.00	0.00	100.56
54	81-1	66.80	0.03	18.93	0.00	0.37	0.03	0.00	0.26	6.86	6.78	0.00	0.06	0.03	0.01	0.00	0.00	100.12
55	81-1	29.37	35.27	0.76	0.00	1.97	0.14	0.06	25.27	0.22	0.03	0.00	0.30	0.13	0.00	0.00	0.02	93.29
56	81-1	23.83	0.00	6.41	0.00	0.01	0.00	0.06	0.02	0.83	0.26	0.01	0.09	0.04	0.01	0.00	0.01	31.51
57	81-1	14.59	0.00	5.97	0.00	0.00	0.02	0.07	0.03	0.78	0.14	0.00	0.01	0.01	0.02	0.01	0.00	21.60
58	81-1	40.30	0.00	30.73	0.01	0.35	0.00	0.02	5.39	14.87	0.25	0.00	0.00	0.00	0.95	0.22	7.90	100.66
59	81-1	29.23	34.49	0.70	0.00	1.91	0.14	0.04	25.21	0.22	0.01	0.00	0.00	0.00	0.01	0.00	0.01	91.96
60	81-1	18.29	0.13	4.21	0.01	4.59	0.02	0.35	0.83	4.57	1.05	0.00	10.01	4.22	0.81	0.14	0.49	40.81
61	81-1	66.63	0.05	18.91	0.02	0.29	0.02	0.00	0.29	7.01	6.50	0.00	0.00	0.00	0.01	0.00	0.02	96.74
62	81-1	67.37	0.06	19.10	0.00	0.35	0.03	0.00	0.39	7.30	6.10	0.02	0.00	0.00	0.00	0.00	0.01	100.73
63	81-1	11.74	0.08	3.25	0.00	0.83	0.00	0.35	1.04	1.84	0.55	0.03	8.18	3.87	0.09	0.02	0.17	25.25
64	81-1	40.55	0.00	30.96	0.00	0.41	0.02	0.01	4.92	15.78	0.24	0.01	0.01	0.00	0.88	0.22	8.45	102.02
65	81-1	40.66	0.00	30.91	0.02	0.39	0.00	0.00	5.04	15.70	0.19	0.00	0.00	0.00	0.91	0.21	8.39	102.01
66	81-1	25.23	0.33	6.90	0.01	1.41	0.10	0.50	1.25	2.91	1.59	0.02	0.18	0.07	0.25	0.06	0.37	40.91
67	81-1	0.00	0.00	0.00	0.00	0.03	0.00	1.06	58.69	0.08	0.05	0.00	0.00	0.00	0.01	0.00	0.01	56.91
68	81-1	0.00	0.00	0.03	0.00	0.00	0.01	0.55	57.23	0.05	0.04	0.00	0.21	0.06	0.00	0.00	0.00	58.03
69	81-1	16.02	0.28	4.59	0.02	0.74	0.05	0.36	1.04	1.44	0.99	0.00	0.00	0.00	0.18	0.04	0.25	25.90

Analysis	Sample	O	Si	Ti	Al	Cr	Fe2	Mn	Mg	Ca	Na	K	Ni	F	Cl	S	Total	X	Y
1	81-2	10.000	0.004	1.171	0.436	0.000	6.222	0.086	0.681	0.007	0.001	0.002	0.000	0.000	0.002	0.000	8.609	63.417	10.382
2	81-2	10.000	3.150	0.088	0.231	0.000	0.360	0.015	1.304	1.488	0.079	0.001	0.001	0.000	0.000	0.000	6.706	63.357	10.384
3	81-2	10.000	0.011	1.163	0.423	0.000	6.228	0.083	0.683	0.015	0.012	0.005	0.000	0.000	0.000	0.000	8.623	63.456	10.379
4	81-2	10.000	3.726	0.002	1.262	0.000	0.014	0.000	0.000	0.036	0.777	0.441	0.000	0.016	0.000	0.000	6.256	63.731	10.375
5	81-2	10.000	3.727	0.003	1.267	0.000	0.015	0.000	0.000	0.036	0.777	0.441	0.000	0.016	0.002	0.001	6.256	63.708	10.372
6	81-2	10.000	3.884	0.005	1.286	0.000	0.016	0.002	0.000	0.062	0.762	0.369	0.001	0.000	0.004	0.002	6.243	63.383	10.366
7	81-2	10.000	3.712	0.004	1.271	0.000	0.015	0.000	0.000	0.048	0.791	0.411	0.000	0.004	0.002	0.000	6.252	63.376	10.361
8	81-2	10.000	3.723	0.003	1.275	0.000	0.017	0.000	0.000	0.045	0.756	0.409	0.000	0.016	0.000	0.000	6.227	63.378	10.359
9	81-2	10.000	2.543	0.313	0.948	0.000	0.827	0.013	1.200	0.823	0.349	0.099	0.001	0.029	0.003	0.002	6.960	62.746	10.327
10	81-2	10.000	2.544	0.318	0.937	0.000	0.853	0.013	1.191	0.821	0.348	0.072	0.000	0.041	0.003	0.002	6.966	62.862	10.325
11	81-2	10.000	0.001	1.123	0.398	0.000	6.417	0.088	0.651	0.002	0.001	0.002	0.000	0.000	0.002	0.000	8.684	63.520	10.311
12	81-2	10.000	0.875	0.018	0.289	0.003	0.180	0.021	0.957	7.518	0.322	0.143	0.000	1.015	0.088	0.108	9.623	63.650	10.328
13	81-2	10.000	0.107	0.000	0.012	0.000	0.028	0.013	0.040	10.098	0.063	0.006	0.000	0.000	0.000	0.000	10.466	63.908	10.326
14	81-2	10.000	3.498	0.039	1.116	0.001	0.227	0.008	0.988	0.374	0.459	0.434	0.000	0.000	0.087	0.047	8.301	64.588	10.289
15	81-2	10.000	3.448	0.030	1.330	0.000	0.181	0.005	1.129	0.241	0.581	0.278	0.000	0.063	0.072	0.042	8.285	64.801	10.288
16	81-2	10.000	3.274	0.040	1.010	0.000	0.512	0.051	1.136	1.411	0.223	0.001	0.000	0.000	0.002	0.000	6.748	71.022	10.348
17	81-2	10.000	3.268	0.028	0.081	0.001	0.479	0.050	1.148	1.440	0.221	0.001	0.002	0.000	0.000	0.000	6.748	70.986	10.348
18	81-2	10.000	3.278	0.034	0.091	0.000	0.481	0.053	1.140	1.466	0.216	0.001	0.000	0.000	0.002	0.000	6.751	70.992	10.348
19	81-2	10.000	0.003	1.025	0.589	0.001	7.215	0.273	0.278	0.021	0.007	0.000	0.004	0.000	0.000	0.000	8.827	71.151	10.348
20	81-2	10.000	2.514	0.389	1.039	0.000	0.658	0.018	1.567	0.003	0.145	0.725	0.001	0.115	0.001	0.004	7.063	72.968	10.359
21	81-2	10.000	2.504	0.380	1.036	0.002	0.653	0.020	1.594	0.000	0.148	0.735	0.002	0.123	0.001	0.003	7.065	73.139	10.362
22	81-2	10.000	0.297	0.011	0.000	0.000	0.072	0.019	0.041	10.135	0.063	0.016	0.000	2.021	0.051	0.038	10.896	73.198	10.358
23	81-2	10.000	0.002	0.000	0.001	0.000	2.510	0.008	0.000	0.001	0.000	0.001	0.000	0.000	0.002	2.493	5.014	77.228	
24	81-2	10.000	2.626	0.038	1.078	0.000	0.655	0.007	0.989	0.079	0.353	0.301	0.000	0.014	0.006	0.444	5.949	77.256	10.386
25	81-2	10.000	2.620	0.034	1.076	0.000	0.653	0.007	0.989	0.079	0.353	0.301	0.000	0.014	0.006	0.444	5.949	77.256	10.386
26	81-2	10.000	0.052	2.985	0.036	0.001	3.181	0.222	0.000	0.001	0.007	0.000	0.000	0.000	0.000	0.000	6.983	77.206	10.400
27	81-2	10.000	2.702	0.256	0.784	0.001	0.808	0.023	1.289	0.779	0.368	0.085	0.000	0.000	0.000	0.000	6.985	77.210	10.408
28	81-2	10.000	2.718	0.252	0.781	0.001	0.593	0.026	1.290	0.769	0.368	0.085	0.000	0.000	0.002	0.002	6.915	78.606	10.417
29	81-2	10.000	2.717	0.254	0.777	0.001	0.617	0.026	1.282	0.759	0.361	0.085	0.000	0.088	0.003	0.002	6.910	78.648	10.415
30	81-2	10.000	2.711	0.283	0.781	0.000	0.599	0.022	1.286	0.755	0.360	0.081	0.002	0.081	0.001	0.001	6.900	78.567	10.415
31	81-2	10.000	0.003	0.981	0.100	0.001	7.350	0.283	0.241	0.000	0.006	0.002	0.000	0.000	0.001	0.002	8.987	73.628	10.436
32	81-2	10.000	0.004	0.984	0.101	0.000	7.319	0.282	0.238	0.000	0.003	0.000	0.000	0.000	0.000	0.001	8.948	73.696	10.441
33	81-3	10.000	3.252	0.021	1.134	0.000	0.107	0.000	0.131	0.170	1.391	0.254	0.006	0.008	0.080	0.187	6.952	63.596	10.307
34	81-3	10.000	3.575	0.024	1.207	0.004	0.118	0.010	0.121	0.258	0.470	0.186	0.002	0.006	0.023	0.008	6.958	62.946	10.307
35	81-3	10.000	2.226	0.086	0.779	0.000	0.639	1.061	0.040	0.708	0.666	0.343	0.885	0.138	0.069	0.063	7.832	52.843	10.418
36	81-3	10.000	0.486	0.000	0.000	3.110	1.804	0.000	0.371	0.085	0.484	0.085	0.225	0.000	0.010	0.000	10.049	63.274	10.391
37	81-3	10.000	3.571	0.027	1.067	0.000	0.191	0.010	0.133	0.218	0.881	0.287	0.008	0.130	0.014	0.063	6.434	54.344	10.298
38	81-3	10.000	3.400	0.032	1.300	0.003	0.140	0.012	0.120	0.181	1.088	0.341	0.000	0.046	0.080	0.036	6.802	54.361	10.310
39	81-3	10.000	4.438	0.002	0.030	0.000	0.004	0.000	0.000	0.366	0.768	0.038	0.000	0.008	0.000	0.010	5.850	54.720	10.311
40	81-3	10.000	3.748	0.002	1.245	0.001	0.013	0.000	0.000	0.014	0.746	0.466	0.000	0.000	0.001	0.000	6.236	66.603	10.435
41	81-3	10.000	3.741	0.003	1.247	0.001	0.014	0.000	0.000	0.021	0.753	0.469	0.000	0.010	0.000	0.000	6.248	66.608	10.441
42	81-3	10.000	3.734	0.019	1.208	0.000	0.070	0.002	0.063	0.126	0.790	0.190	0.007	2.473	0.059	0.398	6.605	65.371	10.450
43	81-3	10.000	2.457	0.033	0.755	0.000	3.727	0.022	0.000	0.357	1.259	0.157	0.000	1.804	0.986	0.158	8.925	66.471	10.470
44	81-3	10.000	2.589	0.283	0.987	0.001	0.808	0.044	1.583	0.000	0.126	0.763	0.000	0.213	0.004	0.002	7.184	69.221	10.558
45	81-3	10.000	3.647	0.043	1.329	0.001	0.178	0.015	0.080	0.037	0.239	0.406	0.002	0.000	0.021	0.008	5.982	69.214	10.559
46	81-3	10.000	2.593	0.280	0.987	0.001	0.808	0.037	1.588	0.000	0.123	0.764	0.002	0.221	0.004	0.002	7.176	72.984	10.588
47	81-3	10.000	3.823	0.073	1.294	0.000	0.261	0.013	0.260	0.041	0.207	0.450	0.002	0.064	0.002	0.006	6.119	72.984	10.588
48	81-3	10.000	-4.778	-0.439	-3.036	-10.100	0.000	-0.118	-0.124	-0.803	0.000	-0.531	0.000	-108.988	-0.282	-4.148	-24.874	73.001	10.587
49	81-3	10.000	4.762	0.041	1.595	0.000	0.231	0.027	0.311	1.785	0.837	0.114	0.040	7.841	0.042	0.273	6.595	73.025	10.597
50	81-3	10.000	3.745	0.034	0.947	0.000	0.189	0.015	0.101	0.235	0.518	0.329	0.000	0.017	0.087	0.040	6.133	75.517	10.604
51	81-3	10.000	3.275	0.036	1.190	0.007	0.239	0.033	0.187	0.331	1.022	0.285	0.001	0.087	0.072	0.078	6.675	75.514	10.610
52	81-3	10.000	0.754	0.001	0.002	0.000	5.379	0.007	0.011	0.003	6.192	0.004	0.000	0.000	0.022	0.000	12.363	75.198	10.602
53	81-1	10.000	3.755	0.002	1.238	0.000	0.016	0.000	0.000	0.012	0.762	0.448	0.000	0.008	0.000	0.000	6.233	69.399	10.019
54	81-1	10.000	3.741	0.001	1.249	0.000	0.017	0.001	0.000	0.016	0.746	0.448	0.000	0.014	0.001	0.000	6.255	69.323	10.019
55	81-1	10.000	2.070	1.870	0.083	0.000	0.118	0.008	0.008	1.509	0.031	0.003	0.000	0.006	0.000	0.001	6.078	69.363	10.019
56	81-1	10.000	3.974	0.000	1.280	0.001	0.001	0.000	0.018	0.004	0.270	0.063	0.002	0.046	0.003	0.001	5.581	69.153	10.019
57	81-1	10.000	3.586	0.000	1.730	0.000	0.000	0.005	0.028	0.007	0.362	0.043	0.000	0.008	0.006	0.000	5.759	69.141	10.019
58	81-1	10.000	2.334	0.000	2.067	0.000	0.017	0.000	0.002	0.334	1.881	0.019	0.000	0.000	0.084	0.344	6.827	68.741	63.626
59	81-1	10.000	2.079	1.846	0.058	0.000	0.114	0.009	0.004	1.921	0.030	0.001	0.000	0.000	0.001	0.000	6.062	72.984	68.798
60	81-1	10.000	4.847	0.025	1.280	0.002	0.076	0.003	0.133	0.228	2.253	0.339	0.000						

Generated from cm02 by V8 Plum system Version 1.09 on 06/05/2006 at 20:33:10 Fe3 recalculated on spinel (magnetite) basis																				
Analysis	Sample	SiO2	TiO2	Al2O3	Cr2O3	Fe2O3	FeO	MnO	MgO	CaO	Na2O	K2O	NiO	F	-OH=F	Cl	-OH=Cl	SO3	Total	
1	81-2	0.04	15.14	3.60	0.00	36.20	37.94	0.89	4.44	0.06	0.00	0.01	0.00	0.00	0.00	0.01	0.00	0.00	100.43	
3	81-2	0.10	14.80	3.44	0.00	36.10	37.00	0.84	4.39	0.13	0.06	0.04	0.00	0.00	0.00	0.00	0.00	0.01	99.01	
11	81-2	0.01	14.39	3.17	0.00	40.39	37.54	1.11	4.21	0.02	0.00	0.02	0.00	0.00	0.00	0.01	0.00	0.00	100.85	
19	81-2	0.02	12.19	0.75	0.01	45.24	36.49	2.89	1.67	0.17	0.03	0.00	0.06	0.00	0.00	0.00	0.00	0.00	99.51	
31	81-2	0.02	11.73	0.78	0.01	46.77	36.98	3.01	1.45	0.00	0.03	0.01	0.00	0.00	0.00	0.01	0.00	0.02	100.80	
32	81-2	0.04	11.82	0.77	0.05	45.91	36.97	2.98	1.43	0.02	0.01	0.00	0.00	0.00	0.00	0.00	0.00	0.02	100.00	
		O	Si	Ti	Al	Cr	Fe3	Fe2	Mn	Mg	Ca	Na	K	Ni	F	Cl	S	Total	X	Y
1	81-2	4.000	0.002	0.406	0.152	0.000	1.031	1.138	0.030	0.237	0.002	0.000	0.001	0.000	0.000	0.001	0.000	3.000	63.417	10.582
3	81-2	4.000	0.004	0.404	0.147	0.000	1.042	1.125	0.029	0.238	0.006	0.004	0.002	0.000	0.000	0.000	0.000	3.000	63.456	10.379
11	81-2	4.000	0.000	0.386	0.134	0.000	1.060	1.126	0.034	0.225	0.001	0.000	0.001	0.000	0.000	0.001	0.000	3.000	63.520	10.311
19	81-2	4.000	0.001	0.344	0.033	0.000	1.279	1.146	0.062	0.084	0.007	0.003	0.000	0.001	0.000	0.000	0.000	3.000	71.151	10.348
31	81-2	4.000	0.001	0.328	0.034	0.000	1.309	1.150	0.066	0.081	0.000	0.002	0.001	0.000	0.000	0.000	0.001	3.000	73.528	10.436
32	81-2	4.000	0.001	0.333	0.034	0.002	1.295	1.159	0.066	0.080	0.001	0.001	0.000	0.000	0.000	0.000	0.000	3.000	73.996	10.441
Generated from cm02 by V8 Plum system Version 1.09 on 06/05/2006 at 20:36:26 Fe3 recalculated on titanite basis																				
Analysis	Sample	SiO2	TiO2	Al2O3	Cr2O3	Fe2O3	FeO	MnO	MgO	CaO	Na2O	K2O	NiO	F	-OH=F	Cl	-OH=Cl	SO3	Total	
25	81-2	0.00	46.33	0.13	0.00	18.06	31.70	3.07	3.73	0.01	0.04	0.00	0.00	0.00	0.00	0.00	0.00	0.00	100.08	
26	81-2	0.81	46.74	0.35	0.02	13.98	31.82	3.09	3.71	0.01	0.18	0.08	0.00	0.00	0.00	0.00	0.00	0.00	100.70	
		O	Si	Ti	Al	Cr	Fe3	Fe2	Mn	Mg	Ca	Na	K	Ni	F	Cl	S	Total	X	Y
25	81-2	3.000	0.000	0.856	0.004	0.000	0.280	0.854	0.064	0.137	0.000	0.002	0.000	0.000	0.000	0.000	0.000	2.000	77.206	10.400
26	81-2	3.000	0.015	0.857	0.010	0.000	0.267	0.851	0.064	0.136	0.000	0.008	0.003	0.000	0.000	0.000	0.000	2.000	77.210	10.406

Generated from cm03 by VB Plum system Version 1.09 on 09/05/2006 at 11:27:20

Analysis	Sample	SiO2	TiO2	Al2O3	Cr2O3	FeO	MnO	MgO	CaO	Na2O	K2O	NO	F	-O=F	Cl	-O=Cl	SO3	Total
1	81-6	39.02	0.01	30.01	0.03	0.32	0.00	0.02	6.76	14.00	0.36	0.00	0.05	0.02	0.59	0.13	9.14	100.15
2	81-6	38.95	0.00	30.13	0.00	0.37	0.04	0.03	6.81	13.80	0.30	0.05	0.03	0.01	0.80	0.14	9.17	100.22
3	81-6	64.51	0.78	19.31	0.00	2.82	0.18	0.33	0.73	4.61	7.59	0.00	0.15	0.06	0.17	0.04	0.11	101.18
4	81-6	0.01	13.17	1.04	0.01	77.27	2.80	2.10	0.01	0.04	0.00	0.01	0.00	0.00	0.00	0.00	0.01	96.47
5	81-6	66.26	0.06	18.80	0.00	0.35	0.03	0.00	0.37	8.79	8.85	0.00	0.00	0.04	0.02	0.01	0.00	96.34
6	81-6	66.46	0.05	18.87	0.02	0.35	0.00	0.00	0.29	8.86	8.84	0.00	0.03	0.01	0.01	0.00	0.01	96.37
7	81-6	65.99	0.06	18.97	0.00	0.40	0.00	0.00	0.59	7.03	8.36	0.03	0.00	0.00	0.01	0.00	0.01	96.09
8	81-6	66.59	0.04	18.80	0.00	0.36	0.00	0.00	0.37	7.03	8.36	0.03	0.00	0.00	0.01	0.00	0.00	96.60
9	81-6	66.61	0.08	18.78	0.00	0.39	0.00	0.00	0.36	6.92	8.41	0.02	0.03	0.01	0.02	0.00	0.00	96.60
10	81-6	65.88	0.03	18.87	0.02	0.33	0.00	0.00	0.40	8.90	8.34	0.05	0.00	0.00	0.01	0.00	0.00	96.41
11	81-6	66.23	0.09	19.00	0.00	0.38	0.00	0.00	0.45	8.98	8.37	0.00	0.04	0.02	0.00	0.00	0.00	96.50
12	81-6	0.02	46.72	0.18	0.00	44.56	3.42	3.56	0.01	0.02	0.05	0.00	0.00	0.00	0.02	0.01	0.01	98.55
13	81-6	29.30	35.98	0.70	0.00	1.74	0.15	0.01	25.83	0.21	0.00	0.00	0.20	0.08	0.00	0.00	0.00	94.12
14	81-6	38.02	6.18	12.51	0.00	12.76	0.48	15.90	0.00	0.91	8.68	0.00	0.95	0.40	0.02	0.01	0.03	96.02
15	81-6	38.52	6.13	12.67	0.00	11.77	0.48	14.26	0.08	1.28	8.38	0.00	0.73	0.31	0.07	0.02	0.07	94.07
16	81-6	28.86	35.06	0.71	0.01	1.90	0.11	0.05	25.80	0.20	0.00	0.05	0.33	0.14	0.01	0.00	0.00	92.76
17	81-6	66.26	0.05	18.88	0.01	0.30	0.03	0.00	0.34	6.77	8.71	0.00	0.00	0.00	0.01	0.00	0.00	96.35
18	81-6	39.52	0.02	29.72	0.02	0.40	0.01	0.06	6.73	13.06	0.38	0.00	0.03	0.01	0.53	0.12	9.09	99.69
19	81-6	39.07	0.02	30.38	0.02	0.38	0.01	0.02	7.09	13.05	0.29	0.00	0.10	0.04	0.53	0.12	8.96	99.69
20	81-6	66.61	0.05	18.85	0.00	0.36	0.00	0.00	0.34	7.28	8.00	0.01	0.03	0.01	0.00	0.00	0.00	96.27
21	81-6	65.93	0.08	19.10	0.00	0.32	0.00	0.00	0.57	7.04	6.17	0.01	0.09	0.04	0.02	0.00	0.00	96.37
22	81-6	66.31	0.07	18.75	0.00	0.35	0.02	0.00	0.37	7.00	6.41	0.00	0.14	0.08	0.01	0.00	0.00	96.37
23	81-6	66.38	0.07	18.75	0.00	0.35	0.02	0.00	0.41	7.04	6.25	0.00	0.01	0.01	0.02	0.01	0.00	96.30
24	81-6	0.02	12.95	0.86	0.00	76.94	2.87	2.05	0.00	0.03	0.01	0.00	0.00	0.00	0.02	0.00	0.00	95.54
25	81-6	66.45	0.03	18.85	0.00	0.29	0.00	0.00	0.33	8.92	8.55	0.01	0.07	0.03	0.00	0.00	0.00	96.47
26	81-6	66.48	0.06	18.73	0.00	0.30	0.05	0.00	0.30	6.81	8.77	0.00	0.02	0.01	0.00	0.00	0.00	96.50
27	81-6	66.23	0.06	18.95	0.02	0.34	0.00	0.00	0.53	6.82	8.38	0.00	0.38	0.08	0.03	0.03	0.01	96.43
28	81-6	29.17	35.58	0.72	0.00	1.96	0.19	0.04	26.85	0.21	0.00	0.00	0.00	0.00	0.03	0.01	0.00	94.73
29	81-6	38.06	5.61	12.47	0.00	12.80	0.56	16.16	0.00	1.02	8.61	0.00	0.91	0.38	0.02	0.01	0.04	95.86
30	81-6	66.57	0.02	18.80	0.00	0.31	0.00	0.00	0.36	6.91	8.42	0.00	0.00	0.00	0.03	0.01	0.00	96.42
31	81-6	66.76	0.07	18.87	0.01	0.29	0.02	0.00	0.29	6.93	8.63	0.00	0.01	0.00	0.01	0.00	0.01	96.88
32	81-6	0.27	0.00	0.00	0.01	0.14	0.14	0.04	52.78	0.10	0.03	0.00	3.55	1.50	0.07	0.02	0.60	56.22
33	81-6	66.26	0.02	18.90	0.00	0.35	0.04	0.00	0.29	6.95	8.73	0.00	0.12	0.05	0.00	0.00	0.00	96.60
34	81-6	66.42	0.04	18.69	0.00	0.31	0.00	0.00	0.33	6.68	8.74	0.00	0.10	0.04	0.02	0.00	0.00	96.28
35	81-6	0.01	12.91	0.91	0.02	77.37	2.86	1.76	0.00	0.07	0.00	0.00	0.00	0.00	0.00	0.00	0.01	95.62
36	81-6	66.43	0.04	18.76	0.04	0.35	0.00	0.00	0.23	6.65	8.62	0.00	0.04	0.02	0.02	0.00	0.00	96.56
37	81-6	37.55	6.36	12.62	0.03	13.67	0.52	15.71	0.00	1.06	8.66	0.03	0.80	0.34	0.02	0.01	0.06	96.96
38	81-6	38.23	5.71	12.49	0.00	13.34	0.46	16.42	0.00	0.96	9.03	0.00	0.89	0.37	0.03	0.01	0.06	97.27
39	81-6	38.12	6.08	12.50	0.00	13.15	0.51	16.11	0.00	1.00	8.61	0.00	0.81	0.34	0.00	0.00	0.05	96.80
40	81-6	37.78	5.87	12.46	0.00	12.74	0.43	16.00	0.56	0.95	8.88	0.00	0.94	0.40	0.03	0.01	0.04	96.27
41	81-6	37.86	5.82	12.26	0.00	13.31	0.52	16.13	0.04	0.91	8.96	0.00	0.93	0.39	0.02	0.00	0.03	96.21
42	81-6	66.45	0.06	19.14	0.01	0.30	0.00	0.00	0.50	7.17	6.01	0.00	0.01	0.01	0.00	0.00	0.01	96.94
43	81-6	66.88	0.04	18.98	0.00	0.29	0.01	0.00	0.36	7.03	6.22	0.00	0.00	0.00	0.00	0.00	0.01	96.81
44	81-6	37.89	5.88	12.30	0.00	13.15	0.51	15.74	0.01	0.96	8.58	0.02	0.96	0.41	0.01	0.00	0.03	95.22
45	81-6	2.84	0.00	0.58	0.00	0.27	0.15	0.07	46.30	0.44	0.25	0.00	3.22	1.36	0.06	0.02	0.19	53.01
46	81-6	0.00	13.29	0.92	0.03	77.39	2.55	2.10	0.00	0.01	0.00	0.00	0.00	0.00	0.00	0.00	0.01	96.31
47	81-4	65.30	0.05	19.31	0.01	0.27	0.00	0.00	0.73	6.54	8.46	0.00	0.04	0.02	0.01	0.00	0.00	96.71
48	81-4	29.35	35.71	0.89	0.04	1.35	0.12	0.02	26.47	0.07	0.00	0.06	0.15	0.06	0.02	0.00	0.00	94.18
49	81-4	0.08	13.87	8.07	2.11	65.57	0.89	8.19	0.03	0.00	0.00	0.15	0.00	0.00	0.00	0.00	0.00	96.78
50	81-4	39.03	5.66	12.55	0.06	14.14	0.37	10.85	11.31	3.02	1.03	0.00	0.14	0.06	0.01	0.00	0.06	96.16
51	81-4	0.82	0.01	0.01	0.02	0.15	0.06	0.02	50.81	0.07	0.05	0.00	2.86	1.20	0.11	0.03	0.22	53.60
52	81-4	65.33	0.04	20.14	0.00	0.21	0.06	0.00	1.49	7.77	4.09	0.01	0.02	0.01	0.01	0.00	0.00	96.17
53	81-4	65.48	0.05	20.46	0.00	0.26	0.01	0.00	1.74	7.84	3.80	0.00	0.09	0.04	0.00	0.00	0.01	96.70
54	81-4	65.31	0.05	19.87	0.02	0.28	0.01	0.00	1.20	7.16	4.95	0.03	0.00	0.00	0.00	0.00	0.02	96.90
55	81-4	63.04	0.05	21.53	0.00	0.28	0.04	0.00	3.01	7.81	2.60	0.04	0.01	0.00	0.00	0.00	0.00	96.40
56	81-4	0.06	9.90	1.47	0.00	79.69	2.12	1.32	0.02	0.05	0.02	0.02	0.00	0.00	0.00	0.00	0.01	94.86
57	81-4	29.68	35.32	0.96	0.00	1.37	0.11	0.01	26.63	0.10	0.01	0.01	0.04	0.02	0.01	0.00	0.01	94.27
58	81-4	65.70	0.00	19.66	0.04	0.23	0.01	0.00	0.93	7.16	5.48	0.00	0.00	0.00	0.00	0.00	0.00	94.62
59	81-4	39.07	6.20	13.00	0.01	10.81	0.14	12.70	11.89	2.67	0.97	0.01	0.19	0.08	0.02	0.01	0.06	96.24
60	81-4	29.74	35.62	0.98	0.02	1.36	0.11	0.01	26.67	0.08	0.02	0.00	0.04	0.02	0.01	0.00	0.00	97.66
61	55-1	1.59	0.06	167.69	0.00	0.21	0.39	0.84	0.01	0.05	0.03	0.00	0.00	0.00	0.18	0.04	0.00	171.00
62	55-1	1.47	0.02	164.67	0.00	0.66	0.56	0.55	0.00	0.03	0.01	0.05	0.00	0.00	0.00	0.00	0.00	168.01
63	55-1	1.44	0.19	112.00	0.26	0.31	0.28	0.86	0.30	0.09	0.29	0.05	0.59	0.25	0.27	0.06	0.24	116.67

Generated from cm03 by VB Plum system Version 1.09 on 09/05/2006 at 11:34:24 Fe3 recalculated on spinel (magnetite) basis

Generated from cm03 by V8 Plus system Version 1.09 on 09/05/2006 at 11:35:11 Fe3 recalculated on ilmenite basis

12	81-6	SiO2 0.02	TiO2 46.72	Al2O3 0.16	Cr2O3 0.00	Fe2O3 14.02	FeO 31.95	MnO 3.42	MgO 3.56	CaO 0.01	Na2O 0.02	K2O 0.05	H2O 0.00	F 0.00	-O=F 0.00	Cl 0.02	-O=Cl 0.01	SO3 0.01	Total 66.96
12	81-6	O 3.000	Si 0.001	Ti 0.008	Al 0.005	Cr 0.000	Fe3 0.261	Mn 0.072	Mg 0.131	Ca 0.00	Na 0.001	K 0.002	Ni 0.00	F 0.000	Cl 0.001	S 0.00	Total 2.000	X 3.936	Y 57.884

Analysis	Sample	SiO2	TiO2	Al2O3	Cr2O3	FeO	MnO	MgO	CaO	Na2O	K2O	NO	F	-O=F	Cl	-O=Cl	SO3	Total
1	46-3	62.13	0.54	20.59	0.01	1.77	0.12	0.13	1.40	5.49	4.67	0.00	0.20	0.06	0.24	0.05	0.06	97.42
2	46-3	40.06	4.58	11.97	0.00	13.26	0.43	11.80	11.81	2.81	1.18	0.00	0.23	0.10	0.01	0.00	0.06	97.89
3	46-3	53.36	0.04	28.56	0.00	0.54	0.01	0.05	11.29	4.78	0.27	0.02	0.01	0.00	0.00	0.00	0.01	98.92
4	46-3	52.88	0.02	28.83	0.00	0.57	0.01	0.07	11.87	4.47	0.28	0.02	0.00	0.00	0.01	0.00	0.01	98.83
5	46-3	0.08	16.03	4.40	0.02	70.56	0.83	5.11	0.03	0.00	0.01	0.05	0.00	0.00	0.00	0.00	0.01	97.14
6	46-3	0.02	15.87	6.24	0.03	67.41	0.57	8.41	0.03	0.00	0.02	0.01	0.00	0.00	0.00	0.00	0.00	96.60
7	46-3	0.43	0.00	0.00	0.00	0.29	0.08	0.26	51.74	0.15	0.01	0.00	2.55	1.08	0.27	0.06	0.78	95.44
8	46-3	40.09	0.00	0.04	0.06	15.69	0.25	45.28	0.33	0.01	0.00	0.14	0.00	0.00	0.02	0.00	0.00	101.92
9	46-3	0.05	16.36	5.99	0.07	68.48	0.57	6.79	0.02	0.02	0.00	0.04	0.00	0.00	0.00	0.00	0.00	98.36
10	46-3	55.49	0.08	27.21	0.00	0.43	0.00	0.03	9.79	5.49	0.43	0.00	0.00	0.00	0.01	0.00	0.01	98.94
11	46-3	55.04	0.05	27.55	0.02	0.53	0.01	0.05	10.10	5.28	0.34	0.00	0.02	0.01	0.00	0.00	0.00	98.96
12	46-3	62.36	0.15	20.24	0.00	0.44	0.01	0.02	2.37	7.56	3.31	0.00	0.00	0.00	0.01	0.00	0.02	96.47
13	46-3	65.51	0.06	18.92	0.01	0.34	0.01	0.00	0.48	6.47	7.02	0.00	0.00	0.00	0.01	0.00	0.02	98.84
14	46-3	40.95	4.49	11.08	0.00	13.22	0.42	11.73	11.47	2.77	1.41	0.00	0.19	0.08	0.03	0.01	0.04	97.72
15	46-3	47.99	2.24	5.23	0.02	7.65	0.28	12.90	22.99	0.65	0.00	0.00	0.10	0.04	0.00	0.00	0.00	99.92
16	46-3	0.01	0.00	0.00	0.05	84.42	0.20	0.02	0.00	0.04	0.01	0.11	0.00	0.00	0.05	0.01	90.64	175.54
17	46-3	0.07	18.05	8.43	0.07	62.41	0.47	8.91	0.01	0.00	0.00	0.00	0.00	0.00	0.00	0.00	0.00	98.41
18	46-3	0.47	0.05	0.02	0.00	0.32	0.00	0.32	52.41	0.13	0.03	0.04	2.85	1.20	0.22	0.06	0.74	96.33
19	46-3	0.24	0.04	0.00	0.00	82.11	0.20	0.02	0.09	0.04	0.04	0.11	0.00	0.00	0.03	0.01	93.71	178.63
20	46-3	0.71	0.01	0.03	0.03	0.41	0.03	0.33	51.43	0.02	0.03	0.00	2.71	1.14	0.22	0.05	0.58	95.33
21	46-3	40.05	5.96	12.39	0.02	10.62	0.14	13.30	11.85	2.68	0.92	0.00	0.16	0.07	0.03	0.01	0.04	97.89
22	46-3	65.81	0.05	19.88	0.01	0.20	0.00	0.00	1.19	7.29	5.02	0.00	0.00	0.00	0.00	0.00	0.00	99.25
23	46-3	65.03	0.02	20.45	0.02	0.22	0.01	0.00	1.82	7.81	3.90	0.03	0.00	0.00	0.00	0.02	0.01	99.49
24	46-3	53.08	0.10	28.17	0.00	0.52	0.03	0.05	10.85	4.89	0.29	0.02	0.00	0.00	0.00	0.00	0.00	97.90
25	46-3	0.39	0.00	0.01	0.01	0.22	0.05	0.28	51.46	0.13	0.01	0.00	2.85	1.12	0.27	0.06	0.60	94.89
26	46-1	66.46	0.09	19.30	0.00	0.35	0.03	0.00	0.72	7.32	5.77	0.00	0.00	0.00	0.00	0.00	0.00	100.05
27	46-1	66.43	0.07	19.40	0.00	0.35	0.03	0.00	0.73	7.18	5.81	0.03	0.00	0.00	0.01	0.00	0.01	100.04
28	46-1	0.00	9.90	0.62	0.00	81.16	3.06	0.83	0.00	0.01	0.00	0.00	0.00	0.00	0.01	0.00	0.03	95.58
29	46-1	0.03	9.80	0.54	0.00	81.30	3.06	0.79	0.01	0.02	0.00	0.00	0.00	0.00	0.01	0.00	0.01	94.20
30	46-1	0.07	9.87	0.63	0.03	79.68	3.03	0.86	0.01	0.00	0.00	0.00	0.00	0.00	0.00	0.00	0.01	94.41
31	46-1	29.19	36.24	0.68	0.00	1.79	0.16	0.02	25.88	0.25	0.01	0.00	0.30	0.13	0.03	0.01	0.00	96.69
32	46-1	66.63	0.05	18.81	0.00	0.32	0.03	0.00	0.28	6.84	6.62	0.00	0.06	0.03	0.00	0.00	0.00	99.67
33	46-1	66.50	0.05	19.00	0.00	0.31	0.00	0.00	0.34	6.88	6.56	0.00	0.04	0.02	0.01	0.00	0.00	98.44
34	46-1	40.33	6.18	12.00	0.00	11.31	0.25	13.13	11.31	2.93	0.84	0.02	0.18	0.08	0.02	0.01	0.03	98.70
35	46-1	40.81	6.33	11.80	0.00	11.05	0.22	13.25	11.55	2.91	0.81	0.02	0.18	0.07	0.03	0.01	0.04	98.64
36	46-1	64.13	0.10	20.91	0.01	0.36	0.00	0.00	2.15	7.90	3.06	0.00	0.00	0.00	0.00	0.00	0.00	98.51
37	46-1	40.34	6.34	12.05	0.00	11.00	0.24	13.07	11.55	2.84	0.80	0.00	0.37	0.18	0.04	0.01	0.03	98.72
38	46-1	40.56	6.31	12.19	0.02	10.81	0.21	13.13	11.61	2.89	0.80	0.00	0.28	0.11	0.03	0.01	0.03	98.47
39	46-1	29.50	35.77	0.78	0.00	1.92	0.13	0.02	25.77	0.17	0.00	0.03	0.18	0.08	0.02	0.01	0.00	94.19
40	46-1	29.60	35.80	0.77	0.00	1.86	0.18	0.03	25.89	0.16	0.00	0.00	0.29	0.12	0.03	0.01	0.00	94.47
41	46-1	40.75	0.00	31.12	0.00	0.38	0.04	0.02	5.43	12.35	0.34	0.05	0.00	0.00	0.92	0.21	7.90	96.10
42	46-1	39.80	0.00	30.42	0.00	0.37	0.00	0.01	5.47	15.26	0.38	0.01	0.06	0.03	1.01	0.23	7.72	100.24
43	46-1	40.65	6.14	12.07	0.00	10.33	0.21	13.38	11.43	2.88	0.78	0.01	0.31	0.13	0.01	0.00	0.05	98.11
44	46-1	39.81	6.38	12.74	0.00	10.43	0.17	13.32	11.88	2.79	0.77	0.00	0.28	0.11	0.00	0.00	0.12	98.52
45	46-1	0.06	16.15	4.34	0.02	70.24	0.86	5.78	0.00	0.03	0.00	0.00	0.00	0.00	0.00	0.00	0.00	97.47
46	46-1	40.10	6.07	12.18	0.01	10.86	0.23	12.90	11.21	2.97	0.80	0.00	0.32	0.14	0.02	0.00	0.04	98.97
47	46-1	57.14	0.09	26.16	0.01	0.47	0.04	0.05	6.19	6.33	0.42	0.00	0.10	0.04	0.02	0.00	0.00	98.77
48	46-1	0.03	13.44	1.28	0.00	76.32	2.40	2.70	0.06	0.01	0.01	0.00	0.00	0.00	0.00	0.00	0.00	100.78
49	46-1	36.90	0.03	29.20	0.01	0.34	0.01	0.14	10.63	12.32	0.50	0.00	0.05	0.02	0.12	0.03	10.28	97.25
50	46-1	61.93	0.11	21.26	0.01	0.29	0.00	0.03	2.92	8.14	2.23	0.01	0.09	0.04	0.29	0.07	0.08	97.25
51	46-1	61.39	0.09	22.55	0.00	0.36	0.00	0.01	4.30	7.53	1.54	0.05	0.01	0.01	0.01	0.00	0.02	97.85
52	46-1	39.75	6.47	12.51	0.00	10.84	0.22	13.20	11.15	2.75	0.73	0.01	0.33	0.14	0.02	0.01	0.05	97.66
53	46-1	66.68	0.04	18.95	0.00	0.24	0.00	0.00	0.34	7.04	6.32	0.00	0.00	0.00	0.01	0.00	0.00	99.62
54	46-1	66.54	0.03	18.96	0.01	0.28	0.00	0.00	0.45	7.04	6.21	0.00	0.00	0.00	0.01	0.00	0.00	99.63
55	46-1	66.75	0.06	18.97	0.02	0.31	0.02	0.00	0.38	7.09	6.26	0.01	0.12	0.08	0.00	0.00	0.00	99.92
56	46-1	0.00	11.92	0.64	0.02	78.43	3.18	1.31	0.02	0.01	0.03	0.00	0.00	0.00	0.00	0.00	0.01	95.06
57	46-1	65.98	0.04	18.68	0.01	0.36	0.00	0.00	0.34	6.94	6.45	0.03	0.00	0.00	0.00	0.00	0.00	97.15
58	46-1	0.03	14.16	2.32	0.00	73.98	1.64	4.06	0.03	0.69	0.02	0.00	0.00	0.00	0.24	0.05	0.04	96.00
59	46-1	66.73	0.02	18.96	0.00	0.32	0.00	0.00	0.30	7.02	6.49	0.01	0.00	0.00	0.02	0.00	0.00	98.77
60	46-1	66.70	0.05	18.87	0.00	0.27	0.00	0.00	0.37	7.01	6.50	0.00	0.00	0.00	0.01	0.00	0.00	99.01
61	46-1	66.26	0.06	19.20	0.00	0.31	0.00	0.00	0.70	7.21	5.91	0.01	0.06	0.03	0.00	0.00	0.01	99.69
62	46-1	0.04	13.92	2.27	0.03	74.77	1.83	3.76	0.04	0.01	0.00	0.00	0.00	0.00	0.01	0.00	0.02	96.50
63	46-1	0.06	18.27	6.69	0.00	65.26	0.45	7.81	0.01	0.01	0.00	0.02	0.00	0.00	0.00	0.00	0.00	98.69
64	46-1	66.56	0.04	18.85	0.02	0.30	0.00	0.00	0.30	6.75	6.92	0.00	0.00	0.00	0.00	0.00	0.00	99.44
65	46-1	66.54	0.05	18.81	0.00	0.33	0.00	0.00	0.39	6.83	6.84	0.00	0.00	0.00	0.00	0.00	0.00	99.50
66	46-1	0.06	15.98	3.99	0.06	71.77	0.85	5.52	0.02	0.01	0.00	0.02	0.00	0.00	0.02	0.01	0.02	98.31

Analysis	Sample	O	Si	Ti	Al	Cr	Fe2	Mn	Mg	Ca	Na	K	Ni	F	Cl	S	Total	X	Y
1	46-3	10.000	3.580	0.024	1.404	0.001	0.088	0.008	0.011	0.087	0.818	0.359	0.000	0.037	0.023	0.003	6.191	14.882	54.672
2	46-3	10.000	2.822	0.028	0.923	0.000	0.728	0.024	1.132	0.828	0.357	0.066	0.000	0.047	0.001	0.003	6.938	14.722	57.888
3	46-3	10.000	3.054	0.022	1.927	0.000	0.026	0.001	0.004	0.862	0.529	0.020	0.001	0.000	0.000	0.000	6.250	8.040	56.951
4	46-3	10.000	3.038	0.001	1.836	0.000	0.028	0.000	0.008	0.718	0.469	0.020	0.001	0.000	0.001	0.000	6.250	8.372	56.246
5	46-3	10.000	0.008	1.211	0.521	0.002	5.932	0.070	0.786	0.004	0.001	0.002	0.004	0.000	0.000	0.001	8.520	7.958	56.329
6	46-3	10.000	0.002	1.177	0.725	0.002	5.956	0.047	0.841	0.003	0.000	0.003	0.001	0.000	0.000	0.000	8.456	7.741	56.322
7	46-3	10.000	0.078	0.000	0.000	0.000	0.045	0.012	0.072	10.144	0.086	0.003	0.000	1.477	0.084	0.108	10.516	9.286	57.408
8	46-3	10.000	2.480	0.006	0.033	0.003	0.812	0.013	4.176	0.022	0.001	0.000	0.007	0.000	0.002	0.001	7.517	9.371	57.819
9	46-3	10.000	0.005	1.191	0.863	0.008	5.543	0.047	0.879	0.002	0.003	0.000	0.000	0.000	0.000	0.000	8.462	9.547	57.866
10	46-3	10.000	3.159	0.003	1.826	0.000	0.021	0.000	0.003	0.967	0.606	0.031	0.000	0.000	0.001	0.000	8.244	9.602	58.506
11	46-3	10.000	3.136	0.002	1.860	0.001	0.026	0.001	0.004	0.817	0.581	0.025	0.000	0.003	0.000	0.000	8.241	9.542	58.617
12	46-3	10.000	3.802	0.006	1.750	0.000	0.021	0.001	0.002	0.147	0.847	0.244	0.000	0.000	0.001	0.001	8.247	11.886	62.231
13	46-3	10.000	3.718	0.003	1.286	0.001	0.018	0.000	0.000	0.029	0.712	0.938	0.000	0.000	0.001	0.001	8.295	12.701	61.429
14	46-3	10.000	2.680	0.221	0.865	0.000	0.723	0.024	1.148	0.804	0.361	0.118	0.000	0.040	0.003	0.002	8.923	12.564	61.968
15	46-3	10.000	3.010	0.108	0.387	0.001	0.412	0.015	1.208	1.525	0.079	0.000	0.000	0.019	0.000	0.000	8.740	18.274	61.142
16	46-3	10.000	0.000	0.000	0.000	0.002	2.567	0.008	0.001	0.000	0.003	0.000	0.003	0.000	0.003	2.473	5.096	61.080	
17	46-3	10.000	0.008	1.258	0.919	0.008	4.825	0.037	1.228	0.001	0.000	0.000	0.000	0.000	0.000	0.000	8.278	16.801	60.989
18	46-3	10.000	0.066	0.007	0.004	0.000	0.048	0.000	0.088	10.186	0.045	0.008	0.006	1.836	0.087	0.100	10.883	16.946	61.048
19	46-3	10.000	0.006	0.001	0.000	0.000	2.447	0.000	0.001	0.003	0.003	0.002	0.003	0.000	0.002	2.858	4.881	60.893	
20	46-3	10.000	0.131	0.001	0.007	0.004	0.063	0.005	0.091	10.143	0.008	0.007	0.000	1.578	0.086	0.078	10.536	16.907	60.914
21	46-3	10.000	2.579	0.289	0.940	0.001	0.572	0.008	1.278	0.804	0.334	0.076	0.000	0.033	0.003	0.002	8.881	16.953	61.245
22	46-3	10.000	3.863	0.002	1.315	0.000	0.010	0.000	0.000	0.071	0.763	0.390	0.000	0.000	0.000	0.000	8.234	17.279	58.668
23	46-3	10.000	3.842	0.001	1.360	0.001	0.011	0.001	0.000	0.115	0.848	0.279	0.001	0.000	0.000	0.000	8.246	17.877	58.686
24	46-3	10.000	3.087	0.004	1.918	0.000	0.025	0.001	0.007	0.528	0.727	0.028	0.001	0.000	0.000	0.000	8.244	9.311	57.152
25	46-3	10.000	0.072	0.003	0.003	0.001	0.004	0.007	0.077	10.281	0.003	0.003	0.000	1.564	0.065	0.000	10.908	16.953	61.142
26	46-1	10.000	3.711	0.004	1.270	0.000	0.018	0.001	0.000	0.043	0.793	0.411	0.000	0.000	0.000	0.001	8.251	36.154	51.307
27	46-1	10.000	3.710	0.003	1.277	0.000	0.016	0.002	0.000	0.044	0.777	0.414	0.001	0.000	0.000	0.001	8.244	36.069	52.104
28	46-1	10.000	0.000	0.848	0.083	0.000	7.735	0.298	0.135	0.001	0.002	0.000	0.000	0.000	0.003	0.003	9.107	41.032	51.148
29	46-1	10.000	0.004	0.841	0.073	0.000	7.783	0.298	0.135	0.001	0.002	0.000	0.000	0.000	0.001	0.001	9.118	40.860	50.882
30	46-1	10.000	0.008	0.866	0.086	0.000	7.883	0.298	0.182	0.001	0.000	0.000	0.000	0.000	0.000	0.001	9.090	40.868	50.832
31	46-1	10.000	2.038	1.903	0.086	0.000	0.105	0.009	0.002	1.936	0.034	0.001	0.000	0.087	0.003	0.000	8.084	40.732	50.386
32	46-1	10.000	3.741	0.002	1.251	0.000	0.015	0.001	0.000	0.016	0.745	0.474	0.000	0.011	0.000	0.000	8.246	41.723	49.942
33	46-1	10.000	3.734	0.002	1.258	0.000	0.014	0.000	0.000	0.021	0.749	0.470	0.000	0.008	0.001	0.000	8.248	42.087	49.987
34	46-1	10.000	2.991	0.296	0.909	0.000	0.806	0.014	1.258	0.779	0.386	0.089	0.001	0.039	0.002	0.002	8.892	40.513	47.422
35	46-1	10.000	2.996	0.305	0.886	0.000	0.806	0.014	1.258	0.779	0.386	0.089	0.001	0.039	0.002	0.002	8.891	40.695	47.422
36	46-1	10.000	3.911	0.004	1.398	0.000	0.017	0.000	0.000	0.130	0.883	0.222	0.000	0.000	0.001	0.000	8.230	37.084	51.979
37	46-1	10.000	2.994	0.307	0.914	0.000	0.591	0.013	1.253	0.796	0.395	0.085	0.000	0.075	0.006	0.002	8.890	35.985	51.427
38	46-1	10.000	2.984	0.304	0.919	0.001	0.578	0.011	1.252	0.796	0.395	0.085	0.000	0.083	0.003	0.001	8.880	35.955	51.427
39	46-1	10.000	2.057	1.876	0.082	0.000	0.112	0.008	0.002	1.928	0.023	0.000	0.001	0.041	0.003	0.000	8.089	34.488	51.790
40	46-1	10.000	2.052	1.875	0.080	0.000	0.108	0.011	0.003	1.932	0.021	0.000	0.000	0.064	0.003	0.000	8.075	34.298	51.818
41	46-1	10.000	2.370	0.000	2.133	0.000	0.019	0.002	0.002	3.388	1.363	0.025	0.000	0.091	0.000	0.000	8.439	34.390	51.979
42	46-1	10.000	2.327	0.000	2.087	0.000	0.018	0.000	0.001	3.343	1.731	0.028	0.001	0.012	0.010	0.000	8.336	34.883	51.880
43	46-1	10.000	2.808	0.286	0.913	0.000	0.554	0.011	1.280	0.786	0.358	0.064	0.001	0.082	0.001	0.003	8.875	36.302	54.414
44	46-1	10.000	2.849	0.307	0.901	0.000	0.599	0.009	1.271	0.813	0.346	0.083	0.000	0.082	0.000	0.008	8.883	35.488	54.249
45	46-1	10.000	0.008	1.212	0.511	0.001	5.882	0.073	0.880	0.000	0.008	0.000	0.000	0.000	0.000	0.000	8.828	34.126	56.774
46	46-1	10.000	2.598	0.286	0.890	0.000	0.599	0.013	1.246	0.778	0.373	0.068	0.000	0.086	0.002	0.002	8.890	32.762	54.979
47	46-1	10.000	3.243	0.004	1.790	0.001	0.022	0.002	0.004	0.466	0.866	0.030	0.000	0.018	0.002	0.000	8.251	32.128	55.653
48	46-1	10.000	0.004	1.063	0.183	0.000	6.900	0.220	0.434	0.007	0.003	0.001	0.000	0.000	0.000	0.000	8.824	31.508	56.700
49	46-1	10.000	2.134	0.002	1.991	0.000	0.016	0.000	0.012	0.677	1.382	0.037	0.000	0.010	0.012	0.000	8.897	30.777	56.388
50	46-1	10.000	3.857	0.006	1.440	0.001	0.014	0.000	0.003	0.179	0.807	0.163	0.000	0.016	0.028	0.003	8.270	36.376	74.043
51	46-1	10.000	3.467	0.004	1.510	0.000	0.017	0.000	0.001	0.262	0.830	0.112	0.002	0.002	0.001	0.001	8.225	35.081	74.208
52	46-1	10.000	2.569	0.314	0.863	0.000	0.575	0.012	1.271	0.772	0.344	0.080	0.000	0.067	0.002	0.002	8.873	37.084	75.151
53	46-1	10.000	3.739	0.002	1.253	0.000	0.011	0.000	0.000	0.021	0.785	0.462	0.000	0.000	0.001	0.000	8.242	36.908	77.749
54	46-1	10.000	3.738	0.001	1.253	0.000	0.013	0.000	0.000	0.027	0.786	0.444	0.000	0.000	0.001	0.000	8.241	36.908	77.511
55	46-1	10.000	3.740	0.002	1.253	0.001	0.014	0.001	0.000	0.023	0.770	0.447	0.000	0.022	0.000	0.000	8.251	36.890	77.886
56	46-1	10.000	0.000	1.003	0.085	0.002	7.339	0.298	0.218	0.002	0.002	0.000	0.000	0.000	0.000	0.000	8.954	38.287	65.358
57	46-1	10.000	3.739	0.002	1.257	0.000	0.017	0.000	0.000	0.020	0.781	0.466	0.002	0.000	0.000	0.001	8.253	36.132	62.919
58	46-1	10.000	0.003	1.118	0.287	0.000	6.487	0.145	0.634	0.004	0.140	0.003	0.000	0.000	0.043	0.003	8.822	40.350	61.756
59	46-1	10.000	3.737	0.001	1.252	0.000	0.015	0.000	0.000	0.016	0.783	0.464	0.000	0.000	0.002	0.000	8.250	36.969	61.163
60	46-1	10.000	3.739	0.002	1.247	0.000	0.013	0.000	0.000	0.022	0.782	0.466	0.000	0.000	0.001	0			

Appendix 4: Microprobe glass analyses

Samples 81-1, 81-2 & 81-3 pg. 223

Samples 81-4 & 81-6 pg. 224

Samples 46-1 & 46-3 pg. 225

Analysis	Sample	SiO ₂	TiO ₂	Al ₂ O ₃	Cr ₂ O ₃	FeO	MnO	MgO	CaO	Na ₂ O	K ₂ O	NiO	F	-O=F	Cl	-O=Cl	SO ₃	Total
1	81-1	59.44	0.61	18.65	0.03	2.80	0.24	0.25	0.64	9.11	5.46	0.03	0.01	0.00	0.30	0.07	0.09	97.80
2	81-1	59.56	0.60	18.33	0.03	2.73	0.22	0.25	0.58	8.35	5.39	0.00	0.16	0.07	0.27	0.06	0.07	96.42
3	81-1	58.01	0.63	17.97	0.00	2.85	0.23	0.28	0.62	8.15	5.44	0.00	0.21	0.09	0.22	0.05	0.05	94.32
4	81-1	57.47	0.81	17.91	0.00	2.77	0.21	0.23	0.65	8.06	5.48	0.00	0.23	0.10	0.24	0.05	0.06	93.77
5	81-1	57.44	0.17	12.26	0.00	1.26	0.05	0.19	0.23	7.13	2.24	0.00	0.00	0.00	0.14	0.03	0.00	81.18
6	81-1	55.98	0.55	17.39	0.00	2.81	0.20	0.26	1.54	8.00	5.29	0.03	0.70	0.26	0.24	0.05	0.10	92.72
7	81-1	60.77	0.48	15.86	0.00	1.47	0.12	0.24	0.48	8.87	3.54	0.00	3.85	1.54	0.49	0.11	0.85	85.00
8	81-1	59.48	0.57	18.45	0.01	2.92	0.26	0.22	0.52	8.88	5.30	0.01	0.14	0.06	0.20	0.05	0.11	96.97
9	81-1	59.58	0.60	18.17	0.03	2.80	0.19	0.23	0.58	8.41	5.28	0.00	0.29	0.12	0.29	0.07	0.15	95.41
10	81-1	58.99	0.80	18.26	0.01	2.98	0.23	0.25	0.67	8.47	5.41	0.02	0.18	0.07	0.28	0.08	0.08	96.26
11	81-1	59.02	0.61	18.42	0.04	3.00	0.28	0.25	0.59	8.79	5.42	0.01	0.21	0.08	0.24	0.08	0.12	96.83
12	81-1	58.63	0.58	18.28	0.00	2.80	0.20	0.26	0.60	8.75	5.44	0.00	0.30	0.13	0.25	0.08	0.08	95.98
13	81-1	44.99	0.34	13.99	0.03	0.43	0.00	0.20	0.27	8.33	1.98	0.00	4.11	1.73	0.22	0.05	0.73	71.83
14	81-2	59.82	0.71	18.06	0.02	2.57	0.19	0.30	0.68	8.26	5.44	0.04	0.28	0.11	0.20	0.05	0.10	98.59
15	81-2	60.11	0.66	18.07	0.01	2.82	0.19	0.27	0.71	8.92	5.51	0.00	0.18	0.08	0.14	0.03	0.09	97.57
16	81-2	60.48	0.68	18.33	0.06	2.83	0.16	0.27	0.66	8.84	5.61	0.02	0.18	0.08	0.21	0.05	0.10	97.86
17	81-2	58.11	0.64	17.80	0.00	2.73	0.15	0.33	3.07	4.71	5.19	0.00	0.17	0.07	0.19	0.04	0.08	93.08
18	81-2	59.81	0.82	18.86	0.05	3.19	0.22	0.27	0.80	9.02	5.87	0.02	0.14	0.08	0.23	0.08	0.07	98.64
19	81-2	60.14	0.69	18.35	0.01	2.89	0.21	0.29	0.61	8.94	5.52	0.04	0.08	0.04	0.22	0.05	0.14	98.01
20	81-2	59.78	0.67	18.67	0.00	3.08	0.24	0.26	0.87	8.98	5.54	0.00	0.12	0.05	0.25	0.08	0.11	98.22
21	81-2	60.04	0.67	18.51	0.02	2.95	0.19	0.29	0.62	8.72	5.86	0.00	0.32	0.14	0.22	0.05	0.10	98.32
22	81-2	59.69	0.63	18.77	0.03	3.16	0.20	0.23	0.53	9.12	5.64	0.00	0.28	0.12	0.26	0.06	0.11	98.48
23	81-2	59.88	0.68	18.75	0.02	2.87	0.23	0.24	0.66	9.20	5.62	0.00	0.21	0.08	0.22	0.05	0.08	98.42
24	81-2	59.90	0.64	18.84	0.06	3.12	0.20	0.24	0.58	9.30	5.47	0.00	0.18	0.07	0.26	0.08	0.13	98.74
25	81-2	59.88	0.58	18.71	0.00	2.92	0.22	0.24	0.56	9.22	5.45	0.00	0.18	0.08	0.24	0.05	0.08	98.11
26	81-2	59.89	0.62	18.78	0.00	2.91	0.22	0.23	0.58	9.20	5.45	0.00	0.22	0.04	0.24	0.05	0.12	98.22
27	81-2	54.68	1.86	17.63	0.00	5.53	0.15	1.75	4.63	6.91	4.00	0.03	0.21	0.09	0.11	0.03	0.24	87.62
28	81-2	55.44	1.88	17.78	0.01	5.17	0.16	1.86	3.75	7.06	4.38	0.05	0.22	0.09	0.14	0.03	0.25	86.01
29	81-2	55.57	1.75	17.56	0.01	5.26	0.21	1.84	3.78	7.22	4.55	0.00	0.18	0.08	0.12	0.03	0.24	86.14
30	81-2	54.00	1.98	17.44	0.00	5.39	0.15	2.01	4.48	7.00	4.19	0.03	0.45	0.19	0.07	0.02	0.21	87.21
31	81-2	55.23	1.99	17.72	0.00	5.44	0.18	1.93	4.43	7.03	3.27	0.00	0.25	0.11	0.09	0.02	0.22	87.64
32	81-2	55.93	1.53	18.21	0.00	4.30	0.13	1.25	3.35	7.31	4.01	0.00	0.11	0.04	0.08	0.02	0.33	86.46
33	81-2	56.17	1.61	18.34	0.00	4.37	0.18	1.33	3.39	7.42	4.22	0.03	0.08	0.18	0.15	0.02	0.33	86.27
34	81-2	54.96	1.59	17.82	0.00	4.62	0.17	1.45	3.99	7.37	3.81	0.00	0.08	0.04	0.09	0.02	0.36	86.16
35	81-2	58.88	1.03	17.89	0.00	3.31	0.13	0.80	1.81	7.50	5.05	0.00	0.23	0.10	0.07	0.02	0.17	98.82
36	81-2	59.75	0.82	17.85	0.00	3.00	0.15	0.58	1.19	7.40	4.90	0.00	0.08	0.04	0.08	0.02	0.15	98.90
37	81-2	54.86	1.91	17.47	0.00	5.47	0.19	1.84	4.21	7.01	4.11	0.00	0.15	0.08	0.08	0.02	0.18	87.20
38	81-2	54.39	1.99	17.54	0.00	5.51	0.13	1.89	4.28	6.89	4.12	0.02	0.33	0.14	0.13	0.03	0.15	87.00
39	81-2	58.04	1.12	18.40	0.00	3.95	0.27	0.83	2.04	8.18	4.98	0.00	0.30	0.13	0.21	0.05	0.09	98.10
40	81-3	59.68	0.69	18.30	0.00	2.85	0.26	0.24	0.62	8.35	5.39	0.00	0.16	0.07	0.27	0.06	0.07	96.42
41	81-3	58.10	0.57	18.11	0.00	2.81	0.16	0.20	0.55	8.51	5.31	0.05	0.18	0.08	0.22	0.05	0.09	94.72
42	81-3	59.20	0.57	18.52	0.03	2.97	0.21	0.23	0.57	8.81	5.85	0.00	0.03	0.01	0.25	0.06	0.07	98.94
43	81-3	59.60	0.58	18.80	0.01	2.84	0.19	0.21	0.55	8.78	5.28	0.00	0.10	0.04	0.21	0.05	0.08	98.95
44	81-3	58.69	0.53	17.71	0.01	2.83	0.24	0.21	0.64	8.42	5.09	0.00	0.25	0.11	0.19	0.04	0.08	92.74
45	81-3	35.88	0.00	27.78	0.03	0.34	0.01	0.00	5.00	19.02	0.22	0.03	0.01	0.00	1.02	0.23	7.81	98.86
46	81-3	57.99	0.80	18.05	0.04	2.71	0.24	0.21	0.54	7.90	5.17	0.01	0.07	0.03	0.22	0.08	0.08	93.74
47	81-3	58.98	0.62	18.34	0.04	2.71	0.26	0.24	0.58	8.75	5.31	0.00	0.23	0.10	0.28	0.05	0.08	98.27
48	81-3	59.40	0.62	18.49	0.04	2.79	0.20	0.23	0.58	8.85	5.31	0.02	0.14	0.08	0.23	0.05	0.13	98.89
49	81-3	59.31	0.58	18.39	0.00	2.81	0.24	0.21	0.57	8.59	5.44	0.00	0.07	0.03	0.30	0.07	0.09	98.50
50	81-3	59.57	0.61	18.68	0.02	2.89	0.26	0.28	0.83	9.18	5.81	0.02	0.21	0.09	0.26	0.08	0.12	98.18
51	81-3	59.11	0.61	18.50	0.01	2.89	0.23	0.24	0.85	8.88	5.29	0.00	0.30	0.13	0.25	0.08	0.08	98.75
52	81-3	58.59	0.59	18.23	0.00	2.93	0.22	0.21	0.88	8.58	5.24	0.00	0.20	0.08	0.26	0.08	0.11	95.67

Analysis	Sample	O	Si	Ti	Al	Cr	Fe ₂	Mn	Mg	Ca	Na	K	Ni	F	Cl	S	Total	X	Y
1	81-1	10.000	3.524	0.027	1.303	0.001	0.139	0.012	0.022	0.041	1.047	0.415	0.002	0.002	0.030	0.004	6.536	9.825	80.111
2	81-1	10.000	3.546	0.028	1.303	0.002	0.138	0.011	0.023	0.037	0.980	0.416	0.000	0.030	0.027	0.003	6.492	9.821	81.754
3	81-1	10.000	3.565	0.029	1.296	0.000	0.136	0.012	0.025	0.041	0.989	0.425	0.000	0.041	0.023	0.002	6.491	9.823	82.818
4	81-1	10.000	3.549	0.028	1.303	0.000	0.143	0.011	0.022	0.043	0.984	0.432	0.000	0.045	0.025	0.003	6.488	9.752	85.385
5	81-1	10.000	3.507	0.012	1.352	0.007	0.100	0.004	0.027	0.023	1.285	0.288	0.000	0.000	0.022	0.000	6.594	7.507	88.502
6	81-1	10.000	3.535	0.028	1.297	0.000	0.149	0.011	0.025	0.111	0.981	0.427	0.001	0.041	0.028	0.005	6.567	13.547	74.779
7	81-1	10.000	3.581	0.025	1.350	0.000	0.099	0.008	0.026	0.038	1.241	0.305	0.000	0.035	0.030	0.006	6.798	15.256	86.814
8	81-1	10.000	3.543	0.025	1.296	0.001	0.148	0.013	0.020	0.033	1.028	0.403	0.001	0.025	0.021	0.005	6.510	18.400	85.011
9	81-1	10.000	3.554	0.027	1.299	0.001	0.142	0.010	0.021	0.038	0.989	0.409	0.000	0.056	0.029	0.007	6.497	16.487	84.900
10	81-1	10.000	3.547	0.027	1.294	0.001	0.149	0.012	0.023	0.043	0.988	0.415	0.001	0.030	0.028	0.004	6.502	17.924	84.683
11	81-1	10.000	3.533	0.028	1.300	0.002	0.150	0.013	0.022	0.038	1.021	0.414	0.001	0.039	0.025	0.005	6.526	17.863	84.328
12	81-1	10.000	3.544	0.027	1.301	0.000	0.142	0.010	0.023	0.039	1.028	0.419	0.000	0.058	0.028	0.004	6.535	16.771	83.980
13	81-1	10.000	3.799	0.021	1.385	0.002	0.050	0.000	0.025	0.046	1.100	0.332	0.046	0.058	0.046	0.005	6.586	16.295	83.818
14	81-2	10.000	3.578	0.023	1.271	0.001	0.128	0.010	0.023	0.057	0.914	0.402	0.0						

Analysis	Sample	SiO2	TiO2	Al2O3	Cr2O3	FeO	MnO	MgO	CaO	Na2O	K2O	NiO	F	-O=F	Cl	-O=Cl	SO3	Total
1	81-6	60.21	0.78	18.19	0.00	2.84	0.15	0.25	0.63	8.23	5.76	0.00	0.00	0.00	0.13	0.03	0.16	97.08
2	81-6	60.05	0.73	18.20	0.02	2.83	0.19	0.28	0.66	8.56	5.73	0.00	0.01	0.01	0.17	0.04	0.11	97.31
3	81-6	60.29	0.68	18.44	0.00	2.78	0.16	0.28	0.65	8.67	5.61	0.05	0.00	0.00	0.22	0.05	0.15	97.92
4	81-6	60.00	0.73	18.19	0.00	2.86	0.19	0.26	0.71	8.39	5.63	0.00	0.08	0.04	0.20	0.05	0.11	97.08
5	81-6	60.04	0.69	18.23	0.02	2.84	0.16	0.28	0.63	8.53	5.42	0.01	0.13	0.05	0.21	0.05	0.12	97.22
6	81-6	60.28	0.74	18.18	0.00	2.77	0.18	0.27	0.62	8.78	5.55	0.00	0.15	0.06	0.21	0.05	0.14	97.76
7	81-6	60.28	0.71	18.28	0.00	2.66	0.26	0.24	0.83	8.79	5.71	0.00	0.15	0.08	0.19	0.04	0.15	97.86
8	81-6	60.10	0.73	18.32	0.00	2.56	0.19	0.27	0.69	8.96	5.58	0.00	0.12	0.05	0.21	0.05	0.15	97.44
9	81-6	60.36	0.74	18.54	0.00	2.79	0.16	0.26	0.66	8.81	5.63	0.01	0.25	0.11	0.15	0.04	0.11	98.13
10	81-6	60.20	0.73	18.44	0.05	2.69	0.17	0.25	0.66	8.57	5.82	0.00	0.48	0.20	0.18	0.04	0.14	98.33
11	81-6	60.28	0.75	18.30	0.00	2.79	0.20	0.27	0.65	8.66	5.64	0.00	0.21	0.09	0.18	0.04	0.18	97.98
12	81-6	60.07	0.71	18.36	0.00	2.84	0.27	0.24	0.65	8.72	5.52	0.00	0.14	0.06	0.20	0.05	0.11	97.74
13	81-6	59.59	0.69	18.44	0.00	3.07	0.18	0.37	0.73	8.91	5.42	0.03	0.31	0.13	0.23	0.05	0.12	97.91
14	81-4	58.94	0.41	19.10	0.01	1.62	0.11	0.16	1.07	6.52	5.24	0.00	0.11	0.05	0.23	0.05	0.04	93.85
15	81-4	60.39	0.49	19.17	0.01	1.14	0.05	0.17	1.52	6.96	4.41	0.01	0.06	0.03	0.06	0.01	0.03	94.77
16	81-4	59.36	0.37	19.02	0.00	1.92	0.08	0.32	1.76	6.96	4.26	0.01	0.06	0.03	0.06	0.02	0.02	94.30
17	81-4	54.59	1.26	18.41	0.01	3.85	0.16	1.39	3.46	6.48	3.72	0.04	0.12	0.05	0.18	0.04	0.07	93.86
18	81-4	57.96	0.43	18.71	0.00	2.14	0.16	0.18	0.84	6.68	5.68	0.00	0.05	0.02	0.26	0.06	0.03	93.07
19	81-4	60.37	0.24	19.90	0.00	1.06	0.01	0.07	2.00	7.34	3.93	0.00	0.00	0.00	0.11	0.03	0.01	95.01
20	81-4	58.05	0.86	18.63	0.03	2.89	0.13	1.07	3.65	6.73	3.28	0.00	0.09	0.04	0.07	0.02	0.03	95.64
21	81-4	56.63	0.40	18.19	0.04	1.95	0.08	0.27	1.79	7.11	3.39	0.00	0.06	0.03	0.06	0.01	0.03	89.96
22	81-4	58.21	0.40	19.05	0.03	1.85	0.14	0.14	1.06	7.20	5.30	0.02	0.07	0.03	0.23	0.05	0.02	93.85
23	81-4	59.34	0.38	19.32	0.01	1.52	0.15	0.11	1.51	7.16	4.72	0.03	0.15	0.06	0.20	0.05	0.02	94.49
24	81-4	61.02	0.20	19.34	0.02	0.99	0.09	0.04	1.57	7.24	4.88	0.00	0.00	0.00	0.08	0.02	0.00	95.47
25	81-4	57.06	0.39	18.61	0.00	1.91	0.17	0.16	0.85	6.96	5.74	0.00	0.04	0.02	0.28	0.06	0.04	91.83
26	81-4	57.36	0.50	18.85	0.00	2.85	0.13	0.17	1.40	6.81	4.48	0.00	0.02	0.01	0.15	0.03	0.01	92.48

Analysis	Sample	O	Si	Ti	Al	Cr	Fe2	Mn	Mg	Ca	Na	K	Ni	F	Cl	S	Total	X	Y
1	81-6	10.000	3.593	0.035	1.268	0.000	0.130	0.007	0.022	0.040	0.944	0.435	0.000	0.000	0.013	0.007	6.481	10.045	59.940
2	81-6	10.000	3.595	0.033	1.270	0.001	0.130	0.010	0.025	0.042	0.983	0.433	0.000	0.002	0.017	0.005	6.486	9.825	59.282
3	81-6	10.000	3.548	0.030	1.279	0.000	0.137	0.006	0.024	0.041	0.969	0.421	0.002	0.000	0.022	0.007	6.486	12.804	52.263
4	81-6	10.000	3.562	0.033	1.273	0.000	0.132	0.010	0.023	0.045	0.986	0.426	0.000	0.016	0.021	0.005	6.474	12.526	52.073
5	81-6	10.000	3.581	0.031	1.275	0.001	0.141	0.009	0.026	0.040	0.981	0.410	0.001	0.024	0.021	0.005	6.478	12.943	51.530
6	81-6	10.000	3.590	0.033	1.268	0.000	0.137	0.009	0.023	0.039	1.006	0.418	0.000	0.027	0.021	0.006	6.488	14.167	51.480
7	81-6	10.000	3.558	0.031	1.270	0.000	0.131	0.012	0.021	0.040	1.006	0.430	0.000	0.027	0.019	0.006	6.506	16.375	55.073
8	81-6	10.000	3.555	0.032	1.277	0.000	0.127	0.006	0.024	0.044	0.984	0.421	0.000	0.022	0.021	0.007	6.489	15.866	54.583
9	81-6	10.000	3.595	0.033	1.285	0.000	0.137	0.008	0.023	0.042	0.983	0.423	0.000	0.047	0.015	0.005	6.494	15.394	54.649
10	81-6	10.000	3.558	0.032	1.285	0.003	0.143	0.009	0.022	0.042	0.982	0.439	0.000	0.060	0.018	0.006	6.519	15.323	54.569
11	81-6	10.000	3.555	0.033	1.272	0.000	0.137	0.010	0.023	0.041	0.980	0.424	0.000	0.039	0.018	0.008	6.485	15.259	52.171
12	81-6	10.000	3.550	0.032	1.280	0.000	0.140	0.013	0.021	0.041	0.999	0.416	0.000	0.025	0.020	0.005	6.496	16.299	51.304
13	81-6	10.000	3.535	0.031	1.290	0.000	0.153	0.009	0.033	0.047	1.025	0.410	0.001	0.059	0.023	0.005	6.537	17.837	48.785
14	81-4	10.000	3.578	0.019	1.397	0.000	0.092	0.005	0.015	0.070	0.767	0.406	0.000	0.020	0.023	0.002	6.323	38.637	58.513
15	81-4	10.000	3.562	0.022	1.344	0.000	0.057	0.003	0.015	0.116	0.806	0.334	0.001	0.012	0.005	0.002	6.291	34.291	58.750
16	81-4	10.000	3.570	0.017	1.348	0.000	0.097	0.004	0.029	0.113	0.810	0.327	0.001	0.012	0.009	0.001	6.318	38.447	59.417
17	81-4	10.000	3.394	0.080	1.345	0.001	0.200	0.009	0.129	0.230	0.779	0.294	0.002	0.023	0.016	0.003	6.434	40.250	59.667
18	81-4	10.000	3.595	0.020	1.368	0.000	0.110	0.008	0.017	0.056	0.797	0.446	0.000	0.010	0.027	0.002	6.374	41.368	59.246
19	81-4	10.000	3.573	0.011	1.388	0.000	0.062	0.001	0.007	0.127	0.842	0.297	0.000	0.000	0.011	0.001	6.297	41.102	57.509
20	81-4	10.000	3.471	0.039	1.327	0.001	0.144	0.007	0.086	0.234	0.781	0.250	0.000	0.016	0.007	0.002	6.350	40.697	54.708
21	81-4	10.000	3.590	0.019	1.348	0.002	0.102	0.004	0.025	0.121	0.867	0.272	0.000	0.013	0.007	0.002	6.322	40.056	55.515
22	81-4	10.000	3.552	0.018	1.370	0.002	0.095	0.007	0.013	0.070	0.852	0.413	0.001	0.014	0.023	0.001	6.394	40.138	54.911
23	81-4	10.000	3.571	0.017	1.370	0.000	0.078	0.007	0.010	0.098	0.835	0.383	0.001	0.026	0.021	0.001	6.349	39.905	55.238
24	81-4	10.000	3.605	0.009	1.347	0.001	0.049	0.005	0.004	0.099	0.830	0.398	0.000	0.000	0.009	0.000	6.316	39.950	54.996
25	81-4	10.000	3.559	0.019	1.361	0.000	0.100	0.009	0.015	0.043	0.842	0.487	0.000	0.006	0.029	0.002	6.408	38.143	56.947
26	81-4	10.000	3.536	0.023	1.370	0.000	0.136	0.007	0.016	0.083	0.814	0.352	0.000	0.004	0.016	0.000	6.348	37.989	57.399

Analysis	Sample	SiO2	TiO2	Al2O3	Cr2O3	FeO	MnO	MgO	CaO	Na2O	K2O	NiO	F	-O=F	Cl	-O=Cl	SO3	Total
1	46-3	54.79	0.36	18.01	0.02	1.78	0.15	0.17	0.85	7.56	5.18	0.00	0.05	0.02	0.22	0.05	0.04	89.00
2	46-3	58.03	0.30	18.86	0.00	1.30	0.10	0.11	1.46	7.21	4.70	0.00	0.22	0.09	0.18	0.04	0.03	92.37
3	46-3	59.39	0.34	19.42	0.01	1.57	0.12	0.12	1.18	7.40	5.27	0.00	0.00	0.00	0.18	0.04	0.04	95.00
4	46-3	58.87	0.35	19.19	0.02	1.09	0.05	0.11	1.89	7.31	4.00	0.00	0.00	0.00	0.10	0.02	0.07	93.02
5	46-3	57.89	0.36	18.85	0.01	1.82	0.12	0.14	1.01	7.84	5.34	0.00	0.14	0.06	0.25	0.08	0.00	93.24
6	46-3	55.24	0.36	18.30	0.01	1.72	0.10	0.16	1.06	7.19	4.89	0.01	0.00	0.00	0.21	0.05	0.10	89.31
7	46-3	59.02	0.36	19.28	0.05	1.78	0.12	0.14	1.07	7.79	5.24	0.02	0.04	0.02	0.19	0.04	0.05	95.06
8	46-3	52.89	1.94	18.46	0.04	8.32	0.24	1.53	5.11	6.87	1.98	0.00	0.00	0.00	0.06	0.01	0.14	98.17
9	46-3	61.61	0.27	19.93	0.00	1.12	0.07	0.07	1.87	7.64	4.01	0.00	0.00	0.00	0.00	0.18	0.04	93.02
10	46-3	59.41	0.30	19.46	0.00	1.53	0.08	0.13	1.26	8.14	5.05	0.01	0.08	0.04	0.18	0.04	0.03	96.89
11	46-3	59.54	0.35	19.46	0.00	1.51	0.10	0.11	1.62	7.82	4.86	0.00	0.25	0.11	0.18	0.04	0.08	95.47
12	46-3	59.06	0.37	19.27	0.01	1.46	0.07	0.17	1.34	7.53	4.88	0.01	0.26	0.11	0.18	0.04	0.04	94.48
13	46-3	58.66	0.36	19.37	0.01	2.06	0.18	0.18	0.98	8.15	5.42	0.02	0.25	0.11	0.23	0.05	0.02	95.66
14	46-3	59.89	0.32	19.42	0.00	1.57	0.04	0.12	1.49	7.74	4.80	0.00	0.00	0.00	0.13	0.03	0.02	95.31
15	46-3	59.27	0.34	19.54	0.00	1.53	0.13	0.13	1.71	7.74	4.74	0.02	0.17	0.07	0.19	0.04	0.10	95.48
16	46-3	58.31	0.41	19.17	0.02	2.06	0.15	0.18	0.74	8.12	5.58	0.00	0.15	0.08	0.27	0.08	0.07	95.95
17	46-3	52.55	0.58	25.05	0.01	2.17	0.08	0.86	9.13	4.95	1.28	0.02	0.18	0.08	0.01	0.00	0.10	95.95
18	46-3	53.92	1.18	18.71	0.01	3.07	0.17	0.70	3.35	8.28	4.81	0.01	0.01	0.01	0.38	0.09	0.73	95.24
19	46-3	56.52	1.15	18.80	0.02	4.14	0.18	0.83	4.16	7.43	2.90	0.00	0.14	0.06	0.12	0.03	0.19	96.45
20	46-3	56.21	1.14	19.11	0.02	3.99	0.10	0.90	3.89	7.44	3.40	0.00	0.00	0.00	0.13	0.03	0.18	96.45
21	46-3	58.36	0.48	19.24	0.01	2.35	0.18	0.21	0.83	7.95	5.64	0.00	0.19	0.08	0.32	0.07	0.04	95.61
22	46-3	55.84	1.19	19.73	0.03	3.72	0.13	1.05	3.84	6.89	3.65	0.00	0.00	0.00	0.09	0.02	0.22	95.67
23	46-3	60.24	0.40	19.08	0.00	1.46	0.08	0.09	1.12	7.77	5.45	0.01	0.08	0.04	0.18	0.03	0.01	96.28
24	46-3	56.98	0.41	19.19	0.00	1.80	0.08	0.25	1.30	7.53	5.16	0.00	0.11	0.04	0.22	0.05	0.02	94.75
25	46-3	54.80	1.43	19.05	0.00	4.79	0.14	1.53	5.12	6.85	2.43	0.00	0.09	0.04	0.04	0.01	0.38	95.50
26	46-3	55.19	1.31	18.85	0.00	4.46	0.25	1.13	5.03	7.23	3.18	0.00	0.18	0.07	0.16	0.04	0.27	95.91
27	46-1	45.07	4.02	15.48	0.00	8.12	0.18	6.30	10.05	4.85	2.34	0.05	0.21	0.09	0.01	0.00	0.20	96.89
28	46-1	51.19	2.10	17.80	0.00	8.12	0.18	2.88	6.24	8.24	3.48	0.00	0.08	0.04	0.14	0.03	0.19	96.24
29	46-1	18.30	1.00	6.34	0.00	2.86	0.03	1.75	35.35	2.42	1.04	0.02	0.08	0.03	0.05	0.01	0.13	99.34
30	46-1	54.93	1.58	17.68	0.00	5.39	0.23	1.67	3.37	7.42	4.35	0.00	0.23	0.19	0.08	0.21	0.05	93.18
31	46-1	47.94	3.13	15.31	0.00	7.11	0.17	4.87	10.38	5.44	2.49	0.01	0.24	0.10	0.10	0.02	0.04	97.04
32	46-1	41.44	1.90	14.26	0.00	6.89	0.14	2.01	14.38	5.97	2.89	0.00	0.28	0.12	0.09	0.02	0.22	96.14
33	46-1	64.57	0.12	18.74	0.00	0.89	0.04	0.01	0.39	7.25	6.16	0.01	0.02	0.01	0.04	0.01	0.08	98.08
34	46-1	6.44	0.19	1.88	0.00	0.56	0.04	0.08	0.27	1.20	1.20	0.00	0.18	0.08	0.42	0.09	0.36	13.54
35	46-1	57.94	1.02	18.48	0.07	4.29	0.20	0.91	2.51	7.73	4.73	0.01	0.25	0.11	0.19	0.04	0.11	98.29
36	46-1	51.27	2.11	17.18	0.00	6.51	0.27	2.55	5.94	6.84	3.78	0.00	0.42	0.18	0.14	0.03	0.14	98.81
37	46-1	42.88	2.48	15.22	0.02	8.08	0.18	2.78	10.81	5.95	2.58	0.01	0.14	0.08	0.08	0.02	0.25	91.28
38	46-1	48.01	2.94	17.79	0.01	8.21	0.20	3.39	6.38	5.30	2.28	0.00	0.13	0.05	0.13	0.03	0.17	95.88
39	46-1	51.47	1.46	18.00	0.06	4.41	0.19	0.71	4.15	5.17	3.29	0.00	0.20	0.09	0.17	0.04	0.17	96.33
40	46-1	48.88	2.75	17.39	0.01	7.90	0.17	2.78	8.44	5.72	2.13	0.00	0.24	0.10	0.07	0.02	0.27	95.64

Analysis	Sample	O	Si	Ti	Al	Cr	Fe2	Mn	Mg	Ca	Na	K	Ni	F	Cl	S	Total	X	Y
1	46-3	10.000	3.830	0.017	1.368	0.001	0.036	0.008	0.017	0.059	0.944	0.427	0.000	0.011	0.024	0.002	6.467	13.903	54.719
2	46-3	10.000	3.575	0.014	1.370	0.000	0.087	0.005	0.010	0.088	0.881	0.386	0.000	0.043	0.019	0.001	6.369	10.779	54.822
3	46-3	10.000	3.557	0.016	1.371	0.001	0.078	0.005	0.011	0.076	0.859	0.403	0.000	0.000	0.018	0.002	6.378	8.801	54.790
4	46-3	10.000	3.567	0.016	1.370	0.001	0.055	0.002	0.010	0.122	0.859	0.308	0.000	0.000	0.010	0.003	6.315	8.952	54.940
5	46-3	10.000	3.556	0.017	1.365	0.001	0.083	0.008	0.013	0.088	0.910	0.418	0.000	0.028	0.028	0.000	6.435	6.300	54.846
6	46-3	10.000	3.531	0.017	1.379	0.001	0.092	0.005	0.015	0.073	0.891	0.389	0.000	0.000	0.023	0.005	6.409	6.052	54.915
7	46-3	10.000	3.545	0.017	1.365	0.002	0.089	0.008	0.013	0.099	0.907	0.401	0.001	0.008	0.020	0.002	6.418	7.729	53.998
8	46-3	10.000	3.198	0.089	1.322	0.002	0.473	0.012	0.136	0.332	0.785	0.153	0.000	0.000	0.005	0.006	6.510	16.865	60.344
9	46-3	10.000	3.590	0.012	1.365	0.000	0.054	0.004	0.008	0.116	0.884	0.297	0.000	0.000	0.008	0.001	6.319	13.655	53.185
10	46-3	10.000	3.547	0.014	1.371	0.000	0.078	0.004	0.011	0.081	0.943	0.385	0.000	0.016	0.018	0.001	6.432	13.642	53.843
11	46-3	10.000	3.557	0.016	1.370	0.000	0.075	0.005	0.010	0.104	0.905	0.385	0.000	0.048	0.017	0.002	6.399	13.696	55.778
12	46-3	10.000	3.595	0.017	1.371	0.000	0.074	0.003	0.016	0.086	0.881	0.378	0.000	0.050	0.016	0.002	6.390	13.462	55.803
13	46-3	10.000	3.532	0.016	1.374	0.000	0.104	0.009	0.016	0.052	0.851	0.416	0.001	0.048	0.023	0.001	6.482	14.571	55.672
14	46-3	10.000	3.657	0.014	1.364	0.000	0.078	0.002	0.011	0.086	0.895	0.385	0.000	0.000	0.013	0.001	6.381	14.291	55.800
15	46-3	10.000	3.542	0.015	1.376	0.000	0.076	0.008	0.011	0.109	0.867	0.381	0.001	0.002	0.019	0.005	6.400	15.115	52.908
16	46-3	10.000	3.530	0.019	1.368	0.001	0.104	0.008	0.016	0.048	0.953	0.431	0.000	0.028	0.027	0.003	6.481	15.275	52.973
17	46-3	10.000	3.123	0.025	1.755	0.001	0.108	0.003	0.049	0.581	0.570	0.097	0.001	0.035	0.001	0.004	6.317	8.570	57.444
18	46-3	10.000	3.319	0.055	1.368	0.000	0.158	0.009	0.084	0.221	0.989	0.378	0.001	0.002	0.040	0.034	6.584	9.115	56.546
19	46-3	10.000	3.395	0.052	1.331	0.001	0.208	0.008	0.074	0.288	0.885	0.223	0.000	0.026	0.012	0.008	6.433	8.910	56.243
20	46-3	10.000	3.378	0.051	1.353	0.001	0.200	0.005	0.081	0.250	0.898	0.280	0.000	0.000	0.013	0.007	6.481	8.036	56.325
21	46-3	10.000	3.524	0.022	1.369	0.001	0.119	0.008	0.016	0.083	0.931	0.434	0.000	0.006	0.033	0.002	6.482	7.507	57.457
22	46-3	10.000	3.354	0.054	1.367	0.002	0.187	0.007	0.094	0.247	0.780	0.272	0.000	0.000	0.009	0.010	6.403	7.343	57.324
23	46-3	10.000	3.598	0.018	1.353	0.000	0.072	0.004	0.008	0.071	0.882	0.419	0.001	0.016	0.015	0.001	6.406	7.310	56.099
24	46-3	10.000	3.554	0.018	1.363	0.000	0.081	0.005	0.022	0.084	0.879	0.398	0.000	0.020	0.023	0.001	6.403	7.125	56.081
25	46-3	10.000	3.303	0.085	1.352	0.000	0.241	0.007	0.137	0.330	0.778	0.187	0.000						

Appendix 5: Instructions for the AMS computer programmes

(1)BODGE: Adjusts the orientation of the AMS axes to the correct geographical position and corrects for bedding. Generates an .OUT file.

Instruction	Response
Open Programme	
Type 0 for SusaM, 1 for SusaR data:	1
Type Input File Name:	? .ASC (e.g. 1.ASC)
Type Output File Name:	? .OUT (e.g. 1.OUT)
Vol Nom =10.00 Vol Act =10 New Vol = 10	10
Drilled in the field =7 Drilled from a block =2	7 or 2
If 7: Input Core Dec, Core Dip, Face Strike	If 7: Azimuth of core, Plunge of the core, Strike of the rock surface
If 2: Input Core Dec, Core Dip, Drill Dip, Drill Pitch	If 2: Strike of the rock surface & Dip of the rock surface (obtained in the field), Drill Dip & Drill Pitch (obtained in the lab)
Bed Dec, Bed Dip	Strike of the bedding, Dip of the bedding

Repeat for each sample in .ASC file. Programme ends automatically when all the samples have been corrected.

(2) MEASUER: Generate .LFP, .PLT and the .RES files.

Instruction	Response
Open Programme	
Name of input file:	? .OUT (e.g. 1.OUT)

Programme ends automatically.

(3) MANIFIG: Plots the Magnetic susceptibility axes on a stereonet. Produces a .PLT file

Instruction	Response
Open Programme	
Screen Dump:	N
HPGL:	Y
Postscript:	N
Specify out name:	Type name: ? (e.g. 1)
Prompt:	a
Type file name on input data:	? .PLT (e.g. 1.PLT)
Type 1 to include error limits in .PAR, 0 to omit:	0
Input plot header:	Type name
Corrected (Bedding =B)	B
Specimen Numbering 0=off, 1=on	1
Ellipses:	0

Press enter return twice to end programme and view the stereonet.

(4) LF Plot: Plots the lineation-foliation plot. Produces a .PLT file

Instruction	Response
Open programme	
Type file name for input:	?LFP (1.LFP)
Speciman numbering 0=off 1=on	1
Error bars 0=off 1=on	0
Input 0 to accept default, 1 to change	0
Screen dump:	N
HPGL:	Y
Postscript:	N
Filename:	Type name
Prompt:	a

L/F plot displayed. Return to exit.

(5) MEASAVR: Generates .AVE file

Instruction	Response
Open programme	
Name of input file:	?OUT (e.g. 1.OUT)
Type 0 for field-corrected, 1 for bed-corrected data:	1
Header for out file:	Type name (e.g. 1)

(6) JELANEW6: Generates .CV6, .PL6, .RS6 files.

Instruction	Response
Open programme	
Name of input file:	?AVE (e.g. 1.AVE)
Mean (0) or population (1) covariance? Input 0/1:	0

Programme ends automatically.

(7) ANISFIG: Plots the mean magnetic susceptibility axes and their 95% confidence ellipses on a stereonet.

Instruction	Response
Open programme	
Screen dump:	N
HPGL:	Y
Postscript:	N
Filename:	Type name
Type file name of input data:	?PL6 (e.g. 1.PL6)
Type 1 to continue (then enter again) & page through specimens; or 0 to quit:	1

Stereonet displayed.